2016

Environmental factors affecting the residence time distribution dynamics of constructed agricultural wetlands

David Immanuel Green
Iowa State University

Environmental factors affecting the residence time distribution dynamics of constructed agricultural wetlands

by

David Immanuel Green

A dissertation submitted to the graduate faculty

in partial fulfillment of the requirements for the degree of

DOCTOR OF PHILOSOPHY

Major: Environmental Science

Program of Study Committee:
William G. Crumpton, Co-Major Professor
Matthew J. Helmers, Co-Major Professor
Chris R. Rehmann
James W. Raich
Roy R. Gu

Iowa State University

Ames, Iowa

2016

DEDICATION

This dissertation is dedicated to my wife, Claudette. Thank you for your immense courage, patience, support, and gentle (and not so gentle) prodding. I love you. I also dedicate this dissertation to my parents Debby and Alex, and to my siblings Rowananne and Marsten. Thank you, Mom and Dad, for instilling in your children a humble curiosity about the world without which this would not have been possible.

TABLE OF CONTENTS

ACKNOWLEDGMENTS

I would like to thank my major professors Drs. William G. Crumpton and Matthew J. Helmers, and my committee members Drs. Chris R. Rehmann, James W. Raich, and Roy R. Gu for their guidance and support throughout my graduate studies at Iowa State University.

In addition, I would also like to thank my friends, colleagues, and the Ecology Evolution, and Organismal Biology departmental faculty and staff for making my time at Iowa State University a unique experience. In particular, I want to also offer my sincere appreciation to those who assisted me with field surveys and data collection, without whom this thesis would not have been possible.

CHAPTER 1. GENERAL INTRODUCTION

The drive towards increased agricultural production in the United States, particularly in the Midwestern Corn Belt region, has concomitantly increased the need for and importance of low-cost solutions for mitigating the environmental impacts of farming, especially with respect to surface water quality (Mitsch and Day, 2006; Crumpton et al., 2012). Constructed wetlands have been proven to be an effective and economical option for addressing this challenge and can serve as an important component of integrative and comprehensive agricultural non-point source nutrient loading management strategies (Woltemade, 2000; Zedler, 2003; Crumpton et al., 2012; Iowa Nutrient Reduction Strategy, 2016).

Wetlands designed to intercept agricultural drainage and runoff have been effectively used to reduce surface water nitrate loads (Fink and Mitsch, 2004), field phosphorous exports (Woltemade, 2000), and pesticides (Stearmean et al., 2003) in a variety of agricultural systems. Currently there is a very large multi-state effort across the Midwestern Corn Belt region to increase the number of constructed wetlands in agriculturally intensive watersheds (Allen, 2005) as an essential component of on and off-field nutrient management efforts (Crumpton et al., 2012; Iowa Nutrient Reduction Strategy, 2016). These actions are taken, in part, in support of a long-term reduction in total annual nutrient loads into the Mississippi River with the goal of reducing the size of the hypoxic zone in the Gulf of Mexico (Iowa Nutrient Reduction Strategy, 2016).

Since 2001, in Iowa alone, approximately 80 wetlands have been constructed under the Iowa Conservation Reserve Enhancement Program (Iowa CREP), with additional wetland acreage established through other wetland restoration programs (Iowa Nutrient Reduction Strategy, 2016) Similar initiatives have been implemented in other agriculture-intensive states (Allen, 2005). This

increase in the prevalence of constructed agricultural wetlands in Iowa and throughout the U.S. Corn Belt region dictates the need for a systematic survey of constructed wetland nutrient removal performance factors to help guide future wetland siting and design. To further these efforts a greater understanding of the mass transport mechanics of these systems is essential.

Wetlands developed to intercept agricultural drainage and runoff differ from more traditional constructed treatment wetlands, such as tertiary treatment systems (e.g. Keefe et al., 2010), in several key ways. For one, agricultural wetlands are typically built at the termini of tile-drained farmed watersheds and as such receive unregulated nutrient mass and hydrological loads. Further, these systems are subjected to continually time-varying atmospheric and ecological conditions, and tend to operate as passive, unmanaged, systems. In some respects, these wetlands can be regarded as small and shallow run-of-the-river type impoundments (e.g. Mossman et al., 1991).

The long-term ability of constructed agricultural wetlands to reduce nutrient loads from farmed watersheds is dependent upon several overarching factors including landscape position (Crumpton et al., 2006); 2), wetland area (Crumpton et al., 2006) and the residence time distribution (RTD) of the system, which characterizes internal mixing patterns (e.g. Kadlec, 1994; Persson, 2000; Kadlec and Wallace, 2008). However, mixing processes in agricultural treatment wetlands are poorly understood even though mixing behavior has been shown to have considerable impact on the constituent removal performance of shallow flow-through basins in general (e.g. Kadlec, 1994; Kadlec and Wallace, 2008; Keefe et al., 2010) and strongly influences some wetland biogeochemical and ecosystem processes. Mixing influences wetland treatment performance by directing the spatial distribution of influent materials throughout the system, thereby determining the area and volume of the basin which is active in treatment, and by dictating the quantity and

rate of delivery of materials to reactive media. For a system operating under steady flow conditions, the rate and extent of mixing is primarily governed by wetland bathymetry and the presence of submersed elements or structures, such as from vegetation. However, mixing in these systems is also highly affected by environmental factors such as the ambient momentum of the inflow channel (Shaw et al., 1997; Holland et al., 2004), wind speed and direction (Thackston et al., 1987; Shaw et al., 1995; Bentzen et al., 2008; Andradóttir and Mortamet, 2016), and the complex interactions between these effects and the seasonal growth and senescence of emergent and submersed aquatic vegetation (e.g. Wörman and Kronnäs, 2005). How these factors influence mixing in these systems individually and in concert is an under-explored topic, particularly with respect to the shallow run-of-the-river type systems exemplified by wetlands developed in agricultural watersheds. A more fully developed understanding of mixing processes in these types of wetlands can aide wetland designers and modelers by providing information on the potential range of mixing conditions within a given system over time (and thus account for these effects in wetland nutrient performance models). This information can provide guidance, in conjunction with existing wetland design best practices (e.g. Perrson 2000), on how to mitigate for deleterious environmental mixing effects by instituting desirable hydraulic performance in the wetland design process, prior to wetland development.

This dissertation explores the topic of mixing in constructed agricultural wetlands, and the environmental factors which control mixing behavior. Further, this dissertation addresses the issue of tracer decay, a common occurrence in natural flow systems, on estimation of the moments of developed RTD, and by extension, on common measures of mixing. The structure of this dissertation is centered around a set of hydraulic tracer studies conducted on a sub-sample of wetlands currently enrolled in the Iowa CREP. Studies were conducted to examine the hydraulic

and mixing behavior of these systems over a range of environmental and vegetated conditions. This information was collected in support of an ongoing effort at Iowa State University to monitor and model the nutrient removal performance of constructed agricultural wetlands, with the explicit intent of understanding the role of mixing on wetland nutrient removal performance.

Dissertation Organization

This dissertation is composed of three manuscripts written for eventual publication in journals which focus on constructed wetland dynamics and water resources.

The first paper is written for submission to the journal *Ecological Engineering*. David I. Green will be the first author, and William G. Crumpton will be the second author. This paper describes an extensive field campaign to observe and document variability of the residence time distribution characteristics of a representative set of Iowa CREP wetlands, accompanied by subsequent analysis of the correlations between temporal characteristics of developed RTD and derived mixing parameters, and aggregate measures of the environmental effects of flow rate, wind shear, wind direction, and vegetation density.

The second paper is written for submission to the journal *Water Resources Research*. David I. Green will be the first author, and William G. Crumpton will be the second author. This paper describes the detailed modeling of mixing dynamics in a single Iowa CREP wetland using the 3-dimensional Environmental Fluid Dynamics Code (EFDC) hydrodynamic and mass transport model. The paper demonstrates the efficacy of the EFDC model for use in simulating mixing in small and shallow flow-through basins, and details the use of the model to assess the relative influences of variable flow rates, wind speeds, and external temperature forcing on simulated residence time distribution characteristics for this wetland.

The third paper is written for submission to the *Journal of Hydrology*. David I. Green will be the first author, Greg Stenback will be the second author, and William G. Crumpton will be the third author. This paper describes the development of a set of algebraic equations relating the raw moments of decay affected RTD and the decay rate coefficients for constant, zero, and first-order decay processes for generic flow domains. The formulas are tested and verified using a simulated set of decay affected RTD.

A general summary chapter (Chapter 5) follows the three papers. References cited in Chapters 1 and 5 are given following Chapter 5.

CHAPTER 2. RESIDENCE TIME DISTRIBUTION CHARACTERISTICS AND SYSTEM-SCALE MIXING PROPERTIES OF CONSTRUCTED AGRICULTURAL WETLANDS

A paper to be submitted to the journal Ecological Engineering

David I. Green and William G. Crumpton

Abstract

Shallow flow-through surface water wetlands are becoming increasingly common in farmed landscapes to mitigate agricultural runoff, with particular emphasis on nutrient abatement. Agricultural wetlands such as those enrolled in the Iowa Conservation Reserve Enhancement Program are positioned in farmed landscapes and receive unregulated hydrological and nutrient loads from upland sources. Further, these systems are continually subjected to transient atmospheric conditions, and feature large seasonal variations in submersed aquatic vegetation growth. As such, these systems can reasonably be considered as shallow run-of-the-river type impoundments, and likely possess highly dynamic mixing characteristics, the drivers of which are not well understood. To obtain information about the variability of the hydraulic characteristics of these types of shallow flow-through basins, we conducted 30 hydraulic tracer studies on 5 wetlands currently enrolled in the Iowa Conservation Reserve Enhancement Program. Tracer studies were conducted over a large range of flow, meteorological, and submersed vegetation growth conditions. Mixing characteristics were assessed by evaluating the temporal features of developed residence time distribution curves. Linear and non-linear

robust regression was used to correlate mixing characteristics with means of measured time-varying environmental effects. The considered environmental effects included mean turbulent bed shear velocities, wind-induced turbulent surface shear velocities, wind speeds relative to respective basin flow directions, and percent vegetative canopy cover. Of the mixing characteristics evaluated, the longitudinal dispersion coefficient and the Péclet number exhibited the greatest degree of variability for all sites, followed by measures of short-circuiting as exemplified by non-dimensional normalized initial and peak arrival times of tracer. All wetlands evaluated demonstrated mixing characteristics that are common to treatment wetlands and shallow flow-through basins in general, suggesting that these run-of-the-river type shallow flow-through impoundments operate with respect to their mixing characteristics in a manner that is similar to other types of treatment wetlands. Further, mass transport in these systems is advection-dominated, but dispersion can be an important factor in basin-scale mixing under some conditions. Robust regression analysis indicated that ambient flow conditions as represented by estimated mean bed shear turbulent velocities maintains the greatest influence on the dimensionless mean residence time and volumetric efficiency, while wind shear most strongly influences short-circuiting and some measures of basin-scale mixing, which notably increases the dimensionless normalized variance of the RTD and the longitudinal dispersion coefficient, and reduces the Péclet number for some systems. Relative wind directions were shown to have a significant effect on some mixing characteristics for some wetlands, notably the non-dimensional normalized mean residence time and the Péclet number. Percent vegetative cover, used as a proxy for vegetation density, was shown to strongly decrease both the volumetric efficiency and longitudinal dispersion

rates of these systems. With the latter, percent vegetative cover above approximately 30% appears to result in an increase in dispersion, likely due to a combination of factors including vegetation patchiness and changes in the vertical canopy structure, resulting in reduced lateral mixing rates.

Introduction

The potential for constructed wetlands to help address agricultural surface water quality concerns is recognized by many United States state and federal agencies involved in water conservation (e.g. state-level Conservation Reserve Enhancement Programs - CREP), and has been realized in several U.S. state and federal collaborative initiatives that work to establish or restore wetlands for the purpose of water quality mitigation (Allen, 2005). Increasing agricultural production in rural regions of the U.S. places constraints on the land resources available to establish constructed wetlands in farmed landscapes. Ensuring that future wetlands that are developed in these areas are able to achieve target nutrient reductions requires a systematic evaluation of wetland performance efficiency factors, and accounting for these factors during wetland siting and design.

Overall, and assuming similar inherent assimilative capacity between systems, the efficiency of constructed wetlands at reducing constituent mass loads is dependent upon several predominant factors including: 1) landscape position (Crumpton et al., 2006); 2) wetland area (Crumpton et al., 2006; Carleton et al., 2001); and, 3) the degree of system-scale bulk mixing, and the internal distribution of hydraulic residence times (e.g. Bodin et al., 2012; Kadlec, 1994). With respect to landscape position, systems will have greater

treatment performance at locations which provide adequate opportunity to intercept constituent loads. For instance, wetlands established under the Iowa Conservation Reserve Enhancement Program (Iowa CREP) are typically developed at the termini of tile-drained watersheds in order to intercept all nitrate-nitrogen loads from those systems. With respect to size, wetlands need to be of sufficient area to adequately handle the loads expected at a given landscape position. Design sizing depends on the amount of available land at a given location, but is typically a function of the upstream contributing watershed area (Crumpton et al., 2006; Carlton et al., 2001). Sizing and siting criteria are based upon prior research, but, unlike with managed tertiary wastewater treatment wetlands wherein time-invariant hydraulic conditions may predominate and systems can be readily designed and configured for optimal hydraulic behavior, few criteria exist to account for the predominant environmental factors which influence mixing in unmanaged rural systems subject to time-varying environmental forcings and ecological conditions.

Agricultural wetlands developed in rural areas, such as those enrolled in the Iowa CREP, differ from other, more highly engineered, wetland systems in several critical ways. For one, these systems are constructed with deference to the constraints of existing local landscape use patterns and landscape morphology. Further, these wetlands are built as impoundments along first-order stream channels, and as a result tend to possess highly variable basin morphologies typified by long and narrow inflow channels proceeded by large mostly open water pools of highly varying width and depth. Finally, these systems receive unregulated hydrological and mass loads, are continually subjected to transient atmospheric and environmental conditions, and tend to be dominated by submersed macrophyte communities which feature strongly seasonal growth and senescence

patterns. The general morphological features of these types of wetlands along with their hydrological and environmental variability arguably place these systems within the category of very small and shallow run-of-the-river type impoundments (e.g. Mossman et al., 1991). In light of this classification these wetlands, unlike tertiary treatment wetland systems or other shallow flow-through treatment basins, likely possess lacustrine, riverine, and wetland characteristics. Combined, these factors increase the likelihood that agricultural wetlands built in farmed watershed possess highly dynamic, possibly seasonal, hydraulic and mixing characteristics.

Shallow flow-through basins, such as agricultural wetland impoundments, tend to feature an intermediate degree of mixing between the theoretical extremes of plug flow and fully mixed conditions (Kadlec and Wallace, 2008; Thackston et al., 1987). The degree and extent of internal mixing within a basin for a given period is strongly influenced by the interplay between prevailing environmental conditions and system-specific morphometry. For an unmanaged wetland system subjected to ambient environmental conditions, the processes expected to influence the bulk hydraulic and mixing behavior include: 1) enhanced turbulent diffusion and the development of large-scale flow recirculation structures resulting from applied wind shear stresses on wind-exposed open water surfaces (Andradóttir and Mortamet, 2016; Bentzen et al., 2008; Thackston et al., 1987 and references therein; Watters et al., 1973); 2) time varying shear dispersion induced by unsteady volumetric flow-through rates and exacerbated by non-uniform channel velocities and bed shear stresses arising from non-uniform basin morphologies (Andradóttir and Mortamet, 2016; Werner and Kadlec, 1996; Thackston et al., 1987; Watters et al., 1973) and 3) the feedbacks between these effects and

heterogeneous spatial and temporal patterns in the growth and senescence of submersed and emergent aquatic wetland vegetation (Keefe et al., 2010; Min and Wise, 2009; Wörman and Kronnäs, 2005; Nepf et al. 1997).

Although it is generally accepted that these effects, individually and in concert, exert significant influence on wetland bulk mixing and hydraulic behavior, currently there is little information regarding the influences of these environmental factors on the hydraulic behavior of these types of small and shallow run-of-the-river flow-through basins, and information gleaned from published studies on the mixing characteristics of engineered and managed systems, such as secondary or tertiary treatment wetland cells or intermittently loaded highway detention ponds, may not be suitable for wetlands of this type. It is important for designers of agricultural treatment wetlands to have information on the potential range of mixing in these systems and the environmental factors controlling mixing, so that informed decisions can be made in the wetland development phase about potential designs modifications that can be instituted to help ensure that the bulk or basin-scale mixing properties of these systems are as close to desirable as is feasible.

This study was designed to document the temporal variability of the observed residence time distribution (RTD) characteristics and common derivative bulk mixing and hydraulic performance indices of a set of Iowa CREP wetlands over a range of flow, meteorological, and vegetated conditions. To accomplish these goals we conducted 30 conservative hydraulic tracer studies on 5 separate sites located in central and north-central Iowa over the period November, 2009 through April, 2013. Observed tracer response curves were transformed into RTD function curves and evaluated using the

method of moments for subsequent estimation of common wetland mixing and hydraulic performance indices. Further, in addition to one-time bathymetric surveys, comprehensive submersed aquatic vegetation surveys and close-interval monitoring of volumetric flow-through rates and local and quasi-local wind speeds and directions accompanied each of the tracer studies. Additionally, robust linear and non-linear regression was used to assess the individual influence of each measured environmental effect on the magnitude of measured and derived wetland-scale bulk hydraulic behavior and mixing characteristics as derived from measured RTD. Conducted regression analyses related measured RTD characteristics with estimates of basin ambient flow-induced bed shear velocities, wind-induced surface shear velocities, relative wind directions, and percent submersed aquatic vegetation cover.

Methods

Site Descriptions

The five wetlands of focus in this study (to be referred to herein as WL1, WL2, WL3, WL4, and WL5) are impounded shallow flow-through basins constructed in the downslope regions of five separate small and intensively farmed and tile-drained low-relief watersheds in central and north-central Iowa. Each wetland was constructed as a participating site in the Iowa CREP sometime between 2005 and 2009.

Wetland planar shape and mean morphometric properties vary significantly between sites and are strongly influenced by local topography and site-specific land-use constraints (Table 1; Figures 1-5). Each system features a single shallow and narrow inflow channel, and a single, site-specific outflow control structure integrated into an

earthen berm. In each case the wetland inflow channel gradually opens into a larger and deeper wind-exposed and seasonally vegetated open water pool. Cross-sectional geometries vary significantly with distance downstream from inlet to outlet. Mean cross-sectional depth also tends to gradually increase from inlet to outlet. Basin full-pool areas and mean full-pool depths range from 1.35 to 4.12 hectares, and 0.35 to 0.69 meters, respectively. Wetland full-pool areas are typically 0.5 to 2 percent of the drainage contributing area as per Iowa CREP requirements (Table 2.).

Bathymetric Surveys and Derivation of Basin Morphometric Properties

Bathymetric Surveys and Modeling of Wetland Depths

Bathymetric surveys were conducted on each wetland prior to initiation of planned tracer experiments and vegetation surveys (Table 3). Each survey consisted of collecting between 3 and 5 replicate point measurements of local water depths at $n > 200$ locations spatially distributed over the entirety of each wetland using a 16 foot surveying staff (± 0.1ft) in accordance with the methods suggested by Kadlec (1994). The horizontal coordinates of each measurement point were recorded using sub-meter hand-held differential GPS (GeoXT, GeoXM, or GeoXH models, Trimble USA, Sunnyvale, CA). Surveyed local water depth measurements were offset by the mean water depth above the respective system full pool elevation estimated for the date of the survey. Mean water depths were subsequently merged with local high-density Light Ranging Detection and Radar (LiDAR) elevation points offset by each respective system's full-pool elevation. Basin full pool boundaries (i.e. the area of inundation when water levels are at the base of the outflow control structure) were digitized using high-resolution 2010

United States Department of Agriculture (USDA) National Agriculture Imagery Program (NAIP) imagery for the site (USDA, 2010, https://gdg.sc.egov.usda.gov/), or by direct surveying of pool areas. Spatial interpolation by kriging of the merged discrete elevation points was performed for each survey in order to form a continuous elevation surface referenced to respective wetland full-pool elevations, encompassing both basin morphometry and surrounding landscape topography. This step was taken to aid in the development of basin volume-depth and volume-area relationships (Table 2). All spatial modeling was conducted using the GSTAT package in the R statistical computing environment (Pebesma, 2004). Owing to an historic flood in August, 2010 the bathymetry of WL1 was re-surveyed in April, 2011; revealing an approximately 10% decrease in total system volume. This change in volume resulted, most likely, from transport and deposition of large quantities of coarse and fine-grained sediments into the wetland basin from upland and upstream sources.

Hypsographic Curves

Volume-depth curves were developed for each wetland by integrating over the basin volumes and planar areas below and up to one meter above each respective full-pool reference elevation. Each curve was fitted to an n^{th}-order polynomial (Table 2). All regression curves had R^2 values of close to 1. Fitted volume-depth and volume-area curves permitted the estimation of time-varying system volumes and planar basin wetted areas from measured water elevations above full pool. Time-varying volumes were subsequently used in calculating dimensionless flow-weighted times, as well as

estimating critical components of system water balances, including instantaneous and mean hydraulic residence times, and mean volumetric inflow and outflow rates.

Basin Morphological Characteristics

Channel centerlines lengths (L_w) were estimated by connecting the centroids of incremental sections of each respective wetland full pool area at specified distances from each system inlet to outlet, and represent the along-length centroids of, and shortest flow paths through, each basin. The mean basin width ($\overline{B}_w$) for each wetland was calculated by averaging the lengths of cross-sections drawn at each of between 20 and 40 locations approximately evenly spaced along the computed wetland channel centerline from inlet to outlet. Using the derived basin centerlines the mean flow direction ($\overline{\theta}_f$) for each system was subsequently estimated by averaging the computed azimuthal angles (relative to true north) of the channel centerline at each of the 100 cross-sections established along the length of each channel centerline. These values were subsequently used to estimate wind directions relative to mean basin flow directions, as discussed in a following section. All aforementioned calculations were performed in the ArcGIS Desktop environment (ESRI, Redlands CA).

Vegetation Surveys and Spatial Modeling of Vegetative Cover

Vegetation Surveys

During periods when vegetation was visibly present, comprehensive submersed aquatic vegetation surveys were performed immediately prior to or around scheduled tracer studies (Table 3). Each survey entailed documenting visible vegetation

characteristics at sampling locations positioned at set intervals along each of several transects established transverse to the predominant system flow direction. Using a 0.071 m^2 quadrat, at each survey location the species present, local water depth, the distance between the water surface and the top of the canopy, as well as the percent vegetative areal cover based on a 20 point modified Daubenmire classification scheme (Elzinga et al., 1998). Because the wetlands of focus in this study are dominated by submersed vegetation surveys largely ignored emergent species, which tended mostly to occur at basin fringes. Only wetlands WL3 and WL4 featured significant emergent beds, both of which were mostly separated from the primary flow regions of each respective system (Figures 3 and 4).

Spatial Modeling of Vegetation

The spatial distribution of the areal percent vegetative cover for each survey was modeled by kriging of surveyed point values using the GSTAT package in the R statistical computing environment (Pebesma, 2004). Spatial predictions of areal percent vegetative cover for each survey were reclassified to the original modified classification scheme used in the field surveys, and the area-weighted mean percent vegetative cover estimated from:

$$\overline{C}_{\mathrm{V}} = \frac{1}{A_{\mathrm{w}}} \sum_{i=1}^{n} \overline{C_{\mathrm{V}(i)}} A_i \tag{2.1}$$

where A_{w}, A_i, and $C_{\mathrm{v}(i)}$ are the total wetland area (m^2), class area (m^2) and class range mid-point values (%), respectively.

Flow and Volume Monitoring

Each wetland was subjected to intensive continuous flow and water volume monitoring over the course of each tracer study. Basin inflow and outflow channel mean water velocity and depth measurements were taken at five minute intervals using submerged area velocity (SAV) meters and stage recorders (Solinst, Ontario CA). Stream cross-section profiles were measured to develop cross-sectional wetted area versus depth relationships at each stream discharge measurement location. Discharge was calibrated on the basis of point discharge measurements taken at multiple water depths at each measurement site. Manual point discharge measurements were determined using the mid-section method (Buchanan and Somers, 1969). Manual velocity measurements were taken with a hand held side-looking 2-dimensional Sontek Flow-tracker Doppler velocimeter (Sontek, San Diego CA) using the 0.6 depth method (Buchanan and Somers, 1969). Point discharge measurements were used to develop stream stage-discharge equations and to calibrate the discharge coefficients for wetland outflow structure discharge equations and SAV-based discharge measurements. Wetland basin pool surface elevations were monitored using Solinst pressure transducers (Solinst, Ontario Canada). Discharge equations for wetland outflow structures were developed on the basis of wetland outflow structure dimensions. Instantaneous discharge was calculated from measured wetland pool water depths and estimated pool volumes. Time-varying wetland pool volumes for each tracer study were estimated using monitored pool elevations and the regression equations developed from the aforementioned hypsographic curves (Table 2). In some cases, because of uncertainty in the flow time-series, daily average flow rates were used in lieu of the close-interval values. These values were subsequently

interpolated to hourly mean flow rates for the purpose of analyzing the measured RTDs. Inflow discharge was not measured on WL1 for studies conducted during the period November, 2009 to December, 2010. Time-varying inflow rates for this site for studies conducted over this period were estimated using the reverse level-pool routing procedure developed by Zoppou (1999).

Area-Weighted Estimates of Wetland Mean Velocities and Reynolds Numbers

Interpolated bathymetry of each basin was sectioned into *n* reaches of between 10 and 15 meters in length; the upstream and downstream ends of which were defined from the aforementioned channel cross-sections. Basin reaches were subsequently used to develop, for each tracer study, weighted estimates of mean basin velocities ($\overline{U_{q(m)}}$) using a reach planar area weighting scheme:

$$\overline{U_{q(m)}} = \frac{1}{A_w} \sum_{i=1}^{n} \frac{\overline{Q_{(in)m}}}{\overline{A_{cs(i)}}} A_{w(i)} \tag{2.2}$$

where A_w is the total planar area (the full-pool area) of the wetland between the tracer injection and detection locations (m^2), $\overline{Q_{(in)m}}$ is the mass-weighted mean inflow rate (discussed in a proceeding sub-section), $A_{w(i)}$ is the planar area of reach *i* (m^2), and $A_{cs(i)}$ is the average reach cross-sectional area (m^2), as determined from the developed bathymetric grids. This technique for approximating mean basin velocities was used to account for the varying channel morphometries of each system between tracer injection and detection locations, and to avoid the over-weighting of inlet channel mean velocities in the determination of the mean condition, as would be the case for a length-weighted scheme. This issue is particularly applicable to sites WL4 and WL5, as these wetland

feature long, narrow, and deep inlet channels, and very broad and comparatively shallow pools.

Likewise, planar-area weighted mean flow Reynolds numbers were estimated using:

$$\overline{\mathrm{Re}_m} = \frac{1}{A_w}\sum_{i=1}^{n}\frac{\overline{U_{ma(i)}}\,\overline{H_i}}{\nu}A_{w(i)} \tag{2.3}$$

where $\overline{H_i}$ is the mean depth of reach *i* (m), and *v* is the kinematic viscosity of water, taken herein as approximately $1.004\text{x}10^{6}$ $\mathrm{m^2\,s^{-1}}$.

Wind Monitoring

Atmospheric conditions, including wind speeds and directions, were monitored at 15 to 30 minute intervals at the sites WL3, WL4, and WL5 using locally installed weather stations (Tycon Power Systems, Bluffdale UT). Anemometers and wind vanes were positioned at an elevation of approximately 2 meters above the local land surface. Wind speed and direction data for WL1 sampled at 60-minute intervals was acquired from the Gilbert, Iowa station (site A130219) of the Iowa State University Agricultural Climate Monitoring Network (ISU-AG; http://mesonet.agron.iastate.edu/), located at a distance of approximately 4 linear miles from the wetland. Wind speed and direction data for WL2 sampled at 30-minute intervals was acquired from the Algona, Iowa Airport Automated Weather Observing System (AWOS) station (site AXA) located approximately 5 linear miles from the wetland for the period spanning early May, 2010 to early July, 2010. In July, 2010 a weather station was installed on-site for more accurate wind speed and direction monitoring. Wind speeds were normalized to a height of 10 meters above the local respective water surface using a power-law vertical wind speed

profile with a constant exponent of 1/7, suitable for lightly vegetated regions (Irwin, 1967):

$$v_{w(10)} = v_{w(r)} \left(\frac{10}{e_r} \right)^{1/7} \tag{2.4}$$

where $v_{w(r)}$ is the wind speed (m s^{-1}) measured at the reference elevation e_r (m) above the local land surface.

Wind directions in relation to the predominant flow direction for small, shallow flow-through basins has been observed to have a potentially significant influence on mixing characteristics of these types of basins (Watters et al., 1973; Thackston et al., 1987; Bentzen et al., 2008). To quantify this effect, mean wind directions relative to the local system flow directions were estimated using the following:

$$\theta_{wf} = \begin{cases} 1 + \dfrac{\Delta_{wf}}{180}, & \Delta_{wf} < 180 \\ 1 + \dfrac{360 - \Delta_{wf}}{180}, & \Delta_{wf} \geq 180 \end{cases} \tag{2.5}$$

where $\Delta_{wf} = \max(\theta_w, \theta_f) - \min(\theta_w, \theta_f)$. Equation 2.3 bounds the relative mean wind direction between a lower value of 1 when winds are aligned with the respective system flow direction, and an upper value of 2 when winds are directionally opposed to the flow direction. A value of θ_{wf} of 1.5 indicates a prevailing mean wind direction that is transverse to the respective system mean flow direction.

Mass-weighted Averaging of Environmental Variables

The hydrological and atmospheric conditions encountered during each study were significantly time-varying, as can be seen in the time-series plots given in Figure 6 (time-series plots for all tracer studies are given in Appendix A). The temporal nature of these environmental variables cause difficulty in deriving meaningful estimates of the aggregate behavior of each over the course of a tracer study; this is especially true if, as is seen for several studies, flow and atmospheric conditions change rapidly at late times. The environmental conditions, especially with respect to flow rates and wind speeds, encountered during the early part of a tracer test may exert significant influence on the overall character of the developed curve (Werner and Kadlec, 1996). Likewise, late-time changes in environmental conditions may have less influence (Werner and Kadlec, 1996; Watters et al., 1973). To give greater weight to early time measured hydrological and atmospheric variables, following Werner and Kadlec (1996), we opted to estimate the mass-weighted means of attendant measured environmental variables (in lieu of simple time-averaged quantities) using the weighting scheme:

$$(\overline{Q_{a,i,o(\mathrm{m})}}, \overline{v_{\mathrm{w}(10)(\mathrm{m})}}, \overline{\theta_{\mathrm{wf}(\mathrm{m})}}) = \frac{\int_0^{t_f} (M_r - M_o(t))(Q_{a,i,o}(t), v_{\mathrm{w}(10)}(t), \theta_{\mathrm{r}}(t))dt}{\int_0^{t_f} (M_r - M_o(t))dt} \qquad (2.6)$$

The estimation of the mass-weighted mean quantities of flow (where the subscripts in Eqn. 2.6 represent the inflow, outflow, and average estimates, respectively), wind speed, and relative wind direction were included in this analysis principally for the purpose of deriving correlations between measured effects. The upper limit of integration, t_f, in Eqn. 2.6 represents the time of the conclusion of the tracer study. Mass-weighted means of measured environmental effects are given in Table 4B.

Tracer Studies

Field Experiments

Conservative tracer studies were conducted at semi-regular intervals on each wetland as flow conditions permitted. In all, 30 studies were conducted over a period of 3 years on 5 separate wetlands. Each tracer study consisted of impulse-injecting a pre-measured mass of Rhodamine WT (RWT; 20% solution; Organic Dye Stuffs Corporation, Providence, RI) over the width and depth of the system inlet channel, accompanied by continual monitoring of effluent dye concentrations at the outlet. To minimize potential initial density effects the measured dye was diluted with up to 5 gallons of influent stream water prior to injection. Dye concentrations were measured in the outflow channels of each wetland at 5-minute intervals using a Turner Designs Cyclops-7 submersible optical fluorometer connected to a Turner Designs Databank data logger (Turner Designs, Sunnyvale CA). Tracer background concentrations were measured at 5 minute intervals for at least one-half hour prior to tracer injection, and typically for 1 to 2 hours before the initial tracer arrival time. Each instrument was secured in custom-made perforated screened grey cylindrical PVC housing designed to minimize sunlight effects on fluorescence measurements, and to prevent measurement interference by floating detritus and algae. Sensors were positioned at approximately one-half of the local water column depth in the outlet channels.

Instrument accuracy over the linear detection range (0-250 μg L^{-1}) was assessed prior to each deployment using 0, 10, 50, 100, and 250 μgL^{-1} RWT standard concentrations prepared with deionized water. Sensor recalibration was performed if the instrument reading and corresponding standard concentration differed by more than 5%.

Tracer Response Curve Data Conditioning

Data conditioning was required of each developed tracer response curve prior to RTD development and analysis. This process involved correcting for mean background florescence, correcting for the effects of water temperature on RWT florescence, and removing and interpolating into obvious deviant concentration time-series values resulting from sensor failure or errant flotsam. Errant values were visually identified to be either sensor drop-outs, or concentration readings that were typically greater than 10 times the apparent peak concentration of the measured time-series curve. For each tracer experiment the effects of water temperature on RWT fluorescence at the point of detection was corrected using (Smart and Laidlaw, 1977):

$$C_c = C_o \exp\left(0.027\left(T_o - 20\right)\right) \tag{2.7}$$

where 0.027 is the temperature correction coefficient specific to RWT, and C_o and T_o the observed tracer effluent concentration and water temperature in degrees Celsius, respectively.

Rhodamine WT has been shown to moderately adsorb to sediments rich in organic material (Smart and Laidlaw, 1977), and is subject to photolysis if present in a sun-exposed system for extended periods (Keefe et al., 2004). Thus tracer loss, and in some cases gain (likely due to time-varying background concentrations or high turbidity), is inevitable in wetland dye studies, and can result in increased analytical uncertainty in measured and derived RTD statistics and mixing parameters (Keefe et al., 2004; Kadlec and Wallace, 2008). To compensate for this potential complication, and to permit RTD analysis using standard methods, all tracer response curves were scaled by the mass recovered; a procedure that is equivalent to scaling the RTD by the fractional mass recovery.

To remove excessive signal noise resulting from large variations in background concentrations, the response curves for the studies WL4_2 WL4_3 and WL4_3 were smoothed using a 7-pass Savitsky-Golay filter (Savitsky and Golay, 1964) using the PRACMA package in the R statistical computing environment. Because of premature study termination, the tails of the response curves for some studies were extrapolated to measured background concentrations using an exponential decay profile fitted to the measured descending limb of the curve (Kadlec and Wallace, 2008). To account for minor periodicity in the tail regions of the response curves for the studies WL2_1, WL2_4, WL2_5, and WL3_4, the descending limbs of measured RTD for each of these studies was extrapolated using a sinusoidal profile imposed on an exponential decay:

$$C_{\mathrm{ex}}(t) = \alpha\, exp(-\beta t)\left(\mathrm{A}\, sin\left(\mathrm{B}t + \mathrm{C}\right) + \mathrm{D}\right) \tag{2.8}$$

where α and β are fitting parameters for the exponential decay function, and A, B, C and D are, the relative amplitude, period, phase shift and vertical shift of observed sinusoidal fluctuations in the tails, respectively. The coefficients of Eq. 2.8 were determined using non-linear least-squares fitting of the receding limb of the observed concentration curves for these studies (data not shown, although the extrapolations can be observed in the time-series plots for these studies, as given in Appendix A).

Residence Time Distribution Analysis for Unsteady Flow Systems

The time-varying flow conditions encountered during most tracer studies necessitated the adoption of RTD transformation and analysis techniques specifically designed to account for transient conditions. The residence time distribution for a flow-through basin derived from an impulse-injection of tracer conducted under unsteady flow

conditions can be expressed in terms of the tracer concentration observed at the system outlet and the dynamic system volume (Werner and Kadlec, 1996; Fernandez-Sempere et al., 1995; Zuber, 1986):

$$g(z) = \frac{C(t)V(t)}{M_r} \tag{2.9}$$

where g(z) is the dimensionless volume-based RTD function, $V(t)$ is the time-varying system volume (m^3), $C(t)$ is the observed effluent tracer concentration ($\mu g\ L^{-1}$). The total observed mass recovered, M_r (kg), is defined as:

$$M_r = \int_0^{\infty} C_o(t) Q_o(t)\, dt \tag{2.10}$$

The time variable z in Eqn. 2.9 is a flow-weighted dimensionless time defined as (Werner and Kadlec, 1996; Fernandez-Sempere et al., 1994; Zuber, 1986):

$$z = \int_0^{t} \frac{Q_o(\tau)}{V_s(\tau)} d\tau \tag{2.11}$$

where τ is a time-like dummy variable of integration. The quantity z physically represents the total volume of water that has transited the variable flow system during the course of a study relative to the dynamic system volume, and can be considered analogous to the dynamic system turn-over time (Werner and Kadlec, 1996). The flow-weighted time is a non-linear function of the water age in normal time units, contracting and expanding with variations in system flow rates and volumes. Under steady and moderately transient flow conditions z is approximately equivalent to time normalized by the mean hydraulic residence time of the system ($\overline{T_a}$):

$$z \cong \frac{Q_o}{V_s} \int_0^{t} dt \cong \frac{t}{\overline{T_a}} \tag{2.12}$$

and,

$$\overline{T_{\mathrm{a}}} \approx \frac{\overline{V_{\mathrm{s}}(t)}}{\overline{Q_{\mathrm{a}}(t)}} \tag{2.13}$$

where $\overline{Q_a(t)}$ represents the time average of the system inflow and outflow rates (Keefe et al., 2004):

$$\overline{Q_a(t)} \approx \frac{\left(\overline{Q_i(t)} + \overline{Q_o(t)}\right)}{2} \tag{2.14}$$

where *t* in the above and proceeding definitions is representative of the age of the tracer beyond an initial injection time t_0.

For most tracer studies, the mean volumetric flow rates and the mean system volumes were moderately unsteady. This condition necessitated the use of Eqn. 2.9 in lieu of more standard techniques developed to account for moderately changing flow conditions (e.g. Kadlec, 1994).

Dimensionless RTD temporal features were obtained directly from measured tracer response curves using their corresponding normal time equivalents by expressing *z* explicitly as a function of *t*:

$$z_{(\mathrm{i,p})} \cong f\left(t_{(\mathrm{i,p})}\right) \tag{2.15}$$

where *z* is a monotonically increasing function of normal time, and the subscripts *i* and *p* represent the initial and peak arrival times of tracer, respectively. For each tracer study, the flow-weighted time *z* was expressed as a cubic spline interpolant of the measured time from injection represented in standard time units (days). The spline interpolating functions were developed using the *stats* package in the R statistical computing environment (R Core Team, 2014). Error from the spline interpolation was minimal (~10^{-}

[5]) because of the high temporal frequency of tracer effluent sampling (5 minute intervals). It should be noted that under moderately varying flow conditions the dimensionless early time metrics of the RTD ($z_{(i,p)}$) are reasonably approximated by their more standard form:

$$z_{(i,p)} \approx \frac{t_{(i,p)}}{\overline{T}_{(i,p)}} \tag{2.16}$$

representing the quotient of the initial, peak and median residence time points on the measured tracer response curve and the average hydraulic residence time (Eqn. 2.14) calculated up to each respective temporal feature.

Temporal Moments of the Flow-varying Residence Time Distribution

In using the above representation of the RTD, the dynamic nature of the flow conditions observed during a tracer study can be accounted for in the analysis of a tracer response curve, and thus in the estimation of derivative mixing and hydraulic performance indices. Variations in tracer concentrations in the tail region of an RTD can induce significant uncertainty in the estimation of higher-order (>2) moments (Naumann and Buffham, 1983). This potential for error can be reduced by utilizing the measured wash-out function in lieu of the standard RTD (Naumann and Buffman, 1983) in the estimation of temporal moments:

$$m_n^* = n \int_0^{z_f} t^{n-1} W(z)\, dz \tag{2.17}$$

where the washout function is defined in relation to the RTD through:

$$W(z) = 1 - \int_0^{z_f} g(z)\, dz = 1 - F(z) \tag{2.18}$$

The function $F(z)$ is the cumulative frequency distribution representation of the volume-based RTD function, and z_f is the upper bound of integration representing the total length, in the flow-weighted time-scale, of the experiment. The zeroth moment about the origin m_0 represents the total fractional mass recovery of tracer observed at the system outlet. The first moment about the origin, m_1^*, is the dimensionless mean residence time of the tracer, and as discussed in a proceeding section, is assumed to be a reasonable approximation of the fractional volume of the system involved in tracer transport. The dimensionless RTD temporal variance (m_{2c}^*) is determined from the second and first moments about the origin:

$$m_{2c}^* = m_2^* - (m_1^*)^2 \tag{2.19}$$

For an impulse input of tracer m_{2c}^* provides a dimensionless characterization of the degree of total mixing within the system relative to the centroid of the tracer plume as it transits the length of the basin (Kadlec, 1994). Because of the increased sensitivity of higher-order moments to noise in the ascending and descending limbs measured RTD, we restricted our analysis to the first and second moments alone.

The normalized variance of the RTD is considered to be a principal unbiased dimensionless index representing the total scale or degree of internal wetland mixing (Kadlec, 1994; Thackston et al., 1987):

$$\sigma^{2*} = \frac{m_{2c}^*}{\left(m_1^*\right)^2} \tag{2.20}$$

When σ^{2*} tends to unity the flow domain approaches a fully mixed state characterized by the exponential mixing model (e.g. Maloszewski and Zuber, 1993), and is representative

of an exponential distribution of residence times. Conversely, when σ^{2*} approaches zero plug-flow conditions dominate, characterized by minimized longitudinal dispersion and complete lateral and vertical mixing over the basin width and depth. The plug flow condition is representative of a uniform distribution of residence times. Most wetlands feature intermediate degrees of mixing however, and values of σ^{2*} for a given tracer study likely will be between these two bounds. The normalized variance in certain circumstances can obtain values greater than unity (Naumann and Buffham, 1983). This condition results from an observed RTD variance that is less than the square of the mean tracer residence time. Such an occurrence may indicate significant mixing within the basin in addition to the presence of tracer short-circuiting and bypassing. This condition could also occur if the basin features significant volume fractions of dead space and short-circuiting pathways (i.e $m_1^* \ll 1$ and $\left(m_1^*\right)^2 < m_2^*$).

For each tracer study, discrete RTDs calculated using Eqn. 2.9 were transformed into cubic spline interpolants expressed as a function of *z*. Moments about the origin and centroid were subsequently calculated for each RTD using Adaptive Gauss-Kronrod quadrature of the spline interpolating functions over the entirety of the time-period of each study. These calculations were performed using the *pracma* package in the R statistical computing environment.

Short-circuiting Indexes and Hydraulic Efficiency

Short-circuiting manifests in measured RTD as early tracer dimensionless initial and peak arrival times, and the appearance of the centroid at a time much less than the mean hydraulic residence time (Lightbody et al., 2009; Thackston et al., 1986). In wetland systems this condition likely results from the presence of preferential flow pathways arising from remnant channels or highly varying topography (Lightbody et al., 2007; Wörman and Kronnäs, 2005), fringing or heterogeneous vegetation (Lightbody et al., 2009; Jenkins and Greenway, 2005), wind-induced mixing (Bardot-Nico et al. 2009; Bentzen et al. 2008; Shaw et al., 1997; Thackston et al., 1987; Watters et al., 1973); and the presence of dead zones or other zones of diminished mixing (Thackston et al., 1987; Watters et al., 1973).

While short-circuiting is likely represented by several RTD characteristics (Teixeira and Siqueria, 2008) we consider this condition to be represented mostly by early time features, including the dimensionless time of tracer arrival (z_i) and the dimensionless time to peak (z_p). The dimensionless arrival time of tracer was estimated as the first z instance on the measured response curve that exceeded 1% of the maximum concentration (Watters et al., 1973). Thackston et al., (1987) describe short-circuiting in shallow basins as being represented by $z_i < 0.2$.

The initial time of arrival in the z-domain, z_i, and z_p each give a time-normalized dimensionless indication of the rate at which tracer moves longitudinally through the system relative to the mean rate of transport. The dimensionless initial arrival time is used in this work as an estimate of the advective transport time-scale, and is a reasonable approximation of the pure advective time-delay (Lees et al., 2000). The dimensionless time of the peak concentration (z_p) is thought to be representative of both the relative

degree of short-circuiting occurring within a system under the flow conditions observed for a given tracer study, as well as the extent of the efficiency of bulk tracer mixing (Persson, 2000; Persson and Wittgren, 2003); although, this definition assumes that the RTD is reasonably represented by the Cells-In-Series model (Persson, 2000). In general, when $z_i \rightarrow z_p \rightarrow m_1^* \rightarrow 1$ the system under consideration tends toward plug-flow conditions. Conversely, when $z_i \rightarrow z_p \ll 1$ and $m_1^* \ll 1$ significant short-circuiting accompanied by the presence of dead zones is observed (Watters et al., 1973; Persson, 2000; Holland et al., 2004). Persson (2000) defined the cutoff for 'good' hydraulic conditions for flow-through detention basins of arbitrary configuration and flow conditions as being $z_p \geq 0.70$.

For a positively skewed RTD developed under steady or moderately varying flow conditions, Watters et al. (1973), Thackston et al. (1987), and Holland et al. (2004) each have proposed that the dimensionless first moment of the volume-based RTD, m_1^* , is representative of the average fractional volume of a variable flow system that is actively involved in tracer transport at the time-scale of the arrival of the RTD centroid, and is closely related to the degree of short-circuiting in the system. This metric, also termed the basin volumetric efficiency, is closely related to the fractional transient storage parameter of the one-dimensional transient storage transport model (Keefe et al., 2010; Martinez and Wise, 2003), and to the dispersive fraction parameter defined in the aggregate dead zone model (Lees et al., 2000; Beer and Young, 1983). When m_1^* is unity the entire flow system is considered to participate in tracer transport. Conversely, when m_1^* is less than unity, the relative fraction of the active volume is diminished. Values of m_1^* greater than

unity are often attributed to poorly determined hydraulic residence times, or to excessive loss of tracer (Kadlec, 2007). However, as is discussed in more detail in a following section, volumetric efficiencies greater than unity may also arise from instances wherein the centroid of the tracer plume becomes trapped in irregular bathymetric features or in patches of submersed aquatic vegetation, or from back-mixing imposed by basin boundaries near the outlet. Thackston et al. (1987) defined reasonable hydraulic behavior for shallow flow-through basins in general as being indicated by $m_1^* \geq 0.75$, suggesting the presence of only moderate dead space.

Longitudinal Dispersion

For quasi one-dimensional flow domains, such as Iowa CREP wetlands and other shallow flow-through basins, the apparent Péclet number, Pe_x, representing the quotient of the time-scales of advection and dispersion, can be estimated from the normalized dimensionless variance as (Levenspiel, 2011):

$$\sigma^{2*} \cong \frac{2}{Pe_x} + \frac{3}{Pe_x^2} \tag{2.21}$$

Values of Pe_x less than unity indicate the dominance of dispersion in tracer transport while the converse represents advection dominance. Estimates of Pe_x and bulk basin flow and morphological characteristics were used to roughly approximate rates of apparent longitudinal dispersion, K_x (m^2 min^{-1}) using (Kadlec and Wallace, 2008):

$$K_x \cong \frac{\overline{Q_{a(m)}}L}{\overline{B}\overline{H}Pe_x} \tag{2.22}$$

where $\overline{Q_{a(\mathrm{m})}}$ is the mass-weighted mean flow rate observed during the tracer study, and $\overline{B}$, $\overline{H}$, and L are the afore-discussed mean basin width (m), mean basin depth (m), and total flow length (m), respectively.

It should be noted that Eqns. 2.21 and 2.22 are suitable for estimating longitudinal mixing only in the region of the flow domain where the tracer is evenly distributed laterally and vertically across the entire basin, and within the portion of the basin that is beyond the zone of the flow that is dominated by advection (the advective zone; Fischer et al., 1979). Table 4B suggests that the average cross-sectional velocities for the systems studied herein are usually on the order of tens of meters per day, to hundreds of meters per day under higher flow-through rates. Thus, ambient internal wetland flow conditions are typically laminar to transitional with Reynolds numbers typically being ≤ 2000 (Table 4B). Bed shear velocities are usually several of orders of magnitude lower. Thus, it is highly unlikely that full lateral and vertical mixing is achievable in wetland systems possessing predominantly laminar to transitional flows, significant fractions of dead space, highly varying cross-sectional geometries, and spatially distributed roughness elements such as from submersed vegetation, and it is possible that the time-scale for achieving complete lateral mixing before tracer exits the system is beyond the time-scale of a standard tracer study. Therefore, estimates of K_x given from Eq. 2.22 are likely significantly higher than actual rates of longitudinal dispersion. Further, because of the time-varying nature of the environmental conditions encountered during each tracer study, presented values of K_x and Pe_x derived from the set of studies reviewed in this work can at most be conservatively interpreted as time, space, and flow-averaged approximations of actual values.

Summary Results

Vegetation Surveys

Submersed vegetation tended to appear in middle to late May (for sites WL1 and WL2), and senesced in late October to early November (observed only for site WL1). When vegetation was present it tended to be ubiquitous, occurring in most cases in over 80% of the area of each wetland (Table 3). Two notable exceptions are the middle June 2011 surveys on sites WL3 and WL4. Both wetlands feature significant, relatively isolated, sections of emergent beds (Figures 3 and 4), and during these surveys exhibited relatively sparse submersed vegetative cover. A representative map of interpolated areal percent vegetative cover is given in Figure 8. Maps of interpolated percent vegetated cover for each vegetation survey are presented in Appendix B.

Site WL1 is the only wetland studied in this work for which a sequence of vegetation surveys spanning an entire growing season (2010) is available. For this wetland for this year, early season growth was shown to be dominated by *Potamogeton pectinatus* (syn. *Stuckenia pectinata*). Vegetative cover for this wetland was observed to reach an apex in middle June to early July ($\overline{C_V}$ = 41.1%). The period of growth of *P. pectinatus* was accompanied by a corresponding increase in both total wetland vegetative cover and $\overline{C_V}$ (Table 3). In 2010 the period early to late July for WL1 witnessed a transition from *P. pectinatus* dominance to *Ceratophyllum demersum* dominance. This period also featured a clear decrease in total percent vegetative cover and $\overline{C_V}$, likely due to the thinner canopy structure observed for *C. demersum* patches. In 2010 while *P. pectinatus* was still present, albeit in small patches, *C. demersum* tended to remain the dominant submergent species until fall senescence. Surveys on WL1 in 2011 revealed

lower percent vegetative cover estimates of *P. pectinatus* in late May and early June than which was observed for 2010.

When *P. pectinatus* was present as the dominant species it was ubiquitous throughout the wetland, but exhibited noticeably thinner canopy structure in deeper sections of the basin relative to shallow littoral regions, as can be observed in the vegetation survey maps for this system in Appendix B and the example map given in Figure 8. This vegetation distribution pattern was also evident during periods of *C. demersum* dominance; however, percent cover estimates are considerably less for periods when this species was dominant. When both species were present, *P. pectinatus* tended to occur in dense patches in wetland shallows, while *C. demersum* tended to inhabit deeper ($\overline{H} > 1$m) sections of the pool, but with a comparatively thinner canopy structure (i.e. low estimates of $\overline{C_V}$). Surveys were not completed for this wetland in the summer of 2011 because of a termination of planned tracer studies due to a region-wide drought.

With respect to surveys conducted in 2010 on site WL2 *P. pectinatus* and *C. demersum* were the dominant species until middle-late June followed by a transition to a greater prevalence of *Chara vulgaris*, and thinner patches of *P. pectinatus*. The wetland-wide growth of *P. pectinatus* during this period is reflected in an increase in $\overline{C_V}$ (Table 3; Appendix B.). The two surveys conducted in 2011 approximately two months apart indicate the presence of denser patches of *P. pectinatus* throughout the early to mid-summer season, and an absence of *C. demersum* and *C. vulgaris*. The depth-distribution patterns noted for WL1 with respect to *P. pectinatus* and *C. demersum* were also evident in this system. *C. vulgaris*, however, tended to occur at all surveyed depths at comparatively uniform densities (i.e. local estimates of $\overline{C_V}$).

Comparatively few vegetation surveys that were coincident with tracer studies were conducted on sites WL3, WL4, and WL5. However, the same general spatial trends observed for wetlands WL1 and WL2 were also observed for these systems. Estimates of $\overline{C_V}$ for the surveys conducted on both WL5 and WL4 are consistent with estimates of $\overline{C_V}$ obtained for sites WL1 and WL2. Also, as with sites WL1 and WL2, *P. pectinatus* was observed to occur at all depths in these systems, but with greater cover in shallow sections of each respective basin. *C. demersum* tended to also occur in relatively deeper sections and exhibited much lower percent areal cover. In contrast to the other systems, wetland WL3 for the single survey conducted at this site, tended to feature comparatively low vegetation densities throughout ($\overline{C_V}$ = 4.5%). However, the same general pattern of the occurrence and depth distribution of species as observed for wetlands WL1 and WL2, was evident.

Estimated values of $\overline{C_V}$ are highly approximate because of inherent uncertainties in objectively measuring percent vegetative cover in field settings using subjective, categorical measurements. Actual values of percent cover are likely to be ± 25% of presented values. Additionally, the percent areal cover is only representative of features directly observable on or near the water surface, and cannot account for the complex three-dimensional growth forms of *P. pectinatus* and *C. demersum* canopies (Duarte and Kalff, 1990b). Because of these uncertainties the presented estimates of vegetative cover are necessarily representative of only relative vegetation canopy properties, and should be considered highly approximate.

Hydrological and Meteorological Monitoring

Figure 7 provides an example of the time-series of measured environmental data and developed RTDs obtained during a tracer study. The entirety of the set of plots of RTDs and associated time-series of flow rates, system volumes, wind speeds, and relative wind directions is given in Appendix A. Monitored inflows, outflows, and volumes tended to be moderately variable for all tracer studies, and in a few cases were observed to change significantly during the course of the tests. For instance, flow rates were observed to increase nearly 7-fold during the study WL1_7. This rapid increase in flow occurred over a period of approximately 0.25 days and began after tracer had initially arrived at the system outlet. Prior to this event, flow rates were approximately constant. Additional examples of the changing flow conditions encountered in this work can be seen in the time-series plots given in Appendix A. Changes in flow rates during a tracer study may significantly and unpredictably influence the shape of the developed RTD. This condition necessarily implies that the measured dimensionless temporal moments and estimated mixing and hydraulic parameters for a given test are not constant (i.e. are changing with changing flow conditions), and, rather, represent aggregate, flow-weighted, values for each study. Flow and dye concentration monitoring for the study WL1_9 was discontinued in early December, 2010 because of icy conditions. Flows for this study after monitoring was ceased were thus estimated using daily average estimates of flows for this site based upon water elevation measured in the basin stop-log structure. Dye concentrations were extrapolated as discussed in a previous section.

Flow Conditions

As shown in Table 4B, by the provided Reynolds number estimates, the flow conditions encountered during this set of tracer studies tended to be laminar to transitional, with only a few studies exhibiting predominantly turbulent conditions ($\overline{\mathrm{Re_m}} > 2000$), on average. Aggregate mass-weighted mean flow rates differed between vegetated and non-vegetated conditions, with the mean of $\overline{Q_{a(\mathrm{m})}}$ being nearly 26% greater during vegetated periods (Table 4B). However, this value may be highly influenced by the handful of studies in which high flows were encountered during the course of the tracer tests.

Wind Conditions

Expectedly, wind speeds and relative wind directions were shown to be highly variable during the course of each study, with several studies exhibiting clear diurnal wind patterns. For all studies, measured wind speeds rarely fell below 1 m s^{-1}, and often exceeded rates of 5 m s^{-1}. As can be seen in Figure 6, and in the plots in Appendix A., high wind periods (defined here as > 3 m s^{-1}) often coincided with the time during which the bulk of tracer mass was still being actively transported through each system. Mass-weighted mean wind speeds encountered during each tracer study are given in Table 4B. In general, mass-weighted mean wind speeds were observed to be approximately 65% of their time-averaged equivalents (data not shown).

The mass-weighted and time-average relative wind directions for each study tended to be transverse or oblique to each respective system flow direction. This pattern, also shown in Table 4B, is remarkably consistent over all studies. On average mass-

weighted mean wind directions were observed to be nearly equivalent to their time-averaged counterparts (data not shown).

Tracer Studies

Qualitative Descriptions of Measured Tracer Response Curves

With the exception of a few studies (notably WL3_5, WL1_5, WL1_7, WL4_2, and WL5_2) most tracer response curves exhibited strong positive skewness, extensive tailing, and relatively early initial and peak tracer arrival times; all of which are characteristics common to wetland tracer studies (Keefe et al., 2010; Kadlec and Wallace, 2008). Such tracer response curve features likely represent advection-dominance in tracer transport, extensive longitudinal mixing, and the presence of significant dead space and short-circuiting (Keefe et al., 2010; Kadlec, 1994; Thackston et al., 1987; Watters et al., 1973). Approximately one-third of the studies produced curves that are much more symmetrical in form, and are indicative of more desirable hydraulic conditions (i.e. characteristic of nominal dead space, and minimal longitudinal, and complete lateral and vertical mixing).

In general, tracer studies conducted under non-vegetated conditions tended to demonstrate noticeably longer tails, and earlier initial and peak arrival times. In contrast, RTD curves developed from studies conducted under vegetated conditions tended to exhibit more symmetrical shapes, narrower profiles, and delayed initial arrival and peak times. These characteristics typically represent flow and mixing regimes more akin to ideal plug flow conditions (Kadlec and Wallace, 2008; Thackston et al., 1987; Watters et al., 1973).

As shown in Appendix A, apparent multiple peaks were notably present in some of the RTD (WL1_3, WL1_6, WL1_13, WL2_1, WL2_2, WL2_3, WL2_4, WL2_5, WL3_4, WL4_3, WL5_2, and WL5_3). It is uncertain whether these features result from the presence of multiple flow paths arising from irregular bathymetry and the presence of vegetation, as has been suggested by several authors (e.g. Keefe et al., 2010; Wörmann and Kronäss, 2005), or by the time-varying flow and wind conditions encountered during these tests. Of the tests exhibiting multiple peaks, only WL1_6, WL2_2, WL2_3, and WL2_5 were conducted when vegetation was present. Highly varying transient flow conditions were encountered during the WL2_2, WL2_5, and WL4_3 tests, also potentially giving rise to the observed multi-peak behavior, as has also been observed by Holland et al. (2004) and by Wörmann and Kronäss (2005). However, because wind was nearly always present during the study periods, and in many cases could be considered to be significant in magnitude (> 3 m s^{-1}), it is difficult with the information at hand to assess whether the observed multiple peaks of some of the RTD doesn't also stem from this effect.

Mass Recoveries

Most tracer studies resulted in total mass recoveries greater than 70%, while a few demonstrated either significant tracer loss (as defined as percent mass recovery less than 70% ; Kadlec, 2007), or excessive spurious gain (arbitrarily defined here as percent mass recovery greater than 110%; Table 5). Tracer mass loss is likely attributable in the case of these experiments to adsorption to organic sediments (Smart and Laidlaw, 1977), as the result of photolysis (Keefe et al., 2004), or from error associated with fluorometer

sensitivity or flow measurements. Although loss of RWT is common in wetland systems (Dierberg and Debusk, 2005), there does not appear to be an overarching pattern to the magnitude of tracer loss observed in the studies discussed herein, although the means of the mass recovery for studies conducted under vegetated conditions are nearly 16% greater than for those studies conducted in the absence of vegetation (approximately 86.1 ± 2.4 and 72.2 ± 1.5% standard error, respectively). Likewise, spurious tracer gain may result from increasing background concentrations during the course of a study, the release of tracer from previous studies from isolated wetland sections, or from fluorometer sensor or flow measurement error. Regardless, in each case tracer response curves were scaled by the mass-fraction recovered (Kadlec, 2007; Dierberg and DeBusk, 2005) prior to the development and analysis of associated RTD curves (Eqn. 2.9). Thus, inaccuracies in the tracer mass balances are unlikely to have significantly influenced some of the RTD analyses and the statistical interpretation of tracer study results. However, significant tracer loss is most likely to influence the centroid of the RTD (Kadlec, 2007).

Aggregate Statistics of RTD Characteristics

Measured RTD statistics and mixing indices for all studies are presented in Table 4C. Aggregate means of all measured statistics and parameters for all wetlands, and individual wetlands, grouped by vegetated conditions (where appropriate) are presented in Tables 5A through 5C.

Short-circuiting Indices

Dimensionless initial times of arrival ranged from approximately 0.01 (WL1_9), indicating extreme short-circuiting, to 0.54 (WL1_7) suggesting moderate short-circuiting conditions. Dimensionless peak arrival times ranged from ~0.01 (WL1_9) to approximately 0.99 (WL1_7). The former indicates significant short-circuiting and poor hydraulic efficiency according to the criteria proposed by Persson (2000), while the latter value represents comparatively 'good' hydraulic conditions. Only one tracer study (WL1_7) met the designation of 'good' hydraulic performance. Aggregate mean and median dimensionless initial and peak arrival times for the entirety of the set of experiments indicates that the systems studied, on average, exhibit moderate to significant degrees of hydraulic short-circuiting, a condition that is common to wetland systems (Keefe et al., 2010; Kadlec and Wallace, 2008).

Comparatively few published studies report estimates of the normalized time of arrival. However, our estimates of z_i encompass a similar range of values to those presented by several researchers who have reported on this metric. Estimates of z_i presented in Thackston et al. (1987) (and references therein) span from 0.009 to 3.6, and present a mean of 0.49, which is significantly greater than our reported mean for this characteristic (Table 5A). Likewise, Speer et al. (2009) give an estimate of z_i of 0.16 for a 0.13 hectare wetland, and Boughton and Shilton (2012) reported a value of z_i of 0.05 and a value of z_p of 0.32 for a 2.5 hectare wastewater treatment lagoon. Our reported mean of z_p is slightly lower than the mean of values (~0.37) given by Kusin et al. (2014) for a set of mining waste lagoons of varying sizes ranging from 0.073 to 1.14 hectares.

Aggregate medians of the dimensionless initial arrival times observed for studies conducted during vegetated conditions are approximately 41% greater than for studies conducted under non-vegetated conditions; although this difference was found to not be statistically significant at the 0.05 level based on a two-sided Mann-Whitney U test (n_{veg} = 14, n_{noveg} = 16, Mann-Whitney $\underline{U}$ = 150, $\underline{p}$ = 0.12). Aggregate medians for dimensionless times to peak under vegetated conditions were determined to be nearly 39% greater than for non-vegetated conditions with this difference being statistically insignificant ($\underline{U}$ = 137, $\underline{p}$ = 0.35).

Dimensionless Moments and Dispersion Indices

Values of the dimensionless mean residence time, m_1^*, range from 0.13 (WL1_9 and WL2_4) indicating extremely poor volume utilization and a large fraction of dead space in these systems for these studies, to an excessively large 2.79 (WL1_5), potentially indicating the entrapment of the dye plume in wetland vegetation, an influence of changing flow rates, error in the estimate of the system outflow for this study, back-mixing, or a combination of these factors. The latter study was conducted when vegetation was present in the system and was reasonably abundant ($\overline{C_V}$ ~38.3%). Additionally, flow rates increased nearly eight-fold during the latter-half of this study, resulting in a rapid expansion of the z-scale, thus inflating the estimate of this metric. The aggregate mean and median of m_1^* are in accordance with estimates obtained by Keefe et al. (2010) and as presented by Thackston et al. (1987), and is significantly greater than the mean of values reported by Kadlec (1994) ($m_1^* \sim 0.54$).

The comparatively high value of the aggregate median of m_1^* for all studies suggests that, on average, approximately 35% of the total volumes of the systems studied are not actively involved in tracer transport at shorter time-scales. The dimensionless mean residence time is observed to be nearly 38% greater when vegetation is present versus when vegetation is absent. The differences in the aggregate medians of m_1^* between vegetated and non-vegetated conditions was found not to be statistically significant ($\underline{U} = 134$, $\underline{p} = 0.2$). Volumetric efficiency has also been noted by Keefe et al. (2010) to tend to increase with increasing vegetative cover; although in this study only the effects of wetland hummocks were evaluated. Several tests demonstrated values of m_1^* significantly greater than unity (WL1_5, WL1_11, WL1_12, and WL3_5). As can be observed in the time-series plots given in Appendix A., rapidly increasing flow conditions were encountered during each of these experiments, thus inflating estimates of this RTD characteristic. If these studies are excluded from the analysis, the aggregate median value for this parameter reduces to 0.61 for all studies considered, and 0.63, and 0.60 for vegetated and non-vegetated conditions, respectively. The close correspondence between vegetated and non-vegetated conditions for the reduced data set suggests that approximately 40% of the volumes of these systems are inactive in bulk transport, regardless of the presence of vegetation. This result may be a more conservative estimate of the actual median amount of dead space in these systems.

The wetlands evaluated tended toward intermediate mixing regimes between the two theoretical extremes of plug flow and fully mixed conditions ($\sigma^{2*} = 0$ and 1, respectively). Dimensionless normalized variances, σ^{2*}, ranged from 0.04 (WL1_7) indicating near plug-flow behavior for this test, to ~0.99 (WL1_9), representing a high

degree of dispersion and basin-scale mixing. The aggregate mean value of σ^{2*} for all studies presented here (Table 5A) is nearly 23% greater than the means of estimates obtained by Kaldec (1994) from tracer studies conducted on the densely vegetated 2 hectare EW3 wetland at the Des Plaines River wetland complex (~0.38 ± 0.04; standard error), and nearly 27% greater than the mean of estimates obtained by Keefe et al. (2010) (~0.37 ± 0.03). The value of σ^{2*} estimated from the study WL1_7 suggests near plug flow conditions were encountered during this test. However, a significant impulse of flow (a nearly 7-fold increase in the mean flow rate) occurred during this study (Fig. 7A, Appendix A), and this value may not be representative of actual hydraulic conditions present in the system prior to the flow event. This caveat also applies to the studies WL1_4, WL1_10, WL1_11, WL2_2, WL2_5, and WL4_3; and to a lesser degree to the studies WL1_5, WL1_8, WL1_9, WL3_4, and WL3_5.

When vegetation was absent, the aggregate median of σ^{2*} was found to be nearly 34% greater than for studies conducted when vegetation was present. Further, results from non-vegetated tests demonstrated significantly less overall variability (43% and 70%, respectively), suggesting more persistent mixing conditions when vegetation is absent from these systems. Observed differences in the median values of σ^{2*} between vegetated and non-vegetated conditions were found to not be statistically significant ($\underline{U}$ = 78, $\underline{p}$ = 0.23).

Longitudinal Dispersion Coefficients and Péclet Numbers

Estimates of longitudinal dispersion coefficients ranged from approximately 651 m^2 day^{-1} (WL4_2) to 140443 m^2 day^{-1} (WL1_5), with a median of 15397 m^2 day^{-1}. Our

estimates of dispersion, while large, overlap with values reported in the literature. For instance, values of K_x measured by Kadlec (1994) on the EW3 wetland ranged from 444 to 3067 m^2 day^{-1}, with a mean of 1461 ± 318 m^2 day^{-1} . Values given by Keefe et al. (2010) ranged from 2409 to 3450 m^2 day^{-1} with an average value of 2797 ± 152 m^2 day^{-1}. Likewise, data from Martinez and Wise (2003) for a set of 23 to 54 hectare wetland treatment cells at the Orlando Easterly wetland complex gives dispersion coefficients ranging from 940 to 153124 m^2 day^{-1} with a mean of 42307 ± 10235 m^2 day^{-1}. Medians of dispersion coefficients for the studies conducted in this work were found to differ by approximately 1% between non-vegetated and vegetated conditions. Needless to say, this difference was found to be statistically insignificant ($\underline{U} = 25$, $\underline{p} = 0.62$).

Péclet numbers (Pe_x) ranged from 2.7 (WL1_9) to 52 (WL1_7). The former indicates extensive dispersion, while the latter indicates advection dominance. The aggregate median of our results ($Pe_x \sim 6.1$) suggests that advection is the dominant transport mechanism in the wetlands studied, although these systems are also moderately dispersive. Aggregate medians of Pe_x observed in this work are larger than the average values for studies conducted on the EW3 wetland (4.3 ± 2.5; Kadlec, 1994), and for studies conducted on the Hayfield 1 wetland (4.0 ± 0.1; Keefe et al., 2010), and are significantly greater than values given by Martinez and Wise (2003) (2.1 ± 0.7).

Aggregate median Péclet numbers observed for studies conducted under vegetated conditions were nearly 35% greater than the median of Pe_x obtained for studies conducted under non-vegetated conditions (Table 5A). Péclet numbers were observed to vary significantly more for studies conducted under vegetated conditions than non-vegetated conditions (Tables 5A and 5B). The difference in the medians of Péclet

numbers between vegetated and non-vegetated conditions was not statistically significant (Mann-Whitney $\underline{U} = 24$, $\underline{p} = 0.7$).

The strong differences in variability between non-vegetated and vegetated conditions of some RTD characteristics particularly m_1^* (Coefficient of Variation; CV ~ 0.54 and 0.73, respectively), σ^{2*} (CV ~ 0.43 and 0.70, respectively), and Pe_x (CV ~ 0.44 and 1.1, respectively) for all studies (Table 5A) suggests that these systems, when considered in the aggregate, tend to exhibit a smaller range of mixing characteristics when operating under non-vegetated conditions. This difference in variability between these two state conditions is particularly striking for WL1 (Table 5B). The primary difference between these two conditions is the absence of the potentially moderating influence of vegetation on both ambient flow-induced mixing processes and on wind-induced effects. It is possible, as is shown in a proceeding section, that the presence or absence of vegetation can have a marked effect on realized RTD for these systems, and particularly for WL1.

Relationships between RTD Features and Environmental Effects

For most shallow surface water flow-through basins, mixing is believed to be controlled by the interactions between wind-driven currents and wind-induced turbulence, and ambient flow conditions, with these interactions being moderated by the presence or absence of submersed aquatic vegetation (Andradóttir and Mortamet, 2016; Badrot-Nico et al., 2009; Bentzen et al., 2008; Wörmann and Kronäss, 2005). With respect to a tracer response curve observed at a system outlet the aggregate result of these process is to enhance apparent dispersion, and thus increase the spread of residence times

observed in the RTD. The large degree of variability observed for each of the considered RTD characteristics and derived mixing indices for the set of tracer studies reviewed in this work strongly suggests that each of the aforementioned environmental effects (i.e. flow rates, wind speeds, relative wind directions, and vegetation) interact in a complex, and possibly intractable, manner to produce the observed responses of these systems to tracer impulses. With the possible exceptions of Thackston et al. (1987) and Watters et al. (1973), no study that we are aware of has qualitatively and quantitatively explored the interactions of wind, flow, and vegetation on influencing the characteristics of measured tracer response curves in shallow surface water flow-through systems.

In this section we discuss apparent patterns present in scatter plots of selected measured environmental effects and measured RTD characteristics for all of the conducted tracer studies. Additionally, where appropriate, we employed iteratively re-weighted robust least squares regression to statistically characterize the strength of important and prominent relationships between RTD characteristics and mass-weighted means of environmental effects. Regression analysis was conducted using the *robustbase* package in the R statistical computing environment (Todorov and Filzmoser, 2010). For simplicity, and to account for non-linearity in some relationships, we considered only linear, power-law, and exponential models to assess the strength of apparent correlations. Model selection was determined based upon a minimum Akaike Information Criterion (AIC) criterion and statistical significance of all regression coefficients evaluated at the 0.05 level. In the following discussion significant relationships are discussed, and estimated R^2 values given. All relationships deemed to be significant, with reported R^2 values, have statistically significant regression coefficients. The presentation of

determined regression models does not imply proposed mechanisms for apparent relationships, but rather, provides a comparatively simple method for the determination of linearity and correlations between reported RTD characteristics and measured environmental effects.

Flow Effects

In these wetlands, ambient flow conditions are controlled by the responses of upstream watersheds to periodic storm events, and are thus highly variable; even during the relatively short time period of a tracer study (this variability in volumetric flow rates can be observed in the figures given in Appendix A). Mixing in shallow surface water systems is believed to be controlled primarily by shear dispersion (lateral variations in the longitudinal velocity field), which is controlled by the interactions between bed-induced turbulence, varying bed shear stresses and longitudinal changes in channel morphometry. Ambient internal basin velocities, and their spatial patterns are, in-turn, controlled by volumetric inflow rates, individual basin morphological characteristics, the friction imposed by both bed material and in-channel vegetation, and by the presence of an outflow control structure and basin boundaries. Typically, mixing rates in open channels scale with characteristic length and turbulent velocity scales. When considering ambient flow conditions alone, these are often taken to be the mean channel depth and the ambient flow-induced turbulent shear velocity (Rutherford, 1994). Using these characteristics, we can define a turbulent shear velocity Reynolds number, which is assumed to scale with the various measures of mixing observed from measured RTD:

$$\overline{\mathrm{Re}_{*q(\mathrm{m})}} \sim \frac{\overline{U_{*q(m)}}\,\overline{H}}{\nu} \tag{2.23}$$

where $\overline{U_{*q}}$ is the average turbulent bed shear velocity within the basin, $\overline{H}$ is the average basin depth (Table 1), and ν is the kinematic viscosity of water (assumed equal to ~ 1.004×10^{-6} m^2 s^{-1}). The average turbulent shear velocity scales with the mean cross-sectional average flow rate as $\overline{U_{*q}} \sim \overline{U_q} / \sqrt{8/f}$, where f is the Darcy-Weisbach friction factor (Yen, 1992). In this work, planar area-weighted values of $\overline{U_{*q}}$ were estimated for each basin for each tracer study using reach-based estimates (as discussed in the section on flow monitoring) of mean shear velocities (refer to the section on the derivation of basin morphology):

$$\overline{U_{*q}} \cong \frac{1}{A_w} \sum_{i=1}^{n} \overline{U_{*q(i)(\mathrm{m})}} A_{w(i)} \tag{2.24}$$

The mean shear velocity for each reach was determined from the mass-weighted mean cross-sectional velocity and reach hydraulic radius R (the average cross-sectional area of the reach divided by the average wetted perimeter expressed in meters), and the estimated reach Manning's roughness coefficient (Chen, 1993):

$$\overline{U_{*q(i)}} \cong n_{t(i)} \overline{U_{q(i)}} \sqrt{\frac{g}{R_i^{1/6}}} \tag{2.25}$$

and,

$$\overline{U_{q(i)(\mathrm{m})}} = \frac{Q_{i(\mathrm{m})}}{\overline{B_i}\,\overline{H_i}} \tag{2.26}$$

where $Q_{i(\mathrm{m})}$ is the mass-weighted inflow rate (Eqn. 2.6), and $\overline{B_i}$ and $\overline{H_i}$ are the mean reach width and depth, respectively. The value of n_t in Eqn. 2.25 incorporates both bed and vegetative roughness. Because bed material composition was not assessed for each wetland, a Manning's bed roughness coefficient (n_b) of 0.052 (s $m^{-1/3}$) was assumed based

on the recommend value for dredged artificial channels with sluggish back water regions given by Yen (1992). Manning's vegetative roughness coefficients were estimated on a reach-by-reach basis using the formula proposed by Shih and Rahi (1982) for channels densely populated with submergent vegetation and reach-specific channel morphological characteristics and estimates of mean percent vegetative cover:

$$n_{t(i)} \cong \frac{\overline{H}_i^{2/3}}{\sqrt{2g}} \sqrt{\frac{\overline{A_{v(i)}}}{\overline{A_{c(i)}} L_i}} + n_b \tag{2.27}$$

where n_b is the assumed value of Manning's n for the channel without vegetation, g is gravitational acceleration (9.81 m s^{-2}), $\overline{A_{v(i)}}$ is the total frontal area of submersed vegetal elements projected along the length of the reach $L_{(i)}$, $\overline{H_i}$ is the average reach depth (at full pool), and $\overline{A_{c(i)}}$ is the mean cross-sectional area of the reach. The quantity $\overline{A_{v(i)}} / \overline{A_{c(i)}}$ in Eqn. 2.27 is representative of the fractional area of the channel cross-section occupied by submersed vegetal elements (stems, leaves, etc.), and is taken in this work to be reasonably approximated by the area-weighted mean percent vegetative cover, $\overline{C_v}$ for each reach, as obtained from the interpolated vegetative cover grids discussed in the section on vegetation modeling. The assumption that the fractional planar area occupied by vegetation (i.e. $\overline{C_v} / 100$) is a reasonable approximation of the fractional cross-sectional area occupied by vegetation necessarily assumes that the vegetation density at all locations is uniform over the water column depth. While this assumption is most certainly not correct, a lack of survey information regarding the vertical structure of vegetation and total channel occlusion by vegetation necessitated its use.

Summaries of estimated Manning's *n* values and planar area-weighted estimates of flow-induced turbulent shear velocities for each wetland for each study are given in Table 4B. Our estimates of vegetative roughness span from 0.052 (the assumed lower limit for bed-induced friction) to 0.081 (WL1_6), with a mean of 0.062 for all studies considered, and mean of 0.073 for studies conducted under vegetated conditions. These values are approximately one-half to one-fourth of the estimates obtained by Shih and Rahi (1982) for wetland flow studies conducted on channels densely populated by *Eichhornia crassipes* (*syn.* water hyacinth), but are within the lower range of values obtained by Bakry et al. (1992) for irrigation canals densely occluded by *P. pectinatus* (the predominant species in the wetlands reviewed in this study).

Equation 2.23 implies that rates of longitudinal dispersion will increase with increasing mean flow rates (and thus increasing turbulence) and water depths, assuming uniform flow conditions. Thus we would expect longitudinal dispersion coefficients to increase linearly with flow and with turbulent shear velocities (Rutherford, 1994), assuming negligible changes in mean basin water depths with increasing flow rates (as is often the case with shallow flow-through basins). Further, because the longitudinal dispersion coefficient is directly derived from the moments of the measured RTD, we can reasonably assume that other RTD features such as the dimensionless first moment and the dimensionless temporal variance are also related to $\overline{\mathrm{Re}_{q^*(\mathrm{m})}}$. These relationships, in addition to relationships between $\overline{\mathrm{Re}_{q^*(\mathrm{m})}}$ and other measured RTD features are explored further in this section.

Scatter plots of considered RTD features as functions of the product of ambient flow-induced shear velocity and mean basin depth are given in Figure 9. In the

proceeding discussion turbulent shear velocities are used in lieu of averages of measured volumetric flow rates because shear velocities scale with flow (and thus explicitly incorporate flow effects) but also include the moderating influence of vegetation on internal bulk flow behavior.

An assessment of the relationships between $\overline{\mathrm{Re}_{q^*(\mathrm{m})}}$ and each RTD characteristic (Figure 9) indicates that ambient flow conditions appear to have little discernable influence on initial and peak arrival times (both measures of short-circuiting) when viewing the set of tracer studies in the aggregate. However, $\overline{\mathrm{Re}_{q^*(\mathrm{m})}}$ appears to have a moderate influence on both the dimensionless initial and peak and arrival times, although the effect is more apparent for the latter measure of short-circuiting. In general, higher flow rates will tend to reduce short-circuiting as represented by these metrics. Further, these plots (panels A and B in Figure 9) highlight the high degree of variability of these systems in response to ambient flow conditions, suggesting that, while flow is a reasonable predictor of short-circuiting in these systems in the aggregate, individuals wetlands likely respond differently. The modest effect of flow rates on short-circuiting, however, is belied by the apparent tendency for increasing flows to result in higher rates and degrees of mixing as indicated by the strong positive relationships between $\overline{\mathrm{Re}_{q^*(\mathrm{m})}}$ and σ^{2^*} and K_{x}, and the modest inverse effect on Pe_{x}. These relationships hold for all studies considered as a set, but do not reflect the general tendency of WL1 under non-vegetated conditions, in particular. For this wetland, increasing flow rates tend to result in a general reduction in bulk and longitudinal mixing, which is reflected in an apparent increase in Pe_{x}. Why this system stands out with respect to its mixing behavior under differing flow conditions is uncertain at this time.

Perhaps the most significant relationship featured in Figure 9 is the high degree of correspondence between $\overline{\mathrm{Re}_{q^*(\mathrm{m})}}$ and the dimensionless mean residence time; a pattern that is prominent for all studies considered regardless of vegetative conditions, and particularly significant for WL1. These relationships strongly suggest that higher flow rates tend to promote greater degrees of volumetric efficiencies for these systems, and for WL1 in particular. However, volumetric efficiency tends to increase above unity with increasing flow rates, suggesting that higher flow rates may promote back mixing and centroid trapping in isolated sections of these systems, the effect of which may be accentuated when vegetation is present. This is a possible explanation for the several tracer studies (WL1_3, WL1_5, WL1_11, WL1_12 and WL3_5) which produced values of m_1^* greater than unity. Additionally, these relationships implicitly indicate greater rates of lateral mixing during higher flows (e.g. Rutherford, 1994), as indicated by the approach of m_1^* to unity. While a diminishment of dead space and back-mixing is desirable in these systems from a constituent mitigation perspective, potential performance gains had by improvements in volumetric efficiencies may be offset by a reduction in mean hydraulic residence times with increasing flow rates.

In riverine systems longitudinal dispersion rates strongly scale with turbulent shear velocities (Rutherford, 1994). Our results seem to confirm that this also the case for the shallow run-of-the-river flow-through type basins evaluated in this work. However, our findings do not affirm the conclusions of Mossman et al. (1991), who observed that turbulent bed shear velocities in Coralville Reservoir, Iowa (another run-of-the-river basin) scaled poorly with longitudinal and lateral mixing rates. Mossman and colleagues attributed this weak scaling to the extremely small turbulent shear velocities modeled in

their system (thus suggesting that turbulent shear dispersion is a small factor in longitudinal and lateral mixing), and to the process of repeated plume contraction and expansion in response to reservoir morphometric contractions and expansions along the length of the system; thus indicating that the tracer plume never left the pre-asymptotic period (i.e. the time-period during a tracer study when complete vertical and lateral mixing has not been achieved). However, the strong correlation between $\overline{\mathrm{Re}_{q^*(\mathrm{m})}}$ and K_x is unsurprising given that this RTD characteristic is estimated using estimates of the basin average cross-sectional velocities. More independent analyses which provide estimates of K_x directly from tracer response curves measured at several locations along the lengths of these sites between system inlet and outlets (Rutherford, 1994; Fischer et al., 1979) are needed to affirm whether these apparent correlations are hold or are spurious.

Wind Effects

For semi-enclosed shallow flow-through surface water basins, an applied wind shear at the water surface can result in increased turbulence of the water column, and the formation of complex gyres and vertical and horizontal patterns resulting from local acceleration of the upper layer of the water column (Andradóttir and Mortamet, 2016; Shaw et al. 1997). In addition to increasing the turbulence of the water column, winds can cause the formation of semi-stable chaotic flow fields, the structure of which has been shown to be highly dependent on the direction of applied winds, and the effective fetch of the basin in the direction of the wind (Andradóttir and Mortamet, 2016; Shaw et al. 1997). Complex wind-induced recirculation patterns and turbulence can promote longitudinal, lateral, and vertical mixing; and has been suspected to cause shallow flow-

through basins to tend toward a complete mixing regime (Liang et al., 2006). In this section, to assess the influence of wind on mixing in this set of wetlands, we consider the effects of wind speed and wind direction on the temporal characteristics of developed RTD.

Mass-weighted average wind speeds (Eqn. 2.6) were used to estimate turbulent shear velocities at the water surface, with estimated percent vegetative cover acting as a wind buffering coefficient:

$$\overline{U_{w*(\mathrm{m})}} \cong \left(1-\overline{f_{cv}}\right)\sqrt{1.5x10^{-3}\frac{\rho_a}{\rho_w}}\overline{v_{w(10)(\mathrm{m})}} \tag{2.28}$$

where ρ_a and ρ_w are the density of air and water (assumed to be 1.2 and 998.1 kg m^{-3}, respectively), and $\overline{f_{cv}} = \overline{C_v}/100$ is the fractional cover of vegetation estimated for each tracer study, as determined from the afore-discussed vegetation surveys. Following Watters et al. (1973), using $\overline{U_{w*(m)}}$ as an appropriate turbulent velocity scale, we define a wind-shear turbulent surface Reynolds number as:

$$\overline{\mathrm{Re}_{w*(\mathrm{m})}} \sim \frac{\overline{U_{w*(\mathrm{m})}}\,\bar{\ell}}{\nu} \tag{2.29}$$

where $\bar{\ell}$ is a characteristic turbulent length scale taken here to be equal to the mean pool depth, as wind tends to act disproportionately over the pool regions of these sites, and is presumed to have relatively little influence on the small, deep, and narrow inflow channels observed for every site but WL3 (Table 1).

Scatter plots of considered RTD characteristics as functions of $\overline{\mathrm{Re}_{w*(\mathrm{m})}}$ are given in Figure 10. The influence of the considered summary primary wind effects ($\overline{\mathrm{Re}_{w*(\mathrm{m})}}$, and $\overline{\theta_{\mathrm{wf(m)}}}$) on RTD characteristics and derived mixing indices is less obvious than the

apparent relationships observed for area-weighted mean Reynolds numbers and overall, wind-associated effects tend to exert less influence on the considered RTD characteristics than flow-associated effects for some features. In general, as shown in Figure 10, for non-vegetated conditions, increasing wind shear velocities tends to result in reduced dimensionless initial arrival times, reduced volumetric efficiencies (particularly for sites WL1 and WL2), and increases in mixing rates, as suggested by the strong positive relationships between wind shear and σ^{2*} and K_x. The tendency for increasing wind speeds to promote bulk mixing and longitudinal dispersion is also reflected in a general reduction in Pe_x with increasing wind speeds, particularly for sites WL1 and WL2.

Wind shear has long been surmised to affect short-circuiting and mixing in shallow flow-through basins (Andradóttir and Mortamet, 2016; Shaw et al. 1997; Thackston et al., 1987), although this topic has received relatively little attention, and empirical estimates of the effects of wind shear on short-circuiting from measured RTD are notably lacking in the primary literature. However, our results do seem to confirm the general conclusions of Bentzen et al. (2008) that increasing wind speeds applied to shallow surface water flow-through basins can result in modest reductions in the dimensionless peak arrival and mean residence times.

In terms of volumetric efficiency, a reduction of m_1^* with an increase in $\overline{\mathrm{Re}_{w*(\mathrm{m})}}$ implies that the effective volumes of these wetlands tend to be reduced with increasing wind shear during non-vegetated states. However, this explanation belies the general observation that increasing wind shear promotes bulk mixing in these systems, as shown in the plots of σ^{2*} and K_x versus $\overline{\mathrm{Re}_{w*(\mathrm{m})}}$, and as claimed by Thackston et al. (1987). A more likely explanation is that increasing surface wind shear results in higher rates of

wind-driven advection, thus causing, in general, the premature arrival of the centroid (relative to the mean hydraulic residence time) at the outlets, while also promoting basin-scale mixing. When vegetation is present, however, it is possible that the potential for wind-induced surface advection to fully form is mitigated by the established aquatic vegetation canopy.

Figure 11 provides scatter plots of measured RTD characteristics as functions of estimated relative wind directions for all studies. In general, our data indicate that winds increasingly oriented against predominant flow directions (i.e. $\overline{\theta_{wf}} \rightarrow 2$) tend to result in a marginal reduction in dimensionless peak arrival and mean residence times, particularly for sites WL2 and WL3, and an increase in bulk mixing for sites WL1 and WL2, regardless of whether vegetation was present, and a reduction in Pe_x for WL1 when vegetation was present. However, under non-vegetated conditions, winds oriented against the flow direction at site WL1 tend to result in a reduction in the value of K_x.

Clearly, the influence of wind directions relative to mean basin flow directions have highly variable influence on some mixing characteristics for some of these sites, particularly sites WL1 and WL2. WL1 is most affected by wind, which likely stems from a lack of surrounding topographic controls (such as hills) on wind shear; a feature that is present for each of the other sites evaluated in this work. However, it is clear from the preceding discussion that the individual results of these effects will produce significantly different responses in different systems, affecting different temporal features of the RTD.

For WL2, the apparent tendency for increasing degrees of bulk mixing with winds becoming increasingly oriented against the predominant flow direction is likely a result of wind sheltering effects for this wetland. This wetland is situated in a partial bowl that

opens to the east, which is also the approximate primary flow direction (Figure 2). Thus, wind effects are expected to be greatest for this wetland when originating from the east. Further, winds oriented against the flow direction for this wetland may push tracer into comparatively quiescent regions of the pool, notably those which are sheltered behind the island positioned on the north-central end of the wetland. This effect may explain the comparatively long tails observed for tracer studies for this site (Figures 14A through 18A, Appendix A).

Why wind direction apparently influences bulk mixing in WL1 when vegetation is present is this system is unclear. One possibility is that winds oriented against the flow direction pushes tracer upstream into the vegetation canopy and into the comparatively sparsely vegetated region along the southern boundary of this wetland (Figures 1B through 5B, Appendix B), thus causing an elongation of the temporal variance for these studies. However, without detailed in-pool surveys of tracer concentrations for this and other sites this possibility is just conjecture.

It is currently uncertain why winds oriented against the predominant flow direction may result in a reduction in the mean residence time for site WL3. One possibility is that winds oriented against the flow will drive a small surface layer of flow against the current, but will elicit a corresponding return current in the direction of flow in the lower layers of the water column, which may also carry the bulk of the flow (e.g. Shaw et al., 1997). Watters et al. (1973) anecdotally report such an effect for studies conducted on field-scale settling ponds, but do not report a numerical correlation for these effects. Further, there is increasing empirical evidence for this flow behavior from several comparatively recent studies, notably Andradóttir and Mortamet (2016) and Shaw

et al. 1997. However, this effect is not reflected in any other considered metric of mixing behavior for this system.

Vegetation Effects

No other study that we are aware of has explicitly evaluated the differences in RTD characteristics and derived mixing indices between vegetated and non-vegetated conditions, or between periods of vegetation growth and senescence for submergent-dominated field-scale wetlands. While several studies have specifically evaluated the influence of emergent vegetation on bulk mixing characteristics (Keefe et al., 2010; Wörmann and Kronäss, 2005), the results from these studies are not directly transferable to wetlands which are submergent-dominated. For one, dense emergent beds may occupy a much greater portion of a system's volume than submergent stands. Additionally, while emergent vegetation tends to extend over the entire water column, submergent vegetation will feature time-varying vertical growth structures, and may occupy only a small section of the water column during early growth stages (Shucksmith et al., 2011). As the growing season progresses, as is shown in the vegetation surveys maps provided in Appendix B, vegetation begins to colonize larger portions of these systems, occurring in both shallows and deeper sections, potentially causing greater channel occlusion and facilitating the formation of short-circuiting pathways. Additionally, nearly all of the species observed in these systems are canopy forming, and during later stages in their respective growth periods, will shade-out the understory thus causing the formation of a comparatively sparse flow region nearest the bed, with a densely vegetated region directly above. Because of these differences, a comparison of our results with other systems with respect

to the response of bulk mixing behavior to the presence of vegetation is not possible; although general trends can be highlighted and compared with other works.

As outlined previously, nearly every RTD characteristic evaluated in this work demonstrated a moderate to large comparative difference in their medians between vegetated and non-vegetated conditions. However, the lack of statistical significance for some RTD characteristics between medians observed under these two conditions suggests that these differences are due either to random chance, or result from the comparatively small sample sizes used in this analysis. Additionally, provided medians for both conditions are heavily weighted toward site WL1, as nearly one-half of all tracer tests conducted under both vegetated and non-vegetated conditions were performed on this wetland. It is possible, therefore, that an expanded dataset that includes additional studies on other sites would reveal statistically significant differences in estimated parameters between the two vegetated conditions. However, despite the lack of statistical significance, there is ample qualitative and empirical evidence to suggest that the presence and absence of vegetation in these systems likely produces distinctly different mixing regimes for a given wetland, on average. For one, as discussed previously, RTDs developed under vegetated conditions show significantly delayed initial and peak arrival times, more symmetrical profiles, and shorter tails. Each of these factors suggest that the total degree of mixing, short-circuiting, longitudinal dispersion, and dead space in these systems is diminished when vegetation is present. Conversely, in the absence of vegetation, tracer response curves tend to show extreme fronting behavior, very early initial and peak arrival times, and extensive and highly irregular tails. Differences in developed RTDs between differing vegetative densities have also been noted for

emergent vegetation dominated systems (Keefe et al., 2010; Wörmann and Kronäss, 2005; Jenkins and Greenway, 2005).

As shown in the plots of percent vegetated cover versus each of the RTD features evaluated in this work (Figure 12), general trends in these relationships are moderately weak at best. Both z_i and z_p for the aggregate set appear to increase slightly with increasing vegetative cover; however, these relationships are not statistically significant for z_i and only marginally so for z_p ($R^2 \sim 0.58$). In contrast to results given by Keefe et al. (2010) and contradictory to the observed differences in means between vegetated and non-vegetated conditions (Table 5B), m_1^* appears to be weakly inversely related to $\overline{C_v}$ ($R^2 \sim 0.55$) for all vegetated studies, but strongly inversely related to $\overline{C_v}$ for WL1. This result suggests that increasing vegetative cover results in slight decreases in system effective volumes. Excluding the studies WL1_5 and WL3_2 (two distinct outliers) this relationship improves considerably ($R^2 \sim 0.87$), which closely matches the fit for this characteristic for WL1 ($R^2 \sim 0.87$). Our results support the findings of Nepf et al. (1997), who inferred from tracer experiments in an artificially vegetated channel greater degrees of dead space with increasing submersed element density.

An additional notable relationship is an apparent decrease in K_x with increasing vegetative cover up to $\overline{C_v} \sim 30\%$; with this relationship being statistically significant using a second-order quadratic model ($R^2 \sim 0.84$ and 0.97 for all vegetated studies and for those conducted on WL1, respectively). Above a $\overline{C_v}$ of 30% K_x appears to increase with increasing vegetative cover for both trend lines. Average turbulent shear velocities tended to decrease with increasing vegetated cover for all sites (data not shown), so a reduction in average shear stresses with increasing vegetative cover is not a likely

explanation for the observed trend in K_x versus $\overline{C_v}$. Several possibilities are thus more likely. One, increasing vegetation density up to a $\overline{C_v}$ of 30% may promote lateral mixing rates by virtue of increased flow tortuosity resulting in significant lateral displacement of flow through the semi-porous vegetal canopy (Kadlec and Wallace, 2008; Nepf, 1997). The net effect of increasing lateral movement of tracer would result in an over-all reduction in K_x. Two, increasing vegetative densities may impose a delay on the transport of tracer through these systems by causing a reduction in mean basin shear velocities as result of increased friction and flow tortuosity. This effect would, in-turn, cause a decrease in longitudinal dispersion rates. And finally, the presence of the aquatic vegetation canopy may dampen the transference of wind energy to these systems, thus reducing the likelihood of both wind-driven advection and wind-induced basin scale mixing occurring. The former two possibilities have been supported by laboratory and theoretical investigations into mixing processes in vegetated flows. For instance, Nepf et al. (1997), using laboratory flumes and submersed rigid dowels (used in their work as a proxy for emergent vegetation), demonstrated that increasing submersed element density resulted in an apparent decrease in the values of longitudinal dispersion coefficients. They attributed their results to a combination of increased mechanical diffusion and an increase in vertical mixing rates. The possibility of the vegetation canopy causing a reduction in basin-scale mixing and wind-driven advection has received scant attention in the literature, with the exception of Herb and Steffan (2004), who used a quasi-numerical model to demonstrate the wind buffering effect of vegetation on vertical mixing rates. However, these studies do not provide a framework for explaining the apparent increase in K_x above a $\overline{C_v}$ of ~30% as observed with our data. It is possible that above this

vegetative cover estimate, the vegetative canopy becomes patchier (as suggested by the vegetative cover plots given in Appendix B), resulting in short-circuited pathways and an increase in effective dead space in these systems, as indicated by the apparent general reduction in volumetric efficiency with increasing vegetative cover (Figure 12). An additional possibility is that above this value the vertical vegetal canopy structure becomes separated into two distinct zones comprised of a relatively sparsely populated flow zone near the bed overlain by a densely vegetated zone. This possibility would imply that vertical mixing would likely not be complete over the water column depth, thus inflating the apparent longitudinal dispersion coefficient. However, the vegetation data collected and presented in this work is too coarse to provide clear conclusions about the mechanisms affecting bulk mixing in these systems, and the explanations given above are presently speculation; additional studies of mixing processes in vegetated channels, with specific attention on low-velocity wetland systems are needed to make further inference about the mechanisms behind the apparent trends observed in this work.

Discussion and Conclusions

Thirty tracer studies were conducted on 5 separate constructed agricultural wetlands designed to intercept and mitigate agricultural nutrient loads. Studies were conducted under a variety of flow, meteorological, and vegetative conditions in order to observe the variability inherent in these systems with respect to their bulk hydraulic and mixing characteristics. Overall, the wetlands considered in this work tended to feature highly non-ideal flow patterns characterized by moderate to significant degrees of short-circuiting, extensive basin-scale mixing, high rates of dispersion, and highly variable

volumetric efficiencies. All of the systems evaluated tended to feature RTD characteristics and derivative bulk mixing indices that are within the ranges of values observed for systems of comparable or larger sizes. However, some metrics tended to fall on or outside of the upper-ends of ranges obtained from some values reported in the literature. This is notably the case for estimates of the longitudinal dispersion coefficient, and the volumetric efficiency. Further, the medians of estimated RTD characteristics between vegetated and non-vegetated conditions are not statistically significant, except for K_x.

The results of the robust regressions of measured RTD characteristics and mass-weighted means of measured environmental effects suggest that the variability in observed RTD features within and between systems arises primarily from the complex interactions between ambient flow rates, wind forcing, and the presence or absence of submersed aquatic vegetation. The particular response of a system to a tracer impulse will strongly depend on both the particular morphology of the wetland and the presence of a submersed vegetative canopy and its representative density, in addition to the unique character of time-varying hydrological and atmospheric conditions. Thus, a single tracer study conducted on a given system will only capture that system's response to the prevailing environmental conditions at the time of the study. The high degree of variability observed for some RTD characteristics measured in this work suggest that multiple tracer studies should be conducted on a given system over a large range of flow, atmospheric, and vegetated conditions in order to obtain a more accurate assessment of the mean mixing behavior of the system.

Additional factors that can influence mixing that have not been considered in this work include diurnal or sub-diurnal stratification, and the temperature and density differences between basin pools and their respective inlets, which would be observed for warmer operating periods for these wetlands. Such complex dynamics may be studied in field settings, but should also be studied with the aid of multi-dimensional numerical flow and mixing models which explicitly incorporate basin morphological characteristics, spatial vegetation characteristics, and external environmental forcings. Such models may be used to further deduce the relative influence of a wide range of environmental forcings, such as wind and flow rates, individually and in combination, on internal mixing characteristics of these types of basins.

Acknowledgements

This study was funded by the Iowa Department of Agriculture and Land Stewardship, with additional funding from the Department of Ecology, Evolution, and Organismal Biology, Iowa State University. We thank Ian Ellickson, Claudette Sandoval-Green, and numerous students at Iowa State University for their assistance with field work, and Greg and Jana Stenback for their assistance with data management. Additionally, we are grateful to the owners of the wetlands studied in this work for granting access and permission to study these sites.

References

Allen, A.W. 2005. The conservation reserve enhancement program. USGS Staff–Published Research. U.S. Department of Interior.

Andradóttir, H. Ó., and M-L. Mortamet. 2016. Impact of wind on storm-water pond hydraulics. Journal of Hydraulic Engineering 142 (10) doi:10.1061/(ASCE)HY.1943-7900.0001150.

Badrot-Nico, F., V. Guinot, and F. Brissaud. 2009. Fluid flow pattern and water residence time in waste stabilization ponds. Water Science and Technology 59 (6):1061–68. doi:10.2166/wst.2009.087.

Bakry, M. F., T. K. Gates, and A. F. Khattab. 1992. Field-measured hydraulic resistance characteristics in vegetation-infested canals. Journal of Irrigation and Drainage Engineering 118 (2): 256–74. doi:10.1061/(ASCE)0733-9437(1992)118:2(256).

Beer, T., and P. C. Young. 1983. Longitudinal dispersion in natural streams. Journal of Environmental Engineering 109 (5):1049–67. doi:10.1061/(ASCE)0733-9372(1983)109:5(1049).

Bentzen, T. R., T. Larsen, and M. R. Rasmussen. 2008. Wind effects on retention time in highway ponds. Water Science & Technology 57 (11):1713. doi:10.2166/wst.2008.267.

Bodin, H., A. Mietto, P.M. Ehde, J. Persson, and S.E.B. Weisner. 2012. Tracer behavior and analysis of hydraulics in experimental free water surface wetlands. Ecological Engineering 49:201–11. doi:10.1016/j.ecoleng.2012.07.009.

Broughton, A., and A. Shilton. 2012. Tracer studies on an aerated lagoon. Water Science and Technology 65(4):611–17. doi:10.2166/wst.2012.906.

Buchanan, T.J., and W.P. Somers. 1969. Discharge measurements at gaging stations USGS Numbered Series 3-A8. Techniques of Water-Resource Investigation. U.S. Govt. Print. Office

Carleton, J. N., T. J. Grizzard, A. N. Godrej, and H. E. Post. 2001. Factors affecting the performance of stormwater treatment wetlands. Water Research 35(6):1552–1562.

Crumpton, W. G., Stenback, G. A., Miller, B. A., Helmers, M. J. 2006. Potential benefits of wetland filters for tile drainage systems: impact on nitrate loads to Mississippi River sub-basins. Final project report to US Department of Agriculture Project number: IOW06682.

Cirpka, O.A., and P.K. Kitanidis. 2000. characterization of mixing and dilution in heterogeneous aquifers by means of local temporal moments. Water Resources Research 36 (5):1221–36. doi:10.1029/1999WR900354.

Dierberg, F.E., and T.A. DeBusk. 2005. An evaluation of two tracers in surface-flow wetlands: rhodamine-wt and lithium. Wetlands 25(1):8–25. doi:10.1672/0277-5212(2005)025[0008:AEOTTI]2.0.CO;2.

Duarte, C.M., and J. Kalff. 1990a. Patterns in the submerged macrophyte biomass of lakes and the importance of the scale of analysis in the interpretation. Canadian Journal of Fisheries and Aquatic Sciences 47(2):357–63. doi:10.1139/f90-037.

Duarte, C.M., and J. Kalff. 1990b. Biomass density and the relationship between submerged macrophyte biomass and plant growth form. Hydrobiologia 196(1):17–23. doi:10.1007/BF00008889.

Elzinga, C.L., D.W. Salzer, and J.W. Willoughby. 1998. Measuring & monitoring plant populations. U.S. Fish and Wildlife Service Staff Report, U.S. Department of the Interior

Fernández-Sempere, J., R. Font-Montesinos, and O. Espejo-Alcaraz. 1995. residence time distribution for unsteady-state systems. Chemical Engineering Science 50(2): 223–30. doi:10.1016/0009-2509(94)00230-O.

Fischer, H.B., J.E. List, C.R. Koh, J. Imberger, and N.H. Brooks. 1979. *Mixing in Inland and Coastal Waters*. Academic Press, New York, N.Y., U.S.A.

Herb, W.R., and H.G. Stefan. 2004. Temperature stratification and mixing dynamics in a shallow lake with submersed macrophytes. Lake and Reservoir Management 20(4): 296–308. doi:10.1080/07438140409354159.

Holland, J.F., J.F. Martin, T. Granata, V. Bouchard, M. Quigley, and L. Brown. 2004. Effects of wetland depth and flow rate on residence time distribution characteristics. Ecological Engineering 23(3):189–203. doi:10.1016/j.ecoleng.2004.09.003.

Irwin, J.S. 1979. A theoretical variation of the wind profile power-law exponent as a function of surface roughness and stability. Atmospheric Environment (1967) 13(1):191–94. doi:10.1016/0004-6981(79)90260-9.

Jenkins, G.A., and M. Greenway. 2005. The hydraulic efficiency of fringing versus banded vegetation in constructed wetlands. Ecological Engineering 25(1):61–72. doi:10.1016/j.ecoleng.2005.03.001.

Kadlec, R.H. 1994. Detention and mixing in free water wetlands. Ecological Engineering 3(4):345–80. doi:10.1016/0925-8574(94)00007-7.

Kadlec, R.H. 2007. Tracer and spike tests of constructed wetlands. ecohydrology & hydrobiology, proceedings from wastewater treatment in wetlands: Theoretical and practical aspects, Starbienino, Poland 10-17 September 2005, 7 (3–4): 283–95. doi:10.1016/S1642-3593(07)70111-8.

Kadlec, R.H., and S. Wallace. 2008. *Treatment Wetlands*, Second Edition. CRC Press. Boca Raton, FL., U.S.A.

Keefe, S.H., L.B. Barber, R.L. Runkel, J.N. Ryan, D.M. McKnight, and R.D. Wass. 2004. Conservative and reactive solute transport in constructed wetlands. Water Resources Research 40(1) doi:10.1029/2003WR002130.

Keefe, S.H., J.S. (Thullen) Daniels, R.L. Runkel, R.D. Wass, E.A. Stiles, and L.B. Barber. 2010. Influence of hummocks and emergent vegetation on hydraulic performance in a surface flow wastewater treatment wetland. Water Resources Research 46(11):W11518. doi:10.1029/2010WR009512.

Kusin, F.M., A.P. Jarvis, and C.J. Gandy. 2014. Hydraulic performance and iron removal in wetlands and lagoons treating ferruginous coal mine waters. Wetlands 34(3):555–64. doi:10.1007/s13157-014-0523-4.

Lees, M.J., L.A. Camacho, and S. Chapra. 2000. On the relationship of transient storage and aggregated dead zone models of longitudinal solute transport in streams. Water Resources Research 36(1):213–24. doi:10.1029/1999WR900265.

Levenspiel, O. 2011. Tracer Technology: *Modeling the Flow of Fluids*. Springer Science & Business Media, Berlin, Germany

Liang, Q., A.G.L. Borthwick, and P.H. Taylor. 2006. Wind-induced chaotic advection in shallow flow geometries. part ii: non-circular basins. Journal of Hydraulic Research 44(2):180–88. doi:10.1080/00221686.2006.9521674.

Lightbody, A.F., H.M. Nepf, and J.S. Bays. 2007. Mixing in deep zones within constructed treatment wetlands. Ecological Engineering 29(2):209–20. doi:10.1016/j.ecoleng.2006.11.001.

Lightbody, A.F., H.M. Nepf, and J.S. Bays. 2009. Modeling the hydraulic effect of transverse deep zones on the performance of short-circuiting constructed treatment wetlands. Ecological Engineering 35(5):754–68. doi:10.1016/j.ecoleng.2008.12.010.

Maloszewski, P., and A. Zuber. 1993. Principles and practice of calibration and validation of mathematical models for the interpretation of environmental tracer data in aquifers. Advances in Water Resources 16(3):173–90. doi:10.1016/0309-1708(93)90036-F.

Martinez, C.J, and W.R Wise. 2003. Analysis of constructed treatment wetland hydraulics with the transient storage model OTIS. Ecological Engineering 20(3):211–22. doi:10.1016/S0925-8574(03)00029-6.

Min, J-H., and W.R. Wise. 2009. Simulating short-circuiting flow in a constructed wetland: the implications of bathymetry and vegetation effects. Hydrological Processes 23(6):830–41. doi:10.1002/hyp.7219.

Mitsch, W.J., and J.W. Day. 2006. Restoration of wetlands in the Mississippi–Ohio–Missouri (MOM) River Basin: experience and needed research. Ecological Engineering 26(1):55–69. doi:10.1016/j.ecoleng.2005.09.005.

Mossman, D.J., F.M. Holly, and J.L. Schnoor. 1991. Field observations of longitudinal dispersion in a run-of-the-river impoundment. Water Research 25(11):1405–15. doi:10.1016/0043-1354(91)90119-B.

Nauman, E. B., and B. A. Buffham. 1983. *Mixing in Continuous Flow Systems*. Wiley, West Sussex, England

Nepf, H. M., C. G. Mugnier, and R. A. Zavistoski. 1997. The effects of vegetation on longitudinal dispersion. Estuarine, Coastal and Shelf Science 44(6):675–84. doi:10.1006/ecss.1996.0169.

Kadlec, R.H. 1990. Overland flow in wetlands: vegetation resistance. Journal of Hydraulic Engineering 116(5):691–706. doi:10.1061/(ASCE)0733-9429(1990)116:5(691).

Pebesma, E.J. 2004. Multivariable geostatistics in S: The GSTAT package. Computers & Geosciences 30(7):683–91. doi:10.1016/j.cageo.2004.03.012.

Persson, J. 2000. The hydraulic performance of ponds of various layouts. Urban Water 2(3):243–50. doi:10.1016/S1462-0758(00)00059-5.

Persson, J., and H.B Wittgren. 2003. How hydrological and hydraulic conditions affect performance of ponds. Ecological Engineering 21(4–5):259–69. doi:10.1016/j.ecoleng.2003.12.004.

R Development Core Team. 2008. R: A language and environment for statistical computing. R Foundation for Statistical Computing, Vienna, Austria. ISBN 3-900051-07-0, URL http://www.R-project.org.

Rutherford, J. C. 1994. *River Mixing*. Wiley, West Sussex, England

Savitzky, A., and M.J.E. Golay. 1964. Smoothing and differentiation of data by simplified least squares procedures. Analytical Chemistry 36(8):1627–39.

Shaw, J.K.E., W.F. Watt, J. Marsalek, B.C. Anderson, and A.A. Crowder. 1997. Flow pattern characterization in an urban stormwater detention pond and implications for water quality. Water Quality Research Journal of Canada 32(1):53-71

Shih, S.F., and G.S. Rahi. 1982. Seasonal variations of manning's roughness coefficient in a subtropical marsh. Transactions of the ASAE 25(1):0116-0119. doi: 10.13031/2013.33488

Shucksmith, J. D., J. B. Boxall, and I. Guymer. 2010. Effects of emergent and submerged natural vegetation on longitudinal mixing in open channel flow. Water Resources Research 46(4):W04504. doi:10.1029/2008WR007657.

Shucksmith, J. D., J. B. Boxall, and I. Guymer. 2011. Determining longitudinal dispersion coefficients for submerged vegetated flow. Water Resources Research 47(10):W10516. doi:10.1029/2011WR010547.

Smart, P. L., and I. M. S. Laidlaw. 1977. An evaluation of some fluorescent dyes for water tracing. Water Resources Research 13(1):15–33. doi:10.1029/WR013i001p00015.

Speer, S., P. Champagne, A. Crolla, and C. Kinsley. 2009. Hydraulic performance of a mature wetland treating milkhouse wastewater and agricultural runoff. Water Science and Technology 59(12):2455–62. doi:10.2166/wst.2009.332.

Stairs, D.B. 1993. Flow characteristics of constructed wetlands : tracer studies of the hydraulic regime. M.S. Thesis. Oregon State University.

Teixeira, E.C., and R.N. Siqueira. 2008. Performance assessment of hydraulic efficiency indexes. Journal of Environmental Engineering 134(10):851–59. doi:10.1061/(ASCE)0733-9372(2008)134:10(851).

Thackston, E.L., D.Jr. Shields, and P.R. Schroeder. 1987. Residence time distributions of shallow basins. Journal of Environmental Engineering 113(6):1319–32. doi:10.1061/(ASCE)0733-9372(1987)113:6(1319).

Todorov, V., and P. Filzmoser. 2009. An object-oriented framework for robust multivariate analysis. Journal of Statistical Software 32 (3).

Watters, G.Z., K.A. Mangelson, and R.L. George. 1973. The hydraulics of waste stabilization ponds. Final Report to the Office of Water Resources Research on Project A-008-Utah. Utah State University.

Werner, T.M., and R.H. Kadlec. 1996. application of residence time distributions to stormwater treatment systems. Ecological Engineering 7(3):213–34. doi:10.1016/0925-8574(96)00013-4.

Woltemade, C. J. 2000. Ability of restored wetlands to reduce nitrogen and phosphorus concentrations in agricultural drainage water. Journal of Soil and Water Conservation 55(3):303–9.

Wörman, A., and V. Kronnäs. 2005. Effect of pond shape and vegetation heterogeneity on flow and treatment performance of constructed wetlands. Journal of Hydrology 301(1–4):123–38. doi:10.1016/j.jhydrol.2004.06.038.

Yen, B.C.(ed.). 1992. *Channel Flow Resistance: Centennial of Manning's Formula*. Water Resources Publications.

Zedler, J.B. 2003. Wetlands at Your Service: Reducing impacts of agriculture at the watershed scale. Frontiers in Ecology and the Environment 1(2):65–72. doi:10.1890/1540-9295(2003)001[0065:WAYSRI]2.0.CO;2.

Zoppou, C. 1999. Reverse routing of flood hydrographs using level pool routing. Journal of Hydrologic Engineering 4(2):184–188.

Zuber, A. 1986. On the interpretation of tracer data in variable flow systems. Journal of Hydrology 86(1–2):45–57. doi:10.1016/0022-1694(86)90005-3.

Table 1. Wetland hydrographic attributes.

Wetland	County	Drainage Area (ha)	Pool Area A_w (ha)	Pool Volume V_w (Ac.-ft)	Mean Depth $\overline{H_w}$ (m)	Mean Width $\overline{B_w}$ (m)	Centerline Length L_w (m)	Mean Flow Direction $\overline{\theta_f}$ (Deg.)
WL1	Story County, IA	226.6	1.35	6.8[a]	0.61[a]	44.4[c]|66.9[d]	327.8[c]|202.7[d]	91.9
WL1	Story County, IA	226.6	1.35	5.93[b]	0.51[b]	44.4[c]|66.9[d]	327.8[c]|202.7[d]	91.9
WL2	Kossuth County, IA	234.7	2.48	13.5	0.67	81.2[c]|131.6[d]	322.3[c]|177.6[d]	248.6
WL3	Story County, IA	439.1	3.95	10.3	0.34	65.7[c]	649.8[c]	328.9
WL4	Boone County, IA	354.2	4.12	25.5	0.49	96.8[c]|127.1[d]	596.7[c]|364.8[d]	264.4
WL5	Marshall County, IA	343	1.96	9.08	0.59	37.8[c]|53.8[d]	516.1[c]|277.5[d]	358.3

[a]April, 2010 survey. [b]April, 2011 survey. [c]Includes the inlet channel and wetland pool. [d]Includes only the wetland pool.

Table 2. Area-depth and volume-depth equations determined from measured and interpolated bathymetric survey data.

Wetland	Survey Date(s)	Number of Survey Points	Spatial Interpolation Method	Volume-Depth Equation	Area-Depth Equation
WL1	4/11/2010; 4/12/2010	449	Kriging	$V(H) = 250.7H^5 + 240.5H^4 + 118.0H^3 + 6131.6H^2 + 13689H + 8418.1$	$A(H) = 477.73H^3 + 1510.4H^2 + 12524H + 13599$
WL1*	4/2/2011	789	Kriging	$V(H) = 224.1H^3 + 6888.1H^2 + 13388.8H + 7355.9$	$A(H) = -6601.1H^6 + 267.1H^5 + 13293.1H^4 - 1716.2H^3 - 5{,}422.6H^2 + 14537.4H + 13811.1$
WL2	5/20/2010; 5/24/2010	290	Kriging	$V(H) = -1533.0H^3 + 7283.9H^2 + 24791.3H + 16651.0$	$A(H) = -4621.8H^2 + 14942H + 24823$
WL3	4/9/2011; 4/30/2011	532	Kriging	$V(H) = 10060H^6 + 2555.9H^5 – 23790H^4 - 616.56H^3 + 43145H^2 + 40302H + 13398$	$A(H) = -24684H^6 + 35749H^5 + 44016H^4 – 70286H^3 – 11736H^2 + 81391H + 40973$
WL4	6/17/2011; 6/28/2011	~500	Kriging	$V(H) = -677.44H^6 + 8360H^5 – 3966H^4 – 13017H^3 + 32416H^2 + 62298H + 31381$	$A(H) = -76325H^6 + 5869.9H^5 + 136671H^4 – 25362H^3 – 66849H^2 + 66514H + 63453$
WL5	5/30/2012; 6/1/2012	257	Kriging	$V(H) = 9025.1H^2 + 19786H + 11194$	$A(H) = -35776H^6 – 74622H^5 – 19293H^4 + 32097H^3 + 8903.4H^2 + 14289H + 19561$

*Re-surveyed after 2010 flood. H is the depth of water above the full pool elevation.

Table 3. Summary of submersed vegetation surveys and spatial modeling of vegetative cover.

Wetland	Survey Date(s)	Number of Survey Points	Resolution (m^2)	Percent Wetland Area with Vegetation (%)	Area-weighted Percent Areal Cover ($\overline{C_v}$) (%)
WL1	6/3/2010	84	1	96.8	35.5
WL1	7/13/2010	78	1	97.2	41.1
WL1	8/27/2010; 9/1/2010	123	1	89.9	27.8
WL1	10/9/2010	109	1	82.7	26.2
WL1	5/19/2011	89	1	90.2	10.5
WL1	7/1/2011	119	1	97.0	36.6
WL2	6/15/2010	40	1	97.1	34.2
WL2	6/24/2010	79	1	99.0	29.1
WL2	7/8/2010	31	1	82.0	18.7
WL2	6/19/2011	114	1	99.4	23.6
WL3	6/13/2011; 6/15/2011	83	2	40.1	4.53
WL4	6/17/2011	53	2	46.4	35.6
WL4	7/25/2011	83	2	81.6	29.4
WL5	5/29/12; 6/1/2012	157	1	98.5	25.2

Table 4A. Partial summary of tracer studies. Additional information such as mean flow rates, mean wind speeds, and mean relative wind directions are given in Tables 4B and 4C.

Wetland	Study	Date/Time Start	Date/Time End	Length (days)	Mass Inj.(kg)	Mass Rec. (kg)	Percent Mass Rec. (%)	Mean Vegetative Cover (%)	Total Vegetative Cover (%)
WL1	WL1_1[1]	11/22/09	12/7/09 23:57	15.3	0.113	0.09	81.3	0.0	0.0
WL1	WL1_2	5/6/10 18:04	5/12/10 12:58	5.8	0.113	0.11	98.5	0.0	0.0
WL1	WL1_3	5/18/10 20:18	5/25/10 11:28	6.6	0.113	0.08	67.4	0.0	0.0
WL1	WL1_4	6/9/10 19:10	6/12/10 16:45	2.9	0.113	0.09	76.1	35.5	96.9
WL1	WL1_5	6/23/10 21:17	6/29/10 9:56	5.5	0.197	0.26	132.4	38.3[3]	97.1[3]
WL1	WL1_6	7/13/10 13:15	7/19/10 10:39	5.9	0.113	0.09	80.0	41.1	97.2
WL1	WL1_7	8/29/10 19:59	9/2/10 14:07	3.8	0.113	0.11	108.4	28.0	89.9
WL1	WL1_8[1]	10/13/10	10/30/10 3:45	16.4	0.113	0.09	78.7	26.4	82.7
WL1	WL1_9[1]	11/20/10	12/2/10 21:55	12.3	0.0226	0.01	61.3	0.0	0.0
WL1	WL1_10[a]	4/18/11 12:01	4/21/11 17:50	3.2	0.0226	0.01	55.3	0.0	0.0
WL1	WL1_11	5/22/11 18:09	5/27/11 14:54	4.9	0.0226	0.03	116.6	10.5	90.3
WL1	WL1_12	5/29/11 20:22	6/3/11 11:26	4.6	0.0226	0.03	115.6	13.6[3]	91.6[3]
WL1	WL1_13	4/23/12 18:55	5/3/12 11:29	9.7	0.0226	0.02	74.3	0.0	0.0
WL2	WL2_1[1]	5/20/10 16:40	6/12/10 5:04	22.5	0.226	0.14	60.5	0.0	0.0
WL2	WL2_2	6/15/10 20:28	6/27/10 9:32	11.5	0.226	0.14	62.4	34.3	97.1
WL2	WL2_3	7/8/10 17:35	7/20/10 14:39	11.9	0.226	0.25	109.2	18.8	82.0
WL2	WL2_4[1]	5/15/11 20:08	5/20/11 10:53	4.6	0.0226	0.00	20.6	0.0	0.0
WL2	WL2_5[1]	6/18/11 14:18	6/27/11 7:58	8.7	0.0226	0.03	120.7	23.6	99.5
WL3	WL3_1	5/3/11 12:24	5/12/11 11:49	9.0	0.0565	0.05	97.0	0.0	0.0
WL3	WL3_2	6/3/11 20:07	6/9/11 0:02	5.2	0.0565	0.04	67.9	4.5	40.1
WL3	WL3_3	4/21/12 17:21	4/29/12 22:51	8.2	0.0565	0.04	78.2	0.0	0.0
WL3	WL3_4[1]	5/11/12 19:14	5/28/12 17:18	16.9	0.0904	0.09	97.1	0.0	0.0
WL3	WL3_5	4/14/13 17:44	4/19/13 8:03	4.6	0.0904	0.10	107.6	0.0	0.0
WL3	WL3_6	4/26/13 18:41	5/2/13 13:51	5.8	0.0452	0.04	88.5	0.0	0.0
WL4	WL4_1	6/14/11 18:26	6/27/11 17:40	13.0	0.0904	0.07	79.7	35.6	46.4
WL4	WL4_2[2]	7/15/11 17:08	8/5/11 13:43	20.9	0.0904	0.01	13.3	29.4	81.6
WL4	WL4_3[2]	5/4/12 18:43	5/14/12 13:52	9.8	0.0904	0.04	39.8	0.0	0.0
WL5	WL5_1	6/1/12 19:53	6/21/12 9:33	19.6	0.0678	0.03	45.0	25.2	98.6
WL5	WL5_2[2]	4/20/13 19:31	4/24/13 8:35	3.5	0.0452	0.03	70.8	0.0	0.0
WL5	WL5_3	4/26/13 19:46	5/2/13 2:41	5.3	0.0452	0.03	56.3	0.0	0.0

Table 4B. Summary of mass-averaged means of measured flow and wind-associated effects.

Study	$\overline{Q_{\mathrm{i(m)}}}$ ($m^3\ min^{-1}$)	$\overline{Q_{\mathrm{o(m)}}}$ ($m^3\ min^{-1}$)	$\overline{Q_{\mathrm{a(m)}}}$ ($m^3\ min^{-1}$)	$\overline{U_{\mathrm{q(m)}}}$ ($m\ min^{-1}$)	$\overline{Re_{\mathrm{m}}}$ (-)	$\overline{T_{\mathrm{m}}}$ (days)	$\overline{n_t}$ ($s\ m^{-1/3}$)	$\overline{U_{q*(\mathrm{m})}}$ ($m\ min^{-1}$)	$\overline{v_{\mathrm{w(10)(m)}}}$ ($m\ s^{-1}$)	$\overline{U_{\mathrm{w*(m)}}}$ ($m\ s^{-1}$) x 100	$\overline{\theta_{\mathrm{wf(m)}}}$ (-)
WL1_1[1]	1.3	1.3	1.3	0.036	462.5	4.4	0.052	0.036	3.5	0.48	1.4
WL1_2	2.5	2.5	2.5	0.071	913.8	2.3	0.052	0.071	4.2	0.57	1.5
WL1_3	3.5	3.5	3.5	0.099	1271.9	1.7	0.052	0.099	2.4	0.33	1.2
WL1_4	3.0	3.1	3.1	0.094	1106.6	2.0	0.078	0.094	2.1	0.28	1.3
WL1_5	8.1	8.1	8.1	0.250	2933.6	0.8	0.080	0.250	2.3	0.31	1.5
WL1_6	1.8	1.8	1.8	0.057	665.3	3.5	0.081	0.057	3.3	0.44	1.5
WL1_7	3.0	3.2	3.1	0.076	1127.7	2.0	0.075	0.076	3.6	0.49	1.4
WL1_8[1]	1.1	1.0	1.0	0.025	372.3	5.9	0.074	0.025	2.4	0.33	1.6
WL1_9[1]	0.2	0.2	0.2	0.005	75.1	28.8	0.052	0.005	3.2	0.42	1.5
WL1_10[a]	2.7	2.7	2.7	0.073	993.7	1.8	0.052	0.073	4.9	0.66	1.1
WL1_11	4.0	4.0	4.0	0.107	1458.1	1.3	0.063	0.107	3.6	0.48	1.5
WL1_12	5.5	5.4	5.5	0.146	1996.1	1.0	0.063	0.146	4.8	0.65	1.5
WL1_13	1.5	1.5	1.5	0.044	621.2	3.1	0.052	0.044	3.1	0.43	1.4
WL2_1[1]	0.9	0.7	0.8	0.016	149.7	14.4	0.052	0.016	2.4	0.32	1.6
WL2_2	2.0	2.0	2.0	0.017	358.8	6.1	0.078	0.017	2.2	0.30	1.4
WL2_3	2.4	2.3	2.3	0.041	419.3	5.3	0.071	0.041	2.5	0.34	1.7
WL2_4[1]	1.4	1.2	1.3	0.047	226.6	9.6	0.052	0.047	3.3	0.44	1.7
WL2_5[1]	3.4	3.4	3.4	0.026	609.6	3.7	0.073	0.026	3.8	0.51	1.6
WL3_1	2.2	2.5	2.4	0.038	989.0	4.1	0.052	0.038	5.4	0.73	1.7
WL3_2	3.2	3.5	3.4	0.056	1382.8	3.0	0.058	0.056	2.9	0.39	1.6
WL3_3	2.5	2.5	2.5	0.040	1034.8	4.1	0.052	0.040	4.4	0.59	1.5
WL3_4[1]	2.6	2.4	2.5	0.040	1029.6	4.1	0.052	0.040	4.2	0.57	1.5
WL3_5	4.3	5.4	4.9	0.077	2011.4	2.1	0.052	0.077	4.9	0.66	1.4
WL3_6	0.6	1.7	1.2	0.018	479.3	8.8	0.052	0.018	3.9	0.52	1.8
WL4_1	2.2	2.2	2.2	0.012	424.0	10.8	0.075	0.012	3.3	0.44	1.6
WL4_2[2]	0.7	0.6	0.6	0.004	121.2	36.0	0.073	0.004	2.6	0.35	1.5
WL4_3[2]	4.1	4.0	4.1	0.019	782.0	5.6	0.052	0.019	5.9	0.79	1.6
WL5_1	0.7	0.6	0.6	0.007	263.6	13.1	0.073	0.007	3.3	0.44	1.6
WL5_2[2]	3.8	3.8	3.8	0.003	172.6	2.4	0.052	0.003	5.9	0.79	1.8
WL5_3	2.0	2.0	2.0	0.020	1077.7	4.5	0.052	0.020	3.4	0.46	1.8

[1]Extrapolation of response curve tail. [2]Savitsky-Golay filtering of tracer response curve prior to RTD analysis. [3]Linearly interpolated.

Table 4C. Summary of measured RTD statistics and derivative short-circuiting and mixing indexes. m_1 and m_{2c} were estimated as $m_1^* \overline{T_m}$ and $m_{2c}^* \left(\overline{T_m}\right)^2$, respectively.

Study	m_1 (day)	m_{2c} (day^2)	m_1^*	m_{2c}^*	z_i	z_p	σ^{2*}	K_x (m^2 day^{-1}) / 1000	Pe_x
WL1_1[1]	3.50	7.45	0.79	0.38	0.07	0.17	0.61	17.8	4.1
WL1_2	1.91	2.37	0.84	0.46	0.09	0.28	0.58	33.7	4.3
WL1_3	1.82	1.27	1.09	0.46	0.22	0.41	0.38	33.0	6.1
WL1_4	1.30	0.43	0.64	0.11	0.13	0.51	0.26	20.0	8.7
WL1_5	2.27	4.05	2.79	6.13	0.17	0.64	0.78	140.4	3.3
WL1_6	2.01	3.23	0.58	0.26	0.05	0.13	0.80	32.3	3.2
WL1_7	2.07	0.29	1.03	0.07	0.54	0.99	0.04	3.1	51.6
WL1_8[1]	2.35	1.96	0.40	0.06	0.10	0.14	0.35	8.1	6.5
WL1_9[1]	3.85	15.52	0.13	0.02	0.01	0.01	0.99	3.9	2.7
WL1_10[a]	1.22	0.97	0.67	0.29	0.04	0.10	0.64	36.4	3.9
WL1_11	1.99	3.69	1.52	2.17	0.05	0.20	0.93	72.9	2.9
WL1_12	1.32	0.70	1.38	0.77	0.23	0.57	0.41	49.3	5.8
WL1_13	3.30	4.87	1.07	0.51	0.25	0.60	0.42	12.7	7.0
WL2_1[1]	4.93	12.8	0.34	0.06	0.03	0.23	0.53	6.8	4.6
WL2_2	4.88	7.66	0.80	0.20	0.17	0.44	0.32	10.5	7.1
WL2_3	3.16	2.47	0.60	0.09	0.11	0.18	0.25	9.7	9.0
WL2_4[1]	1.28	1.06	0.13	0.01	0.02	0.02	0.65	12.2	3.9
WL2_5[1]	3.50	6.18	0.96	0.46	0.04	0.21	0.50	26.5	4.8
WL3_1	2.54	4.33	0.62	0.26	0.08	0.18	0.67	47.1	3.8
WL3_2	1.55	0.67	0.52	0.08	0.12	0.33	0.28	31.0	8.0
WL3_3	1.78	2.35	0.44	0.14	0.06	0.21	0.74	53.6	3.5
WL3_4[1]	3.59	4.65	0.88	0.28	0.19	0.41	0.36	28.9	6.4
WL3_5	2.99	4.43	1.40	0.97	0.09	0.12	0.49	74.0	4.9
WL3_6	3.17	3.00	0.36	0.04	0.02	0.12	0.30	11.3	7.6
WL4_1	7.89	6.02	0.73	0.05	0.28	0.54	0.10	2.1	21.7
WL4_2[2]	9.45	9.12	0.26	0.01	0.09	0.27	0.10	0.7	20.4
WL4_3[2]	2.96	1.66	0.53	0.05	0.11	0.39	0.19	7.5	11.5
WL5_1	5.37	10.65	0.41	0.06	0.04	0.15	0.37	3.4	6.3
WL5_2[2]	1.62	0.53	0.68	0.09	0.16	0.62	0.20	1.1	10.8
WL5_3	2.26	1.95	0.51	0.10	0.08	0.41	0.38	13.0	6.1

[1]Extrapolation of response curve tail. [2]Savitsky-Golay filtering of tracer response curve prior to RTD analysis.

Table 5A. Aggregate statistical summaries of measured flow and wind-associated parameters, and observed and derived RTD statistics for all wetlands studied in this work. Std. refers to the standard deviation of the featured variable. CV is the coefficient of variation. IQR is the inter-quartile range.

Wetland	Statistic	n	$\overline{Q_{a(\mathrm{m})}}$ ($\mathrm{m^3\ min^{-1}}$)	$\overline{Re_{(\mathrm{m})}}$	$\overline{v_{\mathrm{w}(10)(\mathrm{m})}}$ ($\mathrm{m\ s^{-1}}$)	$\overline{\theta_{\mathrm{wf}}}$	m_1^*	σ^{2*}	z_i	z_p	K_x ($\mathrm{m^2\ day^{-1}}$) / 1000	Pe_x
All	Mean	30	2.6	806.	3.6	1.50	0.77	0.46	0.12	0.32	26.7	8.3
	Median		2.4	644.	3.4	1.52	0.65	0.40	0.09	0.25	15.4	6.1
	Std.		1.6	621.	1.1	0.17	0.52	0.25	0.11	0.22	29.6	9.3
	IQR		2.0	716.	1.6	0.17	0.48	0.36	0.12	0.28	25.9	4.0
	CV		0.63	0.77	0.30	0.12	0.68	0.54	0.88	0.70	1.1	1.2
All (No Vegetation)	Mean	16	2.3	706.	4.1	1.53	0.66	0.52	0.10	0.27	24.6	5.7
	Median		2.4	625.	4.1	1.53	0.64	0.51	0.08	0.22	15.4	4.7
	Std.		1.3	428.	1.1	0.20	0.35	0.22	0.07	0.19	20.6	2.5
	IQR		1.6	520.	1.6	0.30	0.43	0.27	0.09	0.29	24.0	2.7
	CV		0.54	0.61	0.27	0.13	0.54	0.43	0.75	0.71	0.70	0.44
All (Vegetation)	Mean	14	2.9	920.	3.1	1.5	0.90	0.39	0.15	0.38	29.3	11.4
	Median		2.7	672.	3.1	1.5	0.69	0.34	0.11	0.30	15.3	6.8
	Std.		2.0	790.	0.76	0.11	0.65	0.27	0.13	0.25	38.1	12.9
	IQR		1.5	753.	1.1	0.15	0.48	0.23	0.11	0.35	27.4	3.9
	CV		0.68	0.86	0.25	0.07	0.73	0.70	0.88	0.66	0.84	1.1

Table 5B. Aggregate statistical summaries of measured flow and wind-associated parameters, and observed and derived RTD statistics for WL1. Std. refers to the standard deviation of the featured variable. CV is the coefficient of variation. IQR is the inter-quartile range.

Wetland	Statistic	n	$\overline{Q_{a(\mathrm{m})}}$ ($\mathrm{m^3\ min^{-1}}$)	$\overline{Re_{(\mathrm{m})}}$	$\overline{v_{\mathrm{w}(10)(\mathrm{m})}}$ ($\mathrm{m\ s^{-1}}$)	$\overline{\theta_{\mathrm{wf}}}$	m_1^*	σ^{2*}	z_i	z_p	K_x ($\mathrm{m^2\ day^{-1}}$) / 1000	Pe_x
WL1 (All)	Mean	13	3.0	1087.	3.4	1.4	0.99	0.57	0.15	0.36	35.7	8.5
	Median		2.7	1001.	3.4	1.5	0.84	0.61	0.10	0.28	32.3	4.3
	Std.		2.1	761.8	0.9	0.1	0.66	0.28	0.14	0.28	37.1	13.1
	IQR		1.8	658.4	1.2	0.1	0.45	0.40	0.17	0.43	23.6	3.3
	CV		0.70	0.70	0.27	0.10	0.66	0.49	0.94	0.78	1.0	1.5
WL1 (No Vegetation)	Mean	6	2.0	729.5	3.6	1.4	0.77	0.63	0.11	0.26	22.9	4.7
	Median		2.1	774.5	3.4	1.4	0.82	0.63	0.08	0.22	25.4	4.2
	Std.		1.2	430.4	0.9	0.2	0.35	0.23	0.10	0.22	13.3	1.6
	IQR		1.3	475.1	0.9	0.3	0.32	0.16	0.14	0.26	19.5	1.7
	CV		0.59	0.59	0.24	0.12	0.46	0.37	0.89	0.83	0.58	0.3
WL1 (Vegetation)	Mean	7	3.8	1394.	3.2	1.5	1.19	0.52	0.18	0.45	46.6	11.7
	Median		3.1	1136.	3.3	1.5	1.03	0.41	0.13	0.51	32.3	5.8
	Std.		2.4	876.2	1.0	0.1	0.82	0.33	0.17	0.32	47.9	17.7
	IQR		2.3	843.9	1.2	0.1	0.84	0.49	0.13	0.44	47.0	4.4
	CV		0.63	0.63	0.30	0.07	0.69	0.65	0.94	0.70	1.0	1.5

Table 5C. Aggregate statistical summaries of measured flow and wind-associated parameters, and observed and derived RTD statistics for wetlands WL2 – WL5. Std. refers to the standard deviation of the featured variable. CV is the coefficient of variation. IQR is the inter-quartile range.

Wetland	Statistic	n	$\overline{Q_{a(\mathrm{m})}}$ ($\mathrm{m^3\ min^{-1}}$)	$\overline{Re_{(\mathrm{m})}}$	$\overline{v_{\mathrm{w}(10)(\mathrm{m})}}$ ($\mathrm{m\ s^{-1}}$)	$\overline{\theta_{\mathrm{wf}}}$	m_1^*	σ^{2*}	z_i	z_p	K_x ($\mathrm{m^2\ day^{-1}}$) / 1000	Pe_x
WL2	Mean	5	2.0	393.8	2.9	1.6	0.57	0.45	0.07	0.22	13.2	5.9
	Median		2.0	400.6	2.6	1.6	0.60	0.50	0.04	0.21	10.5	4.8
	Std.		1.0	199.4	0.7	0.1	0.33	0.16	0.06	0.15	7.7	2.1
	IQR		1.1	215.2	0.9	0.1	0.46	0.21	0.07	0.05	2.5	2.5
	CV		0.51	0.51	0.28	0.08	0.59	0.36	0.88	0.69	0.6	0.4
WL3	Mean	6	2.8	696.4	4.3	1.6	0.70	0.47	0.10	0.23	41.0	5.7
	Median		2.5	622.7	4.3	1.6	0.57	0.43	0.09	0.19	39.1	5.7
	Std.		1.2	307.6	0.87	0.1	0.39	0.19	0.06	0.12	22.0	1.9
	IQR		0.7	179.0	0.78	0.1	0.36	0.31	0.04	0.16	22.6	3.3
	CV		0.44	0.44	0.20	0.09	0.55	0.41	0.60	0.53	0.55	0.3
WL4	Mean	3	2.3	387.5	3.9	1.5	0.51	0.13	0.16	0.40	3.4	17.8
	Median		2.2	371.4	3.3	1.6	0.53	0.10	0.11	0.39	2.1	20.4
	Std.		1.7	289.6	1.7	0.05	0.23	0.05	0.10	0.13	3.6	5.5
	CV		0.75	0.75	0.45	0.03	0.46	0.40	0.64	0.33	1.0	0.3
WL5	Mean	3	2.1	916.0	4.2	1.7	0.53	0.32	0.09	0.39	5.8	7.7
	Median		2.0	859.0	3.4	1.8	0.51	0.37	0.08	0.41	3.4	6.3
	Std.		1.6	680.5	1.5	0.09	0.14	0.10	0.06	0.24	6.3	2.7
	CV		0.74	0.77	0.35	0.05	0.26	0.32	0.63	0.60	1.1	0.3

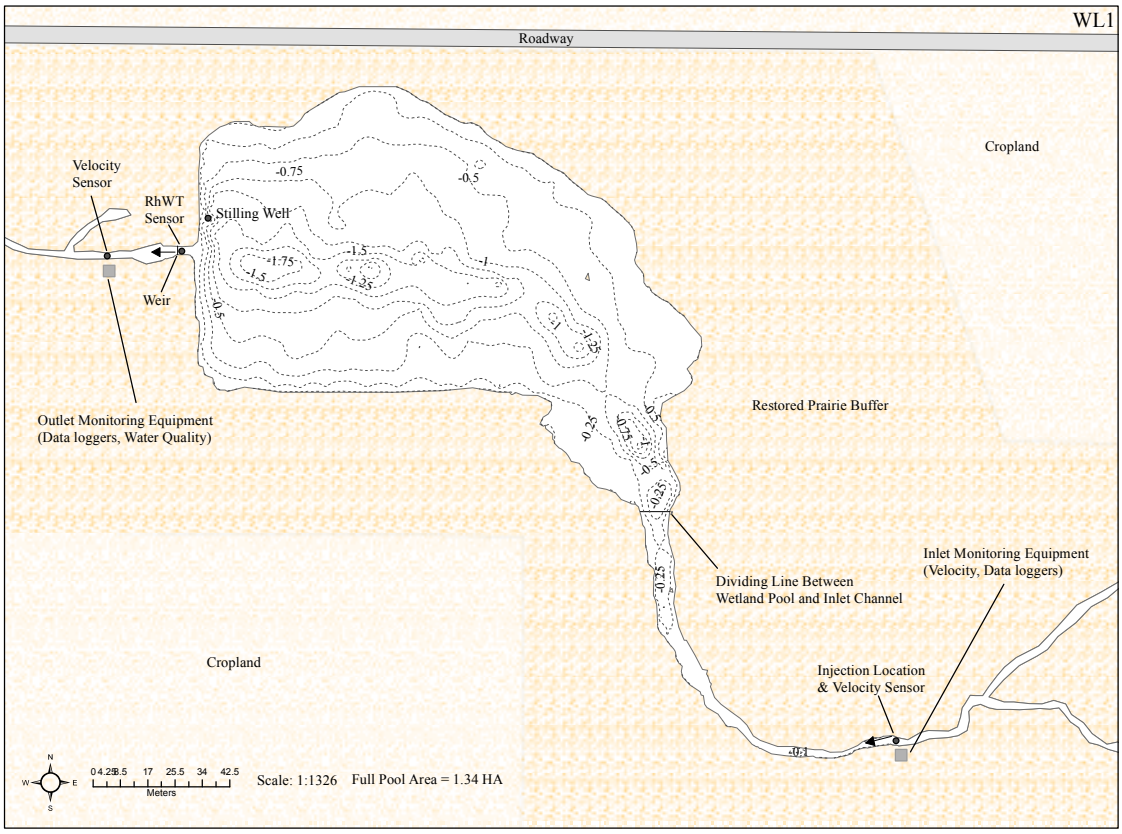

Figure 1. Site map of WL1 (April, 2010 Bathymetric Survey). Monitoring equipment and dye injection and monitoring locations are identified in the figure. Depth contour values are in meters below the water full pool level

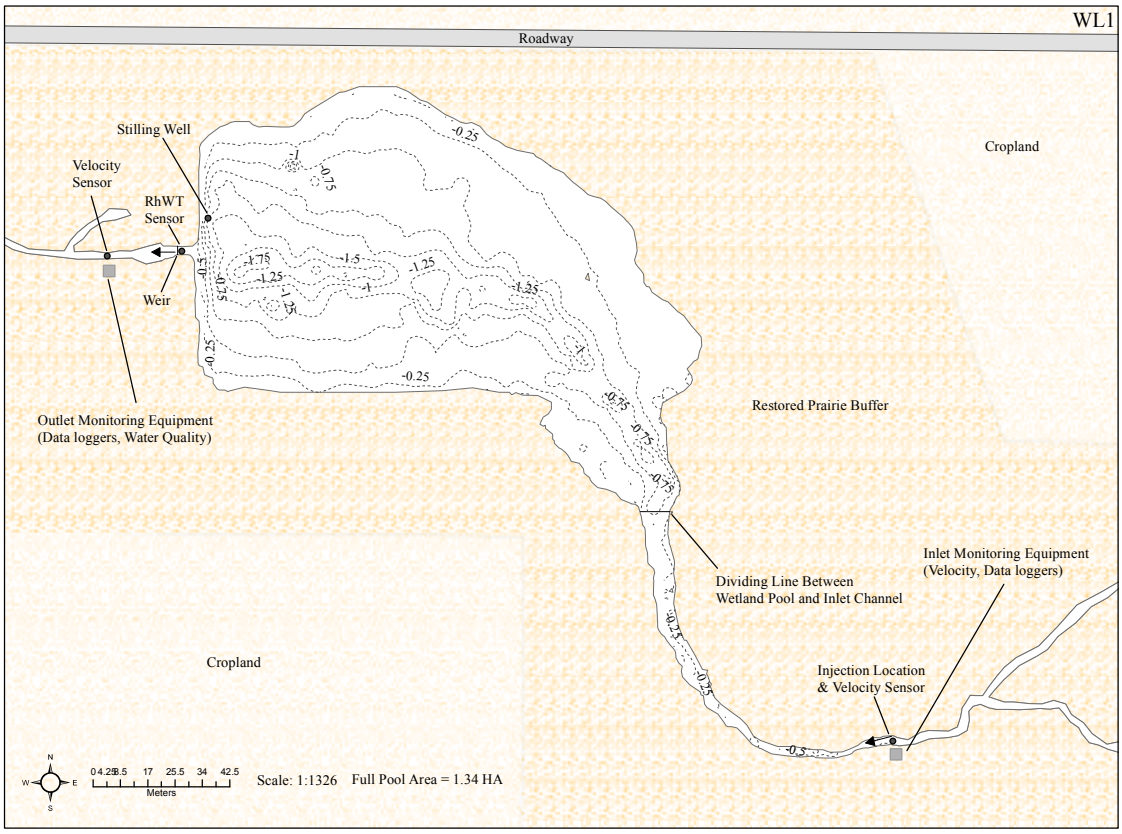

Figure 2. Site map of WL1 (April, 2011 Bathymetric Survey). Monitoring equipment and dye injection and monitoring locations are identified in the figure. Depth contour values are in meters below the water full pool level.

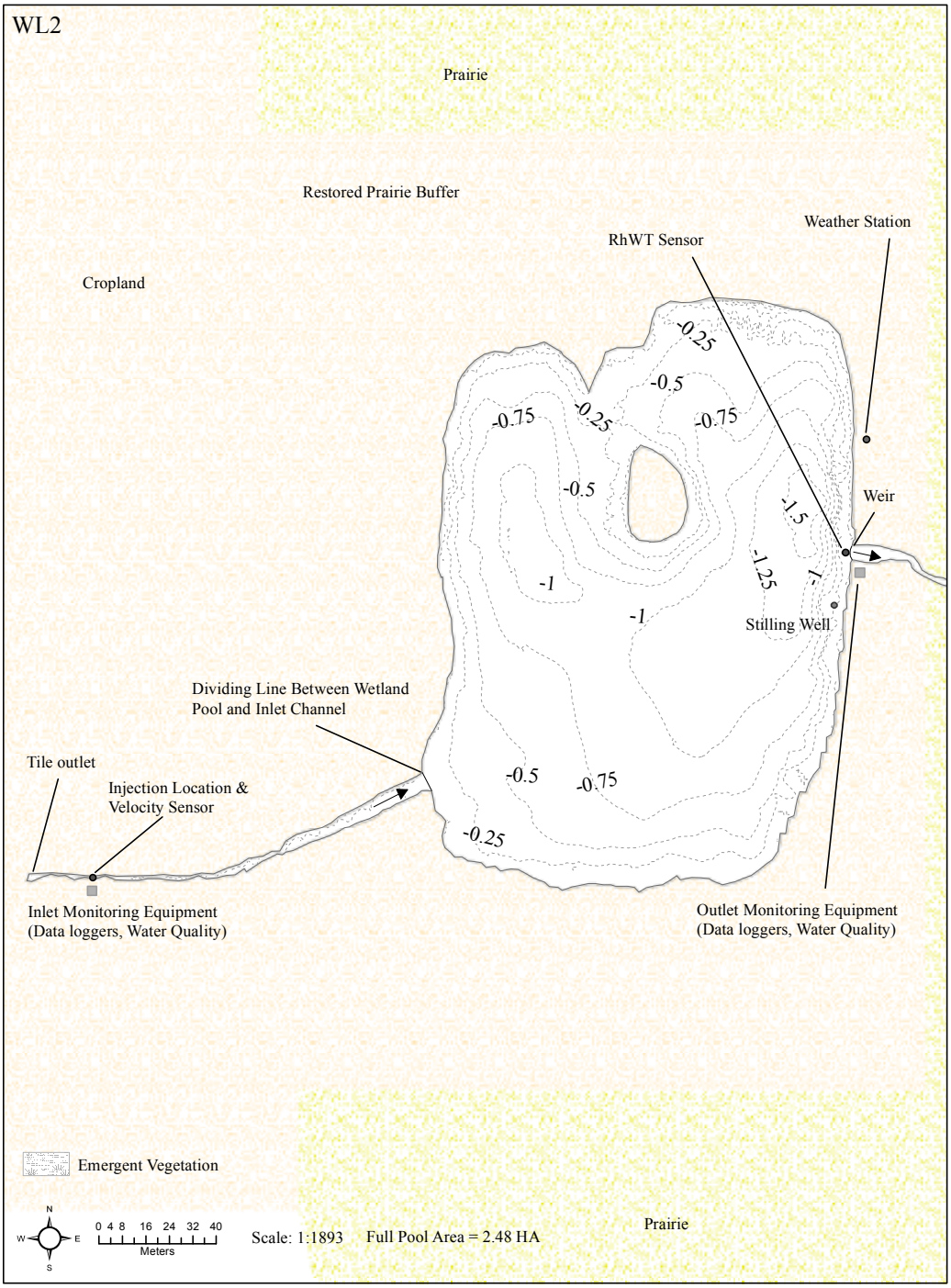

Figure 3. Site map of WL2. Monitoring equipment and dye injection and monitoring locations are identified in the figure. Depth contour values are in meters below the water full pool level.

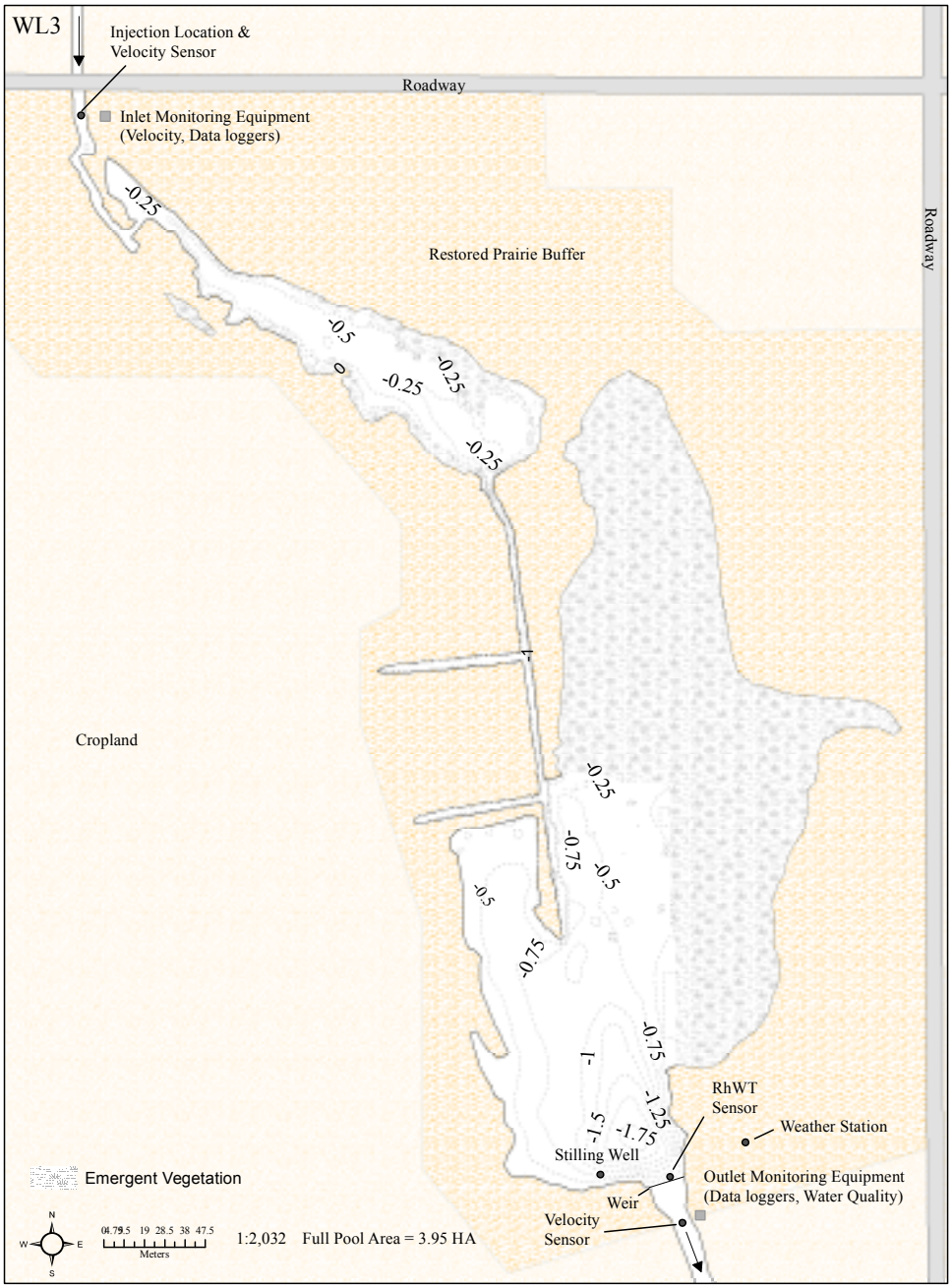

Figure 4. Site map of WL3. Monitoring equipment and dye injection and monitoring locations are identified in the figure. Depth contour values are in meters below the water full pool level.

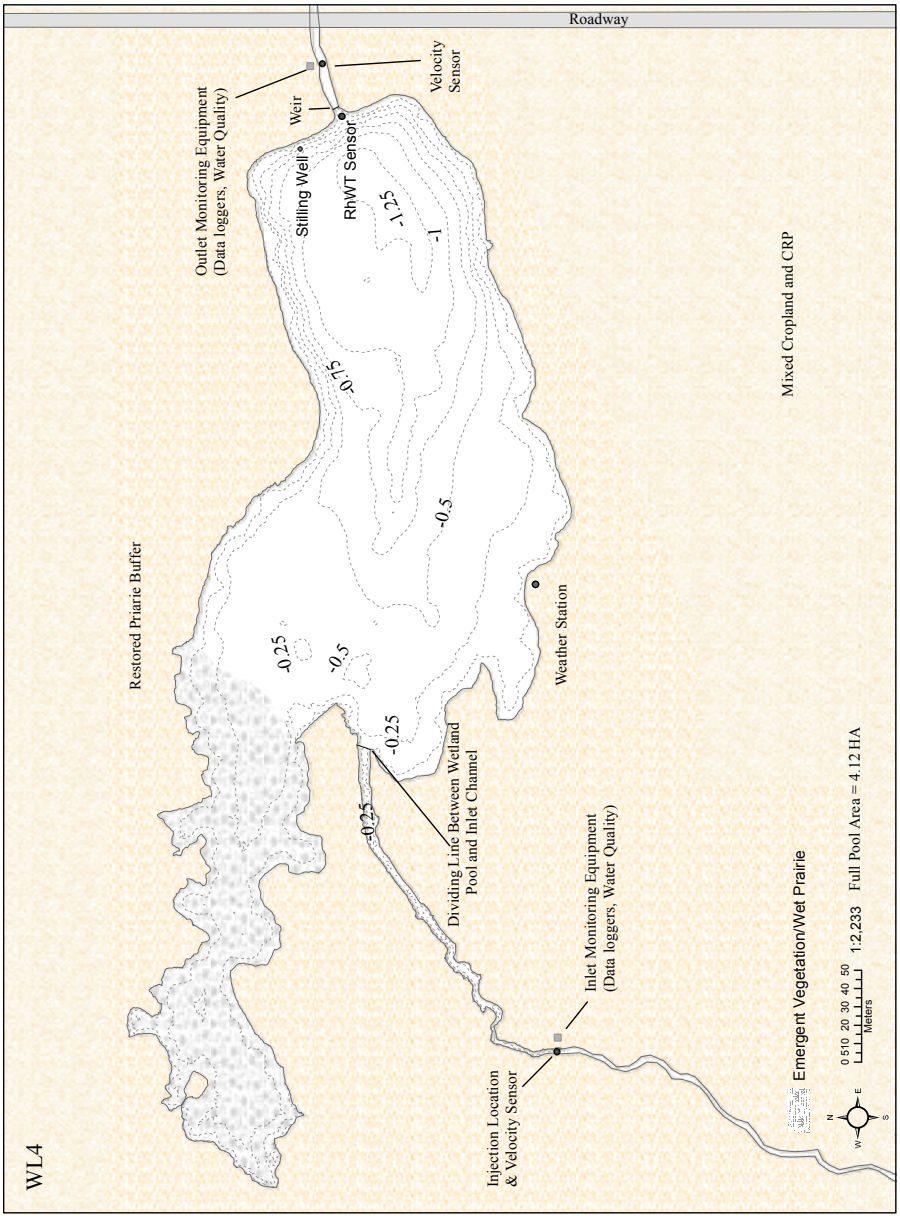

Figure 5. Site map of WL4. Monitoring equipment and dye injection and monitoring locations are identified in the figure. Depth contour values are in meters below the water full pool level.

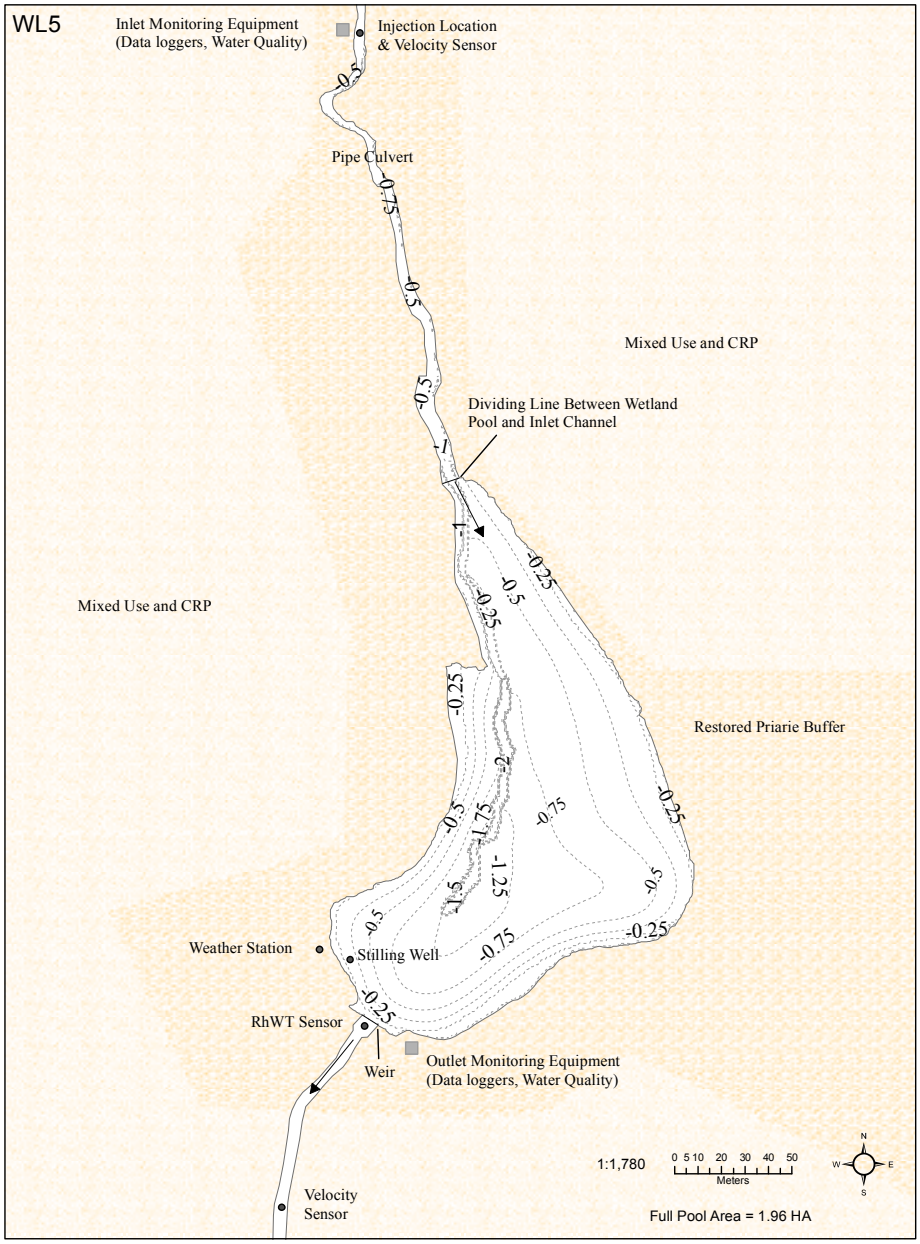

Figure 6. Site map of WL5. Monitoring equipment and dye injection and monitoring locations are identified in the figure. Depth contour values are in meters below the water full pool level.

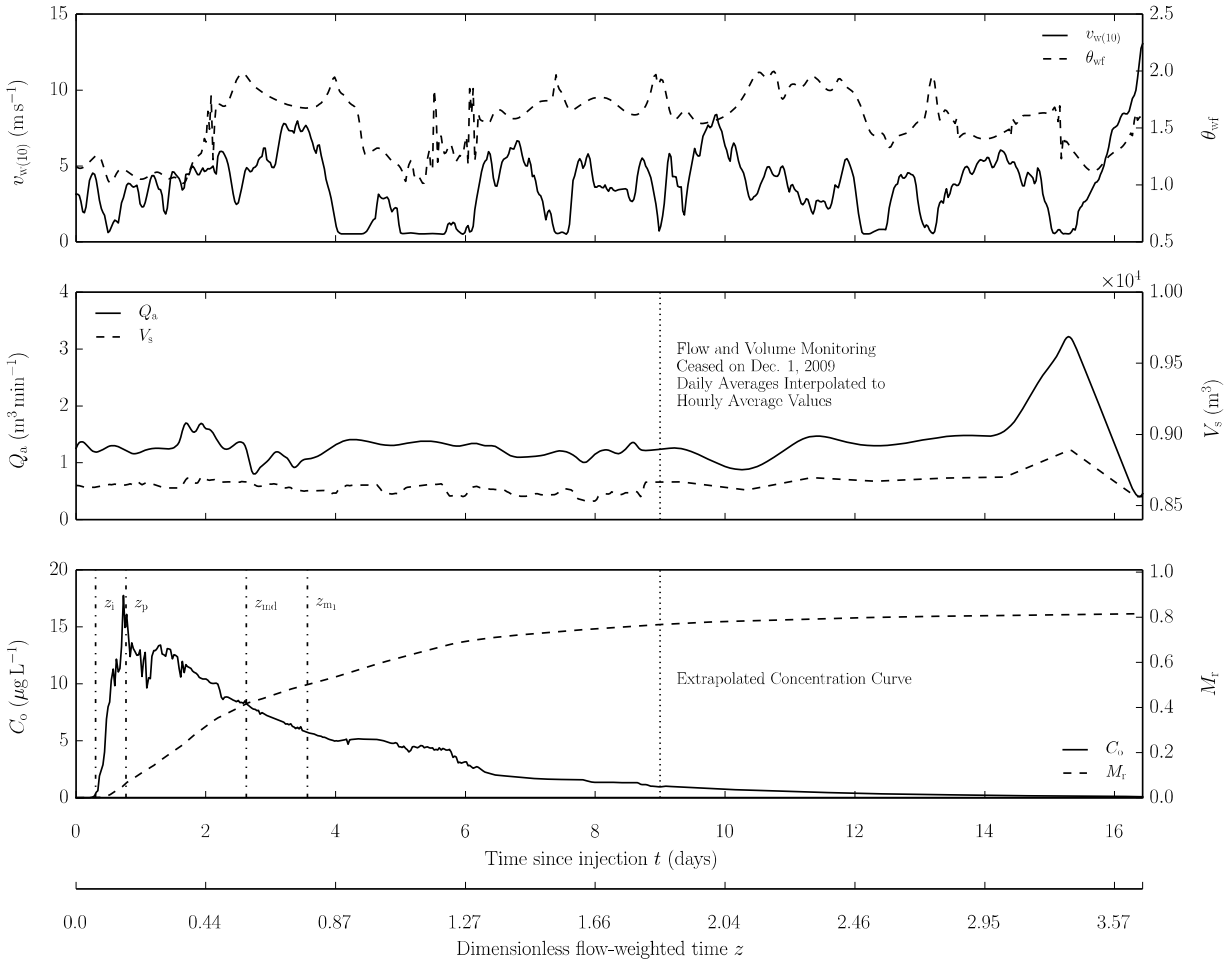

Figure 7. Study WL1_1 (11/22/09 – 12/9/09). Bottom panel: observed RWT concentration, C_o, and measured mass recovery, M_r. Middle panel: time-series of system average flow-through rates (Q_a) and water volumes (V_s). Top panel: time-series of measured wind speeds ($v_{w(10)}$; extrapolated to 10m above local datum) and relative wind directions (θ_{wf}) as defined by Eqn. 2.5 in the text. Some principal temporal features of the tracer response curve are noted in the bottom panel as dashed vertical lines. Flow and volume monitoring ceased on Dec. 1, 2009. Continuous system flow and volume approximated from estimates of daily average flow rates. The tracer response curve for the period beyond Dec. 1, 2009 was extrapolated using an exponential decay model as discussed in the text. z_{50} is the dimensionless median detention time.

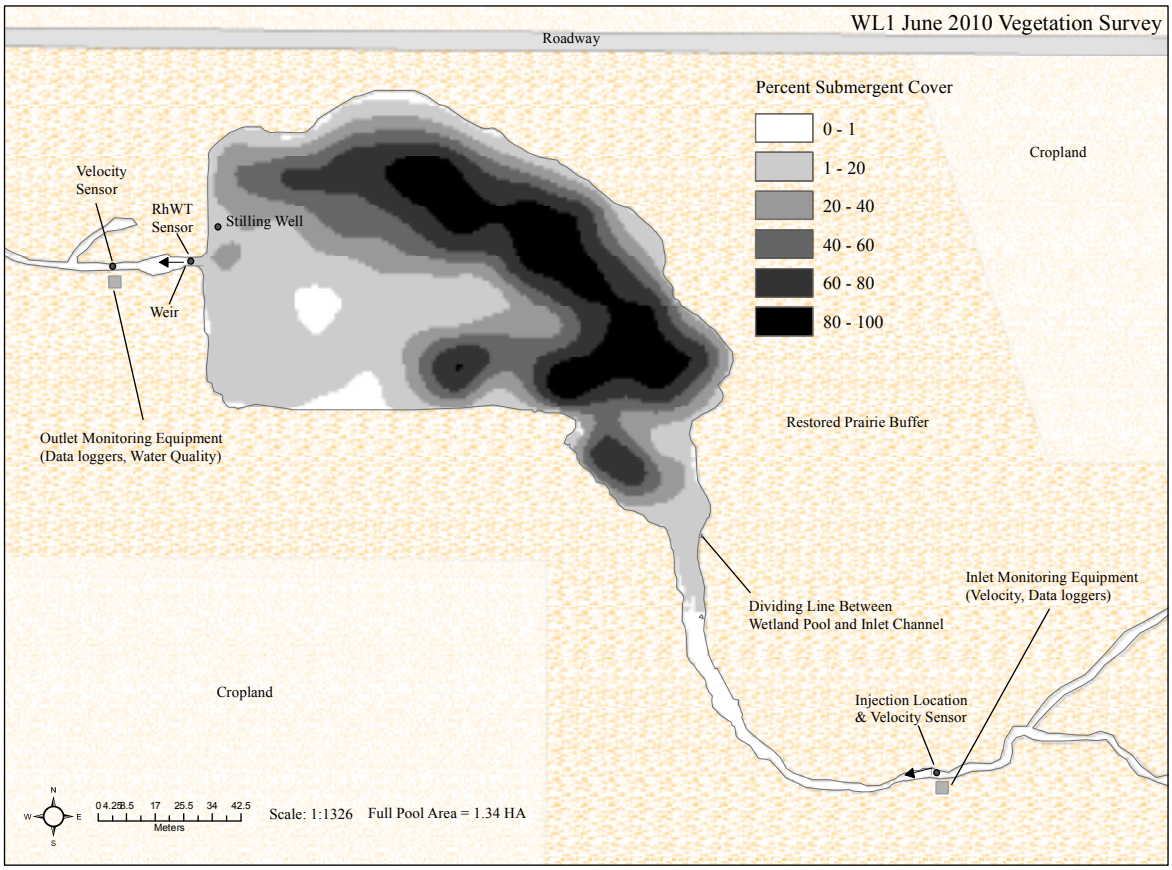

Figure 8. Map of spatially interpolated percent vegetative cover values for the June, 2010 vegetation survey on WL1. Additional vegetation survey maps are provided in Appendix B.

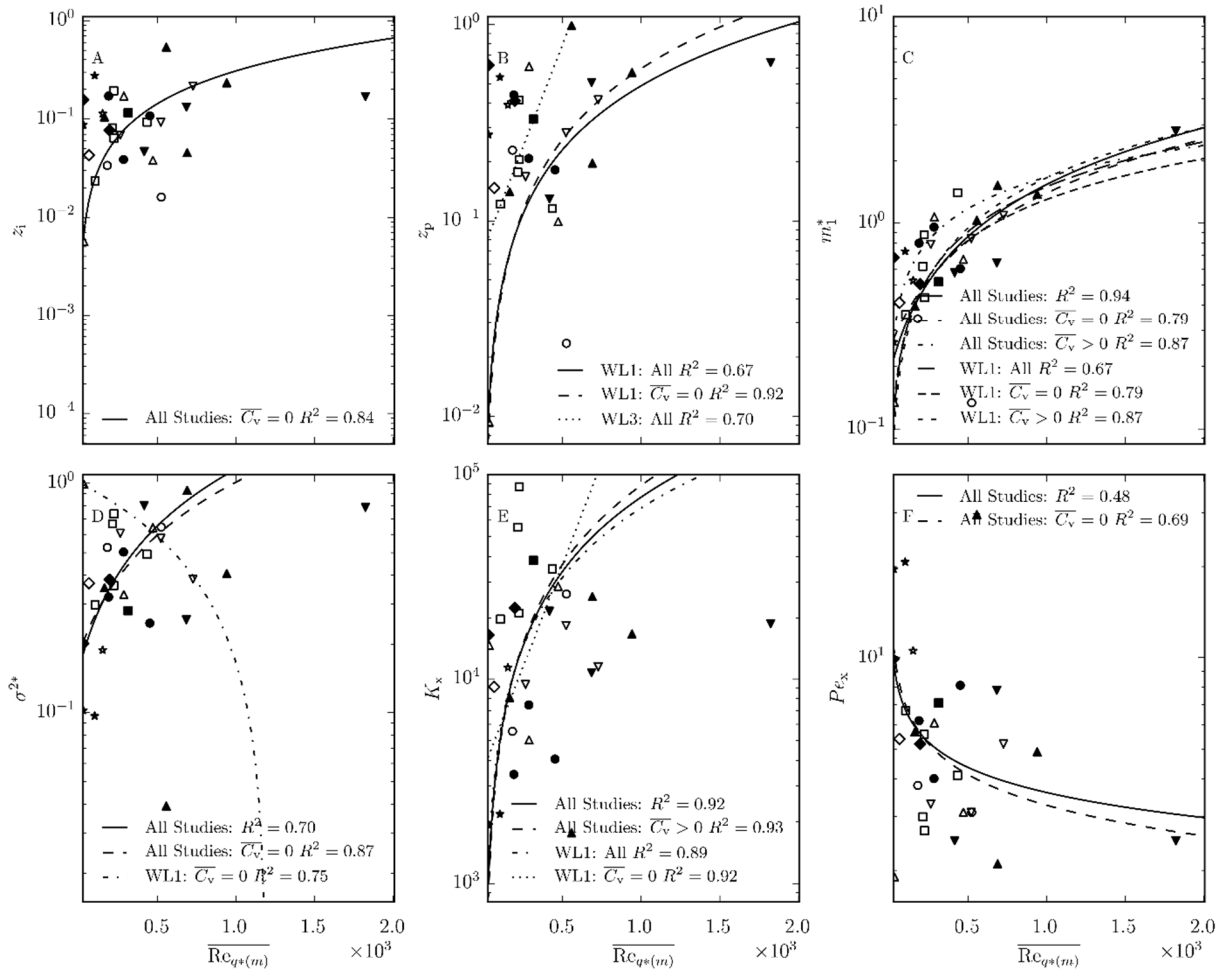

Figure 9. Scatter plots of $\overline{\mathrm{Re}_{q*(m)}}$ versus measured RTD characteristics. Closed symbols represent vegetated studies, open symbols represent non-vegetated studies. WL1: triangles. WL2: circles. WL3: squares. WL4: stars. WL5: diamonds. All regression lines are mentioned in the text.

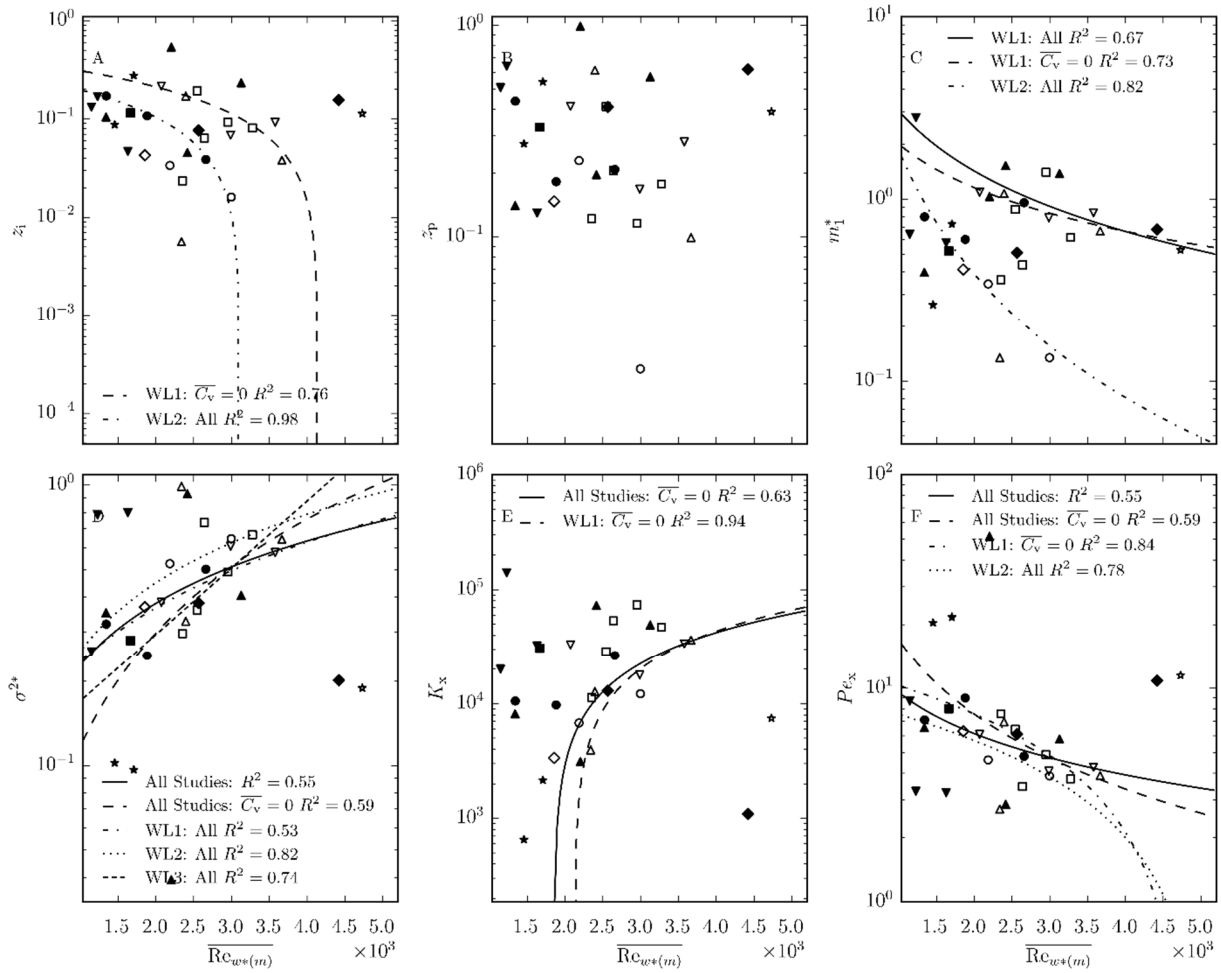

Figure 10. Scatter plot of $\overline{\mathrm{Re}_{w*(m)}}$ versus measured RTD characteristics. Closed symbols represent vegetated studies, open symbols represent non-vegetated studies. WL1: triangles. WL2: circles. WL3: squares. WL4: stars. WL5: diamonds. All regression lines are mentioned in the text.

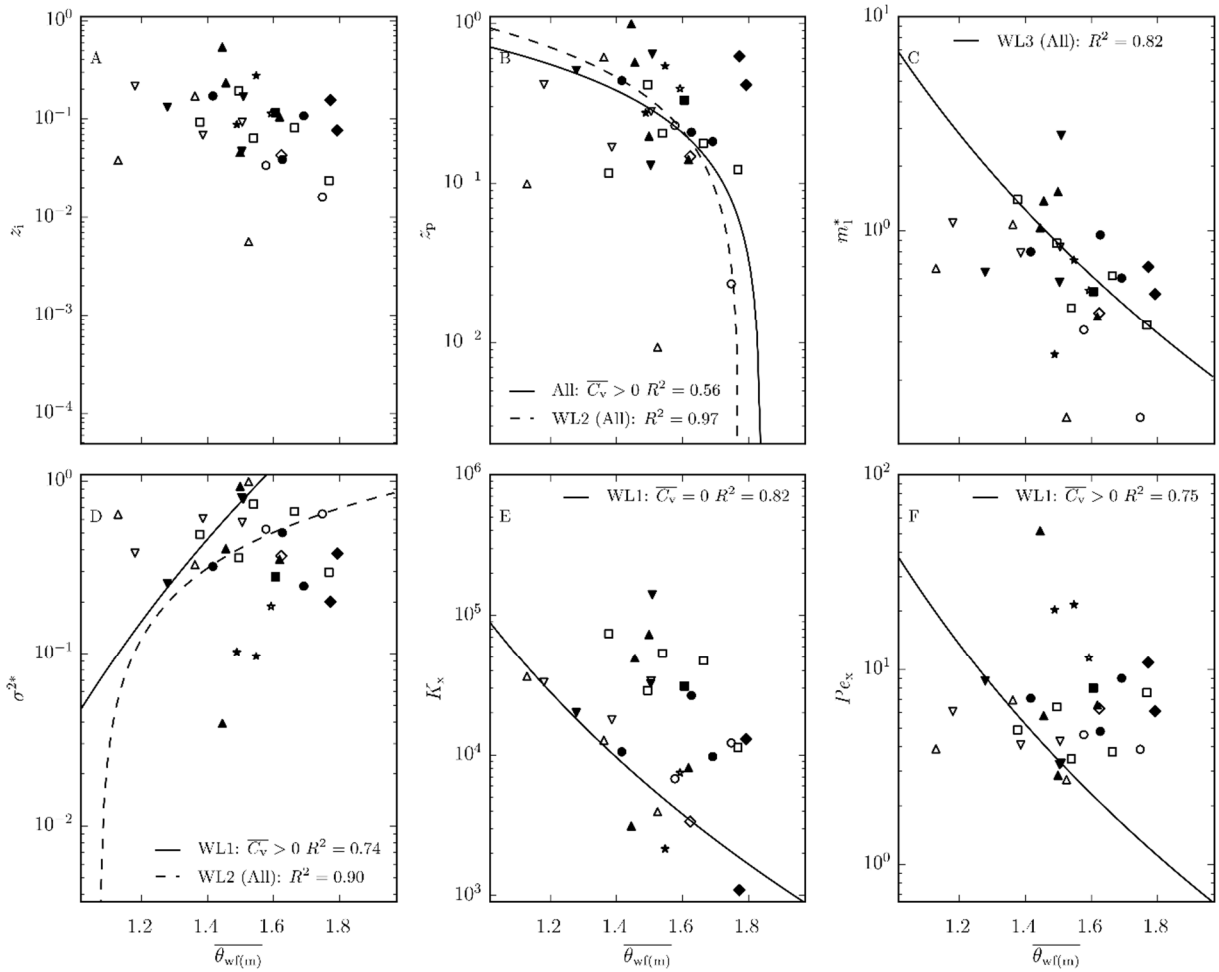

Figure 11. Scatter plot of $\overline{\theta_{wf}}$ versus measured RTD characteristics. Closed symbols represent vegetated studies, open symbols represent non-vegetated studies. WL1: triangles. WL2: circles. WL3: squares. WL4: stars. WL5: diamonds. All regression lines are discussed in the text.

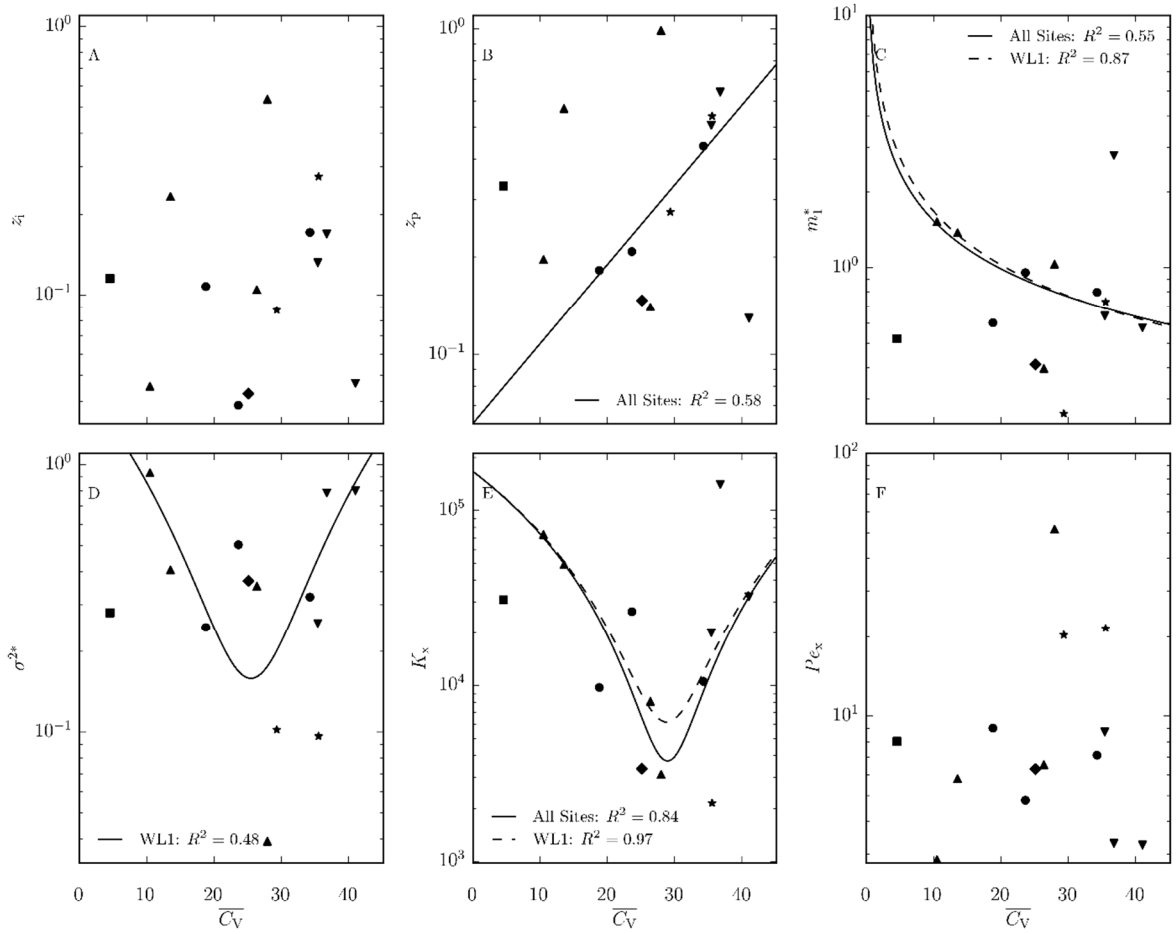

Figure 12. Scatter plots of $\overline{C_v}$ versus measured RTD characteristics. Studies conducted under non-vegetated conditions are not featured. WL1: triangles. WL2: circles. WL3: squares. WL4: stars. WL5: diamonds. All regression lines are discussed in the text.

Appendix A: Time-Series Of Measured Tracer Response Curves And Attendant Flow And Wind Effects

This apprendix presents a collection of time-series plots showing the measured RTD for each tracer study conducted in this work in addition to measured coincident time-series of associated flow and wind effects. The flow effects presented here include the average system flow-through rate $Q_a(t) \approx \left(Q_i(t) + Q_o(t)\right)/2$, where $Q_i(t)$ and $Q_o(t)$ are the measured inflow and outflow volumetric flow rates, respectively; and the measured system volume, $V_s(t)$. The wind effects presented include the measured time-varying wind speeds extrapolated to 10m above the local land surface ($v_{wl0}(t)$), and measured wind directions relative to estimates main basin flow directions ($\theta_{wf}(t)$). The top panel in each chart provides time-series for measured wind speeds and wind directions relative to the predominant system flow direction. The middle panel gives time-series of measured average system flow rates and volumes. The bottom panel gives the measured RTD and mass recovery curves. For each chart presented, the main temporal features of the measured tracer response curves are also given. Additionally, unusual tracer response curve features and important notes about variable monitoring are provided in the charts directly.

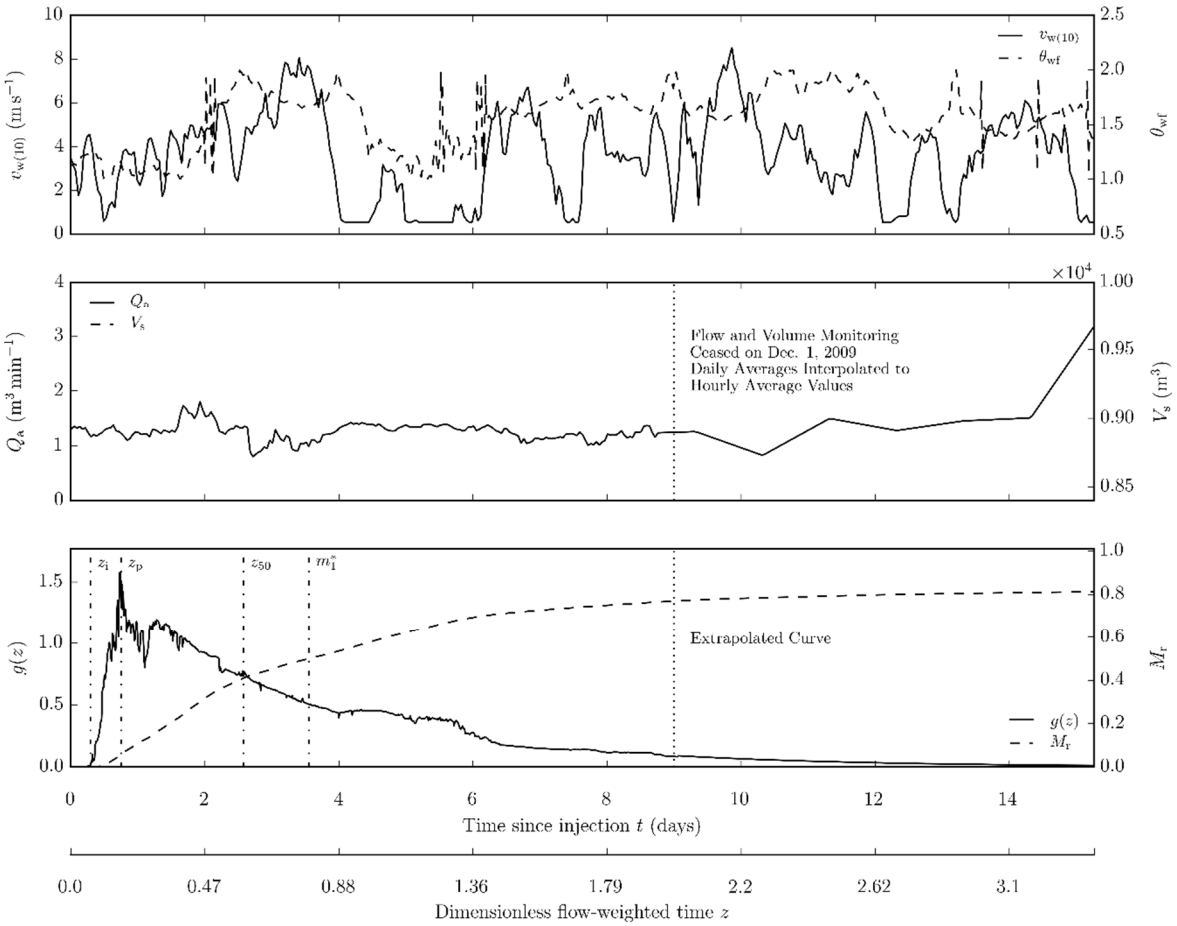

Figure 1A. Study WL1_1 (11/22/09 – 12/9/09). Flow and volume monitoring ceased on Dec. 1, 2009. Continuous system flow and volume approximated from estimates of daily average flow rates. The tracer response curve for the period beyond Dec. 1, 2009 was extrapolated using an exponential decay model as discussed in the text. z_{50} is the dimensionless median detention time.

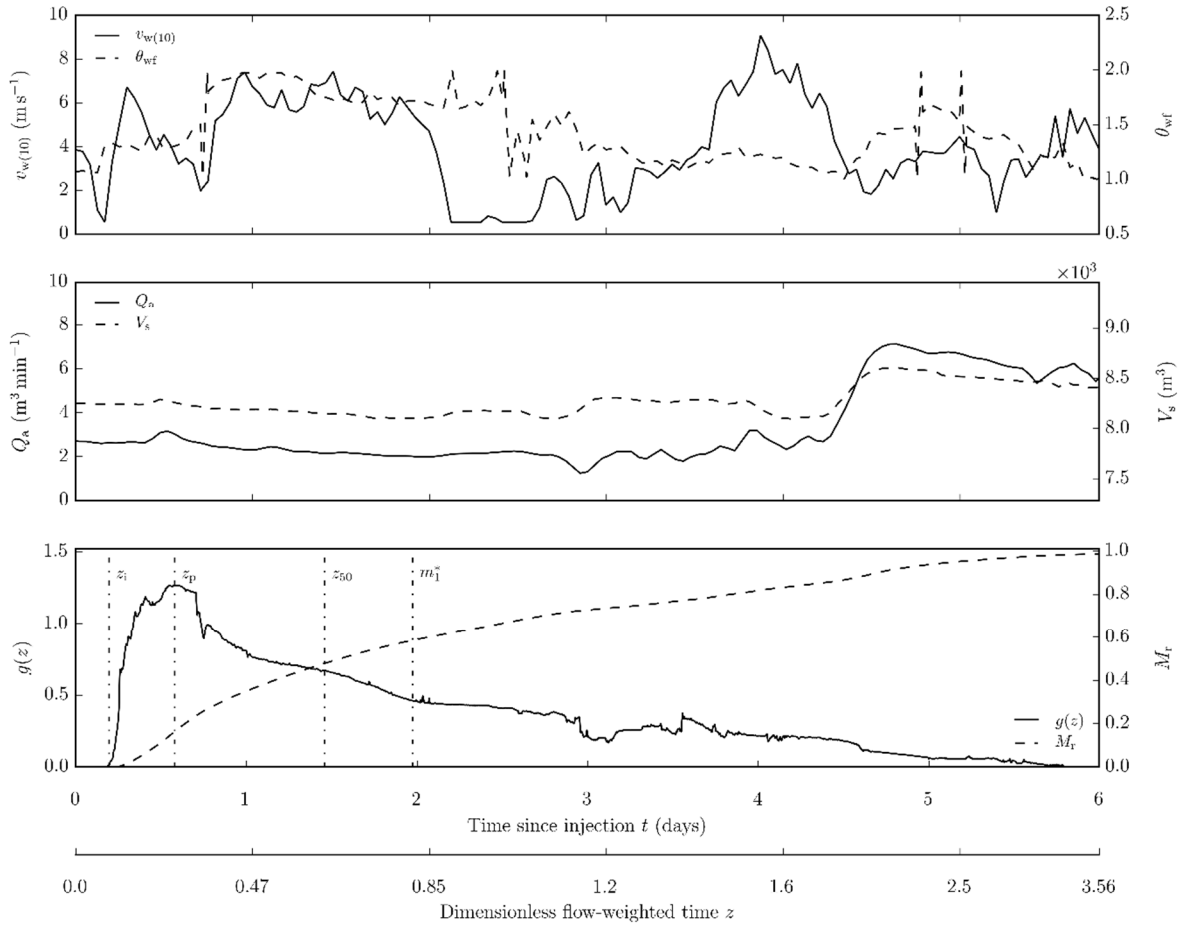

Figure 2A. Study WL1_2 (5/6/10 – 5/13/10)

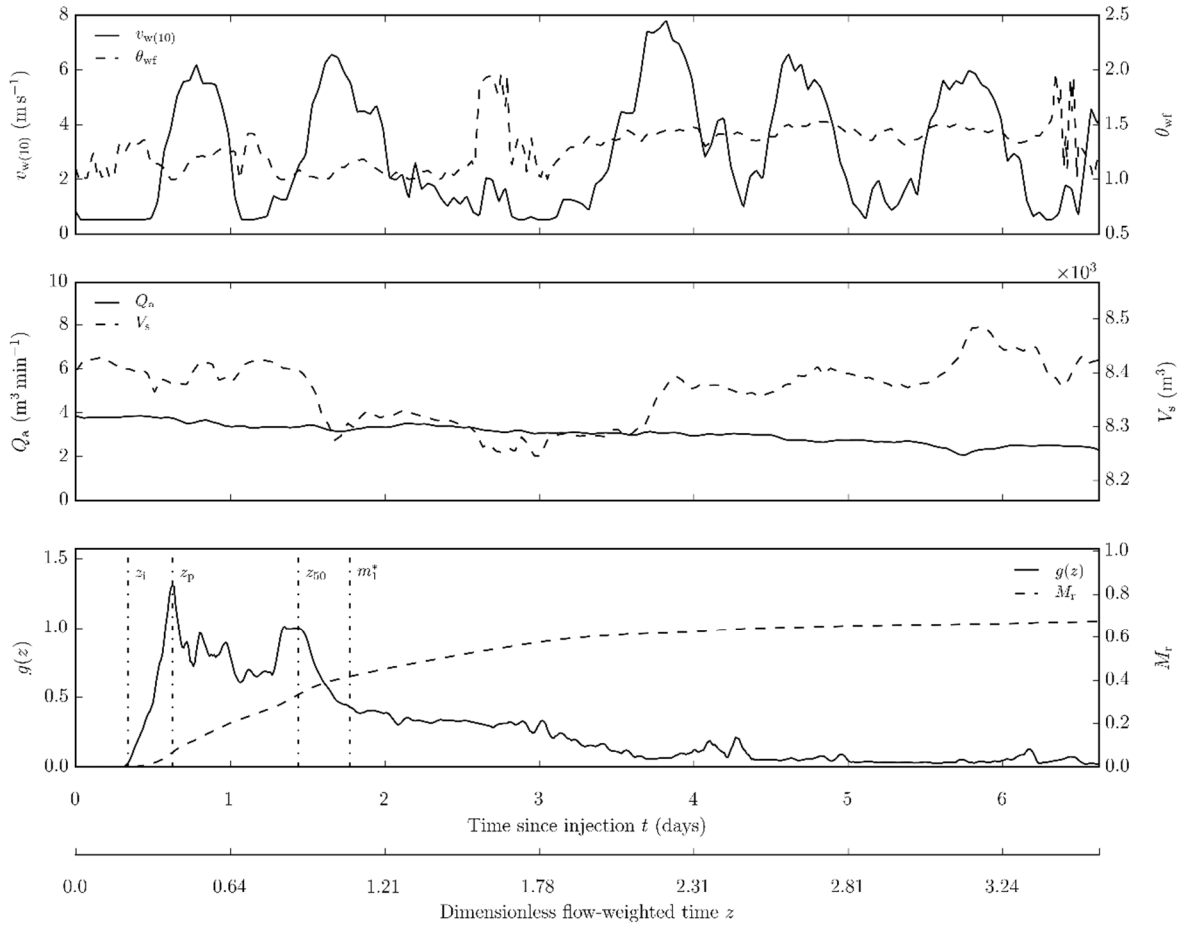

Figure 3A. Study WL1_3 (5/18/10 – 5/25/10).

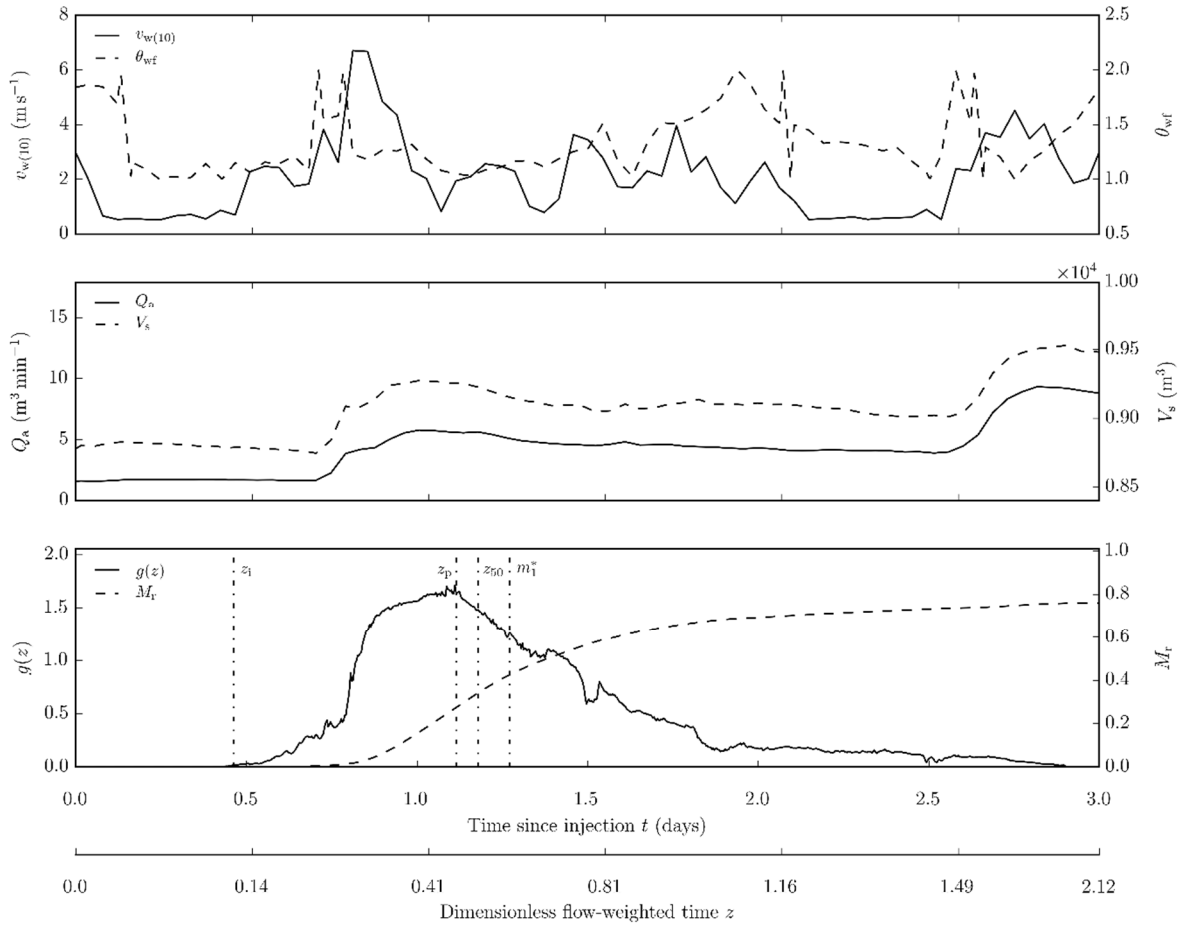

Figure 4A. Study WL1_4 (6/9/10 – 6/13/10).

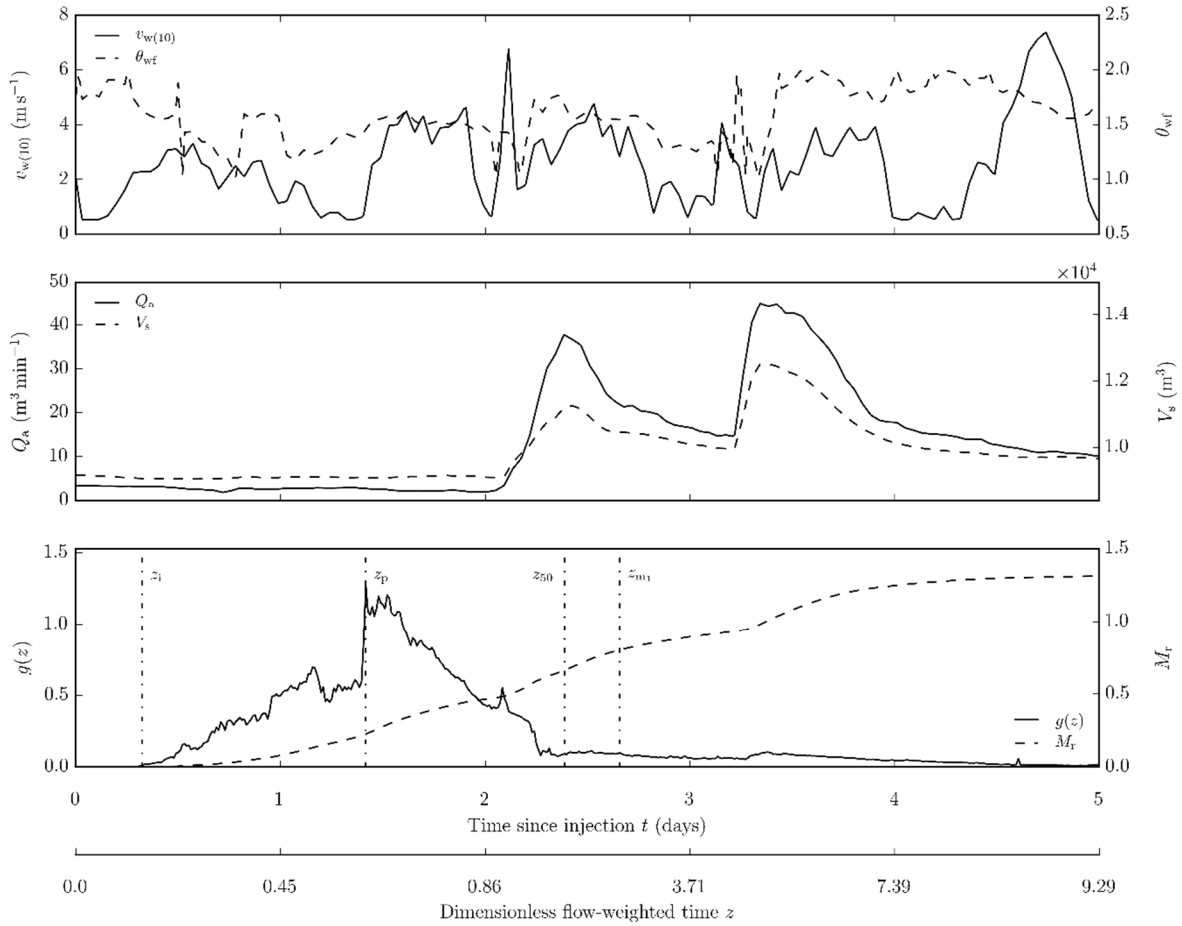

Figure 5A. Study WL1_5 (6/23/10 – 6/29/10).

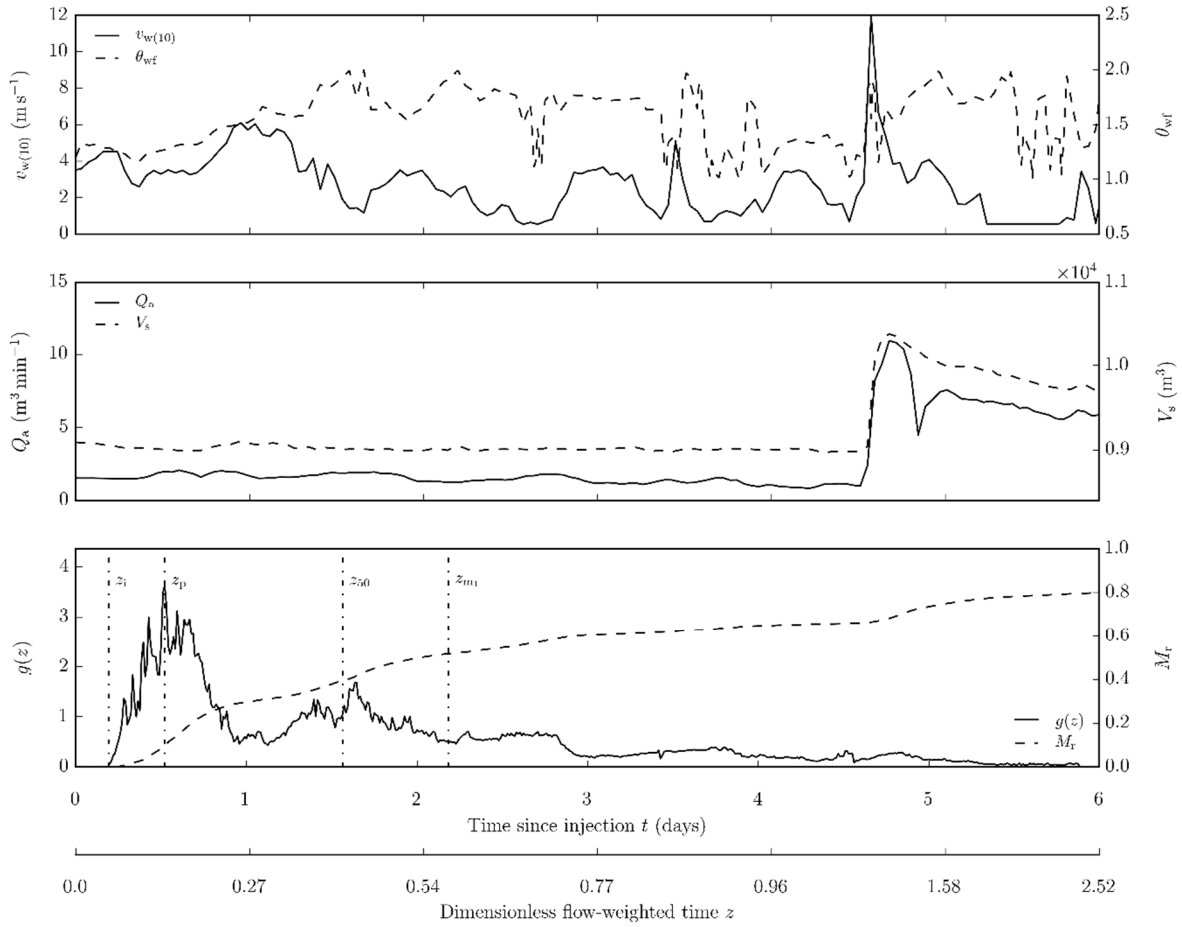

Figure 6A. Study WL1_6 (7/13/10 – 7/19/10).

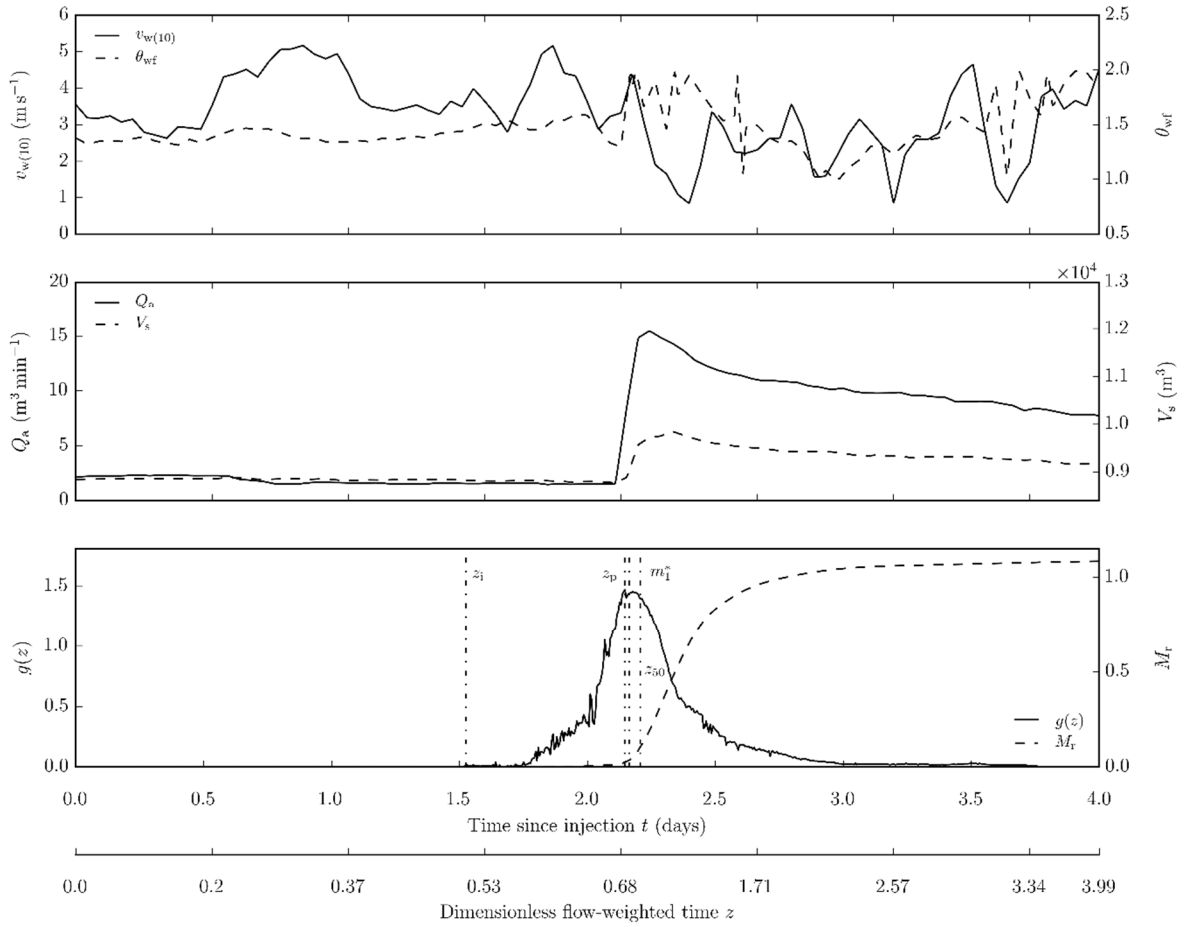

Figure 7A. Study WL1_7 (8/29/10 – 9/3/10).

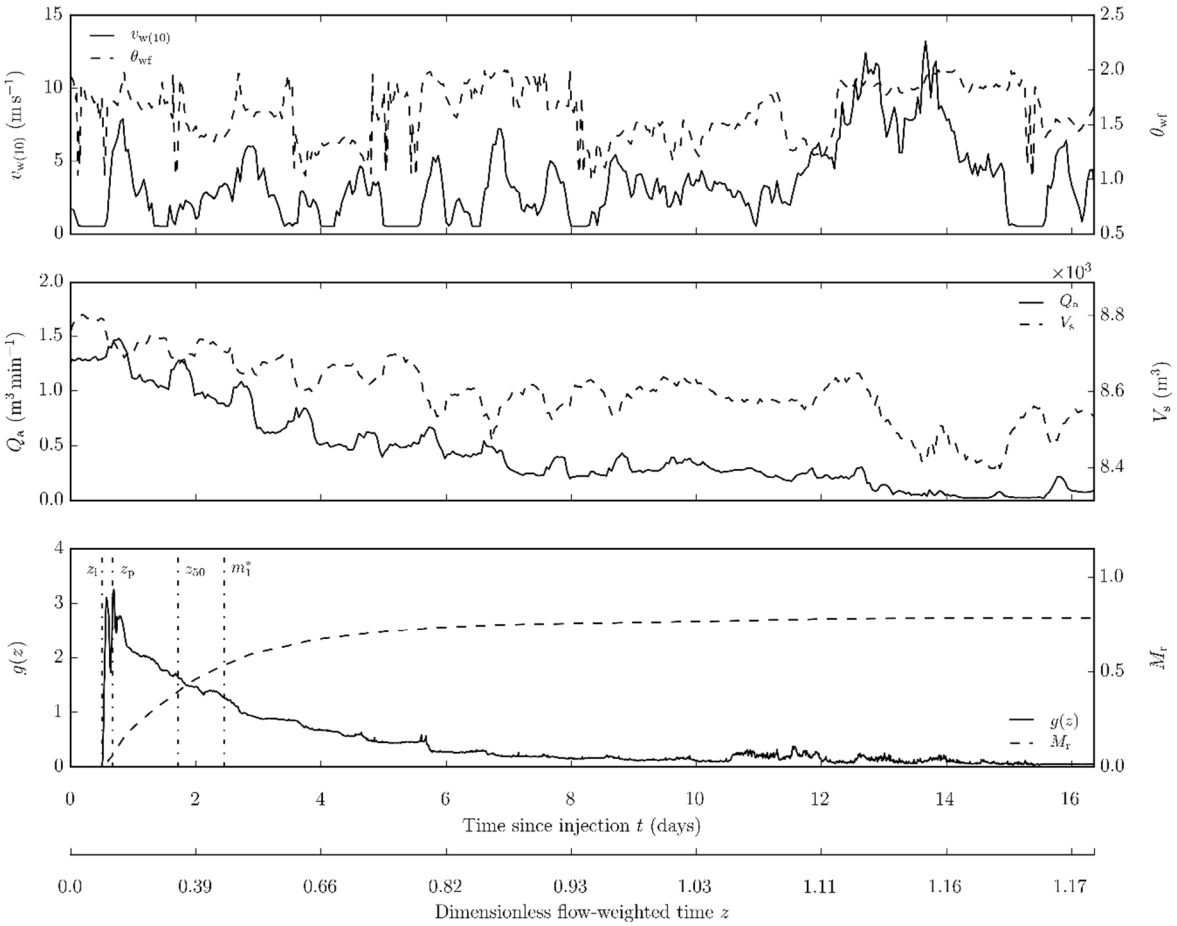

Figure 8A. Study WL1_8 (10/13/10 – 10/29/10). Flow and volume monitoring ceased on Oct. 29, 2010. Continuous system flow and volume approximated from estimates of daily average flow rates. The tracer response curve for the period beyond Oct. 29, 2010 was extrapolated using an exponential decay model as discussed in the text.

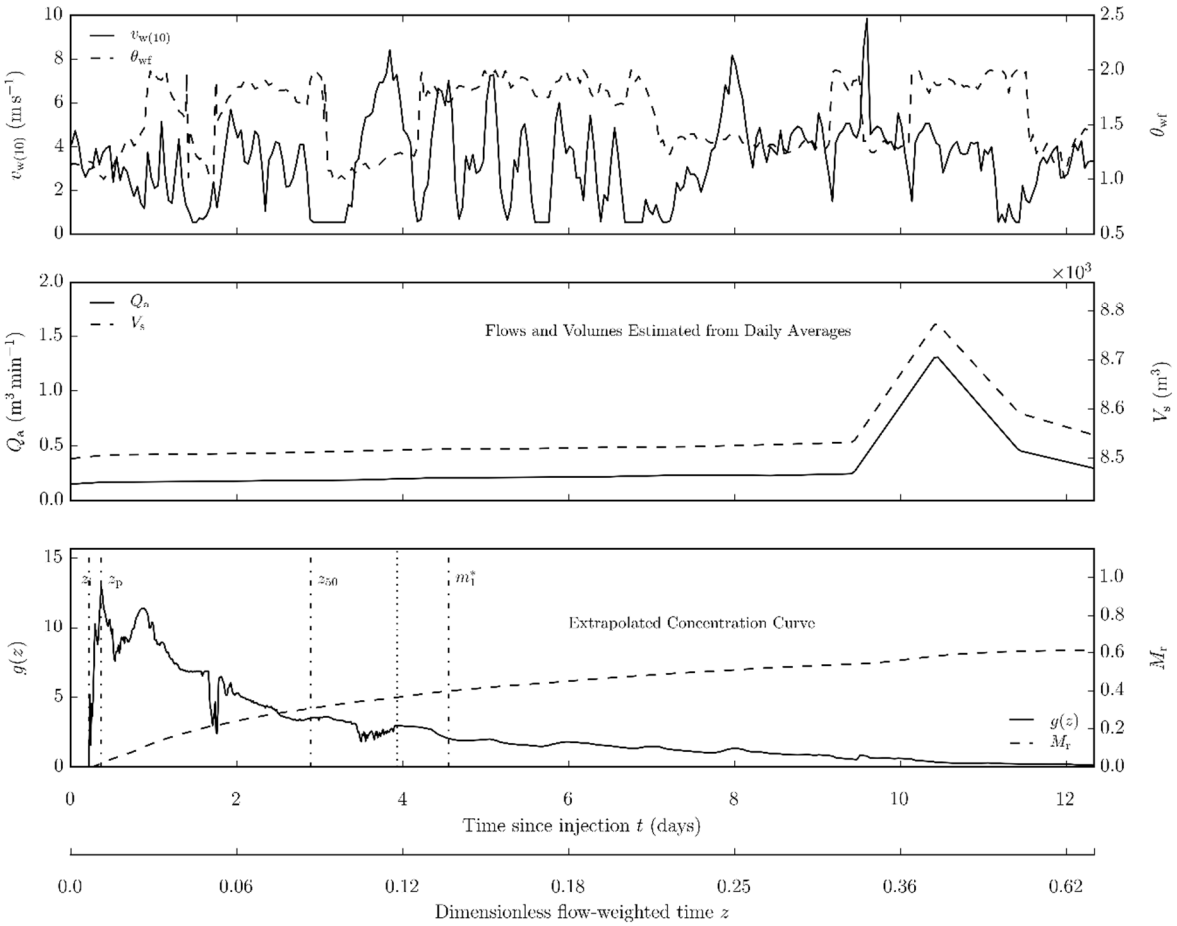

Figure 9A. Study WL1_9 (11/20/10 – 12/2/10) Concentration monitoring ceased on Dec. 2, 2010. Continuous system flow and volume approximated from estimates of daily average flow rates. The tracer response curve for the period beyond Dec. 2, 2010 was extrapolated using an exponential decay model as discussed in the text.

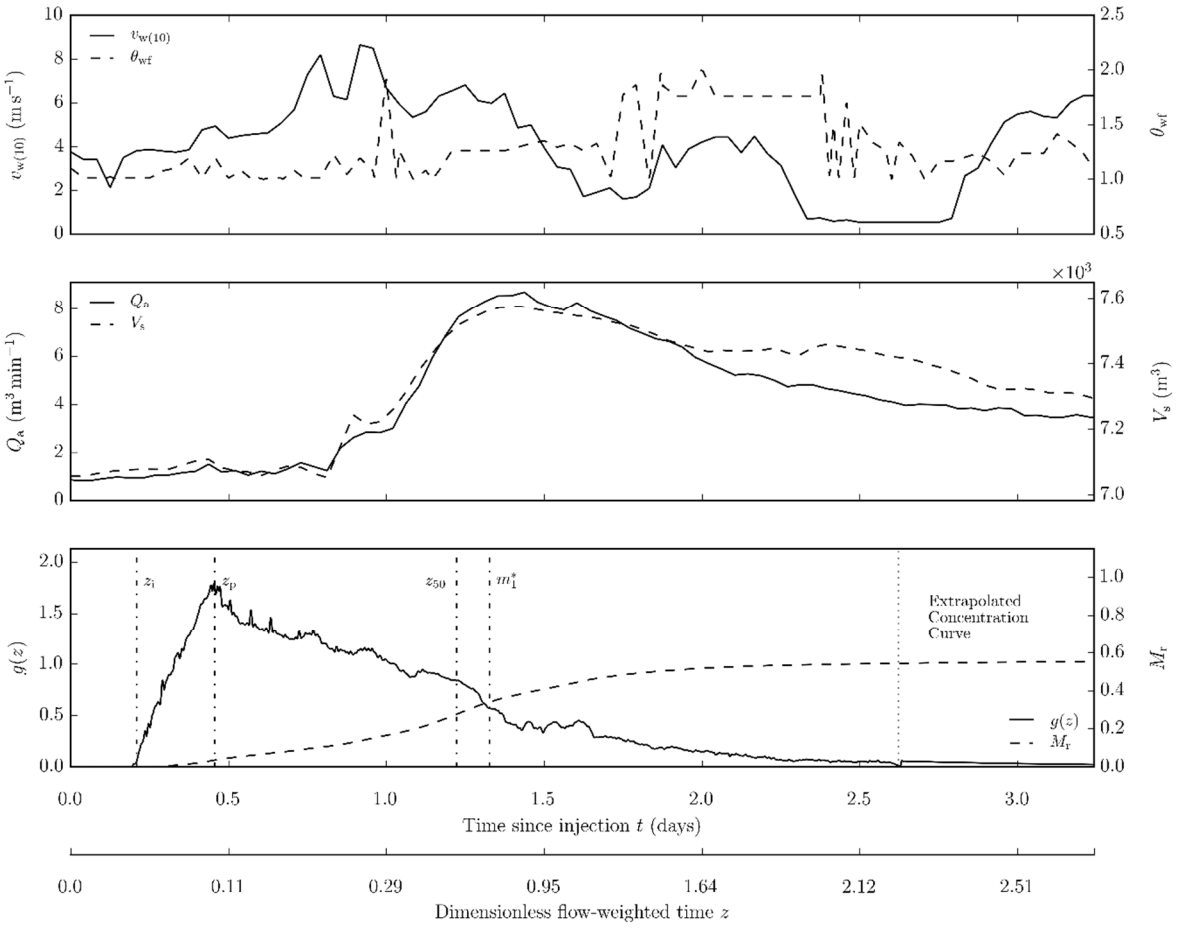

Figure 10A. Study WL1_10 (4/18/11 – 4/21/11).

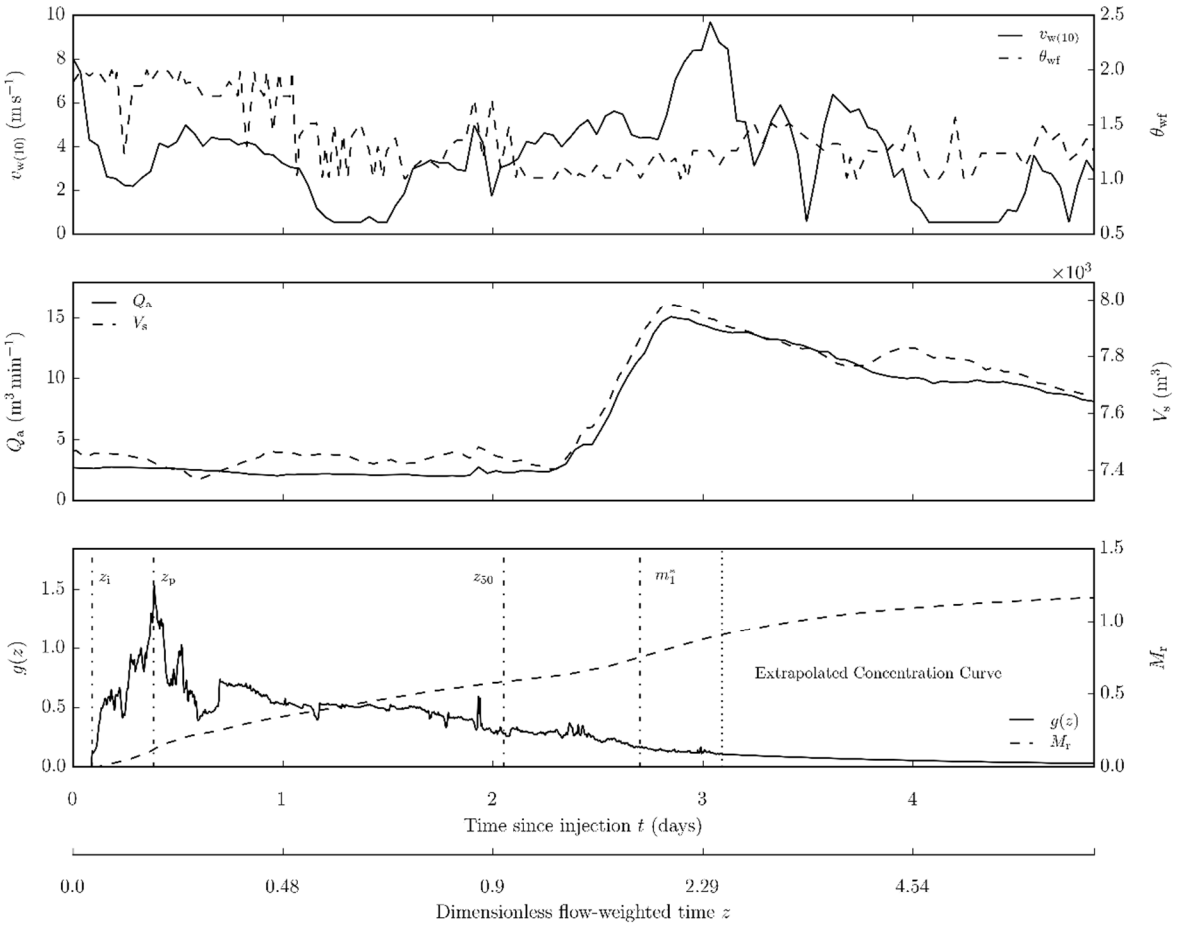

Figure 11A. Study WL1_11 (5/22/11 – 5/25/11). Concentration monitoring ceased on May 25, 2011 due to censor operation issues. The tracer response curve for the period beyond May 25, 2011 was extrapolated using an exponential decay model as discussed in the text.

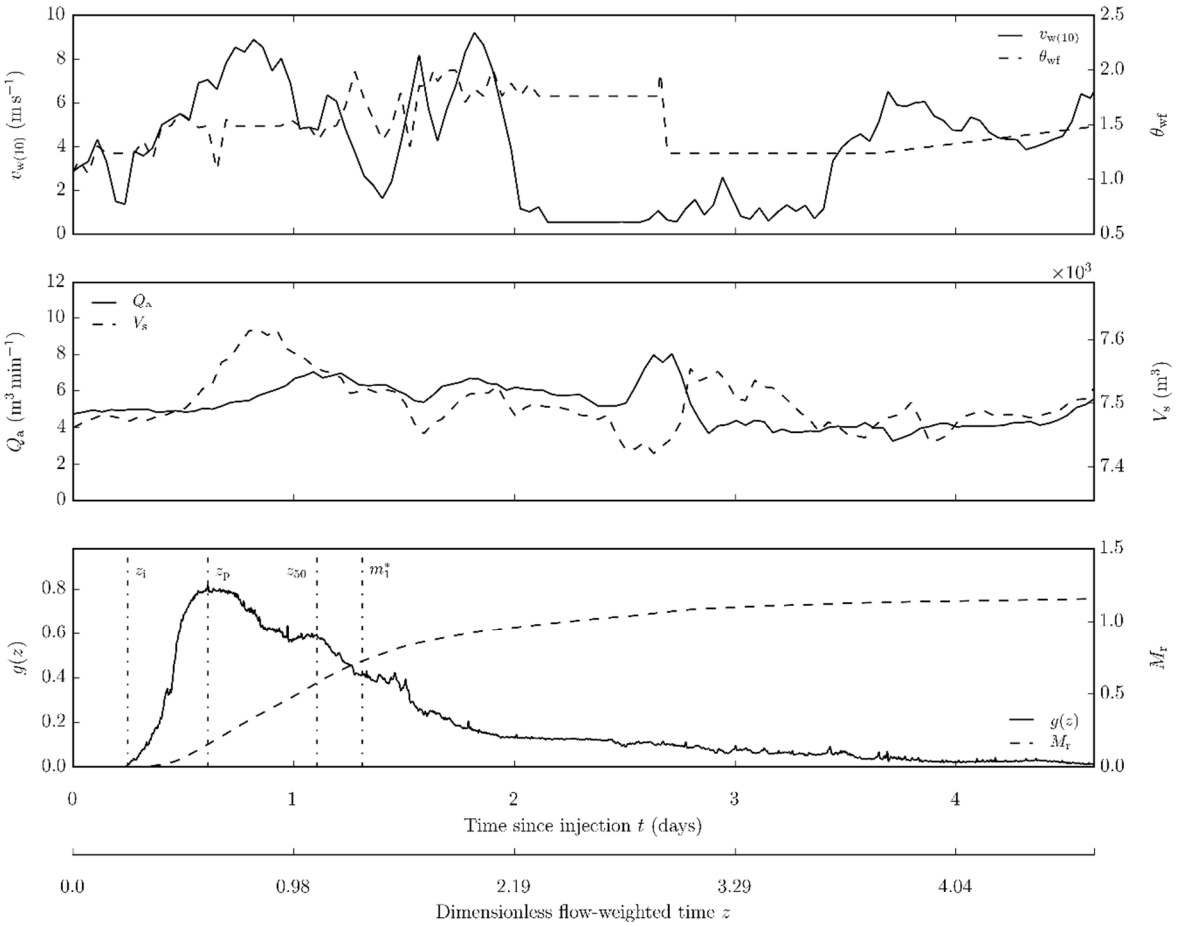

Figure 12A. Study WL1_12 (5/29/11 – 6/4/11).

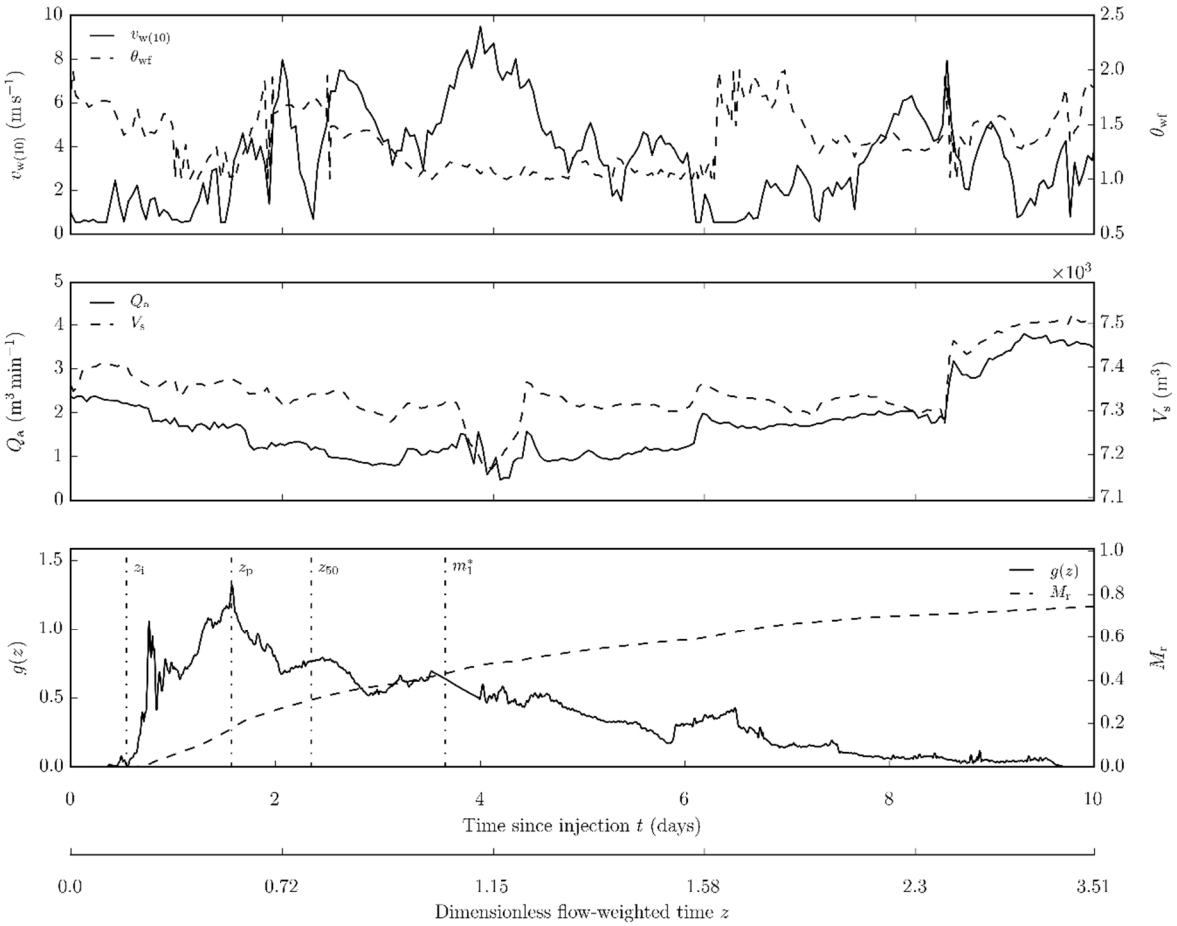

Figure 13A. Study WL1_13 (4/23/12 – 5/3/12). Concentration monitoring ceased on May 3, 2012. The tracer response curve for the period beyond May 3, 2012 was extrapolated using an exponential decay model as discussed in the text.

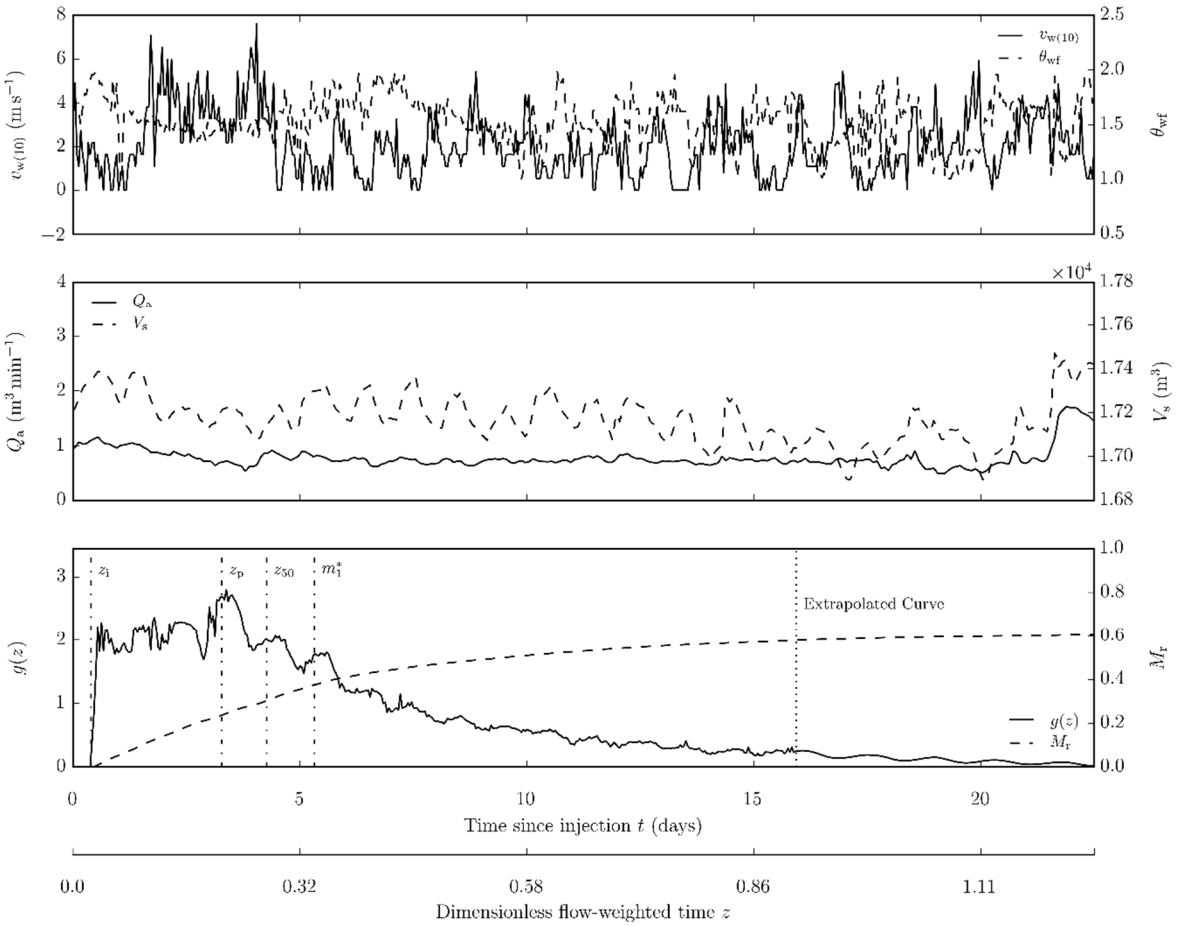

Figure 14A. Study WL2_1 (5/20/10 – 6/14/10). Concentration monitoring ceased on June 14, 2010 due to censor operation issues. The tracer response curve for the period beyond June 14, 2010 was extrapolated using a sinusoidal exponential decay model as discussed in the text.

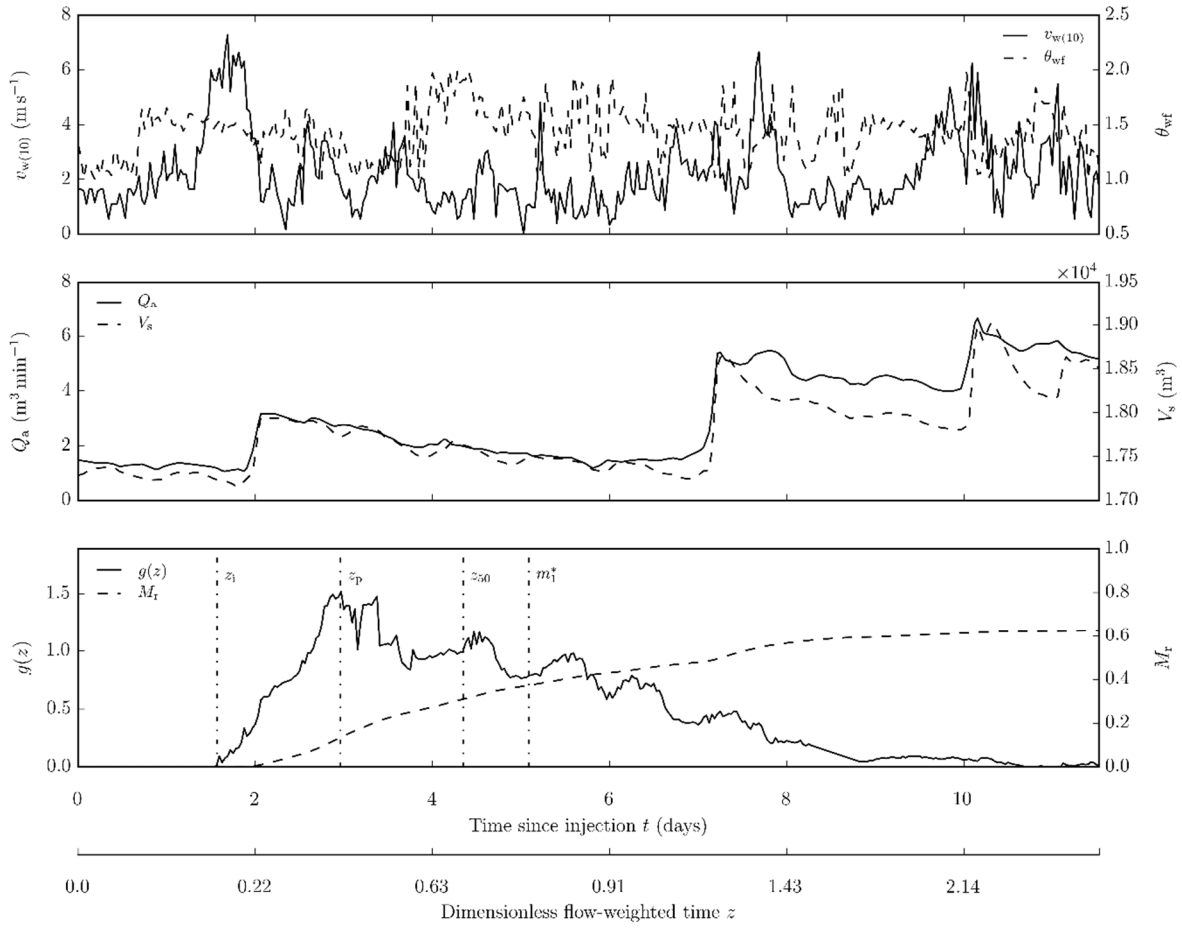

Figure 15A. Study WL2_2 (6/15/10 – 6/27/10).

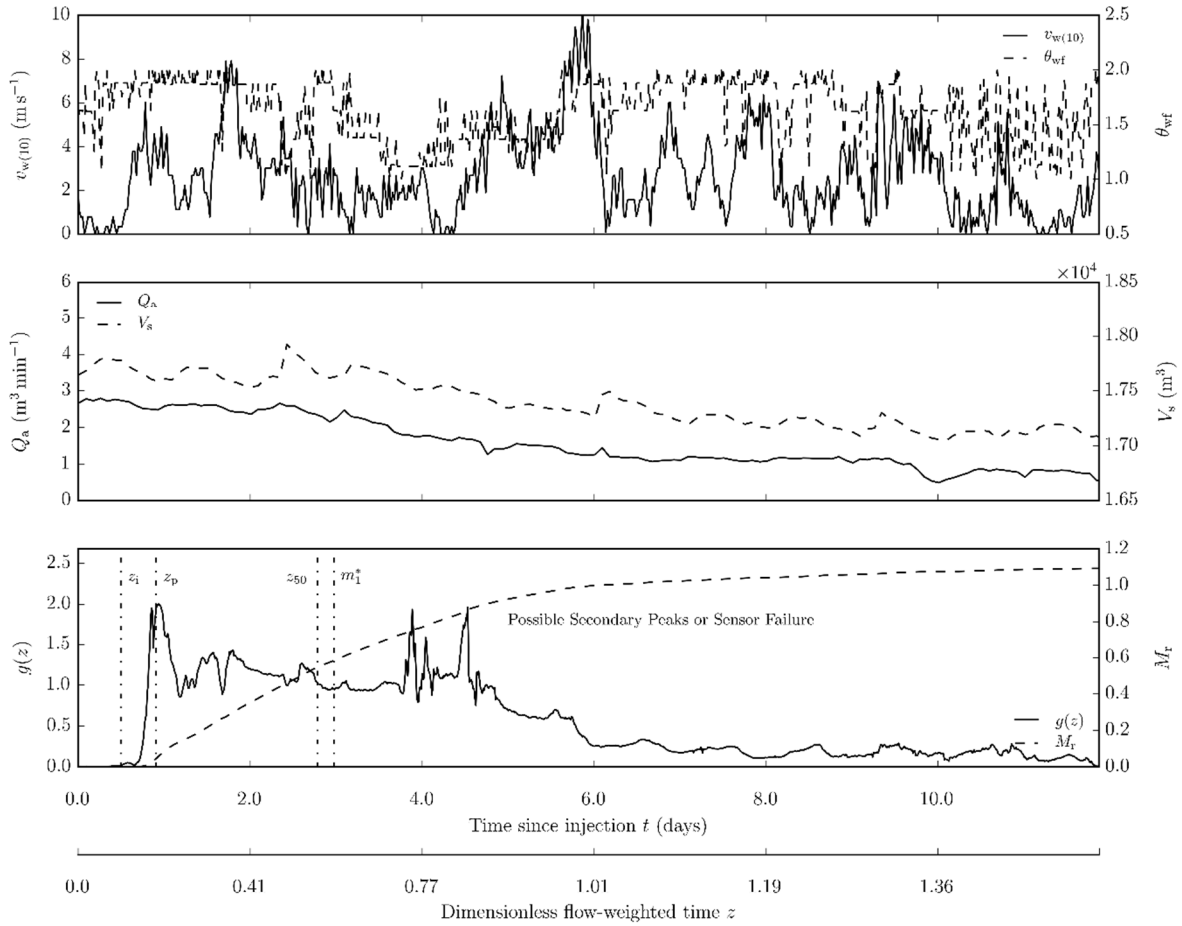

Figure 16A. Study WL2_3 (7/8/10 – 7/20/10).

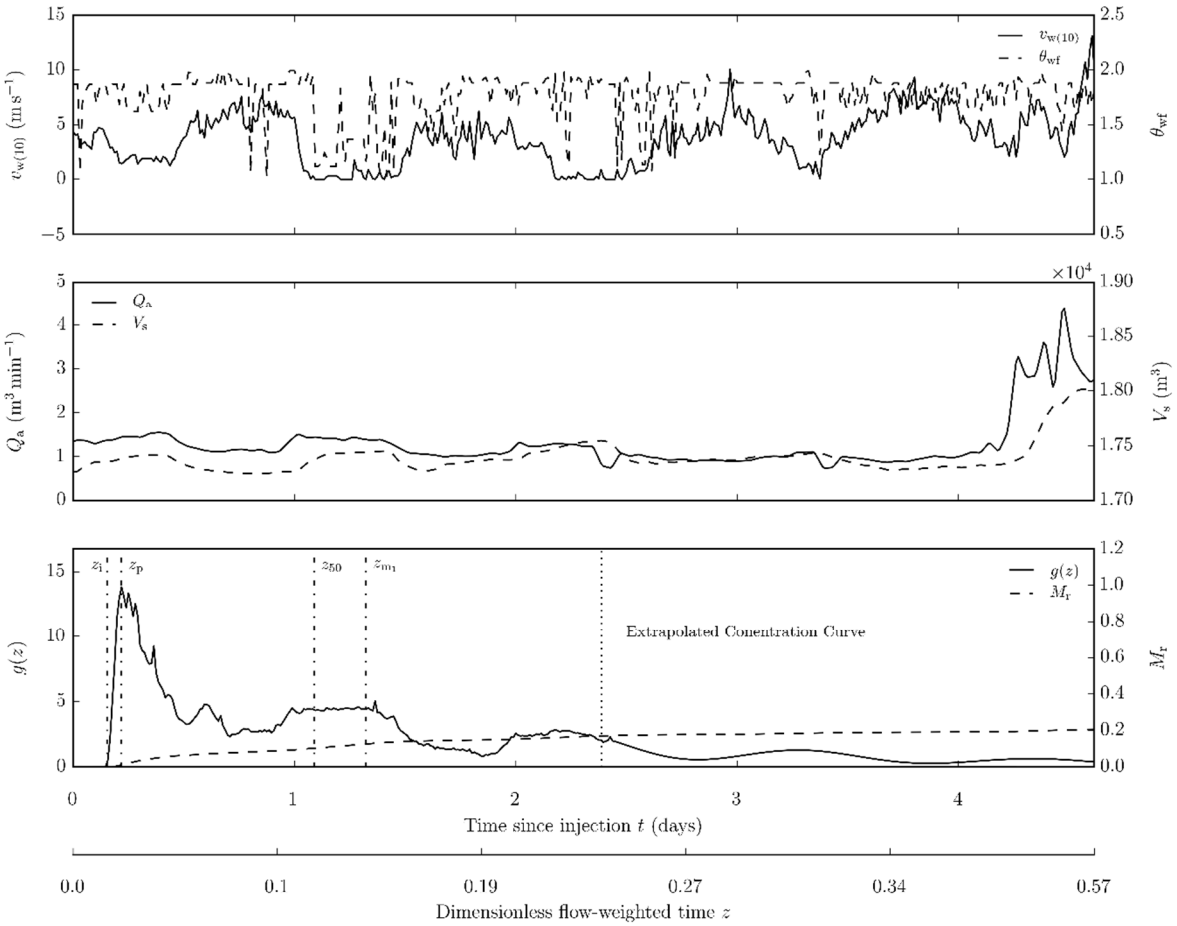

Figure 17A. Study WL2_4 (5/15/11 – 5/18/11). Concentration monitoring ceased on May 18, 2011 due to censor operation issues. The tracer response curve for the period beyond May 18, 2011 was extrapolated using a sinusoidal exponential decay model as discussed in the text.

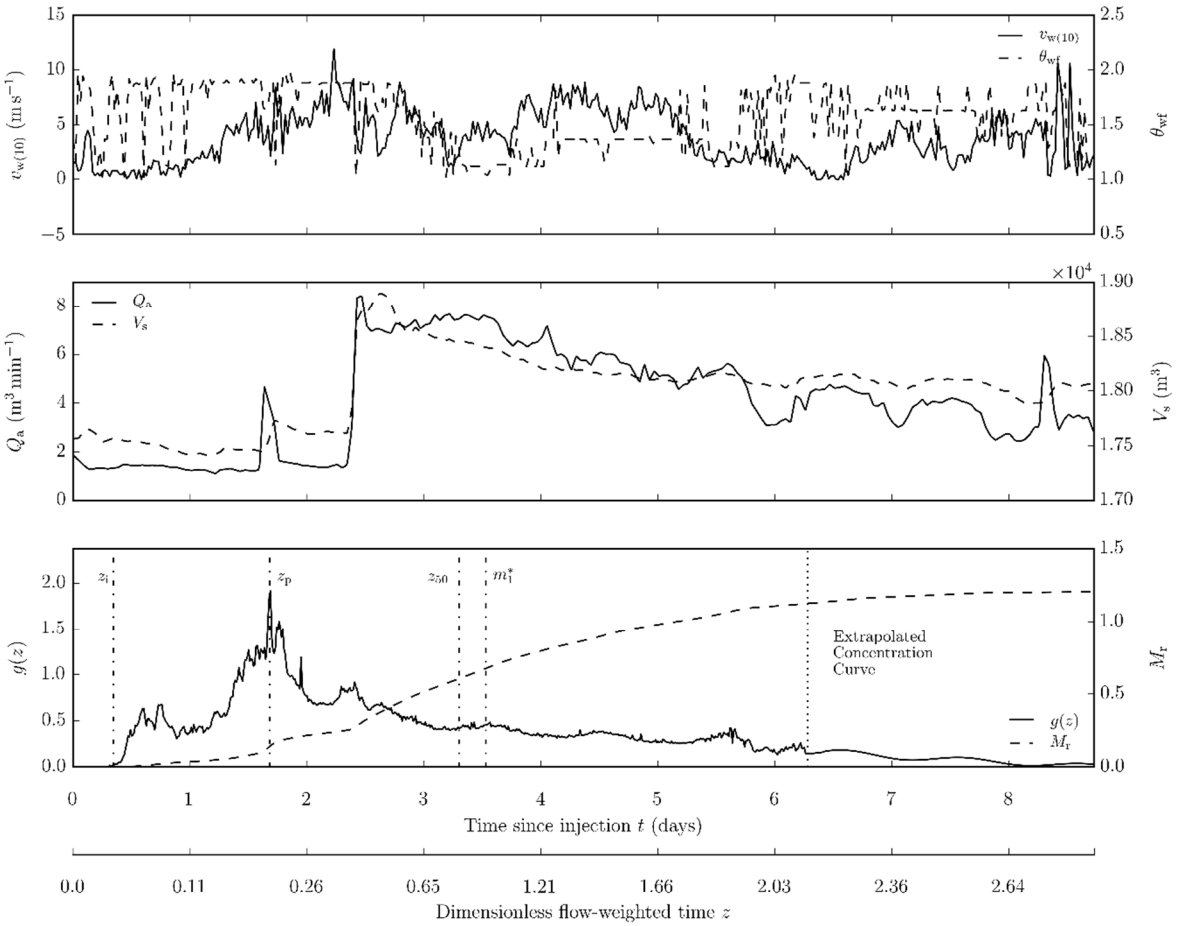

Figure 18A. Study WL2_5 (6/18/11 – 6/27/11). Concentration monitoring ceased on June 27, 2011 due to censor operation issues. The tracer response curve for the period beyond June 27, 2011 was extrapolated using a sinusoidal exponential decay model as discussed in the text.

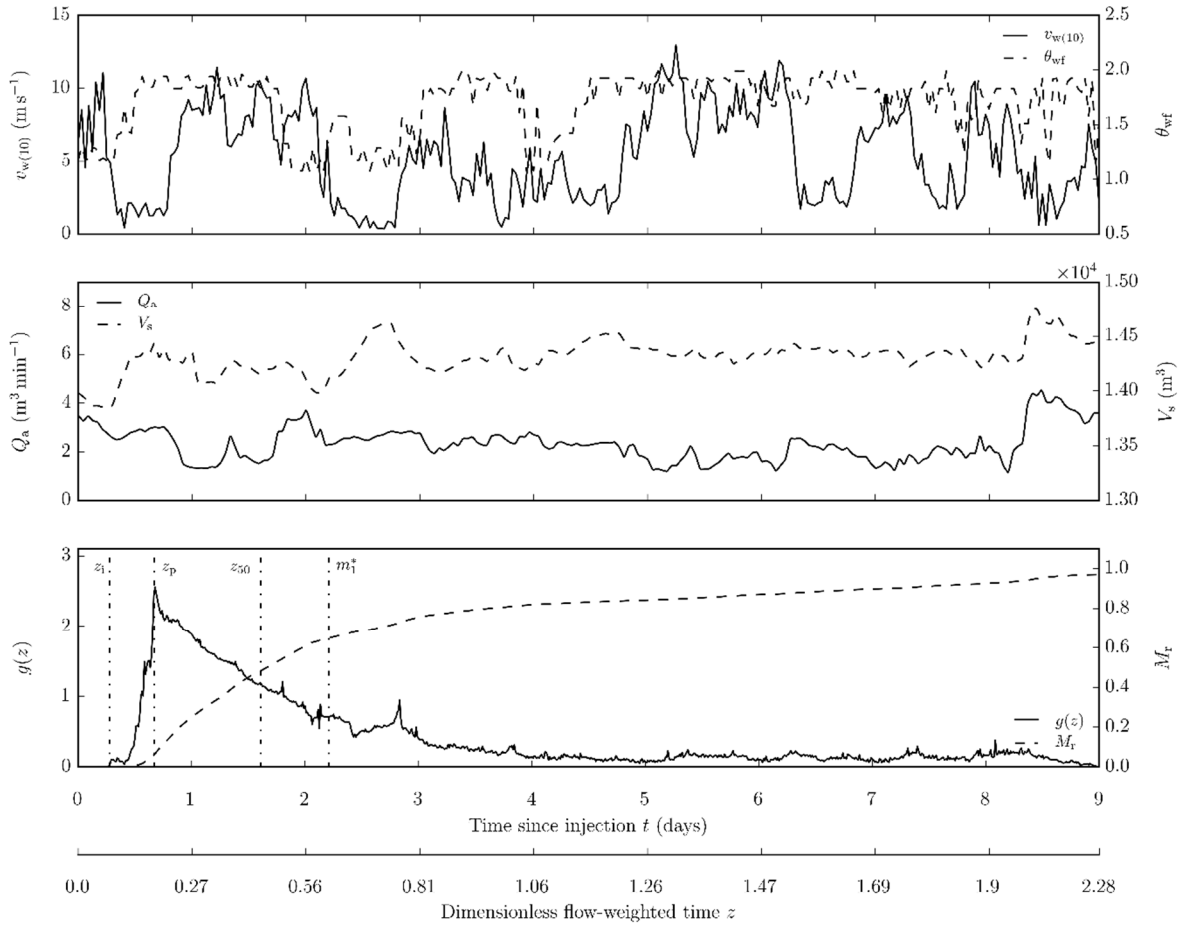

Figure 19A. Study WL3_1 (5/3/11 – 5/14/11).

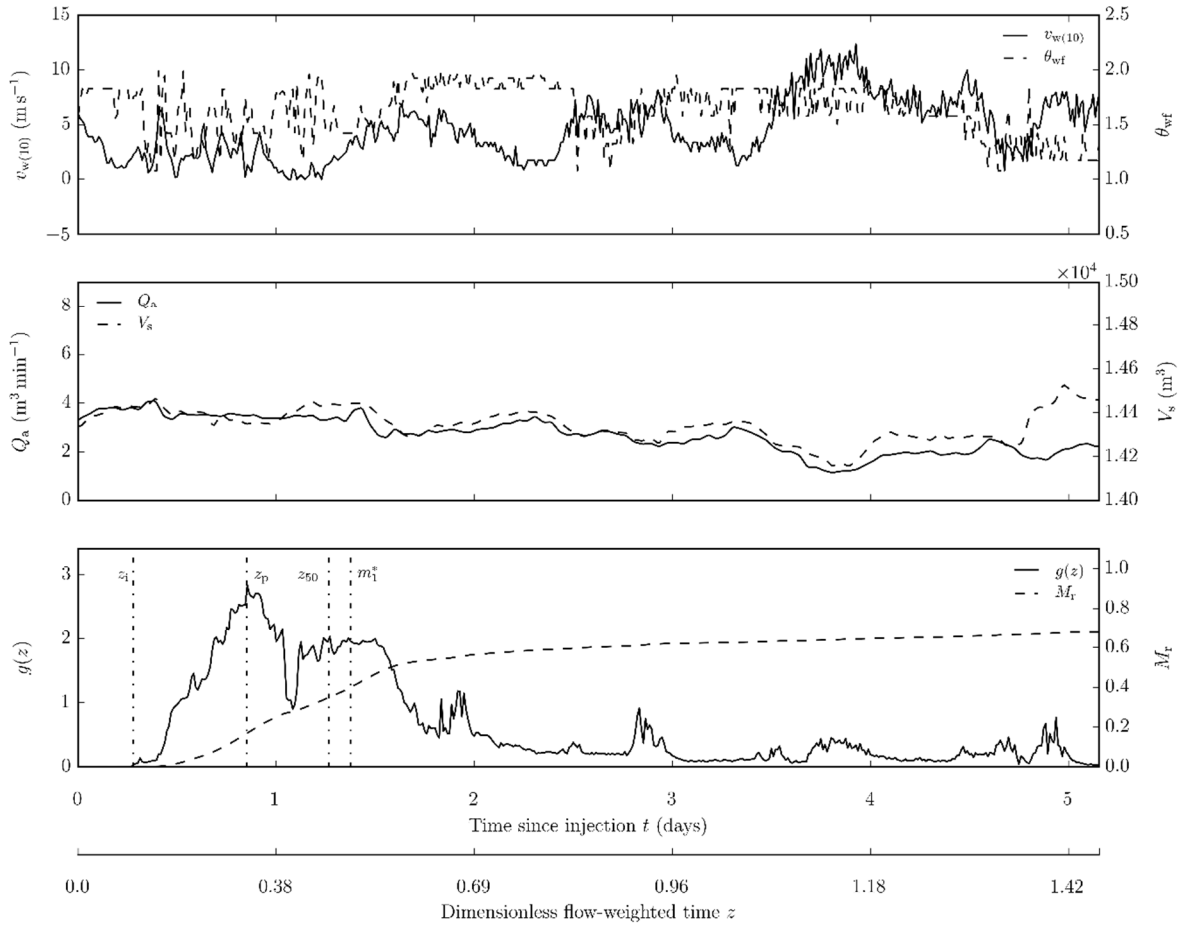

Figure 20A. Study WL3_2 (6/3/11 – 6/9/11).

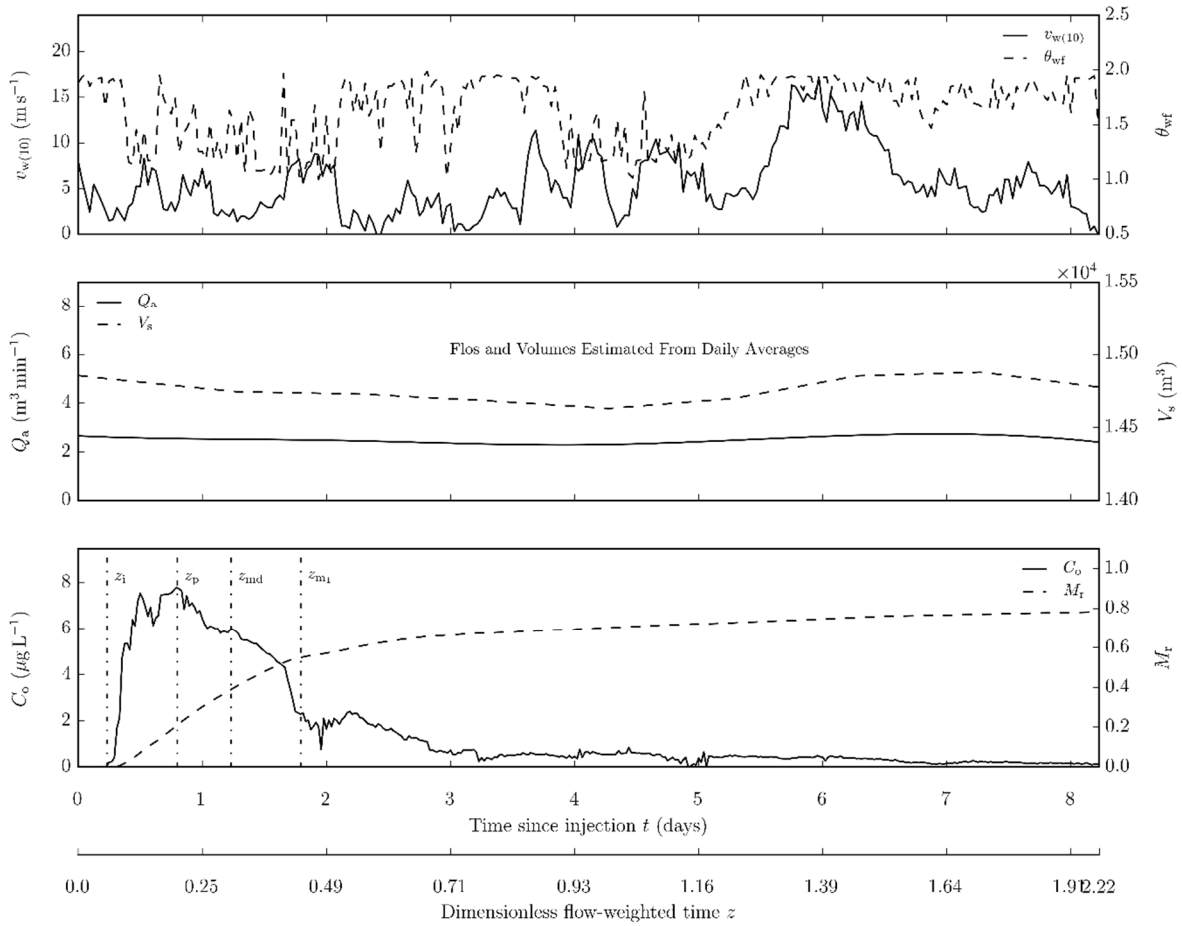

Figure 21A. Study WL3_3 (4/21/12 – 4/30/12).

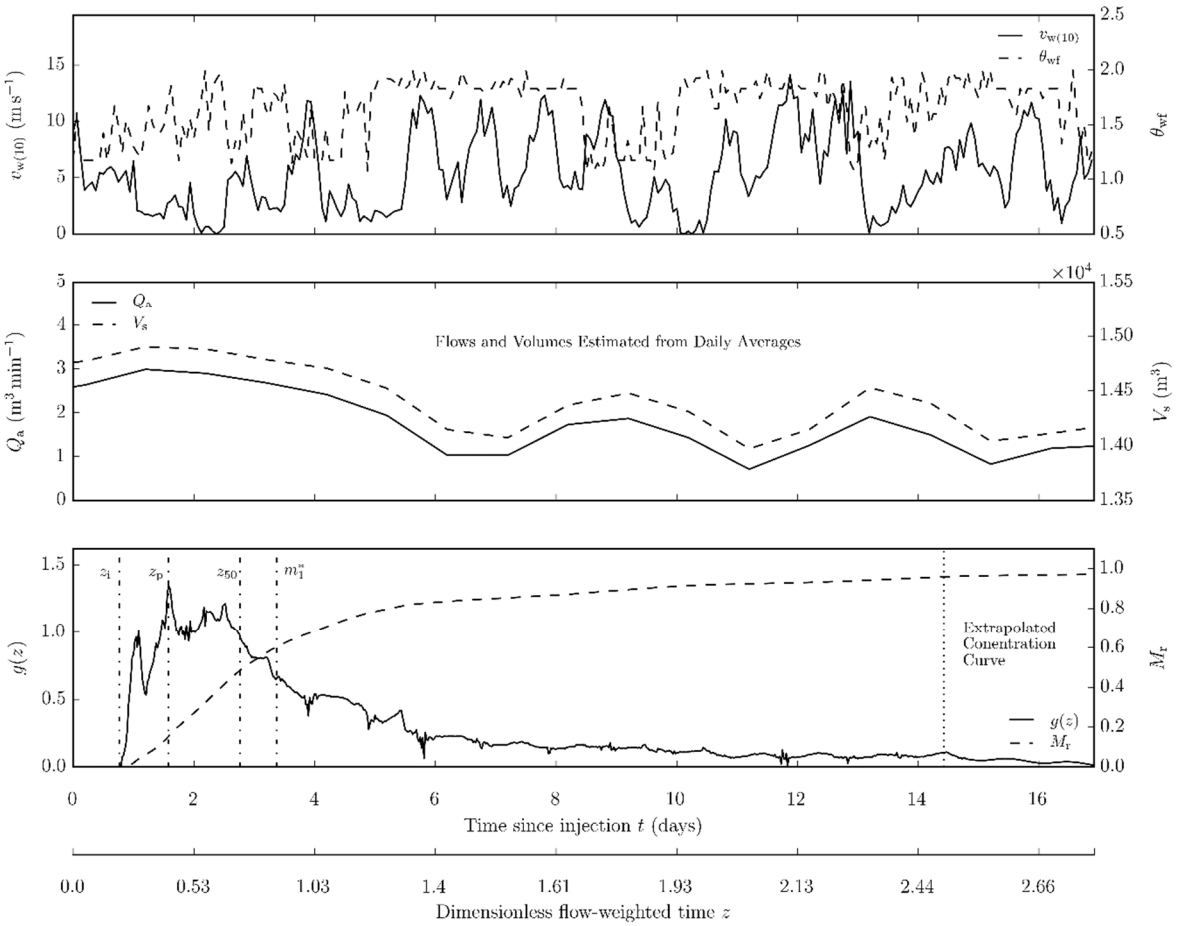

Figure 22A. Study WL3_4 (5/11/12 – 6/4/12). Concentration monitoring ceased on June 4, 2012 due to sensor operation issues. The tracer response curve for the period beyond June 4, 2012 was extrapolated using a sinusoidal exponential decay model as discussed in the text. Continuous flow and volume approximated from daily average estimates.

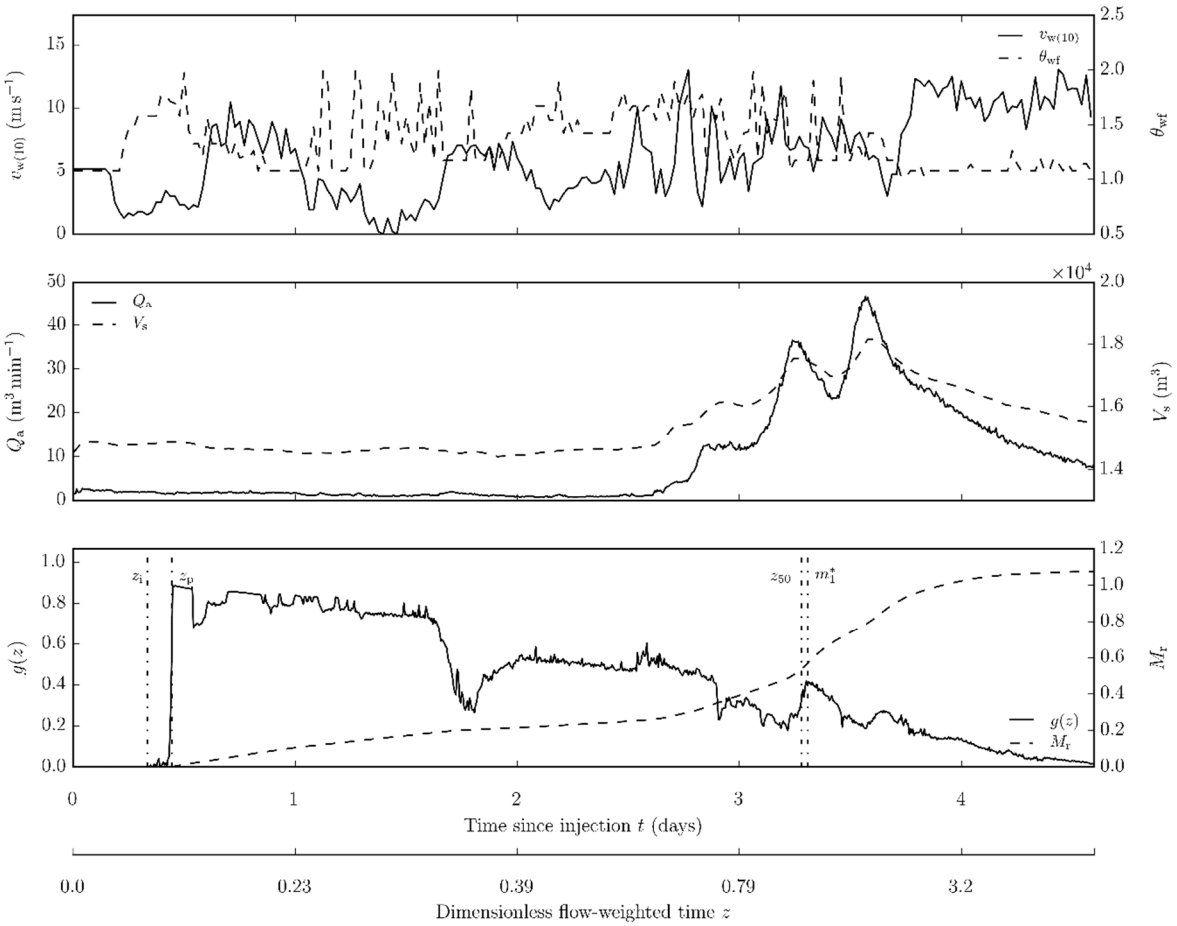

Figure 23A. Study WL3_5 (4/14/13 – 4/19/13).

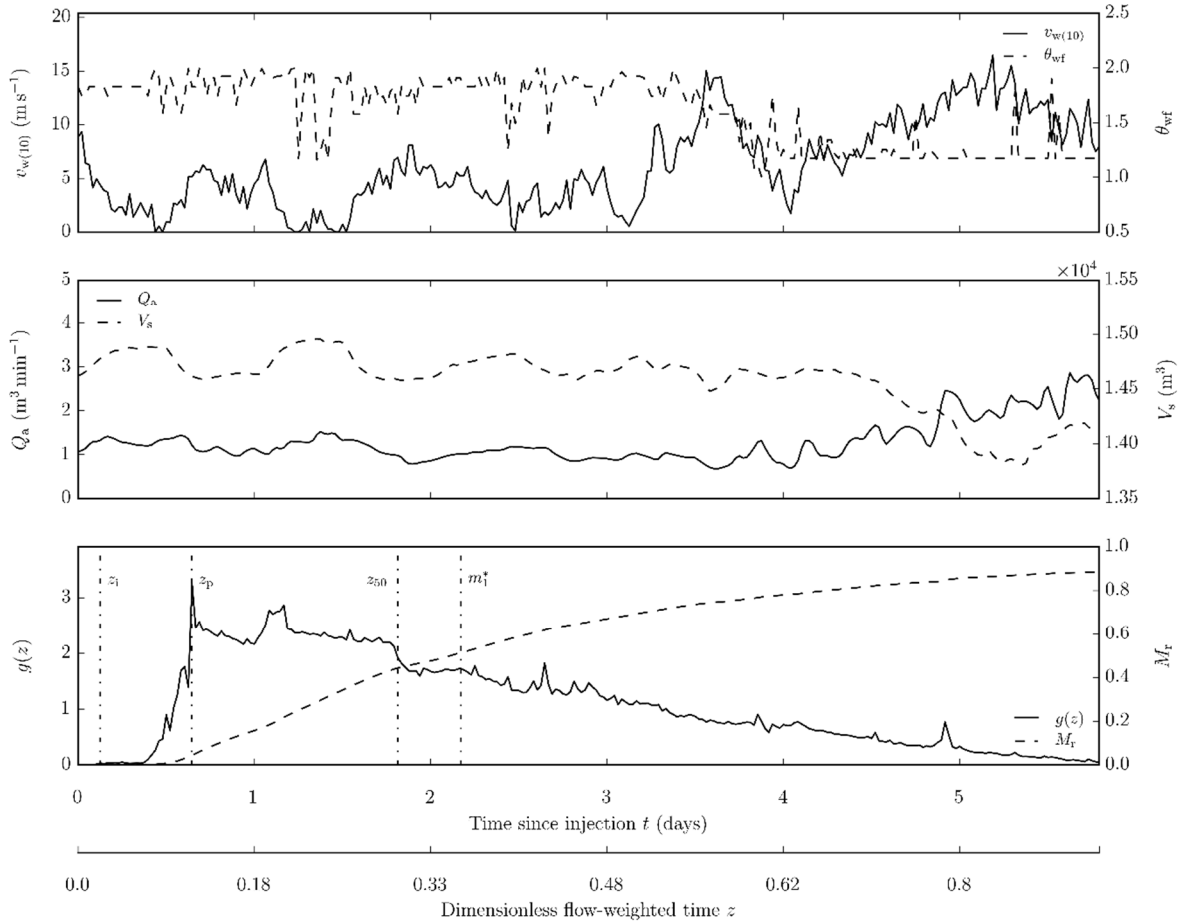

Figure 24A. Study WL3_6 (4/26/13 – 5/3/13).

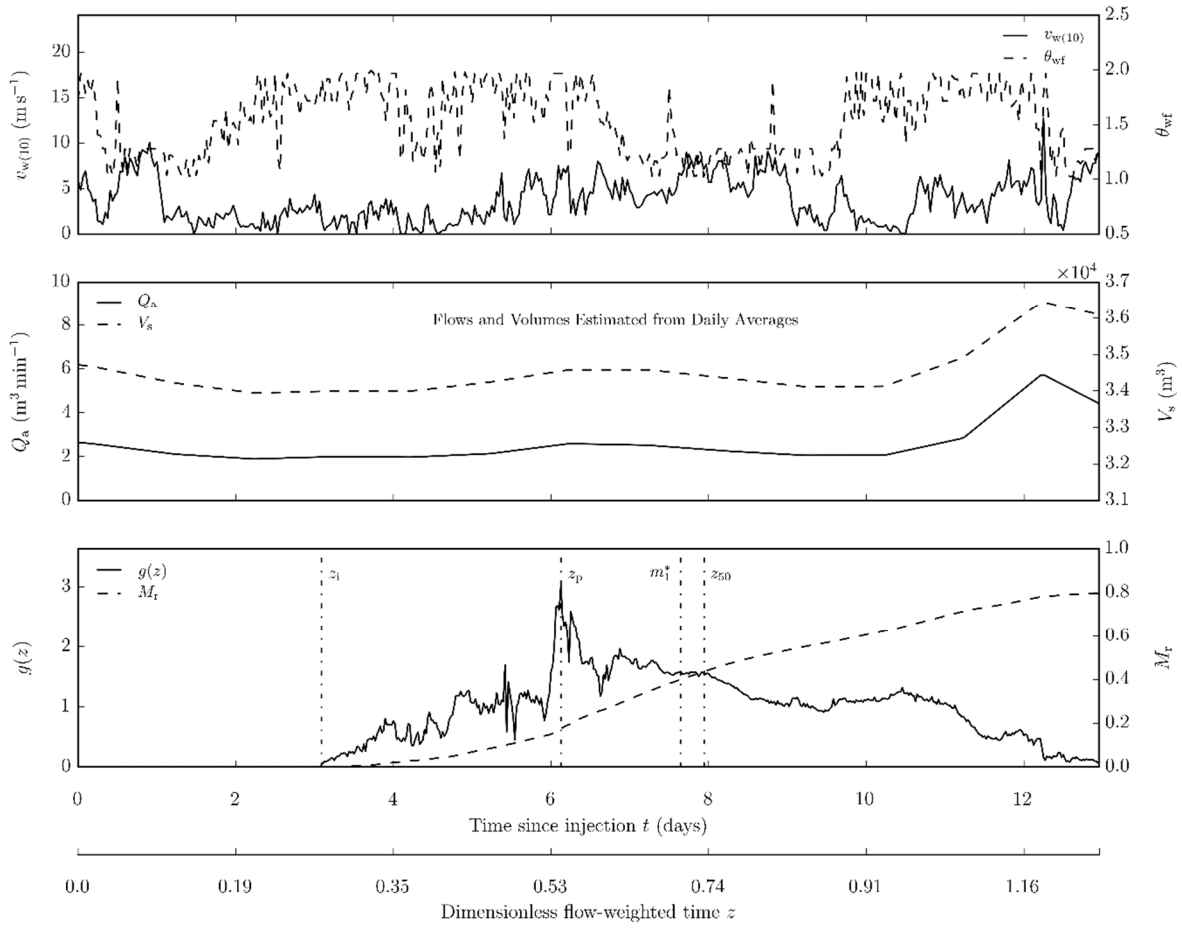

Figure 25A. Study WL4_1 (6/14/11 – 6/27/11).

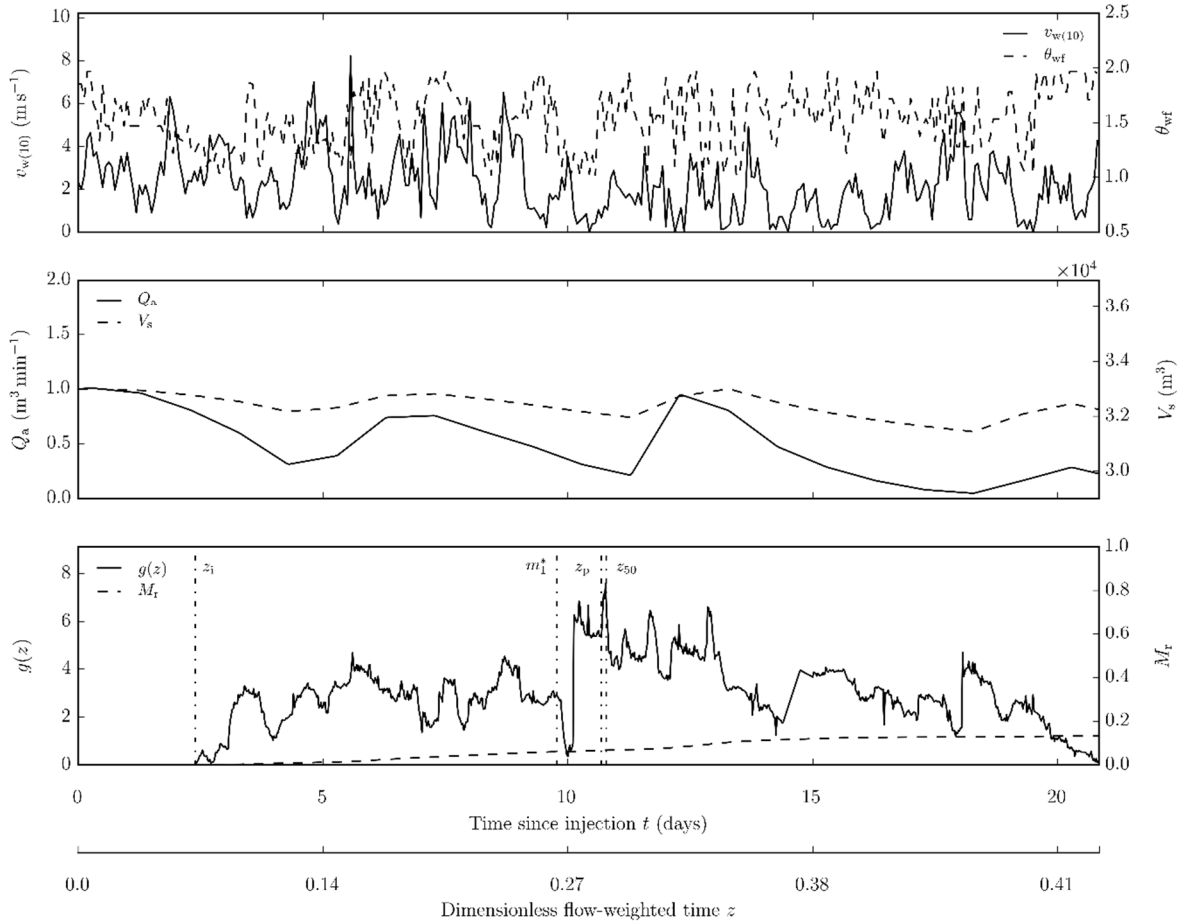

Figure 26A. Study WL4_2 (7/15/11 – 8/5/11). Flow ceased on Aug. 5, 2011.

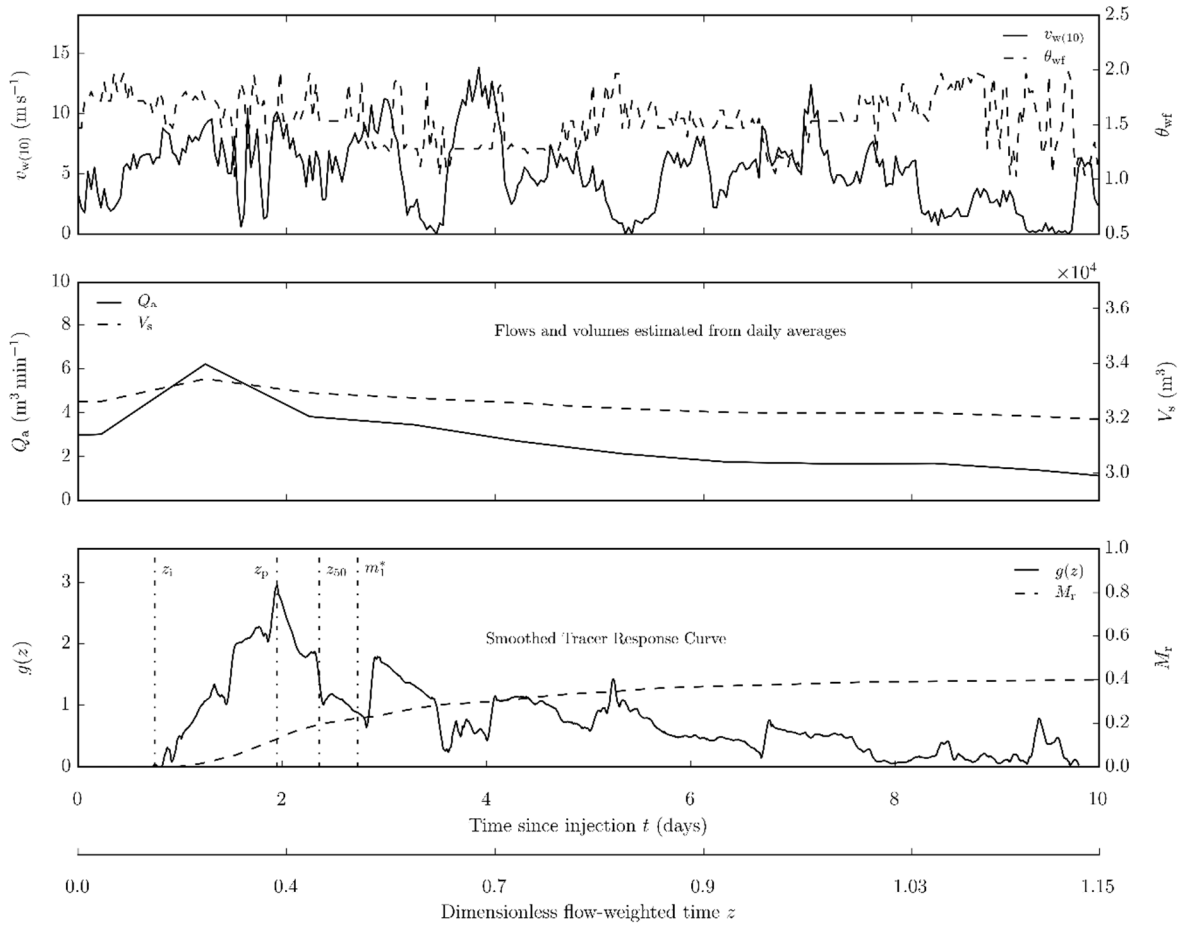

Figure 27A. Study WL4_3 (5/4/12 – 5/14/12).

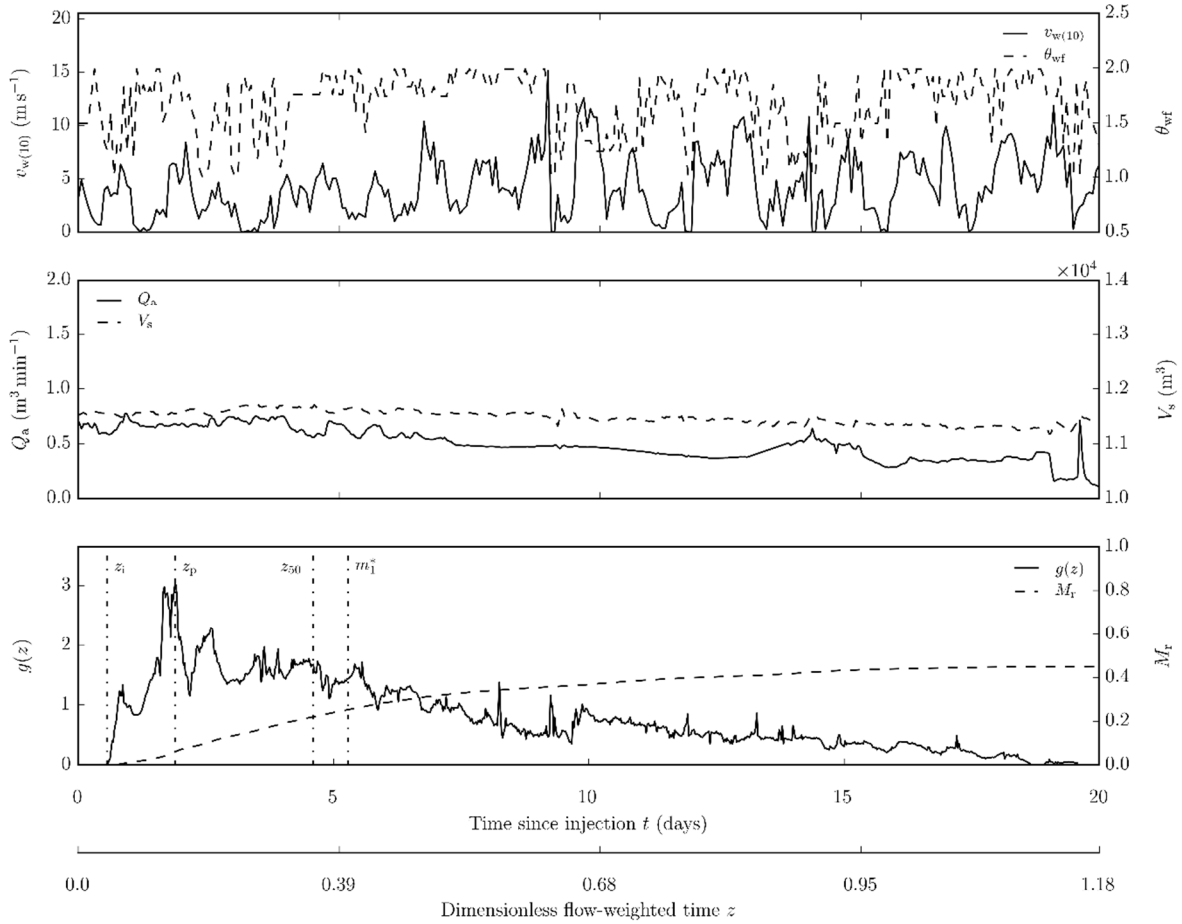

Figure 28A. Study WL5_1 (6/1/12 – 6/22/12).

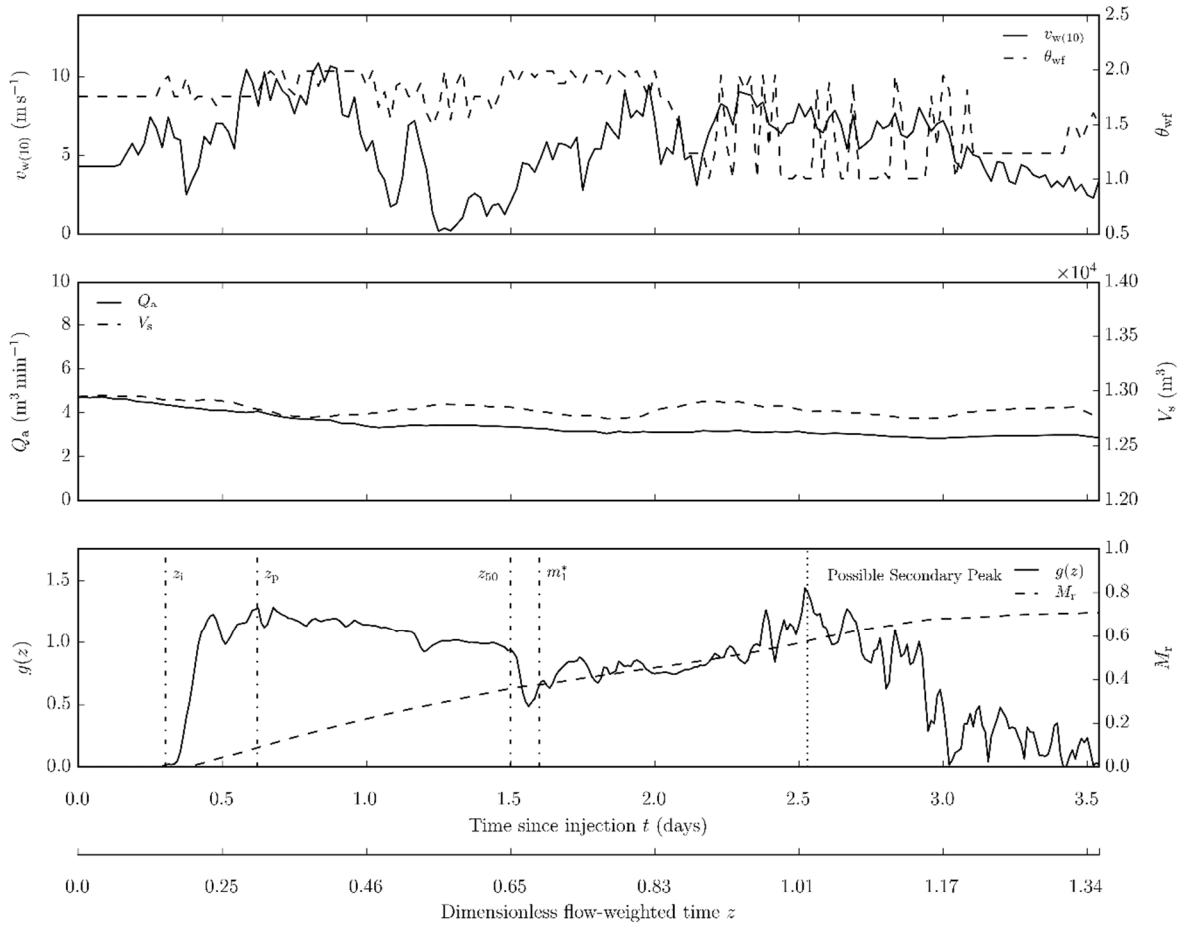

Figure 29A. Study WL5_2 (4/20/13 – 4/24/13).

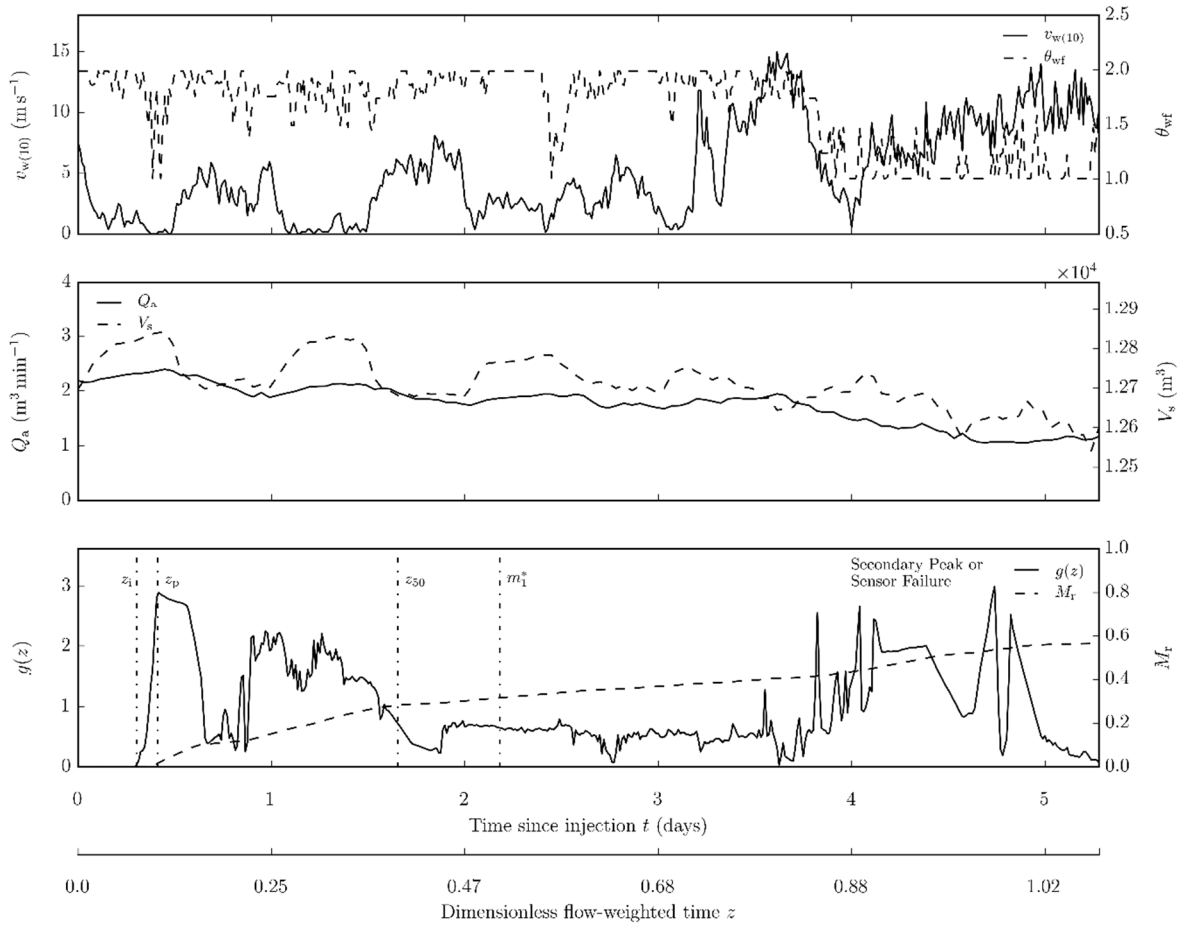

Figure 30A. Study WL5_3 (4/26/13 – 5/2/13).

Appendix B: Vegetation Survey Maps

Vegetation surveys were conducted at times coincident with planned tracer studies. Each survey consisted of surveying local percent vegetative cover using a modified Daubenmire cover classification scheme at approximately uniformaly sapced points throught each wetland. A sufficient number of points were collected during each survey to permit the spatial interpolation of percent vegetated cover (Table 3 in the text).

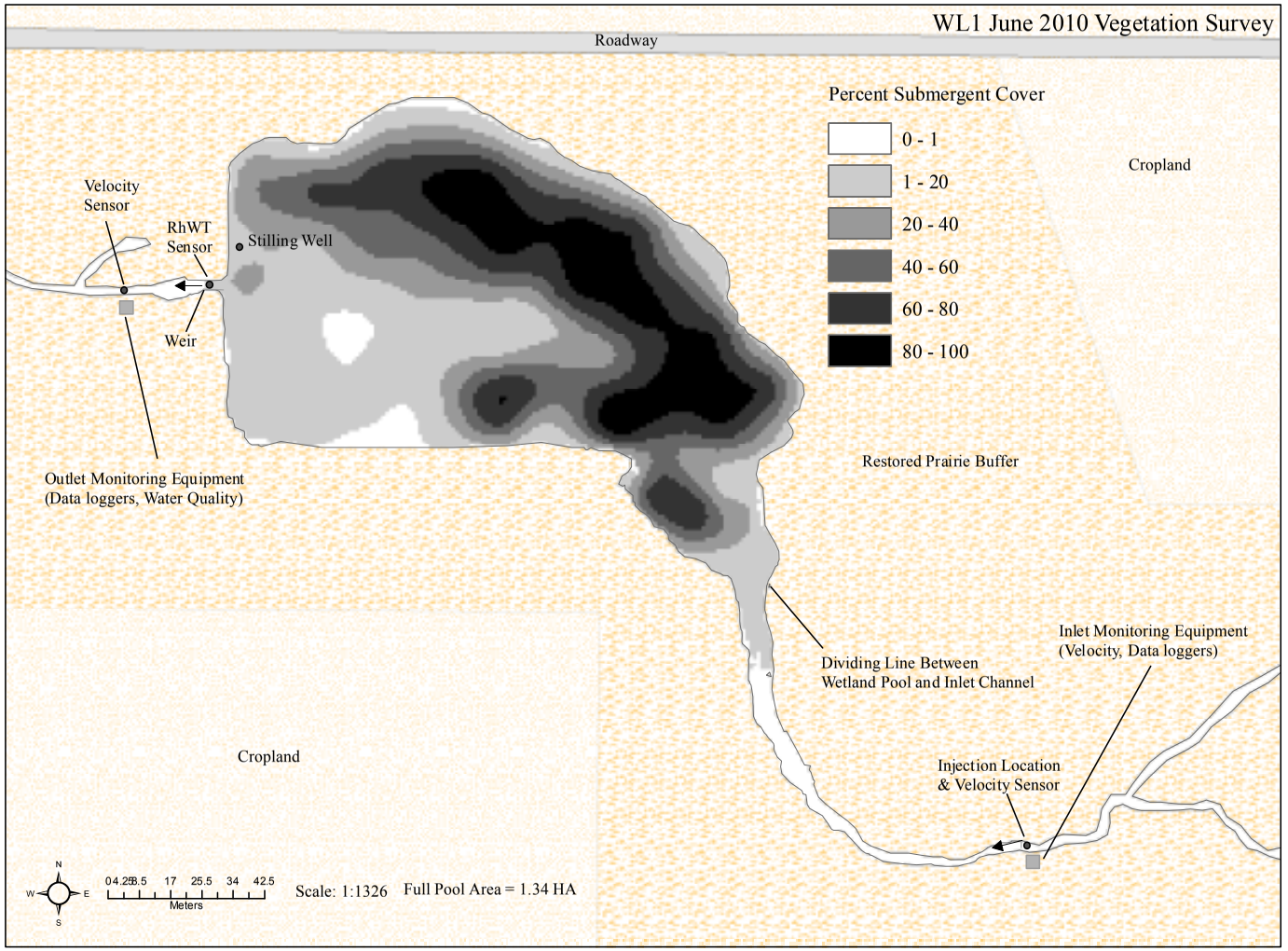

Figure 1B. Map of spatially interpolated percent vegetative cover values for the June, 2010 vegetation survey on WL1.

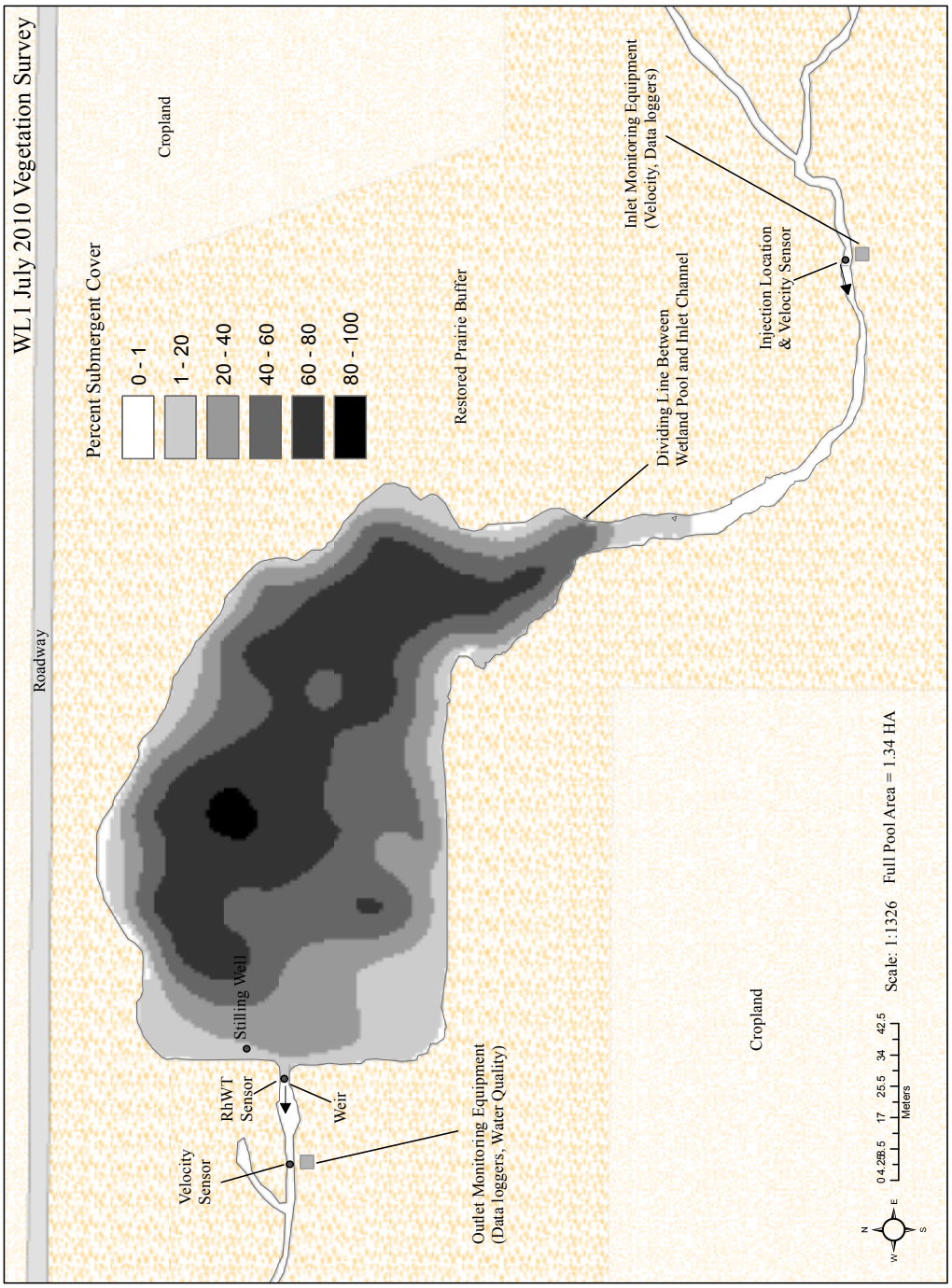

Figure 2B. Map of spatially interpolated percent vegetative cover values for the July, 2010 vegetation survey on WL1.

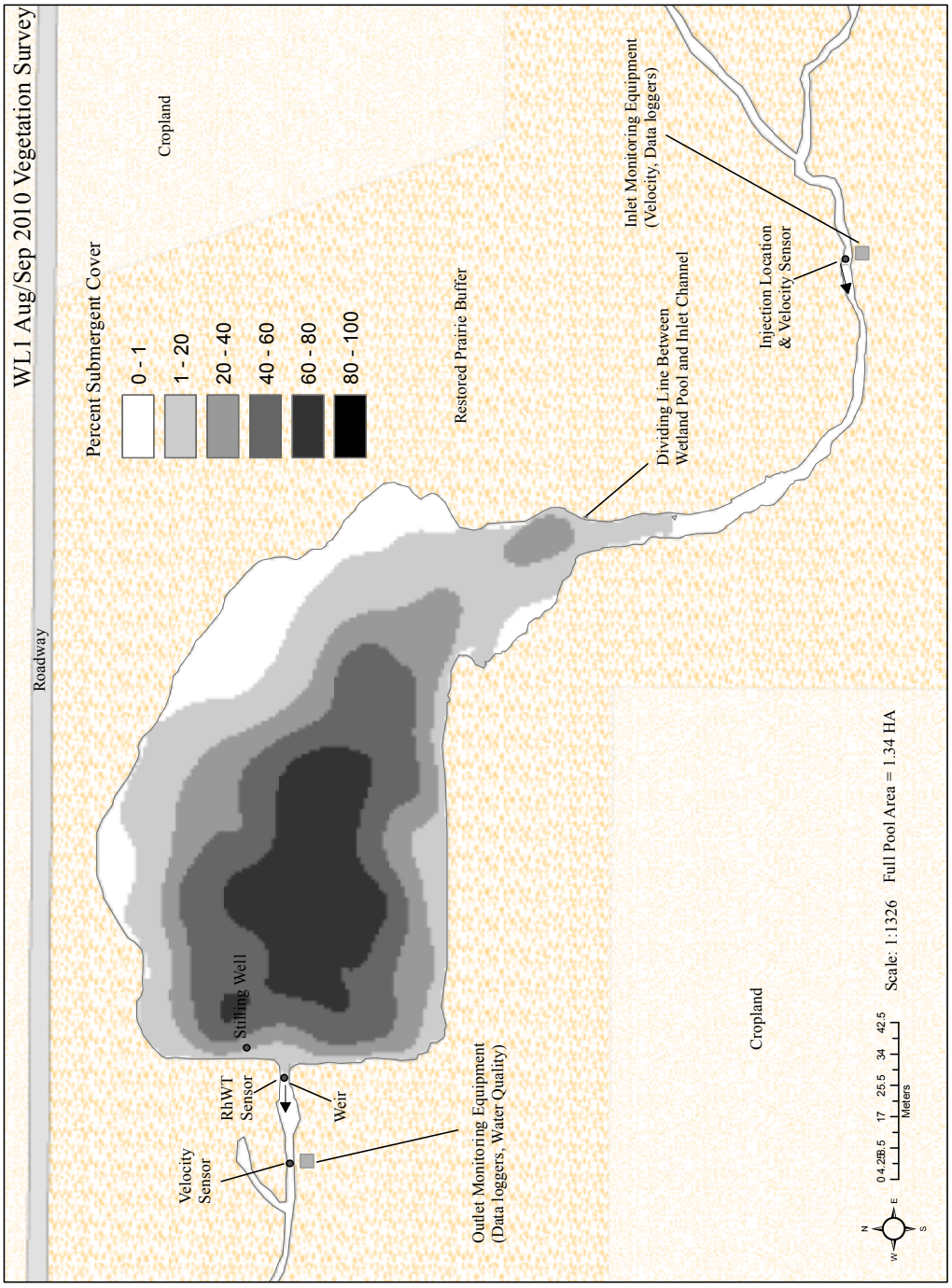

Figure 3B. Map of spatially interpolated percent vegetative cover values for the Aug. 27/Sep. 1, 2010 vegetation survey on WL1.

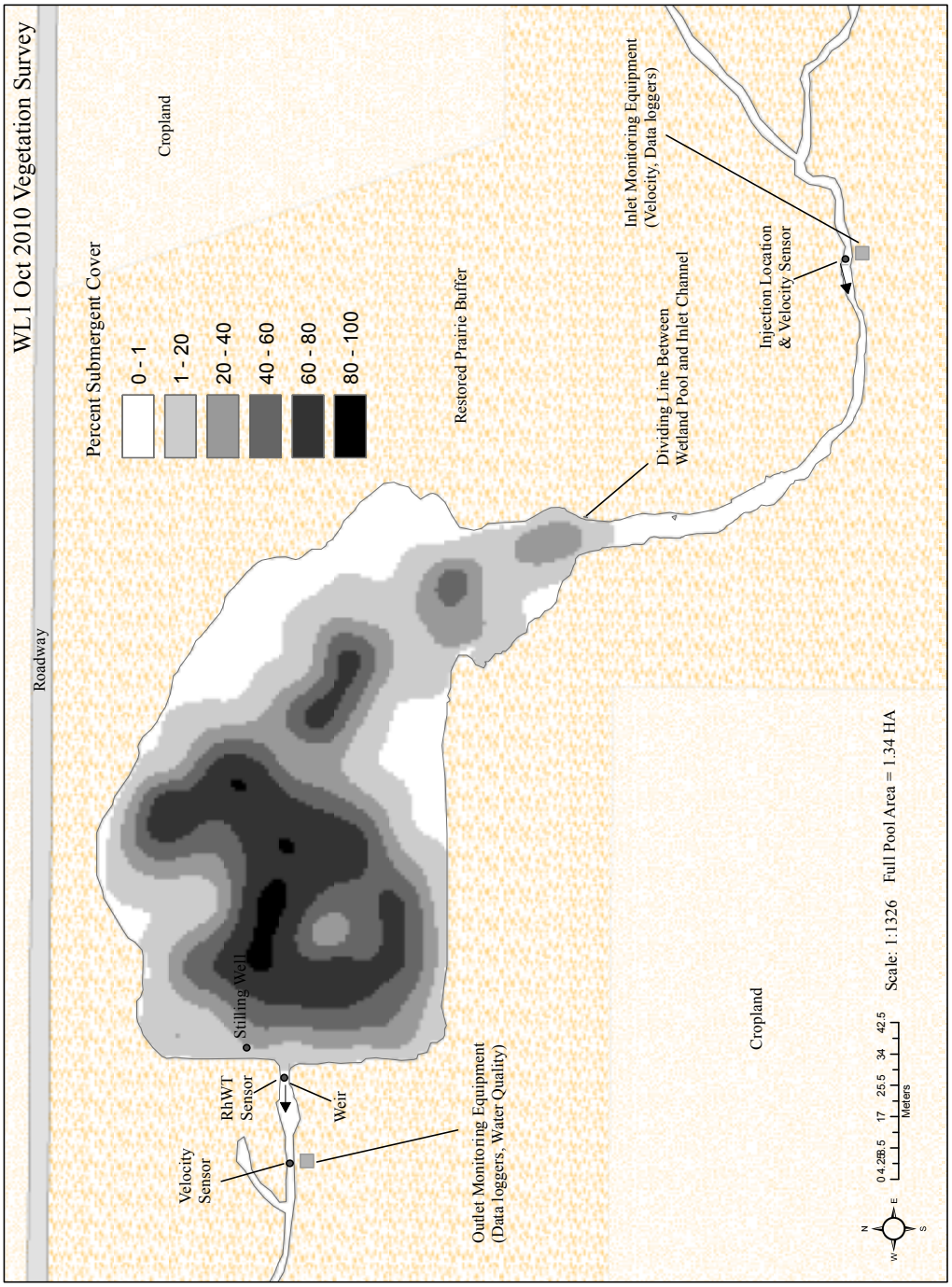

Figure 4B. Map of spatially interpolated percent vegetative cover values for the Oct. 9, 2010 vegetation survey on WL1.

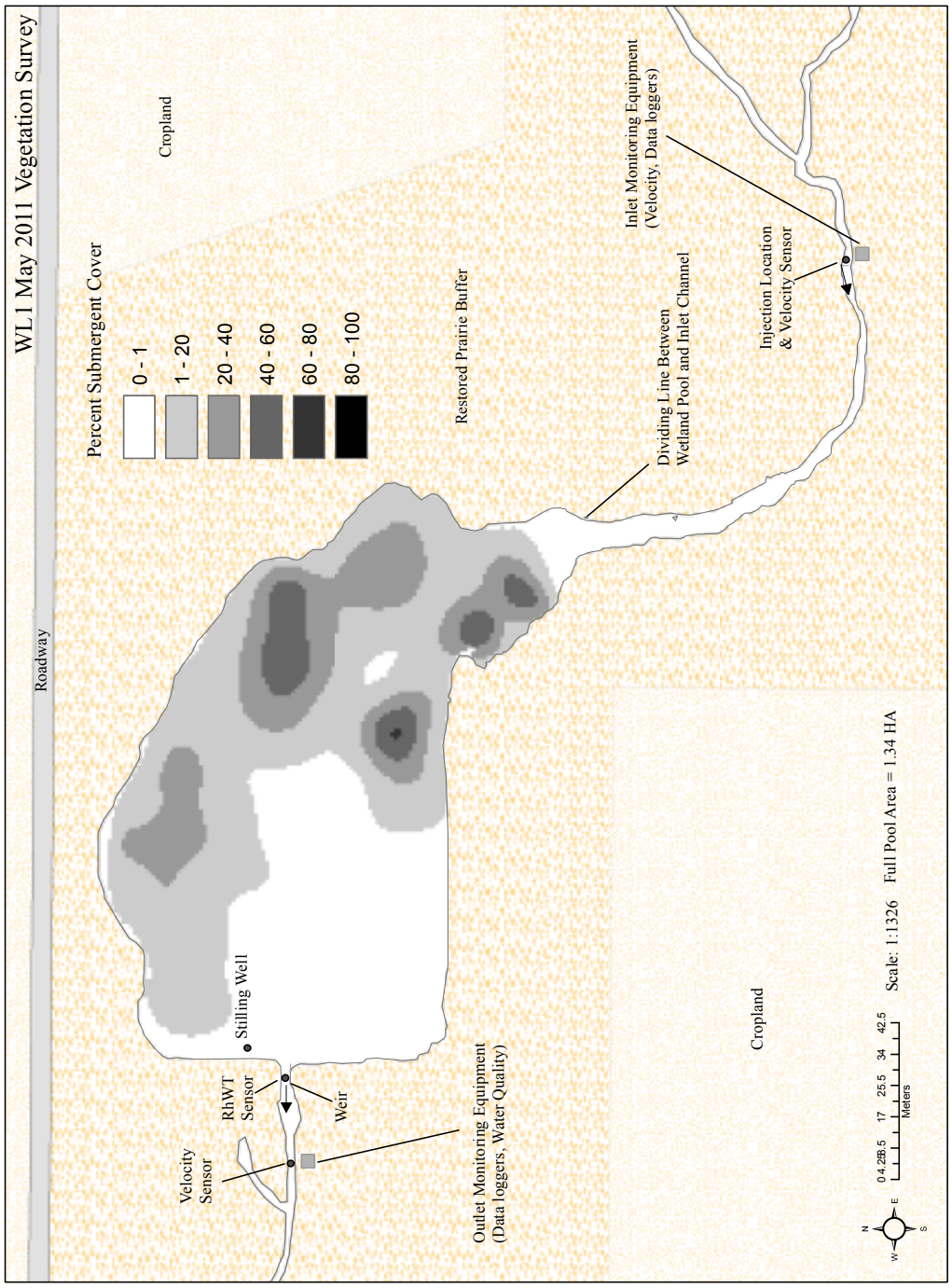

Figure 5B. Map of spatially interpolated percent vegetative cover values for the May, 2011 vegetation survey on WL1.

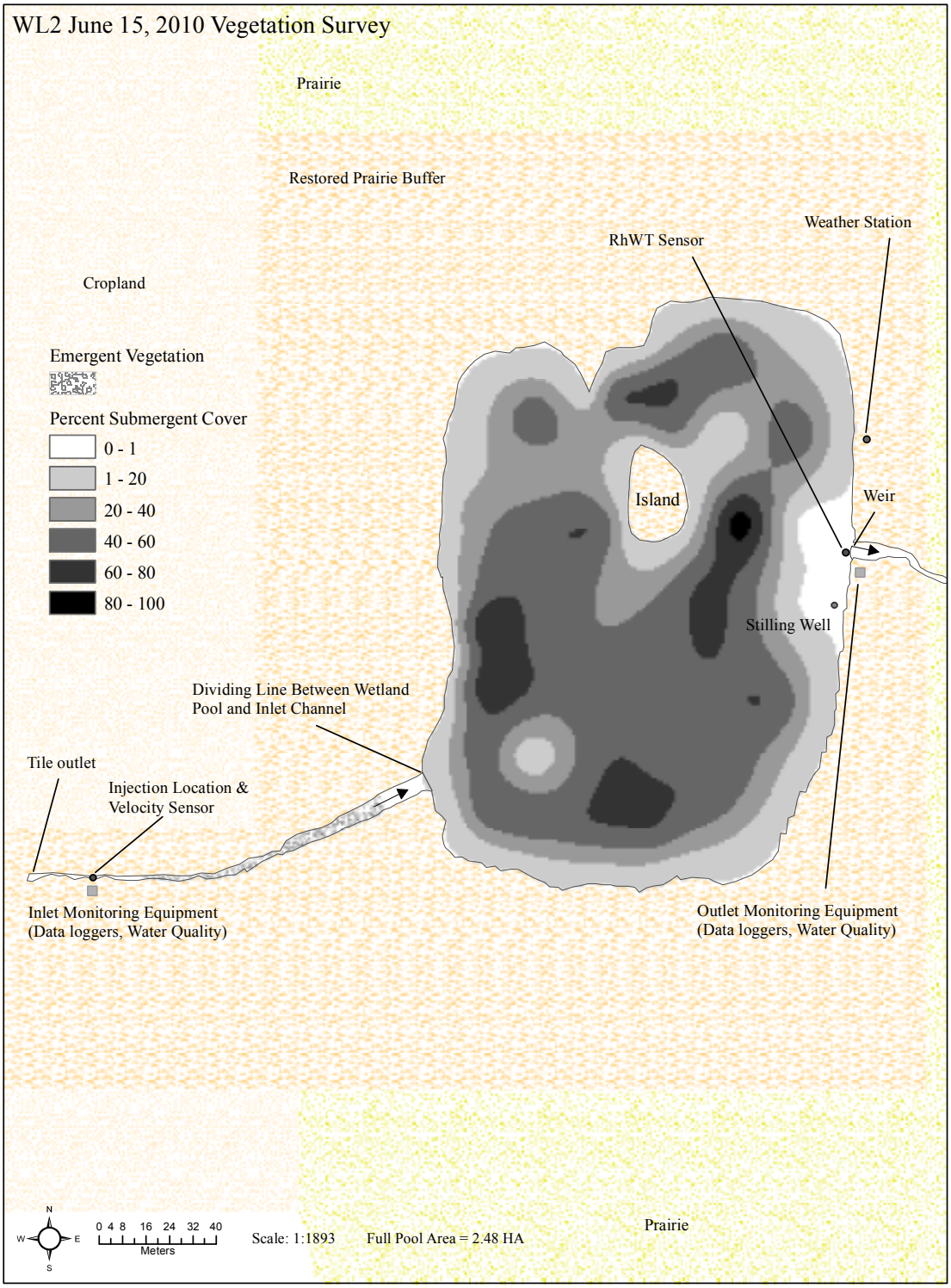

Figure 7B. Map of spatially interpolated percent vegetative cover values for the June 15, 2010 vegetation survey on WL2.

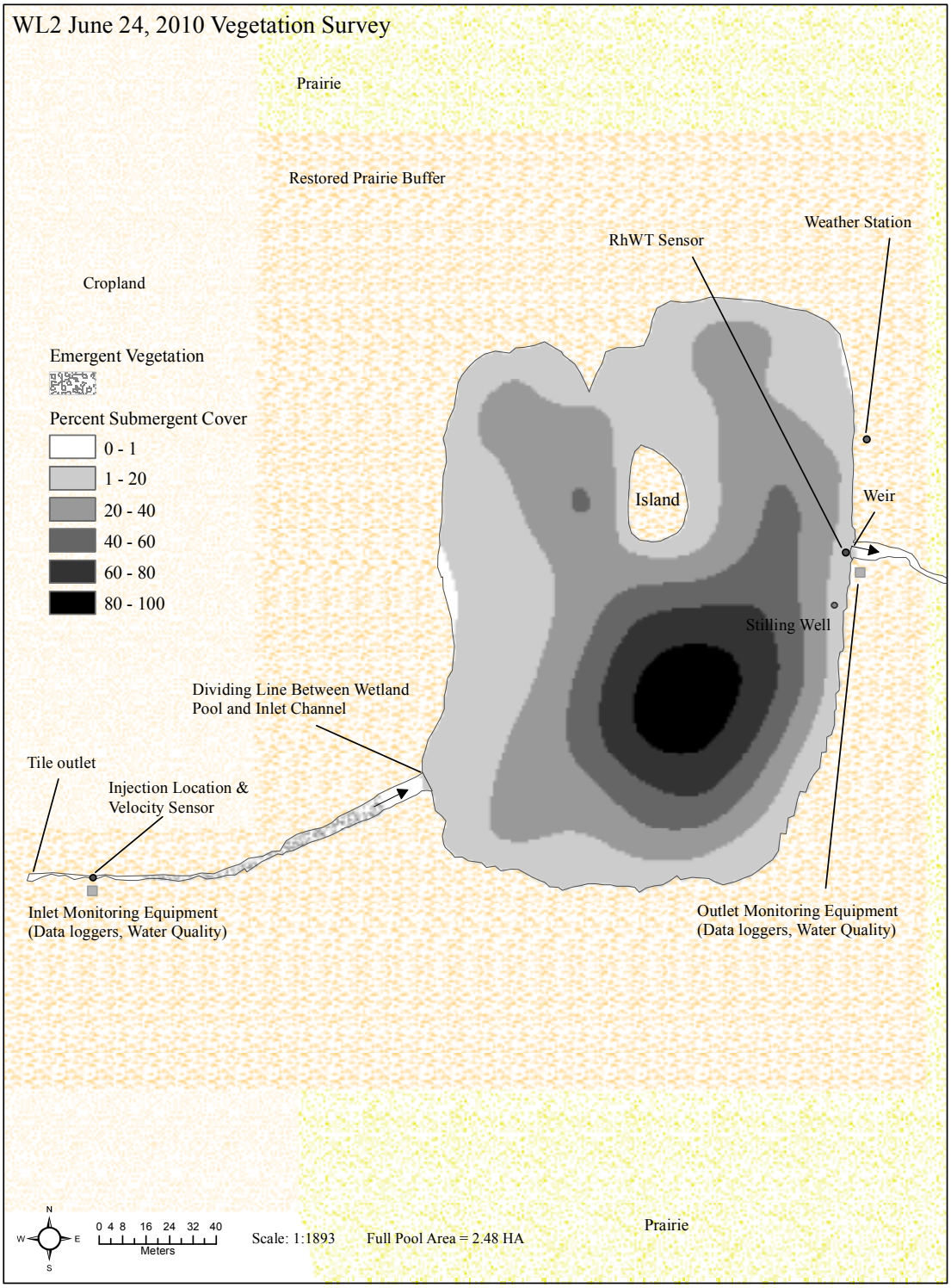

Figure 8B. Map of spatially interpolated percent vegetative cover values for the June 24, 2010 vegetation survey on WL2.

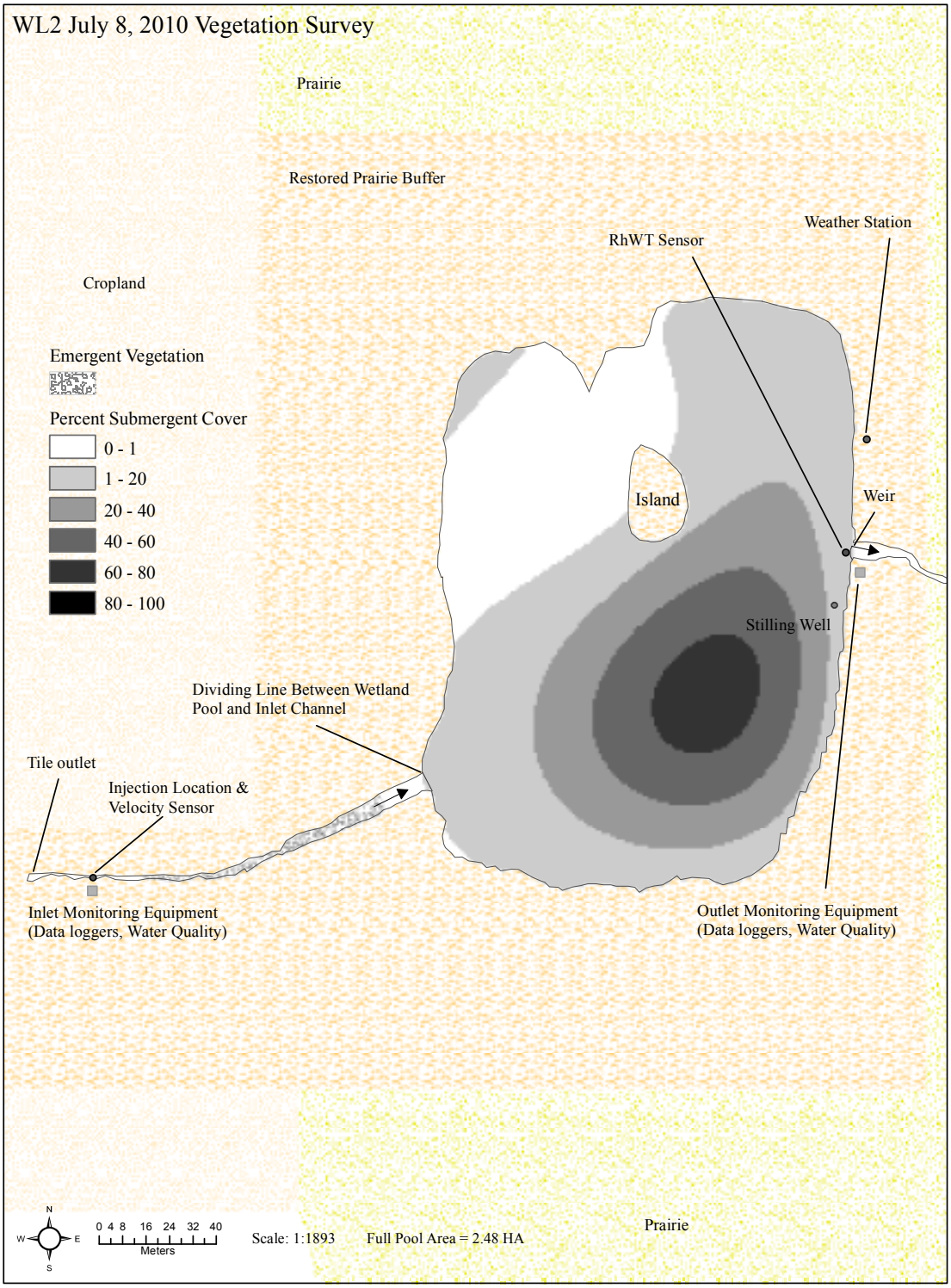

Figure 9B. Map of spatially interpolated percent vegetative cover values for the July 8, 2010 vegetation survey on WL2.

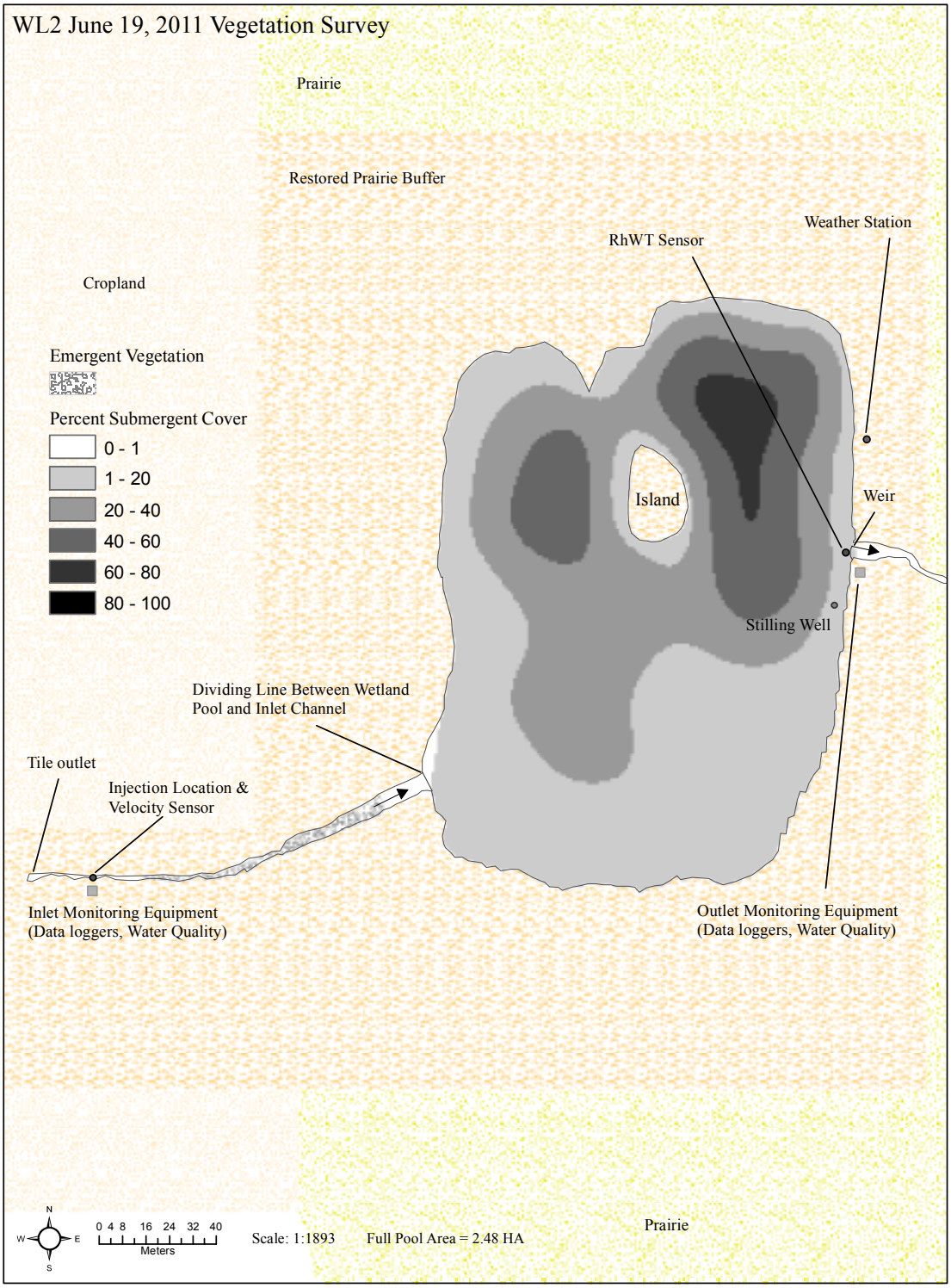

Figure 10B. Map of spatially interpolated percent vegetative cover values for the June 19, 2011 vegetation survey on WL2

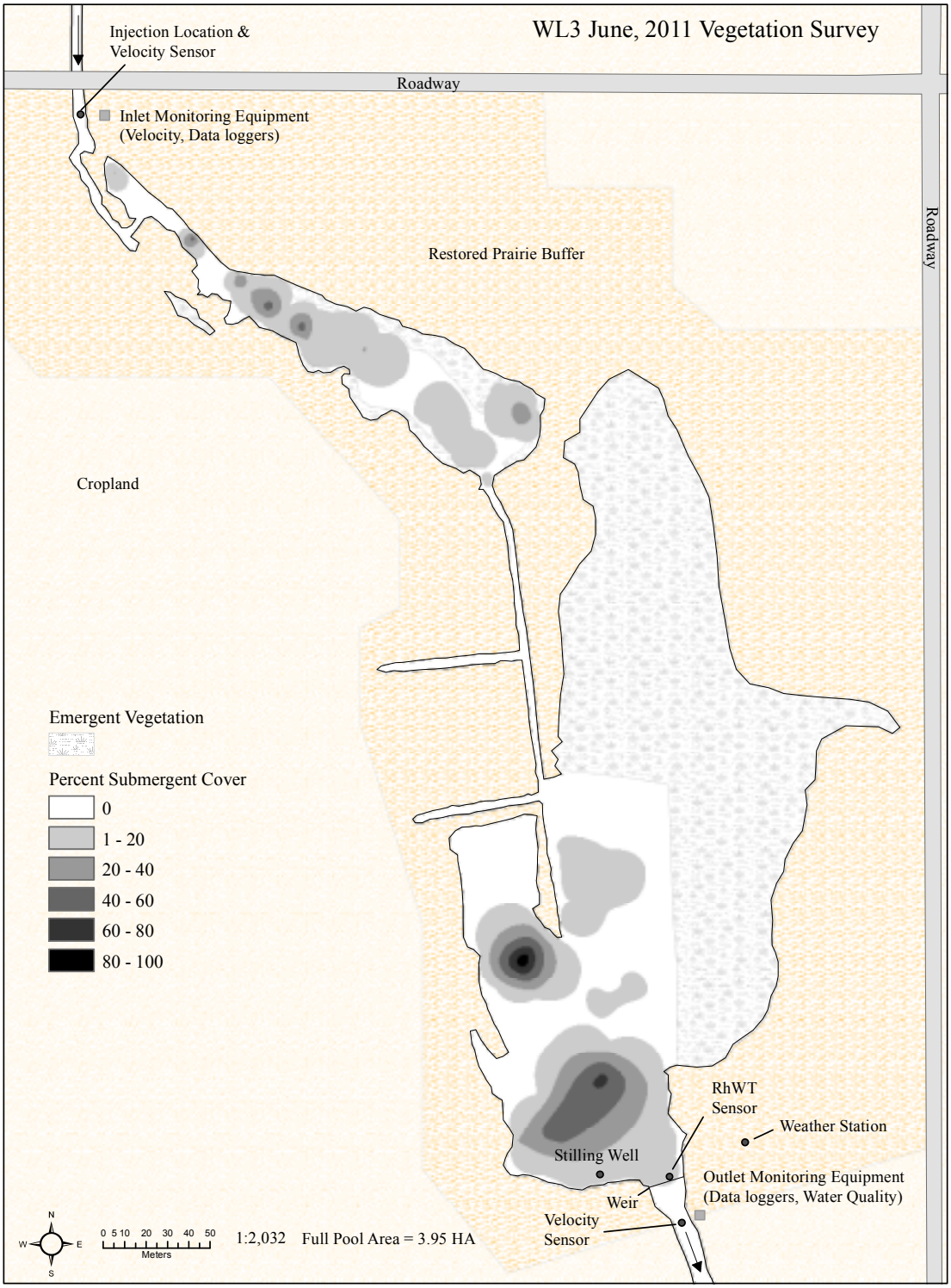

Figure 12B. Map of spatially interpolated percent vegetative cover values for the June, 2011 vegetation survey on WL3.

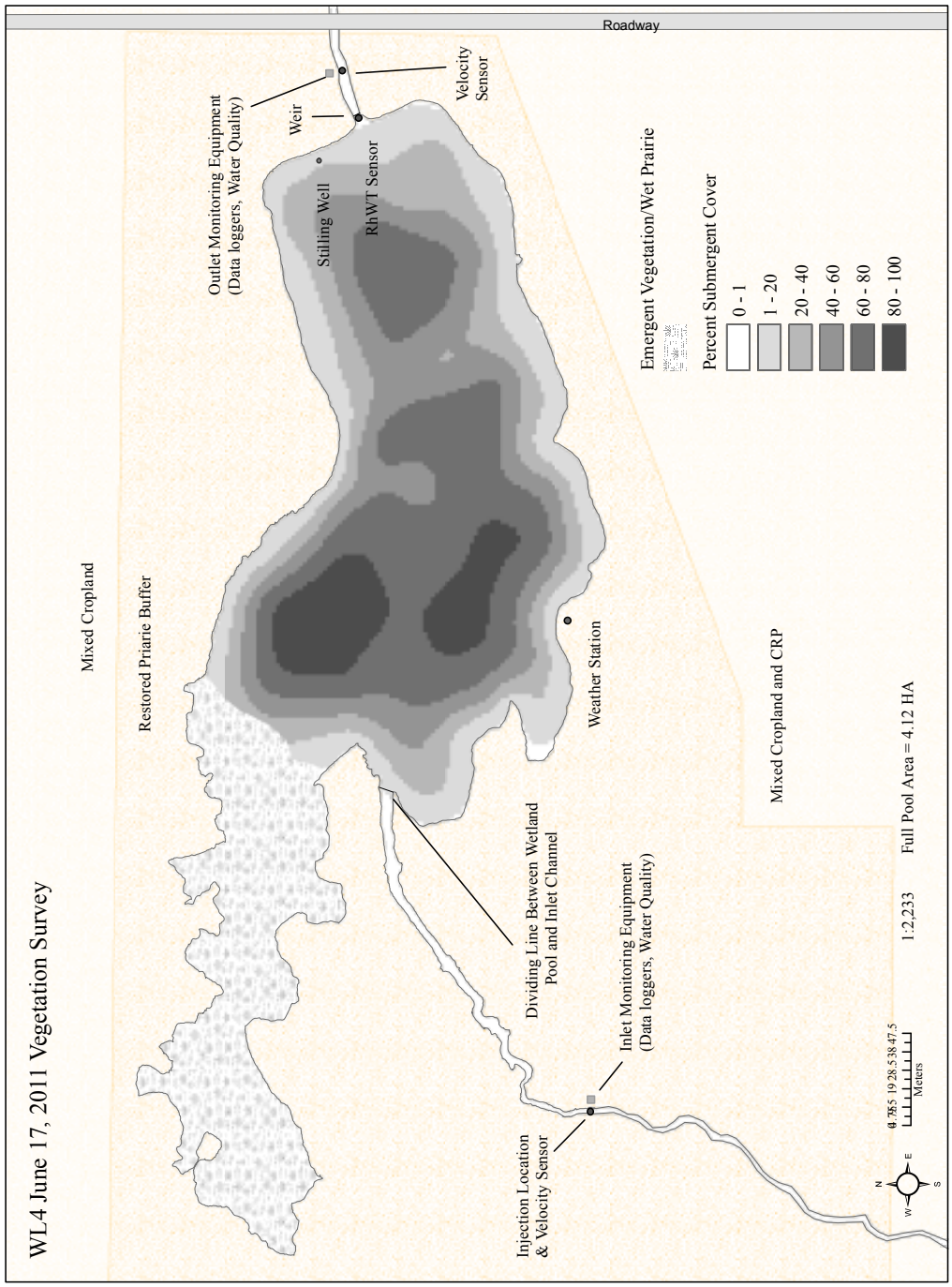

Figure 13B. Map of spatially interpolated percent vegetative cover values for the June, 2011 vegetation survey on WL3.

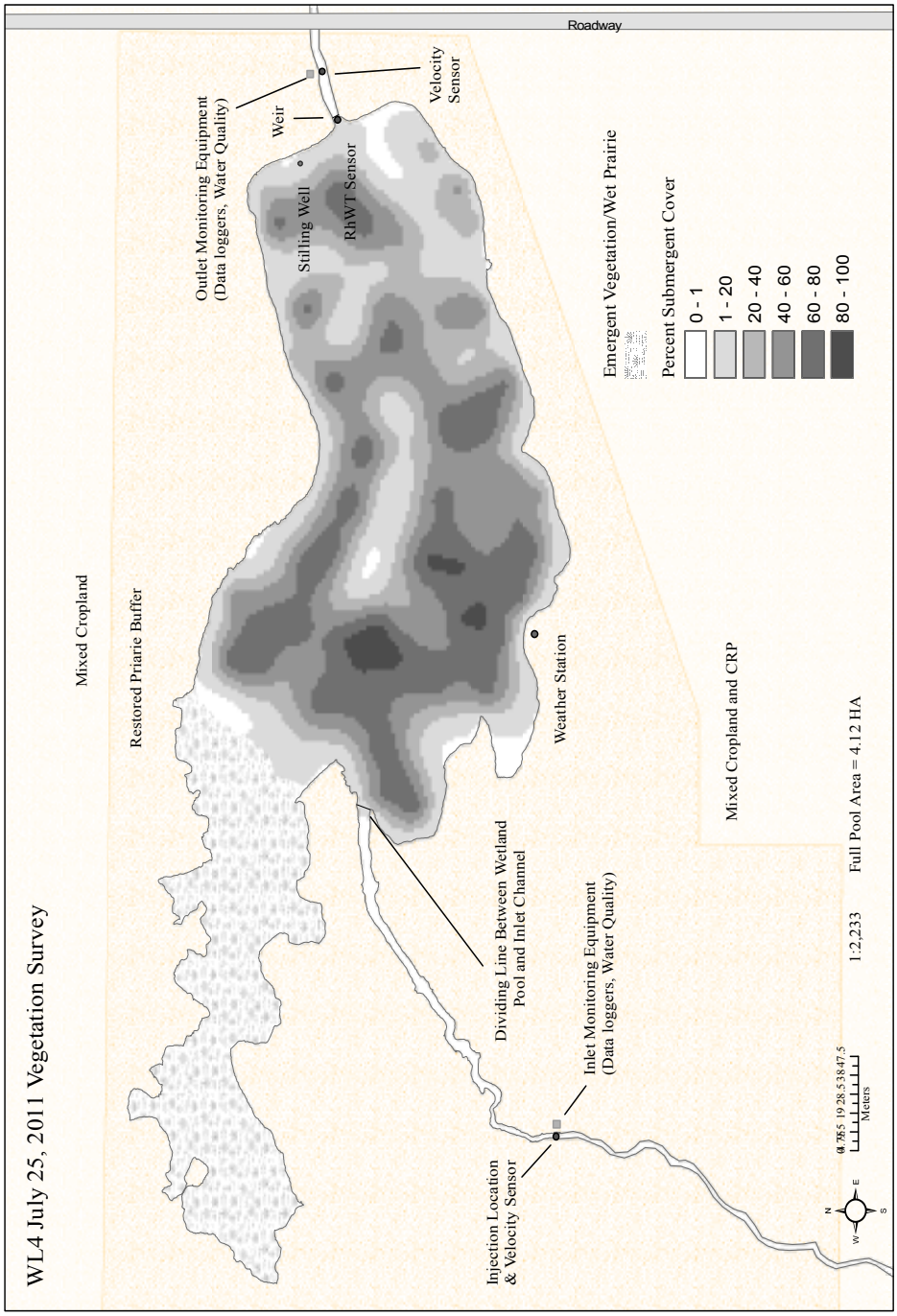

Figure 14B. Map of spatially interpolated percent vegetative cover values for the July, 2011 vegetation survey on WL3

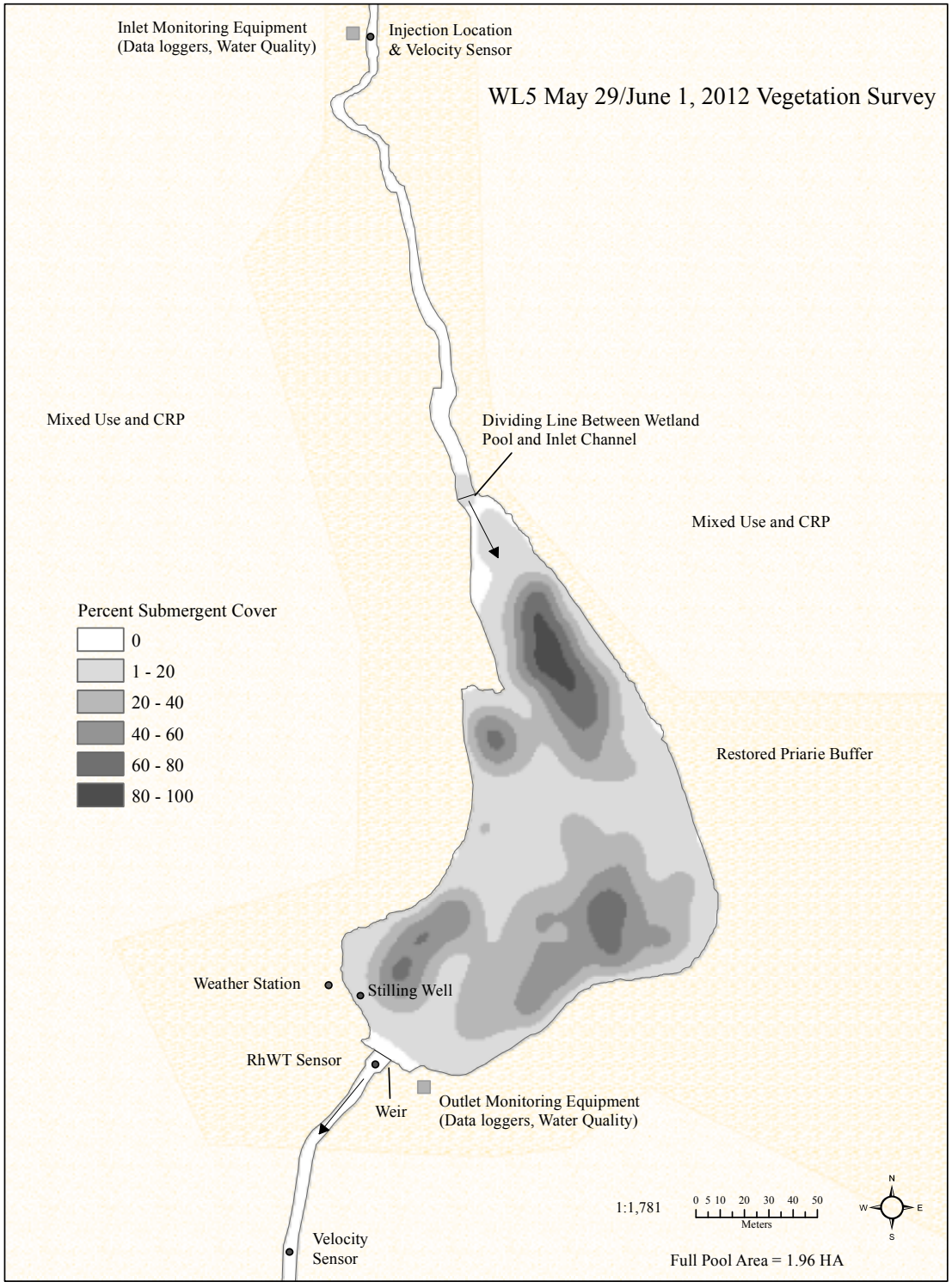

Figure 15B. Map of spatially interpolated percent vegetative cover values for the May-June, 2012 vegetation survey on WL5.

CHAPTER 3. THREE-DIMENSIONAL SIMULATION OF THE TEMPERATURE AND RESDIENCE TIME DISTRIBUTION DYNAMICS OF A CONSTRUCTED AGRICULTURAL TREATMENT WETLAND

A paper to be submitted to Water Resources Research

David I. Green and William G. Crumpton

Abstract

Multi-dimensional numerical hydrodynamic and mass transport models are becoming increasingly used in the study and design of shallow flow-through surface water treatment basins. The potential benefit of the use of such models in facilitating basin design and in understanding the environmental controls on basin hydraulics is especially relevant to the study and development of constructed wetlands for agricultural pollution control. Despite the increasing prevalence of these models in the field of surface water treatment technology, few studies have been conducted for which complementary field-scale tracer studies and system-wide continuous monitoring of state variables have been conducted to verify the veracity of this modeling approach. This study demonstrates the development, calibration, and use of the 3-dimensional Environmental Fluid Dynamics Code (EFDC) hydrodynamic and mass transport model to study the environmental controls on the residence time distribution dynamics of a 1.3 hectare constructed agricultural treatment wetland located in Central Iowa. Incorporating measured time-varying flow boundary conditions and atmospheric forcing, the EFDC model was calibrated against a set of measured wetland basin state variables including internal temperatures, basin hydraulic characteristics, and dye concentration observed at the outlet over the course of 6

independently performed field-scale hydraulic tracer studies conducted in the absence of submersed aquatic vegetation. Model calibrations indicate that EFDC reasonably reproduces observed basin internal hydraulics, temperatures, and mass transport dynamics, with mean absolute relative errors ranging from 0.02 to 16.3%. Model errors were highest for basin volumes and water depths, and lowest for temperatures, dye concentrations, and outflow discharge. The comparatively close correspondence between the observed and modeled volume-based residence time distribution (RTD) characteristics for each tracer study, as indicated by lower relative errors, further affirm the efficacy of EFDC in simulating the RTD dynamics of this system. Sensitivity analyses of the primary environmental factors of external wind shear, time-varying inflow rates, and atmospheric thermal forcing suggest that wind shear at the water surface exerts the greatest control on the development of the modeled (and by extension, observed) RTDs for this system for the environmental conditions encountered. The influence of wind was primarily realized in measures of short-circuiting. Internal temperature dynamics were also shown to maintain considerable influence on RTD characteristics, particularly bulk dispersion, during warmer operational periods. Transient flow conditions, however, were shown to have only nominal influence on most RTD characteristics for all tracer studies, save for mean and median residence times.

Introduction

For constructed agricultural wetlands, the use of multi-dimensional numerical models holds considerable promise for understanding the factors which control wetland mixing dynamics and for ensuring that a given basin will feature optimal residence time distribution (RTD) characteristics as dictated by local land-use and topographical constraints and likely atmospheric forcing conditions. Understanding the environmental controls on wetland mixing is particularly important to the ability of constructed agricultural wetlands to remove target constituents as these systems are highly exposed to ambient atmospheric conditions and often receive continually varying flow and mass loads.

The importance of wetland hydraulics has long been recognized as a critical component of constructed wetland performance. Water entering a wetland system will be partitioned into a distribution of flow paths, resulting in an RTD of both water and transported dissolved scalar quantities. Extensive study of the influence of the shape of the RTD on constituent removal performance has been conducted in the wetland and flow-through treatment basin design literature (e.g. Thiramurthi, 1974; Kadlec and Wallace, 2008). The general consensus for first-order reactions is that water which moves through a basin at a rate equal to the mean residence time and with minimal longitudinal and complete lateral and vertical mixing (the plug-flow condition) will promote optimal constituent reaction rates. Conversely, water that enters a basin and is nearly instantaneously mixed and diluted throughout (the complete mixing case) will result in the lowest mass removal rates (Kadlec, 2000).

The directed control of wetland hydraulics through proper basin design is a critical component of the constructed wetland development process. Given that constructed agricultural wetlands are becoming increasingly prevalent in farming-intensive regions to mitigate large-

scale agricultural water pollution, the importance of implementing proper wetland design prior to expending resources on construction can help to ensure that wetland systems developed in the future are built to maximize the hydraulic potential for a given site, and are built with *a priori* knowledge of the potential range of mixing conditions for a given design.

Field-scale tracer studies are the primary technique for assessing the bulk mixing behavior of a flow-through basin for a given set of environmental conditions. However, as pointed out by Walker (1996), these tests are conducted post-construction and can only give a snapshot of wetland mixing behavior under the environmental and hydraulic conditions present during the test. An alternative approach is to employ multi-dimensional numerical hydrodynamic and mass transport models to study the flow and mixing behavior of these systems. Furthermore, such models can enhance the wetland design process by permitting the simulation of wetland and flow-through basin mixing under realistic time-varying hydraulic and environmental conditions. Additionally, a numerical model reasonably calibrated to an observed field-scale tracer study can further be used to test the relative importance of external environmental forcing on mixing processes in a manner similar to the techniques used by many researchers, some of which are subsequently mentioned.

Recently, efforts have been made to investigate wetland and flow-through treatment basin mixing and constituent reduction processes by utilizing computationally efficient multi-dimensional numerical flow and mixing models. Martinez and Wise (2003) used the one-dimensional transport with inflow and storage model (OTIS; USGS) to evaluate wetland mixing patterns for a set of treatment cells in Central Florida. Likewise, Keefe et al. (2010) used this same model to assess the influence of wetland vegetation and hummocks on bulk mixing and short-circuiting behavior. Walker (1996) used a 2-dimensional, vertically averaged model to

evaluate the flow patterns and RTD characteristics of a storm water treatment wetland located in Adelaide, Australia. Jenkins and Greenway (2004) utilized a general numerical 2D mixing model to simulate the effects of fringing emergent vegetation on RTD characteristics in a set of hypothetical wetlands. More recently, Min and Wise (2009) employed a 2D numerical model (Mike 21; DHI, Delft, Netherlands) to evaluate the role of emergent vegetation and basin bathymetry on RTD characteristics for a large agricultural treatment wetland in Orlando Florida, USA. Persson (2000a) also employed the Mike 21 model to assess the effects of basin bathymetric design configurations on RTD features for a set of hypothetical flow-through basins; with particular emphasis on short-circuiting. Bardot-Nico et al. (2009) used the 3-dimensional COHERNS model to study the effects of wind speed and direction on the velocity, tracer, and temperature distributions of a shallow wastewater treatment pond. Bentzen et al. (2008) utilized a 3-dimensionsal numerical model (Mike 3 DHI, Delft, NL) to simulate the effects of wind forcing on basin-scale mixing and hydraulic transport processes in a small highway detention ponds. In general 2 and 3D modeling is becoming more common in the area of wetland hydrodynamics, and is emerging as an important tool for understanding and simulating the mass transport and mixing dynamics of shallow flow-through basins.

However, despite the comparatively large number of studies summarizing numerical simulations of hypothetical flow-through basins, few studies have been conducted in which numerical flow and mixing models are calibrated against field-scale tracer studies conducted under ambient environmental conditions. Even fewer studies (a notable exception is Bardot-Nico et al., 2009) have reported on the use of calibrated models to test the relative influence of some of the primary environmental controls on mixing in these types of basins, notably temperature stratification. Despite the increasing number of studies that have focused on shallow flow-

through basin hydrodynamics and mixing, comparatively little information in the primary literature is available regarding the environmental controls on mixing in these types of basins, and particularly, as inferred from analysis and detailed modeling of actual field-scale tracer studies.

This study documents the development and calibration of a numerical hydrodynamic and mixing model to several field-scale tracer studies conducted on a single constructed agricultural wetland that is representative of the general morphological configuration of wetlands developed under the Iowa Conservation Reserve Enhancement Program (CREP) program. Further, this work demonstrates the employment of the calibrated model in the study of the relative influences of the primary environmental effects of wind forcing, ambient hydraulic conditions, and internal temperature dynamics on the residence time distribution behavior of this system.

Methods

A total of 6 hydraulic tracer studies were conducted on a representative Iowa CREP wetland over the period November, 2009 through April, 2012 during times when submersed vegetation was absent from the system or minimal in extent (typically during the early to late Spring months of March through early June, and after Fall senescence in late October and early November). Studies were conducted as part of a larger field campaign to document temporal changes in the RTD characteristics of a set of Iowa CREP wetlands under varying hydrological, vegetative, and atmospheric conditions (Green and Crumpton, in prep.).

Each tracer study was subsequently simulated using a 3-dimensional numerical model developed with the Environmental Fluid Dynamics Code (EFDC) modeling platform. Model calibration focused on replicating observed tracer response curves, as well as wetland

temperature dynamics and some basin hydraulic characteristics for each tracer study period. Tracer studies conducted in the absence of vegetation, or for when vegetation cover was minimal, were selected for this work to simplify the modeling process, and to document and characterize the capabilities of the EFDC model during periods when hydrological and nutrient mass loads into these systems are greatest (i.e. early Spring months after the first winter thaw) - and thus when bulk basin hydraulic and mixing characteristics are of most importance to wetland nutrient mass removal performance.

Simulation accuracy was assessed using standard calibration statistics (e.g. Legates and McCabe, 1999) calculated for dye concentrations measured in the wetland outlet channel; water temperatures measured at two interior basin locations; dynamic system volumes; outflow volumetric flow rates; and water levels measured at a single location (Figure 1). Each calibrated simulation was subsequently used to assess the relative sensitivity of modeled tracer response curve characteristics to external hydraulic, wind, and temperature forcing.

Study Area

The wetland of focus in this study (herein to be referred to as WL1 following the convention of Green and Crumpton, in prep.) is a shallow 1.3 hectare surface water impoundment located in northern Story County, Iowa (Figures 1 and 2). This site was developed in 2005 as part of the Iowa CREP to intercept agricultural runoff from an approximately 500 hectare farmed tile-drained watershed. This system begins as a shallow and narrow stream channel that merges with a deeper and wider wind-exposed pool. Bulk basin morphological characteristics are summarized in Table 2. The wetland discharges through a 4 meter wide broad-crested concrete weir built into an earthen dam. Being positioned at the base of a tile-drained

watershed, WL1 is subjected to time-varying influent flow and mass-loading rates and is directly exposed to local atmospheric conditions. Furthermore, as discussed by Green and Crumpton, this site is dominated by seasonally varying submersed aquatic vegetation during late spring through late fall months (typically mid to late May through early November). Prior to and after this period of time – the period of focus of this study – the system typically operates under a non-vegetated state.

Environmental Monitoring and Field Surveys

Bathymetric Surveys and Hypsography

Bathymetric surveys were conducted on WL1 in early April of 2010 and 2011 (Table 2). Repeated surveys were performed to document the change in system bathymetry after an historic region-wide flood event in August, 2010. Each bathymetric survey entailed obtaining between 3 and 5 replicate point measurements of local water depths at $n > 400$ locations throughout the basin. Water depths were measured using a surveyor's staff (± 3.05 *cm*) following the protocol suggested by Kadlec (1994). The horizontal coordinates of each survey point were recorded using sub-meter handheld differentially corrected GPS (GeoXT, GeoXH models, Trimble Corp.; Sunnyvale, CA). Surveyed depths were corrected to full pool depths based on the water level above the crest of the outflow structure observed during each survey. Basin pool boundaries were digitized using high-resolution 2010 United States Department of Agriculture (USDA) National Agriculture Imagery Program (NAIP) imagery for the site (USDA, 2010, https://gdg.sc.egov.usda.gov/). Surveyed depths were merged with local Light Detection and Ranging (LiDAR) point data vertically offset by the estimated pool boundary elevation (Iowa LiDAR Mapping Project; http://www.geotree.uni.edu/lidar/). A continuous 1 m^2 resolution pool

depth surface grid, relative to the basin full pool elevation, was derived by kriging of the merged point datasets. Volume-depth and volume-area curves were developed for the wetland by integrating over the basin volumes and planar areas below and up to one-half meter above the full-pool reference elevation. Each depth-volume and depth-area curve was subsequently fitted to an appropriate n^{th}-order polynomial (Table 2) to permit estimation of time-varying system volumes and planar basin wetted areas from measured water elevations above the base of the weir. Time-varying volumes were subsequently used in estimating instantaneous system volumes, hydraulic residence times, and volumetric inflow rates. Spatial interpolation was conducted using the GSTAT package in the R statistical computing environment (Pebesma, 2004).

The aforementioned flood event of August, 2010 resulted in an approximately 10% reduction in the wetland full pool volume and mean depth relative to the April 2010 survey. The cause of this decrease is likely from transport and deposition of large quantities of coarse sediments into the wetland basin from upland and upstream sources.

Meteorological Monitoring

Atmospheric data including wind speed ($v_{w(10);}$ m s^{-1}) and direction, hourly rainfall depths (m day^{-1}), air temperature (T_a; °C), percent relative humidity (R_h), and incident solar radiation (E_s; W m^{-2}) sampled at 1-hour intervals was acquired from the Gilbert, Iowa station (site number A130219) of the Iowa State University Agricultural Climate Monitoring Network (ISU-AG; https://mesonet.agron.iastate.edu/) located at a distance of approximately 4 linear miles from the wetland. Atmospheric pressure data was obtained from the St. Cecilia, Ames Iowa SchoolNet Weather Monitoring Network station (site number SAMI4).

Measured wind speeds were standardized to a height of 10 meters above the local water surface ($v_{w(10)}$) using a power-law vertical wind speed profile with a constant exponent of 1/7, suitable for lightly vegetated regions (Irwin, 1967):

$$v_{w(10)} = v_{w(r)} \left(\frac{10}{e_r} \right)^{1/7} \tag{3.1}$$

where e_r is the reference elevation of the anemometer (m).

Hydrological Monitoring

Mean water velocity and depth measurements were taken at five minute intervals using submerged area velocity (SAV) meters and stage recorders (Solinst, Ontario CA) in the stream channel below the wetland outflow structure. Stream cross-section profiles were measured to develop cross-sectional wetted area versus depth relationships at the inlet and directly downstream of the wetland control structure. Discharge was calibrated on the basis of discharge measurements taken at multiple water depths at each measurement site. Manual discharge measurements were determined using the mid-section method (Buchanan and Somers, 1969). Manual velocity measurements were taken with a hand held side-looking 2-dimensional Sontek Flow-tracker Doppler velocimeter (Sontek, San Diego CA) using the 0.6 depth method (Buchanan and Somers, 1969). Discharge measurements were used to develop stage-discharge equations and to calibrate the discharge coefficients for the wetland outflow structure discharge equation and SAV-based discharge measurements. Because of a lack of instrumentation in the inlet channel, time-varying inflow rates were estimated using measured volumetric outflow rates and the reverse level-pool routing procedure described by Zoppou (1999).

Dynamic wetland pool volumes for each tracer study were estimated using the regression equations developed from the aforementioned hypsographic curves (Table 2). The local dynamic water depth was monitored at 5-minute intervals at a single stilling well positioned near the basin outlet (as noted in Figures 1 and 2) using a Solinst pressure transducer (Solinst; Ontario, Canada). Dynamic water surface elevations above the crest of the outlet weir were estimated by off-setting the high-resolution measured stilling well water depths by the time-average of periodic manual measurements of water depth on the weir crest.

Field-scale Tracer Experiments

Each tracer study entailed injecting a known mass of Rhodamine WT (RWT; 20% solution; Organic Dye Stuff Corporation, Providence RI) across the wetland inlet channel (as shown in Figures 1 and 2). To minimize potential initial density effects the dye was diluted with approximately 5 gallons of stream water prior to injection. Dye concentrations were measured at the outflow every 5 minutes starting at least one-half hour prior to tracer injection using a Turner Designs Cyclops 7 fluorometer coupled to a Turner Designs DataBank data logger (Turner Designs, Sunnyvale, California). The fluorometer was secured in a custom-made perforated screened grey cylindrical PVC housing designed to minimize sunlight exposure and to prevent measurement interference by floating detritus and algae. The optical sensor was positioned at approximately one-half of the local water column depth at the monitoring location. Tracer background concentrations were measured at the monitoring location for 1 to 2 hours before the initial arrival of tracer at the outlet. The fluorometers were checked for measurement drift prior to each deployment and re-calibrated against pre-made standards as needed. The time duration,

mass injected, and average flow and atmospheric conditions encountered for each tracer study are listed in Table 1.

Tracer response curve data conditioning entailed correcting for background fluorescence, removal of extraneous concentration measurements (identified as sensor drop-outs and sudden single point spikes), and accounting for temperature effects on concentration readings. The effects of water temperature on RhWT fluorescence was corrected using (Smart and Laidlaw, 1977):

$$C_c = C_o \exp\left(0.027\left(T_o - 20\right)\right) \tag{3.2}$$

where 0.027 is the temperature correction coefficient specific to RhWT, and are C_o and T_o the observed tracer concentration ($\mu g\ L^{-1}$) and water temperature (°C), respectively.

The studies WL1_1 and WL1_11 were terminated before all of the dye had exited the system. Tails of the tracer response curves for these studies were extrapolated to measured background concentrations using an exponential decay profile fitted to the measured descending limb of each respective curve (e.g. Kadlec and Wallace, 2008).

Numerical Model Development Calibration and Analysis

The Environmental Fluid Dynamics Code is a 3-dimensional hydraulic and mass transport model designed specifically to simulate shallow surface water hydrodynamics, mixing, and water quality processes (Hamrick, 1992; Hamrick and Wu, 1997). EFDC has been used extensively in lake (e.g. Jin et al., 2000; Jin et al., 2002; Wu and Xu, 2011), reservoir (e.g. Li et al., 2010; Zhang et al., 2013), riverine (e.g. Ji et al., 2002; Huang et al., 2008; Franceshini and Tsai, 2010), and coastal and estuarine (e.g. Ji et al., 2001; Wool et al., 2003) hydrodynamic and biogeochemical modeling studies. However, this modeling platform has not, to our knowledge,

been used for analysis of mixing and temperature dynamics of extremely shallow (< 3 m) flow-through surface water basins such as constructed wetlands. EFDC possesses the capability of simulating eutrophication processes through a linkage to the HEM3D water quality model (Hamrick and Wu, 1997) and temperature dynamics through linkage to the 2-dimensional CE-QUAL-W2 heat exchange model (Cole and Wells, 2005; He et al., 2011). EFDC has also been shown to reasonably simulate vegetated flows in wetland ecosystems (e.g. Jin and Ji, 2013). Thus, this modeling platform has the potential to reasonably simulate the unique flow and biogeochemical dynamics observed in shallow treatment wetland basins such as those constructed under the Iowa CREP.

Governing Equations

EFDC solves the 3-dimensional turbulence-averaged equations of momentum (i.e. the 3-D shallow water equations) using either a Cartesian or orthogonal curvilinear grid system in the horizontal, with a non-dimensional sigma-stretch coordinate system in the vertical. The solution is solved over a vertical sigma-stretched and horizontal orthogonal curvilinear grid using second-order accurate spatial finite differences and a second-order accurate three-time level finite difference scheme for time integration. The 3-dimensional continuity and momentum equations in curvilinear coordinates solved in EFDC are defined as (Hamrick and Wu, 1997; Ji, 2008):

$$\frac{\partial(m_x m_y H)}{\partial t}+\frac{\partial\left(m_y H u\right)}{\partial x}+\frac{\partial\left(m_x H v\right)}{\partial y}+\frac{\partial\left(m_x m_y w\right)}{\partial z}=Q_H \tag{3.3}$$

$$\begin{aligned}&\frac{\partial\left(m_x m_y H u\right)}{\partial t}+\frac{\partial\left(m_y H u u\right)}{\partial x}+\frac{\partial\left(m_x H u v\right)}{\partial y}+\frac{\partial\left(m_x m_y u w\right)}{\partial \sigma}-\left(m_x m_y f_e\right) H v\\&=-m_y H \frac{\partial\left(p+g\eta\right)}{\partial x}-m_y p \frac{\partial p}{\partial z}\left(\frac{\partial h}{\partial x}-z\frac{\partial H}{\partial x}\right)+\frac{\partial}{\partial z}\left(m_x m_y \frac{A_v}{H}\frac{\partial u}{\partial z}\right)+Q_u\end{aligned} \tag{3.4}$$

$$\frac{\partial\left(m_x m_y Hv\right)}{\partial t}+\frac{\partial\left(m_y Huv\right)}{\partial x}+\frac{\partial\left(m_x Hvv\right)}{\partial y}+\frac{\partial\left(m_x m_y vw\right)}{\partial z}-m_x m_y f_e Hu$$
$$=-m_y H\frac{\partial\left(p+g\eta\right)}{\partial y}-m_x p\frac{\partial p}{\partial z}\left(\frac{\partial h}{\partial y}-z\frac{\partial H}{\partial y}\right)+m_x m_y\frac{\partial}{\partial z}\left(\frac{A_v}{H}\frac{\partial v}{\partial z}\right)+Q_v \tag{3.5}$$

$$\frac{\partial p}{\partial z}=-gH\frac{\left(\rho_w-\rho_0\right)}{\rho_0}=-gHb \tag{3.6}$$

$$w=w^*-z\left(\frac{\partial\eta}{\partial t}+\frac{u}{m_x}\frac{\partial\eta}{\partial x}+\frac{v}{m_y}\frac{\partial\eta}{\partial y}\right)+\left(1-z\right)\left(\frac{u}{m_x}\frac{\partial h}{\partial x}+\frac{v}{m_y}\frac{\partial h}{\partial y}\right) \tag{3.7}$$

$$m_x m_y f_e=m_x m_y f-u\partial_y m_x+v\partial_x m_y \tag{3.8}$$

where H is the free water surface elevation (L); u, v, w are the horizontal, lateral, and vertical velocity components (L T^{-1}); x and y are the horizontal Cartesian coordinates (L) and z the stretched vertical sigma coordinate (L); A_v is the vertical turbulent (eddy) viscosity (L^2 T^{-1}). The coefficients m_x and m_y are used to transform the governing equations into their Cartesian equivalents (Ji, 2008). The Q_u and Q_v terms in Eqns. 3.4 and 3.5 represent sources and sinks of horizontal and vertical turbulent diffusion, respectively. The term Q_H in the 3-dimensional continuity equation (Eq. 3.7) represents volumetric sources and sinks of water including precipitation, evaporation, groundwater fluxes, inflows, outflows, and other internal point and non-point additions and withdrawals. Coriolis acceleration, f_e, is incorporated into the x and y momentum equations, and is determined by the Coriolis parameter, f (9.761×10^{-5} s^{-1} for this site), and local accelerations induced by grid curvature (Eq. 3.8). Equation 3.6 is the hydrostatic approximation, with b representing buoyancy, defined as the normalized deviation of water density from a standard reference value (Ji, 2008). Equation 3.7 relates the vertical velocity in the curvilinear coordinate system to the physical velocity, w^* (Ji, 2008).

Mass and Heat Transport

EFDC couples the continuity and momentum equations to a generic 3-dimensional transport equation for dissolved conservative and reactive scalar substances (Hamrick, 1992; Hamrick and Wu, 1997; Ji, 2008):

$$\frac{\partial\left(m_x m_y HC\right)}{\partial t}+\frac{\partial\left(m_y uHC\right)}{\partial x}+\frac{\partial\left(m_y vHC\right)}{\partial y}\frac{\partial\left(m_x m_y wC\right)}{\partial z} = m_x m_y \frac{\partial}{\partial z}\left(H\frac{\partial\left(A_b C\right)}{\partial z}\right)+m_x m_y HR_c+Q_c \tag{3.9}$$

where C is the spatially and temporally varying constituent concentration; A_b is the vertical turbulent mass diffusivity ($m^2\ s^{-1}$); R_c is the lumped constituent reactive source and sink parameter; and Q_c represents additional constituent volumetric sources and sinks, and the effects of horizontal turbulent diffusion of mass transport (discussed further in a proceeding section).

The equation governing 3-dimensional heat transport is defined as (Hamrick, 1992; Hamrick and Wu, 1997; Ji, 2008):

$$\frac{\partial\left(m_x m_y HT\right)}{\partial t}+\frac{\partial\left(m_y HuT\right)}{\partial x}+\frac{\partial\left(m_x HvT\right)}{\partial y}+\frac{\partial\left(m_x m_y HwT\right)}{\partial z} = \frac{\partial}{\partial z}\left(\frac{A_b}{H}\frac{\partial T}{\partial z}\right)+HR_T \tag{3.10}$$

where T is the time and space-varying temperature; A_b is the vertical turbulent mass diffusion coefficient; and R_T is the input of heat from solar radiation (Ji, 2008). The heat transport equation implemented in EFDC is coupled to the CE-QUAL-W2 equilibrium temperature model to define atmospheric and sediment heat fluxes.

The CE-QUAL-W2 equilibrium temperature model incorporates surface heat exchange using a water surface-atmosphere heat balance (Cole and Wells, 2005):

$$J_n = J_s + J_a + J_e + J_c - \left(J_{sr} + J_{ar} + J_{br}\right) \tag{3.11}$$

where J_n is the net rate of heat exchange across the water surface; J_s is the incident short wave solar radiation; J_a is the incident long wave radiation; J_{sr} and J_{ar} are the reflected short and long wave radiation from the water surface, respectively; J_e is the evaporative heat loss; and J_c is the surface heat conduction. All terms in Eqn. 3.11 are expressed in W m^{-2}.

The short wave solar radiation is provided from measured solar radiation time-series (see previous section on atmospheric monitoring). Long wave radiation is computed from air temperature, total incident solar radiation, and vapor pressure using Brunt's formula (Koberg, 1964). Back radiation from the water surface is determined from (Cole and Wells, 2005):

$$J_{br} = \varepsilon\varphi\left(T_w + 273.15\right) \tag{3.12}$$

where ε is the emissivity of water (0.97), φ is the Stephan-Boltzmann constant (5.67×10^{-8} W m^{-2} K^{-4}), and T_w is the water surface temperature (degrees Celsius). The evaporative heat loss is internally computed as a function of wind speed standardized to 2 *m* above the water surface:

$$J_e = f(v_{w(2)})(e_{sat} - e_a) \tag{3.13}$$

where e_{sat} and e_a are the saturation and air vapor pressures (millibar), respectively. The evaporative wind speed function (W m^{-2} mb^{-1}) is defined as (Cole and Wells, 2005):

$$f(v_{w(2)}) = 9.2 + 0.46 v_{w(2)}^{\ 2} \tag{3.14}$$

The wind speed standardized to a height of 10 *m* is internally scaled to an approximate speed at 2 m by assuming a logarithmic profile with variable roughness heights. Surface heat convection is computed as:

$$J_c = \omega f\left(v_{w(2)}\right)\left(T_w - T_a\right) \tag{3.15}$$

where ω is Bowen's coefficient (0.47 mmHg $^{o}C^{-1}$), and T_a is the dry air temperature (^{o}C).

Direct evaporation from the water surface is incorporated into the model water balance as a function of wind speed, and is computed as:

$$E = f\left(v_{w(2)}\right)\left(p_{v(w)} - p_{v(a)}\right) \tag{3.16}$$

where $p_{v(w)}$ and $p_{v(a)}$ are the saturation vapor pressure at the water surface and air (mb), respectively. The attenuation of solar radiation through the water column is described by Beer's Law:

$$J_s(z) = (1 - f_r) J_{z=0} \exp(-\lambda z) \tag{3.17}$$

where $J_s(z)$ is the depth-varying solar radiation (W m^{-2}), $J_{z=0}$ is the radiation at the water surface, f_r is the fraction of short-wave radiation absorbed by the water body at the water surface, λ is the vertical light extinction coefficient (m^{-1}), and z is the water depth below the surface. When incoming short-wave solar radiation is completely absorbed at the water surface, f_r is unity, and from this formulation, no radiative energy reaches the sediment. Conversely, when f_r is less than unity, the fraction of incoming solar radiation that reaches the sediment surface is primarily controlled by the extinction coefficient.

The equilibrium temperature formulation employed in CE-QUAL-W2 assumes that the water column will experience a net surface efflux or influx of heat until a reference equilibrium temperature is established (Martin and McCutcheon, 1999), allowing the net surface heat exchange to be expressed as (Cole and Wells, 2005):

$$J_{aw} = -K_{aw}(T_w - T_e) \tag{3.18}$$

where J_{aw} is the rate of surface atmospheric heat exchange (W m^{-2}); K_{aw} is the coefficient of surface heat exchange (W m^{-2} °C^{-1}); and T_w and T_e are the water surface and equilibrium temperatures (°C), respectively. The coefficient of surface heat exchange is determined internally

in the model as the first derivative of the net surface heat balance with respect to the surface temperature. Finally, heat exchange between the water column and sediment is modeled using:

$$J_{sw} = -K_{sw}\left(T_w - T_s\right) \tag{3.19}$$

The sediment-water heat exchange coefficient K_{sw} is, in this study, assumed to be a constant equal to 0.3 W m^{-2} $^oC^{-1}$, a value consistent with simulations conducted by Li et al. (2010) and Jin et al. (2000) on shallow surface water reservoirs.

Turbulence Modeling

Turbulence closure is achieved using the model developed by Mellor and Yamada (1982) and modified by Galperin et al. (1988). This scheme relates the vertical turbulent viscosity (A_v) and diffusivity (A_b) to the turbulence intensity q and a turbulence length scale l (Jin et al., 2000):

$$A_v = 0.4\frac{\left(1+8Ri_q\right)ql}{\left(1+36Ri_q\right)\left(1+6Ri_q\right)} + A_{vo} \tag{3.20}$$

$$A_b = \frac{0.5ql}{\left(1+36Ri_q\right)} \tag{3.21}$$

$$Ri_q = -\frac{gH\dfrac{\partial b}{\partial z}}{q^2}\left(\frac{l}{H}\right)^2 \tag{3.22}$$

where A_{vo} is the background vertical eddy viscosity, and Ri_q is the densimetric Richardson number. The turbulent intensity and length scales are determined by explicit solution of a set of turbulence transport equations (the reader is referred to Jin et al., 2000 and Hamrick, 1992 for further information).

Horizontal turbulent viscosities are resolved in EFDC using a constant background turbulent eddy viscosity (A_{ho}) imposed on the internal solution of Smagorinsky's sub-grid scale

turbulence scheme (Smagorinsky, 1963), relating horizontal mixing to internal shear stresses and model grid cell size (Ji, 2008):

$$A_h\left(x,y,t\right)=C_s\Delta x\Delta y\left[\begin{array}{l}\left(\frac{\partial\left(m_y u\right)}{\partial x}\right)^2+\left(\frac{\partial\left(m_x v\right)}{\partial y}\right)^2+\\0.5\left(\frac{\partial\left(m_x u\right)}{\partial y}+\frac{\partial\left(m_y v\right)}{\partial x}\right)^2\end{array}\right]^{1/2}+A_{ho} \tag{3.23}$$

where A_h is the computed horizontal turbulent eddy viscosity ($m^2\ s^{-1}$); C_s is a dimensionless turbulent mixing coefficient; and Δx and Δy are the local grid cell lengths (m) in the x and y directions, respectively. The background horizontal turbulent eddy viscosity, A_{ho}, describes the intrinsic sub grid-scale turbulence of the flow field, as dictated by ambient atmospheric and flow conditions and horizontal grid resolution. This parameter is specifically grid size-dependent in EFDC, and as such, typical values are initially approximated from the average grid cell size, with refinement of parameter estimates being made during model calibration. Horizontal and vertical turbulent scalar mass transport in EFDC is assumed to be equal to turbulent mass transport. The effects of horizontal turbulent diffusion, expressed as A_h in the above, are incorporated into the Q_h term in the mass and heat transport equations (Eq. 3.9 and 3.10).

Vertical Boundary Conditions

Vertical boundary conditions for solution of the momentum equations include wind stresses at the water surface, and bottom channel shear stresses (Hamrick and Wu, 1997). Wind shear stresses are estimated from measured wind speeds, standardized to a height of 10 meters above the water surface (Hamrick and Wu, 1997):

$$\left(\tau_{sx},\tau_{sy}\right)=c_s\sqrt{U_{w(10)}^2+V_{w(10)}^2}\left(U_{w(10)},V_{w(10)}\right) \tag{3.24}$$

where τ_{sx}, τ_{sy}, $U_{w(10)}$ (m s^{-1}) and $V_{w(10)}$ (m s^{-1}) are the x and y components of the calculated wind shear stress (N m^{-2}) and measured wind speed $v_{w(10)}$, respectively. The wind stress coefficient is given by:

$$c_s = 0.001\frac{\rho_a}{\rho_w}\left(0.8 + 0.065\sqrt{U_{w(10)}^2 + V_{w(10)}^2}\right) \tag{3.25}$$

where ρ_a and ρ_w are the time-varying densities of air and water (kg m^{-3}), respectively. Bed shear stresses are determined from:

$$\left(\tau_{bx}, \tau_{by}\right) = c_b\sqrt{u_{bl}^2 + v_{bl}^2}\left(u_{bl}, v_{bl}\right) \tag{3.26}$$

where the subscript *bl* refers to the bottom layer of the model, and c_b is the bottom drag coefficient defined as (Ji, 2008):

$$c_b = \left(\kappa\left[\ln\left(\frac{H\Delta_{bl}}{2z_0}\right)\right]^{-1}\right)^2 \tag{3.27}$$

where κ is the von Karman constant (0.41); z_0 is the hydrodynamic bottom roughness height (m); and Δ_{bl} is the dimensionless thickness of the bottom layer. Equation 3.27 explicitly assumes a logarithmic velocity profile exists between the solid boundary and the middle of first adjacent vertical layer. The bottom drag coefficient is used specifically to estimate bed shear stresses in the x and y directions (Ji, 2008).

The surface vertical boundary condition for solution of the 3-dimensional heat transport equation incorporating the CE-QUAL-W2 equilibrium temperature model is defined as (Ji, 2008):

$$-\frac{\rho c_p A_b}{H}\frac{\partial T}{\partial z} = J_n \tag{3.28}$$

where c_p is the specific heat of water, and ρ_w is the density of water at the surface.

For heat transport, the vertical boundary condition at the bottom is defined as (Ji, 2008):

$$\frac{A_b}{H}\frac{\partial T}{\partial z} = -c_{hb}\frac{\rho_w c_p}{\rho_b c_{pb}}\sqrt{u_1^2 + v_1^2}\left(T_b - T_1\right) \tag{3.29}$$

where c_{hb} is the dimensionless convective heat exchange coefficient (set to 0.001 for all studies based upon Ji et al., 2008); c_{pb} is the specific heat of the sediment-water matrix; c_p is the specific heat of the water ; ρ_w and ρ_b are the water density in the layer directly above the bed, and the sediment density, respectively. The subscripts *b* and *1* represent the sediment bed and the adjacent water layer, respectively.

Model Domain and Discretization

The basin depth grids derived from each bathymetric survey (April 2010 and April 2011) defined the bathymetry of the model domain for the pre and post-flood tracer study simulations. The domain computational grid was developed to feature an orthogonal curvilinear grid in the inlet channel merged with a quasi-Cartesian grid for the central pool (Figure 5). This discretization scheme permitted a more refined definition of inlet channel morphometry and was necessary to account for the highly varying bathymetry of this section of the system. The entire model domain consisted of 3211 horizontal cells and 5 vertical layers, totaling 16055 active grid cells. Average horizontal cell sizes for the pool and inlet channel sections were 2 and 1.1 m^2, respectively. This model grid configuration required a time-step of 0.3 seconds to maintain numerical stability. Additional refinement of the vertical discretization to 6 layers provided no discernable difference in model results with respect to each of the modeled variables of interest. The suitability of 5 layers to resolve vertical velocity, temperature, and mixing dynamics in this

system is consistent with other numerical models of shallow surface water systems (e.g. Jin and Ji, 2005).

Hydrodynamic Roughness

The hydrodynamic roughness length, z_0, used to calculate internal friction losses and bottom shear stresses (Eq. 3.26) represents sediment grain and channel bedform roughness within the model domain. Information on the sediment grain size distribution is not available for this wetland. Instead, as a lumped proxy, spatially-varying bedform roughness heights (z_0) were determined from each bathymetric grid as one-quarter of the root mean squared height of predicted basin depths (H_p) using a 3m x 3m moving window over the entire domain:

$$z_0(x,y) = 0.25\left(\frac{\sum_{i=1}^{9}(H_k - \overline{H_k})^2}{n-1}\right)^{1/2} \tag{3.30}$$

Spatially varying roughness lengths were calculated using the *focal* function of the *raster* package in the R statistical computing environment (Hijmans and Etten, 2012). The coefficient of 0.25 in Eq. 3.30 was used to ensure that roughness lengths did not exceed the depth of water in the active grid cells, however the choice of this value is somewhat arbitrary. Sensitivity analysis of simulated outflows, dye concentrations, water depths, and internal temperatures suggested that a doubling of this coefficient slightly reduced the magnitude of calculated performance metrics (discussed in a proceeding section) for each simulated variable. The reduction in model performance was minor for each simulation, and suggests that significant changes in this coefficient, above or below currently unknown thresholds, should have little overall influence on simulation results. The relative insensitivity to uniform changes in

roughness lengths is likely due to the predominantly laminar flow conditions encountered during each tracer study simulation. Other researchers have reported a general insensitivity of model results to the magnitude of z_0 as well (Jin et al., 2000; Li et al., 2010).

The technique used in this study for calculating spatially-varying roughness lengths follows from the work of Nield et al. (2013). These researchers utilized high-resolution elevation raster datasets to determine local landscape surface roughness characteristics for use in the parameterization of aerodynamic models of the near surface, and found reasonable correlations ($R^2 \sim 0.75$) between measured surface roughness lengths and raster-derived estimates using a variant of this method. While this technique diverges from the standard method of specifying a uniform roughness height over the entire model domain, the authors feel that the method proposed by Nield et al., and implemented here, provides a more realistic estimation of hydrodynamic roughness lengths within this wetland. Average roughness lengths resulting from the method employed in this work (0.011 m and 0.012 m for the 2010 and 2011 bathymetric surveys, respectively) are within range of the normal roughness lengths typically used in simulations of surface water reservoirs (e.g. Jin et al., 2000; Li et al., 2010). Considering that most of the bed material within this wetland is composed of small grain sands and mud, and that the bathymetry is highly irregular over small areas, the average roughness lengths derived in this work are, in our opinion, reasonable. Maps of estimated roughness lengths for each bathymetric survey are given in Figures 3 and 4.

Initial and Boundary Conditions and External Forcing

Initial Conditions

For each simulation, initial conditions were specified for water depth above the weir elevation, sediment bed temperature, and water column temperature (Table 3). A lack of data precluded specification of initial internal pool velocities. A ramp-up period of 1 day was used to allow modeled velocities and temperatures to stabilize prior to simulation of the tracer studies. Longer ramp-up periods were found to have little influence on simulation results.

Flow Boundary Conditions

Time series of estimated average hourly influent flow rates (discussed in a previous section) were supplied as an upstream flow boundary condition for each tracer study simulation conducted prior to April, 2012. For the simulation WL1_1, continuous outflow monitoring was terminated on December 1, 2009. Outflow discharges after the termination of flow monitoring for this study were estimated from water level measurements obtained from continuous monitoring of the stoplog stilling well water level positioned near the wetland outlet.

For all simulations, the model outflow boundary condition was designated as a control structure, with modeled outflow rates ($m^3\ s^{-1}$) calculated from the discharge equation for a horizontal broad-crested weir:

$$Q_o(t) = \alpha H(t)^{3/2} \tag{3.31}$$

where H is the simulated depth of water in model cells directly upstream of the weir (m), and α is the discharge coefficient set to 4.23 $m^{3/2}\ s^{-1}$ specific to the 4 meter long weir for this wetland. The discharge equation for the wetland outflow structure was developed on the basis of the weir dimensions and outflow discharge measurements obtained in the system outflow channel.

Temperature and Tracer Flux Boundary Conditions

Each tracer study was simulated by specifying an instantaneous injection of dye of a known concentration at the upstream boundary of the model domain. The concentration specified at the inlet boundary was estimated from the mass injected for each respective field study (Table 1) and the instantaneous volumetric flow rate at the time of injection. The time of injection for each simulation was set equal to the time of injection for each respective field experiment.

Time-series of inlet temperatures for upstream thermal forcing were estimated from a linear regression (Figure 6) of air temperatures observed at the ISU-AG weather station against hourly averages of instantaneous observed inlet channel temperatures for the period late March through late May, 2012 for this wetland ($R^2 = 0.67$). The use of linear regression between air and surface water temperatures has been used in prior studies as a reasonable approximation for these missing data (e.g. Pilgrim et al., 1998; Devkota et al., 2013). For each simulation, inflow temperatures were assumed to be uniform over the inlet channel width. This condition was found to have no discernable influence on model results for any of the simulations.

Meteorological Forcing

Meteorological data acquired from the ISU-AG and Iowa SchoolNet weather monitoring stations were used to apply atmospheric boundary forcing for each tracer study simulation to simulate wind-driven currents, calculate external heat fluxes and internal evaporation rates using the CE-QUAL-W2 formulation given in Eq. 3.11-3.19, and to model internal basin temperature transport using Eq. 3.10. Atmospheric data were supplied to the model as hourly measurements.

Simulation Calibrations

Each tracer study simulation was calibrated against tracer dye concentrations observed at the wetland outlet, water temperatures observed at the basin stilling well and in the outlet channel, dynamic basin volumes and water levels estimated from measured water surface elevations at the basin stilling well, and basin volumetric outflow rates. The accuracy of each simulation was assessed using several performance statistics. The metrics used for the calibration of simulations included the Modified Index of Agreement (MIA; Willmott et al. 1985), the relative root mean square error (RRMSE; Ji, 2008), the mean absolute error (MAE: Legates and McCabe, 1999), and the mean absolute relative error (MARE; Ji, 2008), defined respectively as:

$$MIA = 1 - \frac{\sum_{i=1}^{n} \left| Y_{o(i)} - Y_{m(i)} \right|}{\sum_{i=1}^{n} \left(\left| Y_{m(i)} - \overline{Y_{o(i)}} \right| + \left| Y_{o(i)} - \overline{Y_{o(i)}} \right| \right)} \tag{3.32}$$

$$MAE = \frac{1}{N} \sum_{i=1}^{n} \left| Y_o - Y_m \right| \tag{3.33}$$

$$MARE = \frac{\sum_{i=1}^{n} \left| Y_o - Y_m \right|}{\sum_{i=1}^{n} Y_o} \cdot 100 \tag{3.34}$$

$$RRMSE = \frac{\sqrt{\left(\overline{\left(Y_o - Y_m \right)^2} \right)}}{\mathrm{Max}\left(Y_o \right) - \mathrm{Min}\left(Y_o \right)} \cdot 100 \tag{3.35}$$

where Y_o and Y_m are the time-matched discreet observed and modeled variables of interest, respectively. Overbars in Eq. 3.32 – 3.35 represent time averages. The MIA statistic was selected in lieu of the more standard Nash-Sutcliffe Efficiency Index (NSE), as the latter tends to emphasize lack of fit in peak regions, and other curve regions exhibiting sudden changes in value

(Legates and McCabe, 1999). The MIA statistic was designed to compensate for this bias (Willmott et al. 1985).

For each calibration routine for each simulation period, the vertical and horizontal turbulent mass transport parameters A_{vo}, and A_{ho}, and the temperature heat balance parameters f_r and λ, were systematically adjusted until the best fits between simulated and observed values for dye concentrations were obtained. These parameters were adjusted over the ranges $1x10^{-6}$ to 0.01 $m^2\ s^{-1}$; $1x10^{-4}$ to 0.025 $m^2\ s^{-1}$; 0.45 to 0.90 (-); and 0.1 to 0.9 m^{-1}, respectively (Table 4). Preliminary model testing found that the Smagorinsky sub-grid scale dimensionless diffusion coefficient, C_s, exerted only minor influence on model results for all dynamic target variables with larger values resulting, for some cases, in better model performance for water surface elevations. As such, a constant value of C_s of 0.15 (a value that is in the middle of the normal range of values reported for this parameter; e.g. Jin et al., 2000; Jin et al. 2002; Li et al., 2010; Devkota et al. 2013) was used for all simulations. Additionally, preliminary simulations indicated that the atmospheric equilibrium transfer coefficient (0.0015; Eq. 3.18), the bulk sediment heat transfer coefficient (0.3; Eq. 3.28), and the dimensionless convective sediment-water heat exchange coefficient (0.001; Eq. 3.29) each exerted little to no influence on simulated temperatures. Because of simulated temperature insensitivity, values for these parameters were set to estimates obtained from works by Jin et al., 2000; Jin et al. 2002; and Li et al., 2010. Additionally, because the active thermal depth of the sediment (the depth of the sediment layer that is actively involved in heat exchange with the water column) is unknown for this system, a constant sediment bed thermal thickness of 0.25 m was used for all simulation periods. This value is within the range of values reported for other surface water bodies (Jin et al., 2000; Li et al., 2010). Estimates of all considered calibration parameters for all of the simulations (Table 4)

are within the range of those reported in other studies conducted on enclosed or semi-enclosed basins.

During the calibration process, greater emphasis was placed on obtaining reasonable fits for simulated dye concentrations and temperatures than for hydraulic variables because the primary focus of this work was the replication of observed tracer response curves and internal temperature time-series. Furthermore, the survey methods used in determining the bathymetry of this system and the measurement methods used for estimating dynamic water levels are subject to unquantifiable error, suggesting the prudent approach of placing emphasis on those quantities for which measurement error is likely significantly less (i.e. temperatures and dye concentrations).

Residence Time Distribution Analysis

A critical component of this study involved conducting a comparison between observed and simulated RTD statistical and temporal characteristics to assess the suitability of the EFDC model as a tool for evaluating the bulk hydraulic characteristics of constructed surface water flow-through wetlands during the basin design phase prior to construction. To facilitate this comparison, the observed and simulated best fit (calibrated) tracer response curves were converted to volume-based RTD functions using the transformation (Zuber, 1986; Werner and Kadlec, 1996):

$$g_{(o,m)}\left(z_{(o,m)}\right) = \frac{C_{(o,m)}(t)V_{(o,m)}(t)}{M_{\mathrm{r}(o,m)}} \tag{3.36}$$

where $g(z)_{(o,m)}$ is the dimensionless volume-based RTD function for the observed or simulated tracer response curves; $V(t)$ is the observed or simulated time-varying system volume (m^3); $C_{(lc,m)}(t)$ is the loss-correct observed, or simulated effluent tracer concentration ($\mu g\ L^{-1}$). Because

flow conditions were varying during each field tracer study and corresponding simulation, the volume-based RTD function was used in lieu of more standard steady-state transformations (e.g. Kadlec and Wallace, 2008). The simulated and observed mass recovery, $M_{r(o,m)}$, is defined as:

$$M_{r(o,m)} = \int_0^{t_f} Q_{(o,m)}(t) C_{(o,m)}(t)\, dt \approx \sum_{i=0}^{n} Q_{i(o,m)}(t) C_{i(o,m)}(t) \Delta t \tag{3.37}$$

where the last term in Eq. 3.37 is the discrete time-step approximation of the integral. The time-step, Δt, was set to 5 *min* for both observed and simulated time-series. As discussed in Green and Crumpton (In prep.), the quantity z in Eq. 3.36 represents a dimensionless flow-weighted time, used to represent the elapsed time from tracer injection on a common scale, and is defined as (Zuber, 1986; Werner and Kadlec, 1997):

$$z_{(o,m)} = \int_0^{t_f} \frac{Q_{o(o,m)}(\tau)}{V_{(o,m)}(\tau)} d\tau \tag{3.38}$$

where τ is a time-like dummy variable of integration; $Q_{o(o,m)}(t)$ and $V_{(o,m)}(t)$ are the observed or modeled time-varying volumetric outflow rates and system volumes, respectively. The quantity within the integral represents the turn-over time and is the inverse of the instantaneous hydraulic residence time.

Dimensionless temporal features of each simulated and observed RTD, such as initial and peak arrival times and median detention times, were obtained directly by expressing z explicitly as a function of t (Zenger, 2003; Green and Crumpton, in prep.):

$$z_{(\mathrm{i,p,50})} \cong f\left(t_{(\mathrm{i,p,50})}\right) \tag{3.39}$$

where z is a monotonically increasing function of normal time. The flow-weighted time z was expressed as a cubic spline interpolant of the measured time from injection, represented in standard time units (*days*). Spline interpolants were developed using the *stats* package in the R statistical computing environment (R Core Team, 2014). For this study, the initial (z_i), peak (z_p),

and median (z_{50}) tracer arrival times were estimated using Eq. 3.39. Additional information about the use of this technique for capturing z-scaled RTD temporal features is given in Green and Crumpton (in prep).

The dimensionless initial and peak arrival times are considered to be reasonable metrics of tracer short-circuiting in the basin. Thackston et al. (1987) suggest that "significant" short-circuiting is indicated by an initial dimensionless arrival time, z_i, as being less than 0.2. Likewise, Persson et al. (1999) and Persson (2000a) suggest that significant short-circuiting, as well as diminished basin hydraulic efficiency, is implied for dimensionless peak arrival times, z_p, of less than 0.75. We adopt these general conventions in this work as well.

Method of Moments and Bulk Mixing Indices

Each observed and corresponding simulated RTD curve was analyzed using the method of moments to calculate primary RTD temporal statistics including the centroid (the first moment about the origin; $m_{0(o,m)}$), the temporal variance (the second moment about the centroid; $m_{2c(o,m)}$), and the normalized temporal variance ($\sigma^{2*}_{(o,m)}$), defined respectively as (Kadlec, 1994; Kadlec and Wallace, 2008):

$$m^{*}_{1(o,m)} = \int_0^{t_f} z g_{(o,m)}(z)dz \approx \sum_{i=1}^{n} z g_{(o,m)}(z)\Delta z \tag{3.40}$$

$$m^{*}_{2c(o,m)} = \int_0^{t_f} \left(z - m^{*}_{1(o,m)}\right)^2 g_{(o,m)}(z)dz \approx \sum_{i=1}^{n} \left(z - m^{*}_{1(o,m)}\right)^2 g_{(o,m)}(z)\Delta z \tag{3.41}$$

$$\sigma^{2*}_{(o,m)} = \frac{m_{2c(o,m)}}{\left(m^{*}_{1(o,m)}\right)^2} \tag{3.42}$$

where, for simplicity, z in Eq. 3.40 – 3.42 represents both measured and modeled estimates obtained from Eq. 3.38. The centroid of the RTD is the dimensionless mean residence time of dye as it transits the system. Under steady flow conditions with complete basin volume utilization the dimensionless mean residence time is reasonably approximated by the quotient of the tracer mean residence time in normal time units (m_1), and the mean hydraulic residence time (i.e. $m_1 / \overline{T}_R = m_1 V / Q = 1$, where V and Q are the steady basin volume and flow-through rates, respectively). Under unsteady flow conditions the centroid of the RTD is not necessarily well approximated by the mean hydraulic residence time of the system (Holland et al., 2004). Because of the close relationship between m_1 and V/Q, some researchers have argued that m_1^* represents the fractional volume of the system that is involved in tracer transport during a tracer study (e.g. Thackston et al., 1987; Holland et al. 2004), and provides a measure of the amount of dead space within the domain. We adopt this convention in this work, as well.

The variance of the RTD describes the degree of dispersion about the centroid, and is often used as an approximate measure of the total degree of basin mixing during tracer transit (Thackston et al., 1987; Kadlec, 1994). Because $m_{1(o,m)}$ and $m_{2c(o,m)}$ are both strongly dependent on basin flow conditions, $\sigma^{2*}_{(o,m)}$ has been proposed as an unbiased dimensionless approximation of the total degree of mixing to have occurred within the basin from the point of injection to the observation location (Thackston et al., 1987; Kadlec, 1994). The normalized variance ranges from 0 - indicating pure translational (plug) flow with complete vertical and lateral mixing and no longitudinal dispersion - to unity, suggesting complete basin-wide mixing exemplified by an exponential distribution of residence times, and/or significant short-circuiting of tracer during transit. The differentiation between these two conditions has long been recognized as being important to basin constituent removal performance, with maximal constituent removal

performance for a system occurring under steady plug-flow conditions (Kadlec, 1994; Kadlec and Wallace, 2008).

The normalized variance of each observed and simulated RTD was used to roughly approximate the observed and simulated system Peclet number, $Pe_{x(o,m)}$ using (Levenspiel, 2011):

$$\sigma^{2*}_{(o,m)} \cong \frac{2}{Pe_{x(o,m)}} + \frac{3}{Pe^2_{x(o,m)}} \tag{3.43}$$

The Peclet number represents the ratio of the time-scales of advection and dispersion within the system, with values less than unity indicating a dominance of dispersion in tracer transport. Conversely, values greater than unity indicate advection dominance. The simulated and observed bulk rates of dispersion for each tracer response curve was estimated from the Peclet number and bulk approximations of basin morphometric characteristics using (Kadlec and Wallace, 2008):

$$K_{x(o,m)} \cong \frac{\overline{Q_{a(o,m)}} L}{\overline{B}\,\overline{H} Pe_{x(o,m)}} \tag{3.44}$$

where $K_{x(o,m)}$ is the bulk quasi-longitudinal dispersion coefficient for the tracer study (m^2 min^{-1}); $\overline{Q_{(o,m)}}$ is the time average of the arithmetic mean of the simulated or observed inflow and outflow rates over the duration of each study; and $\overline{B}$, $\overline{H}$, and $\overline{L}$ are the average width (m) and depth (m), and the total length of the basin from the point of injection to the monitoring location. Derivation of these bulk morphometric characteristics for this wetland are given in Green and Crumpton (In prep.).

Results

Model Calibrations

Time-series plots of simulated, observed, and the minimum and maximum prediction bounds for all considered dynamic variables are given in Figures 7 through 12. Best-fit calibration parameters and fit statistics are given in Tables 4 and 5, respectively. The minimum and maximum prediction bounds given in these plots represent the prediction envelopes of simulated time-varying temperature, dye, and hydraulic variables over the tested parameter ranges given in Table 4. These envelopes provide an indication of the potential range of simulated response variables over the tested parameter ranges, which in the case of the primary turbulence calibration parameters, A_{ho} and A_{vo}, spanned between 4 and 5 orders of magnitude.

Water Surface Elevations, Volumes, and Outflows

As shown in Table 5, basin water depths (referenced to the maximum basin depth of ~1.97 m) of best-fit simulations reasonably matched observed values for most of the tracer study simulations. Despite the comparatively large percent error shown for some of the simulations, mean absolute errors range from only a millimeter to nearly one centimeter. Estimates of MAE for simulated water depths for this study are significantly less than errors reported in other studies (e.g. Jin et al., 2000; Li et al., 2010).

In general, basin volumes for each simulation period exhibited levels of error similar to those reported for simulated depths. While the RRMSE estimates, ranging from 12.6 to 37%, indicate fairly significant overall error in simulated volumes for some model runs, the moderately small MAE (2.64 – 79.3 m) and maximum difference estimates (11.8 – 266.8 m) suggest reasonably accurate dynamic volume estimates over all simulations.

Simulated outflow discharges corresponded closely with observed values, and in all cases resulted in an RRMSE of less than 5%. The high degree of correspondence between simulated and observed outflow discharges across all studies suggests that EFDC can realistically simulate outlet rates under a range of flow conditions.

Simulated depths and volumes were found to be highly sensitive to the value of A_{vo}, and not affected by A_{ho} (data not shown). Only minor changes in the time-series and fits for these parameters were observed with changes in the Smagorinsky dimensionless turbulent diffusion coefficient (C_s). In general, higher values of A_{vo} resulted in greater depths, and larger simulated volumes. The minimum-maximum prediction bounds shown for these simulated time-varying variables shows that unique A_{ho} and A_{vo} parameter combinations result in widely varying model responses. In several cases, notably WL1_3 and WL1_1, the model was not capable of replicating the observed curves for either time-varying variable using any of the tested background turbulence parameter combinations. In these two cases, the minimum-maximum prediction bounds and the best-fit simulation results deviate from the observed curves for nearly the entirety of each simulation. The remainder of the simulations show better correspondence, and selected best fit curves fall within, or at least reasonably tracked between, the minimum-maximum prediction bounds.

Discrepancies between observed and simulated depths and basin volumes may be attributable to the inherent error associated with estimating time-varying depth in the field (as discussed previously), with additional uncertainty possibly stemming from unknown error in the estimates of spatially-varying basin depths and error associated with the reverse level-pool routing procedure used to estimate instantaneous influent discharges. The notable discrepancies for WL1_1 and WL1_3 with respect to simulated depths and volumes may also be due to

inaccuracies in the precipitation data supplied to the model, or, and equally likely, error in the measured time-series. For WL1_3, the latter case is more likely considering the measured and simulated outlet discharges for this study also show a declining water level throughout the study period. Regardless, as is shown in a following section, inaccuracies in these simulated variables have only moderate influence on simulated RTD temporal features when evaluated using standard unsteady flow RTD analysis techniques.

Temperatures

Time-varying temperatures resulting from each determined best-fit simulation reasonably matched temperatures observed at the wetland outlet monitoring location, and at the wetland stilling well. However, the accuracy of the simulated temperature time-series is distinctively variable between simulation periods, as is shown in Table 5.

For all simulation periods, temperatures measured at the dye monitoring location in the outlet channel are better reproduced by the model than temperatures measured in the stilling well. The difference in model accuracy between these two locations, despite their close spatial proximity, may be attributable to isolating effects of the stilling well casing, or by uncertainty of the exact depth at which the pressure transducer thermistor was located within the stilling well. All considered fit statistics reported in Table 5 exhibited a similar discrepancy between the outlet channel and stilling well monitoring locations. A notable exception is the high degree of difference between outflow and stilling well temperatures for the study WL_13. The cause of the discrepancy between these two locations is unknown at this time.

Simulated temperatures were observed to be highly sensitive to the magnitude of A_{vo}, and relatively insensitive to A_{ho}, f_r, and λ. Higher values of A_{vo}, corresponding to increased ambient

background vertical mixing rates, tended to result in lower overall predicted temperatures and dampened diurnal temperature fluctuations at both monitoring locations. In contrast, A_{ho} was observed to exert little influence on simulated temperature patterns for all of the simulations. The temperature calibration coefficients f_r and λ were found to primarily influence the magnitude of simulated temperature curves, but exerted little influence on diurnal patterns at both monitoring locations. Of these two parameters f_r maintained stronger influence on model results. In general, as would be expected, decreases in f_r, representing diminished short-wave radiation absorption at the water surface, resulted in higher overall simulated temperatures; however, this effect was comparatively small, resulting in no more than a 0.5 °C maximum difference in simulated and observed temperatures at both locations over the tested range. All error statistics exhibited similarly minor changes over the tested range of this parameter. In general, lower values of λ resulted in overall elevated temperatures at both monitoring locations, indicating increased sediment bed heating resulting from reduced short wave radiation attenuation. The lack of data pertaining to the actual values of these parameters for this system over the simulation periods tested necessarily preclude inference about their validity, and their respective roles in influencing simulated temperatures beyond the qualitative descriptions given here. The best-fit temperature calibration coefficients are within range of those reported by several authors (e.g. Jin et al., 2000; Jin et al.,2002; Li et al., 2010; Devkota et al., 2013; Jin and Ji, 2013).

Due to an absence of instrumentation inlet water temperatures were estimated from the linear regression model between air and water temperatures, as discussed previously (Figure 6). The comparatively high correspondence between simulated and observed temperatures at both monitoring locations for all studies but WL1_13 suggests that the model is relatively insensitive to inaccuracies in inlet boundary temperatures. This finding naturally suggests that the

temperature dynamics of this system are driven primarily by in-pool heat exchanges between the wetland sediment and the water column, and from applied atmospheric thermal forcing, a conclusion also reach by Sweeney et al. (2005) and by Bardot-Nico et al. (2009). However, the use of this regression model to estimate inlet temperatures cannot be discounted as a potentially major source of the error reported for the temperature simulation results. Regardless, considering the comparatively good fit between observed and simulated temperatures for every simulation but one, the total overall error from use of this approximation is likely small, but the exact error induced by this approximation cannot be quantified at this time. The spread in the minimum-maximum prediction bounds for simulated temperatures is likely due to the influence of the background vertical turbulent diffusion coefficient, although some of this spread can be attributed to the range of tested f_r and λ coefficients.

Tracer Concentrations

Tracer concentrations of the selected best-fit simulations, as observed at the monitoring point in the outlet channel, were in reasonable agreement with observed tracer concentrations. For several studies (notably WL1_1, WL1_3, and WL1_11), simulated tracer response curves featured earlier arrival and peak times and sharper fronts than corresponding observed curves. Additionally, in every case but WL1_3 and WL1_13, simulated peak concentrations were between 1 and 5 $\mu g\ L^{-1}$ less than observed (corresponding to percent differences of between 7 and 20%) . In the case of these two exceptions, simulated peak concentrations were between 0.5 and 1 $\mu g\ L^{-1}$ greater than observed peak concentrations. The calibration process revealed that the overall shape and initial and peak arrival times were highly sensitive to the magnitudes of both A_{vo} and A_{ho}. Optimized values of A_{ho} ranged from 0.025 to 0.0001 $m^2\ s^{-1}$. In general, larger values

of A_{ho} induced earlier initial arrival times, and longer and smoother response curve tails. Optimized values of A_{vo} ranged from $2.5x10^{-4}$ to $1x^{-6}$ m^2 s^{-1}, with smaller values resulting in earlier tracer initial and peak arrival times and sharper ascending limbs. That different combinations of A_{vo} and A_{ho} produced variable best-fit statistics for the simulations considered suggests that these parameters are likely sensitive to ambient hydraulic and atmospheric conditions, and are thus moderately time-varying in most cases, at least for small surface water bodies such as Iowa CREP wetlands.

The sensitivity of the early time features of the simulated tracer response curves to the varying combinations of A_{vo} and A_{ho} tested in this work is illustrated in the minimum-maximum bounds of simulated dye concentrations for each simulation period as shown in Figures 7 through 12. These bounds also show the relative insensitivity of response curve tails to the magnitudes of A_{vo} and A_{ho}. The shapes of these bounding curves suggest that model simulations intended to calibrate against initial and peak tracer arrival times (both metrics are commonly considered to be indicators of the degree of short-circuiting within a basin; e.g. Thackston et al., 1987; Persson, 2000) will be highly sensitive to values of these parameters. However, if simulations are intended to emphasize mean residence times over short-circuiting metrics, the values of these parameters appear to be less important. Furthermore, these figures provide an illustration of the range in potential RTD shapes for this wetland, which were presumably dictated by the prevailing flow and atmospheric conditions encountered during each study, as shown in Green and Crumpton (in prep.)

Residence Time Distribution Analyses

Modeled and observed RTD moments and temporal features are shown to be in good general agreement (Table 6). For most studies, the dimensionless initial time of tracer arrival was reasonably replicated, with minimum and maximum percent differences between simulated and observed values of 0.07 (WL1_2) and 33.2% (WL_1), respectively. Simulated dimensionless peak arrival times generally fell to within 10% of observed z_p, with the notable exception of WL1_11, which peaked at a time nearly 50% earlier than what was observed. Simulated and observed median and mean dimensionless residence times were in reasonably good agreement, with percent differences ranging from 0.74 (WL1_10) to 22 (WL1_11) %, and 1.4 (WL1_10) to 35 (WL1_11) %, respectively. The exception again is WL1_11, for which simulated values for both statistics were significantly lower than observed values. This same significant deviation is observed for this study for all considered RTD statistics and temporal features.

The WL1_11 tracer study was conducted when submersed aquatic vegetation was becoming established in the wetland. The area-weighted average percent areal cover of submersed aquatics was ~11%, and vegetation occupied only ~80% of the total wetland area (Green and Crumpton, in prep.). The presence of vegetation in the wetland during this tracer study may have an, as yet poorly understood, influence on the discrepancy between the observed and modeled RTD characteristics for this study. In their work, Green and Crumpton found that peak arrival times were delayed for tracer studies conducted under vegetated conditions for this wetland and others. The EFDC simulation for this study does not take into account the presence of vegetation, and shows a sharply earlier peak arrival time of tracer than what was observed; although the initial arrival time and mean detention time are roughly in agreement.

Model Sensitivity Analysis

As shown in Green and Crumpton (in prep.), environmental effects such as wind speed, wind direction, and ambient flow conditions can have significant, but varying, influence on considered tracer response curve characteristics for this wetland. Similar observations regarding the influence of wind and flow effects on RTD characteristics of shallow flow-through basins have been made by other researchers (Thackston et al., 1987; Holland et al., 2004; Bentzen et al., 2008; Bardot-Nico et al., 2009). Applied wind shear at the water surface and influent volumetric flow rates supply the primary sources of energy available for mixing to these systems; with the effect of wind being particularly important in the absence of vegetation. Applied wind shear at the water surface can act as a stirring mechanism, enhancing horizontal and vertical turbulent mixing rates, and increasing internal rates of local advection. An additional environmental effect that may strongly influence mixing and RTD characteristics is temperature-induced vertical and horizontal density inhomogeneity. While wind and flow effects have been considered by other researchers, the effect of temperature on RTD development has only been investigated in a select number of systems. For instance, Macdonald and Ernst (1986) and Sweeney et al. (2005) report that vertical stratification may be a significant cause of short-circuiting in moderately shallow ($\overline{H} \sim 1$ m) flow-through basins. What is less clear is whether vertical and horizontal variances in internal basin temperatures can exert an effect on bulk mixing and RTD characteristics for extremely shallow systems ($\overline{H} < 1$ m) which are also highly wind-exposed. The influence of temperature-induced density differences on the hydraulic behavior of Iowa CREP wetlands may be significant, as these systems receive the majority of their flows from upland subsurface tile systems, which, during the late summer and spring seasons, tend to export water at temperatures that can be significantly cooler than the receiving systems.

To isolate the relative influence of these previously mentioned environmental effects on the varying observed RTD characteristics of this wetland, we conducted a series of sensitivity analyses with each of the calibrated best fit EFDC simulations discussed in the previous section. These sensitivity analyses entailed performing additional simulations that systematically, and alternately, excluded wind and atmospheric and inlet temperature forcing from the model. Additionally, to isolate the influence of observed time-varying flow rates on modeled RTD characteristics, we conducted alternate steady-flow simulations in which the inflow boundary discharge was set to the flow rate observed at the time of dye injection for each tracer study. A total of 7 sensitivity scenarios were conducted for each simulated tracer study. Table 7 enumerates the considered sensitivity scenarios.

Simulated tracer response curves for these sensitivity runs were subsequently analyzed using the afore-discussed RTD analysis techniques, and derived RTD statistics were compared with corresponding statistics for the best fit simulations. The presumption underlying this analysis is that the calibrated modeled temperatures and tracer response curves, despite the comparatively small number of calibration locations for temperature fit assessment and the linear regression utilized to estimate inlet boundary temperatures, reasonably represents the interior tracer dispersion and temperature dynamics of this system over the periods studied.

Sensitivity Analysis Results

As is illustrated in Table 8, the model sensitivity analyses suggest significantly varying influences of each of the considered environmental effects on simulated RTD statistics. Time-series plots of calculated RTD functions for each tested scenario for each simulated tracer study

are given in Figure 13. Aggregate summary statistics for all tested scenarios are graphically presented in Figure 14.

As shown in Figures 13 and 14 wind and temperature forcing, separately and in concert, strongly influence considered short-circuiting indices and measures of bulk basin mixing. This is clearly evident for the tested scenarios 2, 3, 4, and 5. Wind forcing is shown to exert the greatest control over initial arrival times of arrival of tracer, resulting in a nearly 100% average increase in this RTD characteristic – an effect that is consistent regardless of whether steady or transient flow boundary conditions are specified for the model. A similar effect of wind forcing is observed for the time to peak of the RTD (an average increase of nearly 75% above the best-fit case) and for all bulk measures of mixing considered in this work. RTD dimensionless variance and estimated longitudinal dispersion coefficients are shown to decrease by nearly 20%, on average, in the absence of wind alone, regardless of the presence of transient flow conditions (scenarios 2 and 4). These observed average changes in σ^{2*} and K_x correspond to a nearly 20% increase in average system Péclet numbers. In general, wind forcing, when considered independently, is shown to have only minor influence on the magnitude the median and mean detention times. The exclusion of temperature forcing with the retention of wind forcing, regardless of the specification of time-varying flow boundary conditions (scenarios 6 and 7), is shown to have little influence on each of the considered RTD statistics.

When temperature and wind forcing are both removed from the simulations (scenarios 3 and 5) initial and peak arrival times increase, on average, by nearly 150% above the best-fit cases regardless of whether time-varying flow boundary conditions are specified. Increases in these RTD metrics are nearly 50% above that observed for the no-wind cases. Mean and median residence times also increase, on average, by approximately 5% for these scenarios – an

approximately 0% increase above the no-wind case. In contrast, σ^{2*} and K_x decrease on average by approximately 60 and 40% with respect to the best-fit case. These decreases are nearly 200 and 100% greater than those observed for the no-wind cases discussed previously (scenarios 2 and 4). The Peclet number for these cases increases by nearly 100% above the best-fit case and increases by nearly 300% above the no-wind case.

Considered in the aggregate, these results suggest that wind forcing exerts the greatest influence on most considered RTD statistics, with particular influence on measures of short-circuiting (z_t and z_p). While temperature dynamics have, when compared to the effect of wind, only a moderate influence on tracer short-circuiting, this effect has a marked influence on measures of internal mixing and dispersion rates, as is shown in Figures 13 and 14. The effects of internal temperature dynamics on the magnitudes of σ^{2*}, Pe_x, and K_x are shown to be significantly greater than the influence of wind forcing, overall. Additionally, neither of these effects appear to have had a strong influence on the median and mean residence times, suggesting that these RTD characteristics are mostly influenced by mean basin flow rates. This finding is in agreement with the observations of Bentzen et al. (2008), who found through numerical simulation of wind effects on the RTD characteristics of a shallow highway detention pond that both wind speed and direction under steady time-invariant forcing strongly influence mean detention times.

Wind forcing has long been considered to be a potential driver of mixing in shallow flow-through basins, such as the one featured in this work. Several authors have noted the presence of wind-driven surface current accompanied by bottom-layer return currents (e.g. Shaw et al., 1997; Andradóttir and Mortamet, 2016), which, when present, may cause these systems to become more fully mixed, as suggested by Thackston et al. (1987) and by Watters et al. (1973). Indeed,

Watters and colleagues demonstrated in wind-tunnel experiments the tendency for increasing wind shear to increase longitudinal dispersion rates in enclosed basins, with dispersion rates being strongly correlated to the direction of the applied wind (a factor not considered here). Their results appear to confirm the theoretical work of Wu (1969), which are also seemingly supported in this work. Whether apparent increases in dispersion resulting from applied wind shear can be attributable to wind-induced differential advection, or increases in the overall degree of turbulence is uncertain at this time.

The underlying mechanisms that result in increased dispersion and short-circuiting when temperature forcing is included in the model simulations is not currently well understood; however, other researchers have noted that shallow basins can vertically stratify during warmer periods (Macdonald and Ernst, 1986; Gu et al., 1996; Sweeney et al., 2005), especially if influent water temperatures are significantly lower than receiving water temperatures. In this case, colder and denser influent water may plunge into the basin, causing some tracer to remain confined within deeper layers of the pool. That fraction of the influent that does not get transported to the deeper layers of the system may then be subjected to buoyancy driven mixing, resulting from density-differentiated layers of flow. This is likely the case for tracer studies conducted when temperature differences between the influent water and the pool is greatest (i.e. all studies but WL1_1). Indeed, Macdonald and Ernst (1986) observed a temperature effect on short-circuiting in maturation ponds (a reasonable analogue for Iowa CREP wetlands), and attributed this behavior to vertical stratification. Likewise, Pedahzur et al. (1993) attributed tracer short-circuiting in a shallow (~1 *m*) stabilization pond to the presence of vertical stratification as well, but also visually confirmed rapid lateral and longitudinal distribution of tracer in the epilimnion (the top 20 *cm* of the water column) of their system, suggesting that warmer and more buoyant

water layers may transport tracer at a rate significantly faster than the mean, depth-averaged, transport rate. In addition to vertical stratification, horizontal inhomogeneity in the internal basin temperature field may, under some atmospheric conditions, also help to confine entering waters to a centralized, and possibly short-circuited, pathway. Comparatively few studies have been conducted on the time-varying extent of horizontal temperature heterogeneity in shallow flow-through reservoirs and the effects of such dynamics on internal hydraulic short-circuiting and mixing behavior of these systems. A notable exception is Sweeney et al. (2005) who found that even short-duration temperature inhomogeneity in these systems may have a large influence on their hydraulic and mixing characteristics, particularly with respect to short-circuiting.

Conclusions

Our study demonstrates the efficacy of the EFDC model in simulating the outflow, temperature, and tracer transport dynamics of this wetland over a range of flow and environmental conditions. For dynamic temperature and tracer concentrations, the differences between simulated and observed values are reasonably low, ranging from 0.3 to ~6% for tracer concentrations, and 0.6 to ~16% for temperatures; thus further supporting the applicability of EFDC as a general modeling tool for evaluating the temperature and mixing dynamics of these types of extremely shallow surface water systems. Additional model refinements such as employing higher vertical and horizontal grid resolutions, or trying alternate derivations of basin roughness heights may improve volume and water surface elevation estimates. However, considering the moderately low errors for simulated temperature and dye concentrations, these refinements are not likely to significantly improve model accuracy for these variables. Further, while the use of linear regression for estimating inlet temperatures produced reasonably accurate

results, model efficacy may be further improved through continuous inlet temperature and flow monitoring for future studies. Finally, a potentially significant shortcoming of this study is the small number of internal temperature monitoring stations by which model accuracy is assessed. This lack of temperature monitoring at more interior points within the basin may detract from the relative accuracy of the models developed in this work. Further, the lack of internal basin velocity measurements does not permit an assessment of the relative accuracy of the simulated internal basin velocity fields. Future studies should attempt to correct for these deficiencies.

In addition to accurately simulating the raw, untransformed, dynamic state variables of interest, the EFDC model was shown to be capable of realistically replicating the considered calculated RTD curve statistics for each field tracer study. The greatest degree of deviation between simulated and observed statistics were seen for the study WL1_11 for all considered RTD features. This tracer study was conducted during a period in which submergent vegetation was beginning to become established, but which only occupied a comparatively small percentage of the wetland (see Green and Crumpton for reference). Whether the presence of vegetation explains the relatively large differences between modeled and observed RTD statistics for this study is unknown at this time, but recent results from Green and Crumpton (in prep), suggest that the presence of vegetation can delay the peak arrival time of tracer under some flow conditions, suggesting that the discrepancy between modeled and observed results for this study may be attributable to this effect. However, considering the comparatively good fits between modeled and observed response curves for the other studies considered in this work, the presence of vegetation is offered as a potential reasonable explanation for this observed deviation. Additional simulations should be conducted for this tracer study that explicitly account for spatially varying vegetation characteristics and roughness – a current capability of the EFDC model.

While the model was seemingly capable of replicating some dynamic variables for the tracer studies evaluated herein, the variable vertical and horizontal turbulent mixing coefficients (A_{vo} and A_{ho}) found to produce the best correspondence between observed and simulated tracer response curves varied significantly between tracer studies and in some cases differed by several orders of magnitude. Further, the testing of these variables on the simulated response curves provide a very large range of potential predicted responses for tracer concentrations (i.e. the minimum-maximum prediction bounds shown in Figures 7 through 12). These findings suggest that any application of this model to test mixing and temperature dynamics on a shallow flow-through basin, absent a set of corresponding field-scale tracer studies and continuous in-pool temperature measurements, must take careful consideration of the values of these two primary model calibration coefficients. Any conceptual test application of the model to a non-tested system should account for a range of possible tracer response curve responses as dictated by a span of A_{vo} and A_{ho} values of several orders of magnitude. Prior to adopting EFDC as a wetland design tool, future work should also focus on determining the relative influence of ambient wind, temperature, and flow conditions on dictating the approximate magnitude of these primary model calibration coefficients.

The results from the conducted sensitivity analyses suggest that ambient flow conditions, on average, maintain minimal impact on most of the RTD characteristics considered in this work, save for the mean and median residence times. For the set of tracer tests performed, early and late time changes in flow rates were shown to have some impact on median and mean detention times, and on estimates of short-circuiting; despite the purported ability of the volume-based RTD function to remove these effects through implementation of the flow-weighted time scheme (Eq. 3.38). Neither early nor late-time changes in flow rates were shown to have an appreciable

influence on observed RTD variances and derived measures of bulk basin mixing. Additional research should be conducted into determining the appropriate RTD and time-transformations necessary for deriving non-flow affected estimates of RTD statistics.

While significant differences exist between studies, the test scenarios also indicated that, on average, wind and temperature forcing both strongly influence RTD development and derived basin mixing. The relative contribution of these effects on the ultimate shape of the RTD observed at a system outlet, however, appears to be variable, and is likely dictated by factors such as the total degree of temperature variations within the basin, time-varying temperature differences between influent and ambient pool water, and the timing and magnitude of wind forcing. A case in point is the WL1_1 tracer study, wherein temperature forcing was shown to have little influence on the simulated (and by extension, observed) RTD for this study. In this case, wind was the dominant factor in causing tracer short-circuiting and in setting-up the degree of basin-scale mixing. In contrast, for the studies WL1_2, WL1_11, and WL1_13, wind forcing strongly influenced short-circuiting, but temperature forcing was observed to maintain the strongest influence on basin dispersion and mixing, suggesting that horizontal and vertical stratification may play a significant role in the mass transport behavior of this system and other similarly functioning shallow flow-through basins. For the remaining studies (WL1_3 and WL1_10), wind and temperature forcing were shown to exert roughly equal influence on short-circuiting and bulk mixing. Both wind and temperature forcing were shown to have only a nominal influence on calculated median and mean detention times. The influence of horizontal and vertical temperature inhomogeneity on RTD development in Iowa CREP wetlands should be explored more in future research.

Acknowledgments

This work was funded in part by the Iowa Department of Agriculture and Land Stewardship, and by the Department of Ecology, Evolution, and Organismal Biology at Iowa State University. Gratitude is given to Greg Stenback for providing flow and water depth data, and his general assistance with data management. Additional thanks are given to Ian Ellickson, Claudette Sandoval-Green, and the several undergraduate students at Iowa State University who assisted with the collection of field data. Additionally, we are grateful to the owners of the wetland studied in this work for granting access and permission to study this site.

References

Barrot-Nico, F., V. Guinot, and F. Brissaud. 2009. Fluid flow pattern and water residence time in waste stabilization ponds. Water Science & Technology 59(6):1061. doi:10.2166/wst.2009.087.

Bentzen, T. R., T. Larsen, and M. R. Rasmussen. 2008. Wind effects on retention time in highway ponds. Water Science & Technology 57(11):1713. doi:10.2166/wst.2008.267.

Buchanan, T.J., and W.P. Somers. 1969. Discharge measurements at gaging stations. USGS Numbered Series 03-A8. Techniques of Water-Resource Investigation. U.S. Govt. Print. Office. http://pubs.er.usgs.gov/publication/twri03A8.

Carleton, J. N, T. J Grizzard, A. N Godrej, and H. E Post. 2001. Factors affecting the performance of stormwater treatment wetlands. Water Research 35(6):1552–62. doi:10.1016/S0043-1354(00)00416-4.

Cole, T.M., and S.A. Wells. 2003. CE-QUAL-W2: A two-dimensional, laterally averaged, hydrodynamic and water quality model, Version 3.1. Instruction Report EL-03-1. Vicksburg, MS: US Army Engineering and Research Development Center.

Crumpton, W. G., A. van der Valk, W. Hoyer, and D. Osterberg. 2012. Wetland restoration in Iowa: challenges and opportunities. Iowa Policy Project Report. Iowa Policy Project, Iowa City, Iowa.

Devkota, J., X. Fang, and V. Z Fang. 2013. Response characteristics of the Perdido and Wolf Bay system to inflows and sea level rise. British Journal of Environment and Climate Change, July, 229–56. doi:10.9734/BJECC/2013/3516.

Franceschini, S., and C.W. Tsai. 2010. Assessment of uncertainty sources in water quality modeling in the Niagara River. Advances in Water Resources 33(April): 493–503. doi:10.1016/j.advwatres.2010.02.001.

Galperin, B., L. H. Kantha, S. Hassid, and A. Rosati. 1988. A quasi-equilibrium turbulent energy model for geophysical flows. Journal of the Atmospheric Sciences 45(1): 55–62. doi:10.1175/1520-0469(1988)045<0055:AQETEM>2.0.CO;2.

Gu, R., F.N. Luck, and H.G. Stefan. 1996. Water quality stratification in shallow wastewater stabilization ponds. Journal of the American Water Resources Association 32(4):831–44. doi:10.1111/j.1752-1688.1996.tb03480.x.

Green, D.I., and W.G. Crumpton. In Prep. Residence time distribution dynamics of constructed agricultural wetlands. Manuscript in preparation.

Hamrick, J.M. 1992. A three-dimensional environmental fluid dynamics computer code: Theoretical and computational aspects. The College of William and Mary, Virginia Institute of Marine Science, Special Report 317, 63 pp.

Hamrick, J.M., and T. S. Wu. 1997. Computational design and optimization of the EFDC/HEM3D surface water hydrodynamic and eutrophication models. Next Generation Environmental Models and Computational Methods. G. Delich and M. F. Wheeler (eds). Society of Industrial and Applied Mathematics, Philadelphia, 143-156.

He, G., H. Fang, S. Bai, X. Liu, M. Chen, and J. Bai. 2011. Application of a three-dimensional eutrophication model for the Beijing Guanting Reservoir, China. Ecological Modelling 222(8):1491–1501. doi:10.1016/j.ecolmodel.2010.12.006.

Hijmans, R.J., J. van Etten. 2012. raster: Geographic analysis and modeling with raster data. R package version 2.0-12. http://CRAN.R-project.org/package=raster

Holland, J.F., J.F. Martin, T. Granata, V. Bouchard, M. Quigley, and L.Brown. 2004. Effects of wetland depth and flow rate on residence time distribution characteristics. Ecological Engineering 23(3):189–203. doi:10.1016/j.ecoleng.2004.09.003.

Huang, W., X. Liu, and X. Chen. 2008. Numerical modeling of hydrodynamics and salinity transport in little manatee river. Journal of Coastal Research, January, 13–24. doi:10.2112/1551-5036-52.sp1.13.

Irwin, J.S. 1979. A theoretical variation of the wind profile power-law exponent as a function of surface roughness and stability. Atmospheric Environment (1967) 13(1):191–94. doi:10.1016/0004-6981(79)90260-9.

Jenkins, G.A., and M. Greenway. 2005. The hydraulic efficiency of fringing versus banded vegetation in constructed wetlands. Ecological Engineering 25(1):61–72. doi:10.1016/j.ecoleng.2005.03.001.

Jin, K-R., J.H. Hamrick, and T. Tisdale. 2000. Application of three-dimensional hydrodynamic model for Lake Okeechobee. Journal of Hydraulic Engineering: (ASCE)." doi:10.1061/(ASCE)0733-9429(2000)126:3A10(758).

Jin, K-R., and Z-G. Ji. 2013. A long term calibration and verification of a submerged aquatic vegetation model for Lake Okeechobee. Ecological Processes 2(1):1–13. doi:10.1186/2192-1709-2-23.

Jin, K-R., Z-G. Ji, and J.H. Hamrick. 2002. Modeling winter circulation in Lake Okeechobee, Florida. Journal of Waterway, Port, Coastal, and Ocean Engineering 128 (3): 114–25. doi:10.1061/(ASCE)0733-950X(2002)128:3(114).

Jin, K-R, Z-G. Ji, and R.T. James. 2007. "Three-dimensional water quality and sav modeling of a large shallow lake." *Journal of Great Lakes Research* 33 (1): 28–45. doi:10.3394/0380-1330(2007)33[28:TWQASM]2.0.CO:2.

Ji, Z-G. 2008. *Hydrodynamics and Water Quality: Modeling Rivers, Lakes, and Estuaries*. John Wiley & Sons, West Sussex, England

Persson J., N. Somes, and T. Wong. 1999. Hydraulics efficiency of constructed wetlands and Ponds. Water Science and Technology 40(3):291-289.

Kadlec, R.H. 1994. Detention and mixing in free water wetlands. Ecological Engineering 3(4):345–80. doi:10.1016/0925-8574(94)00007-7.

Kadlec, R.H., and S. Wallace. 2008. *Treatment Wetlands, Second Edition*. CRC Press. Boca Raton, FL., U.S.A.

Keefe, S.H., J.S. Thullen Daniels, R.L. Runkel, R.D. Wass, E.A. Stiles, and L.B. Barber. 2010. Influence of hummocks and emergent vegetation on hydraulic performance in a surface flow wastewater treatment wetland. Water Resources Research 46(11). doi:10.1029/2010WR009512.

Koberg, G.E. 1964. Methods to compute long-wave radiation from the atmosphere and reflected solar radiation from a water surface. US Government Printing Office.

Legates, D.R., and G.J. McCabe. 1999. Evaluating the use of 'goodness-of-fit' measures in hydrologic and hydroclimatic model validation. Water Resources Research 35(1):233–41. doi:10.1029/1998WR900018.

Levenspiel, O. 2011. *Tracer Technology: Modeling the Flow of Fluids*. Springer Science & Business Media, Berlin, Germany

Li, Y., K. Acharya, D. Chen, and M. Stone. 2010. Modeling water ages and thermal structure of Lake Mead under changing water levels. Lake and Reservoir Management 26(4):258–72. doi:10.1080/07438141.2010.541326.

Li, Yiping, C.T., J. Zhu, B. Pan, D.O. Anim, Y. Ji, Z. Yu, and K. Acharya. 2015. Parametric uncertainty and sensitivity analysis of hydrodynamic processes for a large shallow freshwater lake. Hydrological Sciences Journal 60(6):1078–95. doi:10.1080/02626667.2014.948444.

Macdonald, R. J., and A. Ernst. 1986. Disinfection efficiency and problems associated with maturation ponds. Water Science and Technology 18 (10): 19–29.

Martinez, C.J, and W.R Wise. 2003. Analysis of constructed treatment wetland hydraulics with the transient storage model OTIS. Ecological Engineering 20(3):211–22. doi:10.1016/S0925-8574(03)00029-6.

Mellor, G.L., and T. Yamada. 1982. Development of a turbulence closure model for geophysical fluid problems. Reviews of Geophysics 20(4):851–75. doi:10.1029/RG020i004p00851.

Miller, B.A., W.G. Crumpton, and A.G. van der Valk. 2009. Spatial distribution of historical wetland classes on the Des Moines Lobe, Iowa. Wetlands 29(4):1146–52. doi:10.1672/08-158.1.

Min, J-H., and W.R. Wise. 2009. Simulating short-circuiting flow in a constructed wetland: the implications of bathymetry and vegetation effects. Hydrological Processes 23(6):830–41. doi:10.1002/hyp.7219.

Mississippi River/Gulf of Mexico Watershed Nutrient Task Force. 2008. Gulf hypoxia action plan 2008 for reducing, mitigating, and controlling hypoxia in the Northern Gulf of Mexico and improving water quality in the Mississippi River basin. Washington, DC.

Mitsch, W.J., and J.W. Day. 2006. Restoration of wetlands in the mississippi–ohio–missouri (MOM) river basin: Experience and needed research. Ecological Engineering 26(1):55–69. doi:10.1016/j.ecoleng.2005.09.005.

Nield, J.M., J. King, G. F. S. Wiggs, J. Leyland, R.G. Bryant, R.C. Chiverrell, S.E. Darby. 2013. Estimating aerodynamic roughness over complex surface terrain. Journal of Geophysical Research: Atmospheres 118(23):2013JD020632. doi:10.1002/2013JD020632.

Pebesma, E.J. 2004. Multivariable geostatistics in S: The gstat package. Computers & Geosciences 30(7):683–91. doi:10.1016/j.cageo.2004.03.012.

Pedahzur, R., A. M. Nasser, I. Dor, B. Fattal, and H. I. Shuval. 1993. The effect of baffle installation on the performance of a single-cell stabilization pond. Water Science and Technology 27(7-8):45–52.

Persson, J. 2000. The Hydraulic Performance of ponds of various layouts. Urban Water 2(3):243–50. doi:10.1016/S1462-0758(00)00059-5.

Pilgrim, J.M., X. Fang, and H.G. Stefan. 1998. Stream temperature correlations with air temperatures in minnesota: implications for climate warming. Journal of the American Water Resources Association 34(5):1109–21. doi:10.1111/j.1752-1688.1998.tb04158.x.

R Development Core Team (2008). R: A language and environment for statistical computing. R Foundation for Statistical Computing, Vienna, Austria. ISBN 3-900051-07-0, URL http://www.R-project.org.

Shaw, J.K.E., W.F. Watt, J. Marsalek, B.C. Anderson, and A.A. Crowder. 1997. Flow pattern characterization in an urban stormwater detention pond and implications for water quality. Water Quality Research Journal of Canada 32(1)53-71

Smagorinsky, J. 1963. General circulation experiments with the primitive equations. Monthly Weather Review 91(3):99–164. doi:10.1175/15200493(1963)091<0099:GCEWTP>2.3.CO;2.

Smart, P. L., and I. M. S. Laidlaw. 1977. An evaluation of some fluorescent dyes for water tracing. Water Resources Research 13(1):15–33. doi:10.1029/WR013i001p00015.

Sweeney, D. G., J. B. Nixon, N. J. Cromar, and H. J. Fallowfield. 2005. Profiling and modelling of thermal changes in a large waste stabilization pond. Water Science and Technology 51(12):163–72.

Thackston, E.L., D.Jr. Shields, and P.R. Schroeder. 1987. Residence time distributions of shallow basins. Journal of Environmental Engineering 113(6):1319–32. doi:10.1061/(ASCE)0733-9372(1987)113:6(1319).

Thirumurthi, D. 1974. Design criteria for waste stabilization ponds. Journal of the Water Pollution Control Federation 46(9):2094–2106.

Walker, D.J. 1998. Modelling residence time in stormwater ponds. Ecological Engineering 10(3):247–62. doi:10.1016/S0925-8574(98)00016-0.

Watters, G.Z., K.A. Mangelson, and R.L. George. 1973. The hydraulics of waste stabilization ponds. Final Report to the Office of Water Resources Research on Project A-008-Utah. Utah State University.

Werner, T.M., and R.H. Kadlec. 1996. Application of residence time distributions to stormwater treatment systems. Ecological Engineering 7(3):213–34. doi:10.1016/0925-8574(96)00013-4.

Willmott, C.J., S.G. Ackleson, R.E. Davis, J.J. Feddema, K.M. Klink, D.R. Legates, J. O'Donnell, and C.M. Rowe. 1985. Statistics for the evaluation and comparison of models. Journal of Geophysical Research: Oceans 90(C5):8995–9005. doi:10.1029/JC090iC05p08995.

Wool, T.A., S.R. Davie, and H.N. Rodriguez. 2003. Development of three-dimensional hydrodynamic and water quality models to support total maximum daily load decision process for the Neuse River Estuary, North Carolina. Journal of Water Resources Planning and Management 129(4):295–306.

Wu, J. 1969. An estimation of wind effects on dispersion in wide channels. Water Resources Research 5(5):1097–1104. doi:10.1029/WR005i005p01097.

Wu, G., and Z. Xu. 2011. Prediction of algal blooming using efdc model: Case study in the Daoxiang Lake. Ecological Modelling 222(6):1245–52. doi:10.1016/j.ecolmodel.2010.12.021.

Zenger, K. 2003. Modelling, Analysis and controller design of time-variable flow processes. Espoo: Helsinki University of Technology.

Zhang, C., X. Gao, L. Wang, and Y. Chen. 2013. Analysis of agricultural pollution by flood flow impact on water quality in a reservoir using a three-dimensional water quality model. Journal of Hydroinformatics 15(4):1061–72. doi:10.2166/hydro.2012.131.

Zoppou, C. 1999. Reverse routing of flood hydrographs using level pool routing. Journal of Hydrologic Engineering 4(2):184–88.

Zuber, A. 1986. On the interpretation of tracer data in variable flow systems. Journal of Hydrology 86(1–2):45–57. doi:10.1016/0022-1694(86)90005-3.

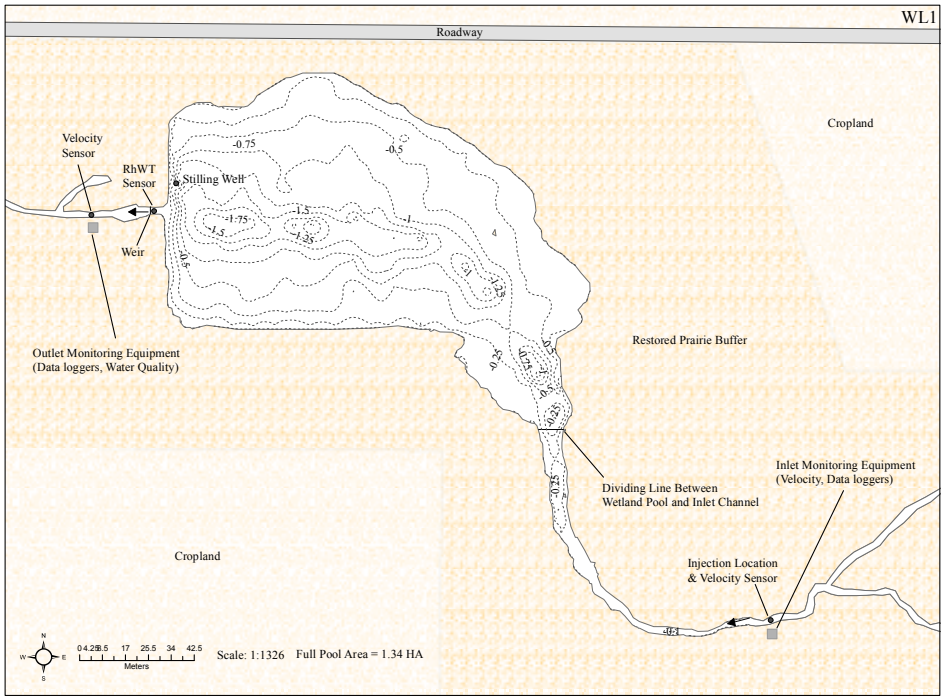

Figure 1. April, 2010 Bathymetry

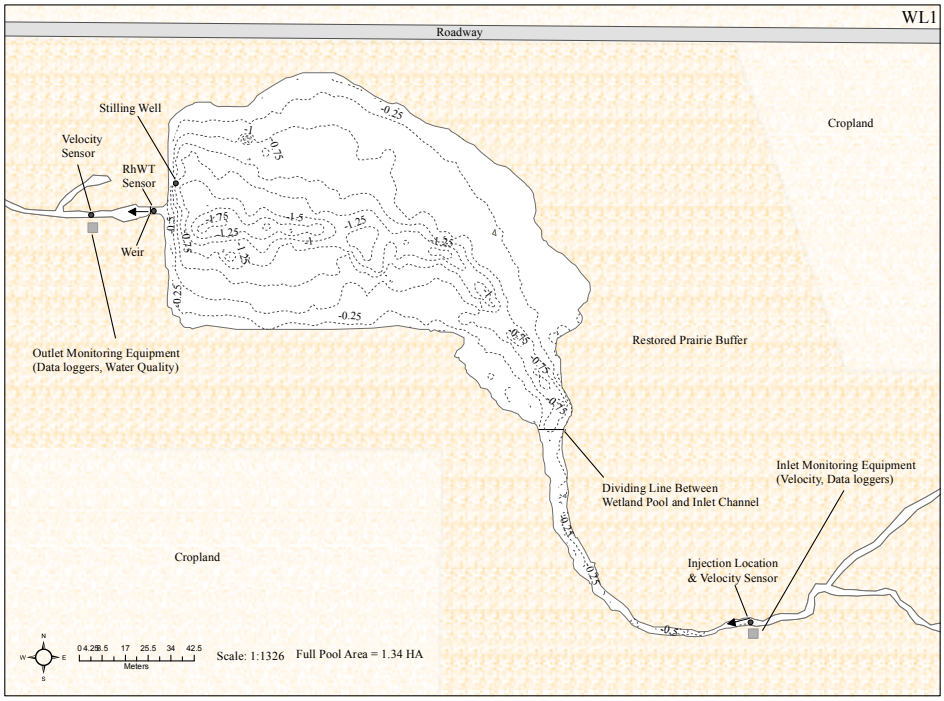

Figure 2. April, 2011 Bathymetry

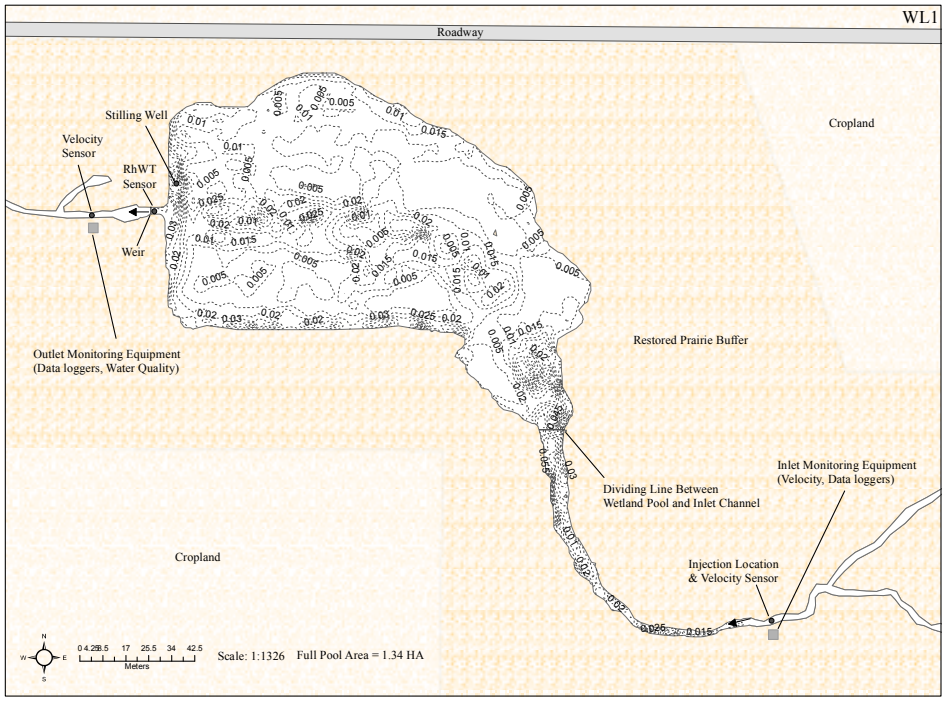

Figure 3. Derived roughness heights (m) for the April, 2010 bathymetric survey

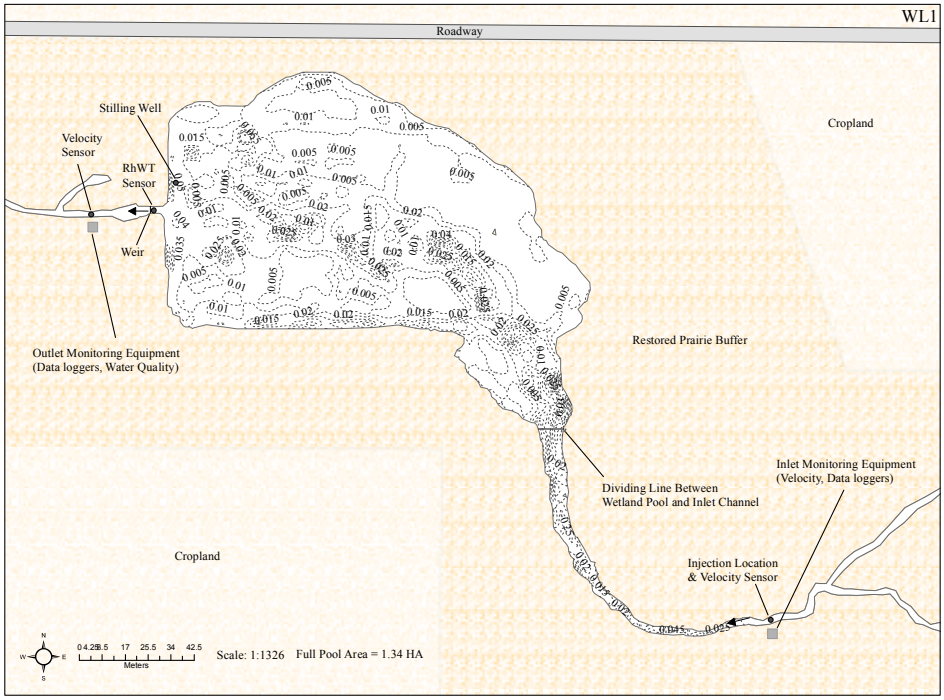

Figure 4. Derived roughness heights (m) for the April, 2011 bathymetric survey

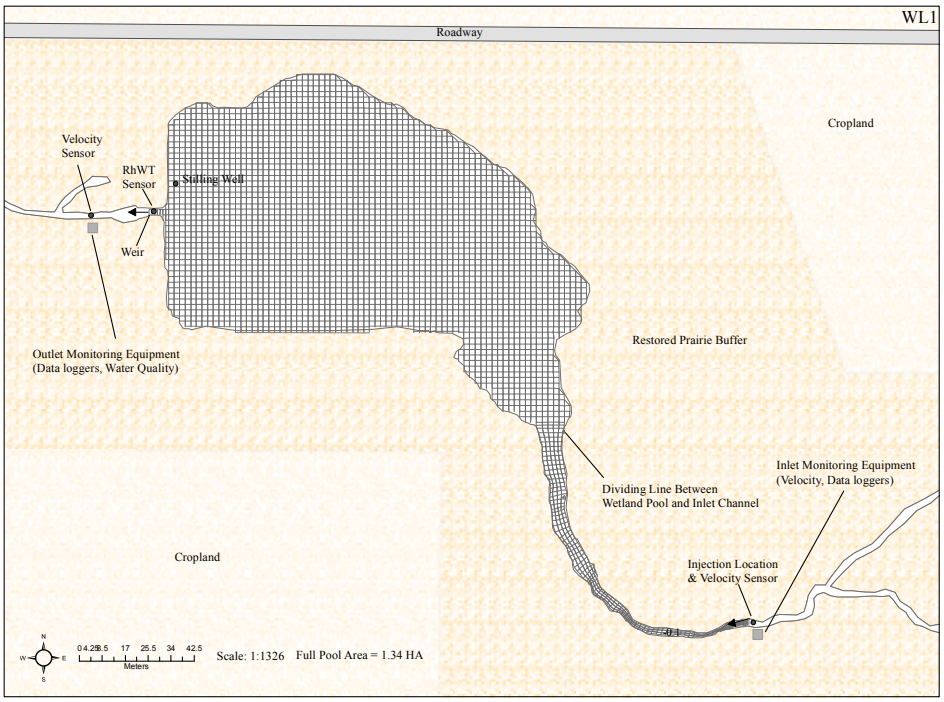

Figure 5. EFDC model grid used for all simulations. The August, 2010 floods caused a reconfiguration of the basin bathymetry, but did not affect the planar shape of the system.

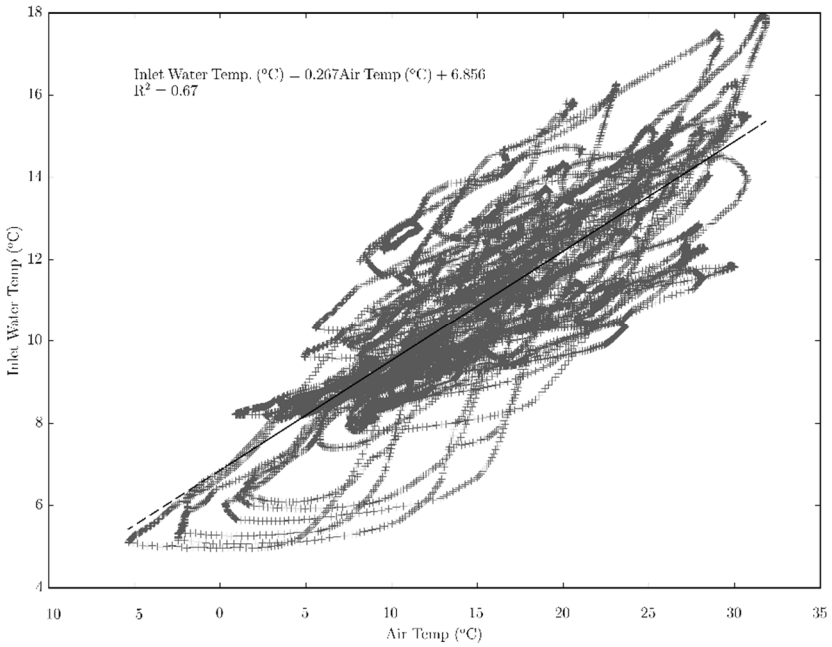

Figure 6. Linear regression of air and inlet water temperatures for the period 3/31/2012 - 6/1/2012. The resulting model was used to estimate inlet boundary temperatures for the model simulations.

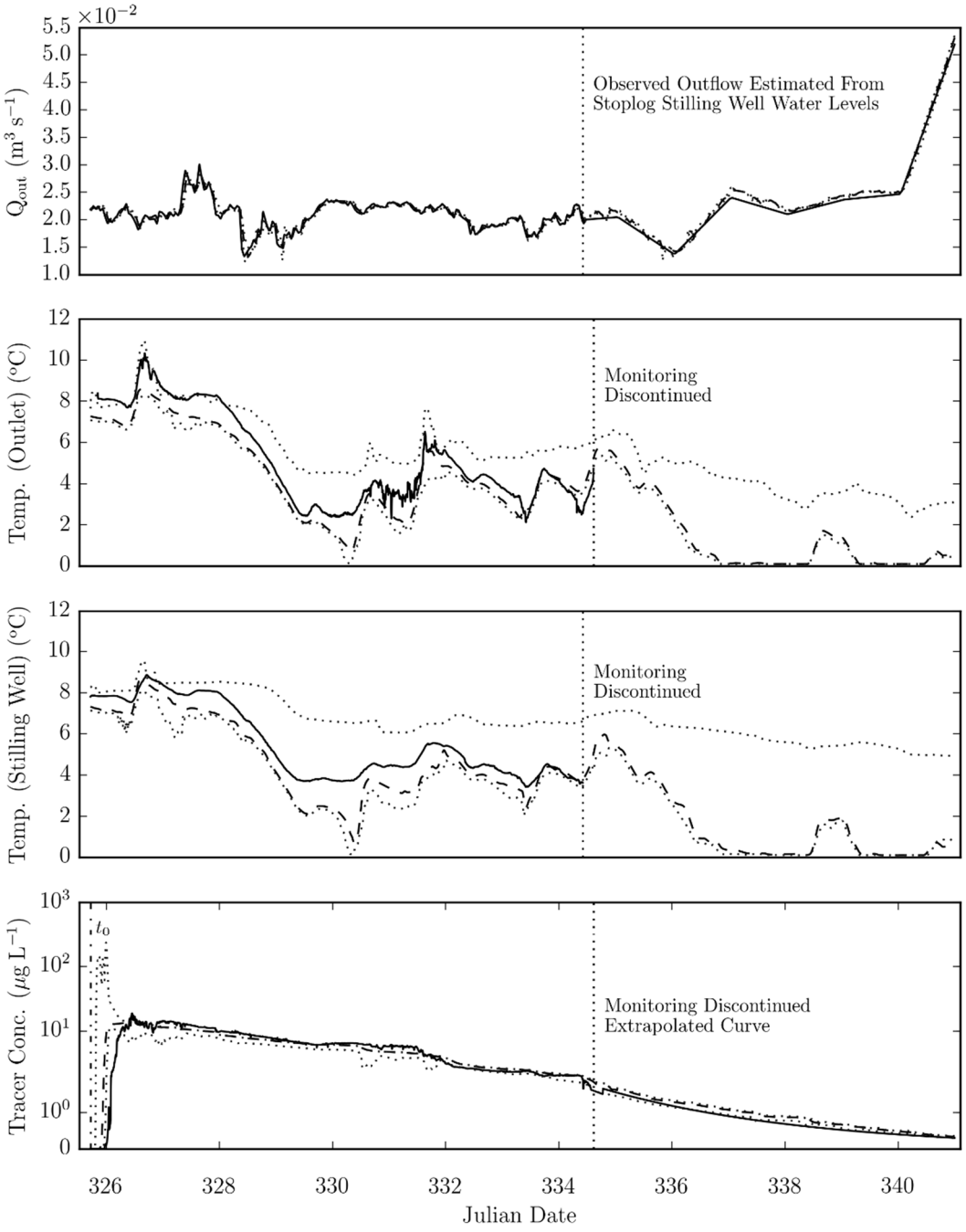

Figure 7. Time-series plots illustrating the correspondence between modeled and simulated variables for the study WL1_1 conducted over the period 11/22/09 - 12/7/09. The solid black line and thick dashed lines represent the observed and modeled variables, respectively. The minimum-maximum prediction envelope for each variable is shown as the lighter dashed lines. The initial time of tracer injection is shown as a vertical dashed line in the bottom panel. Temperature and dye concentration monitoring were discontinued for this study on 12/1/09 because of freezing temperatures (marked by lighter vertical dashed lines).

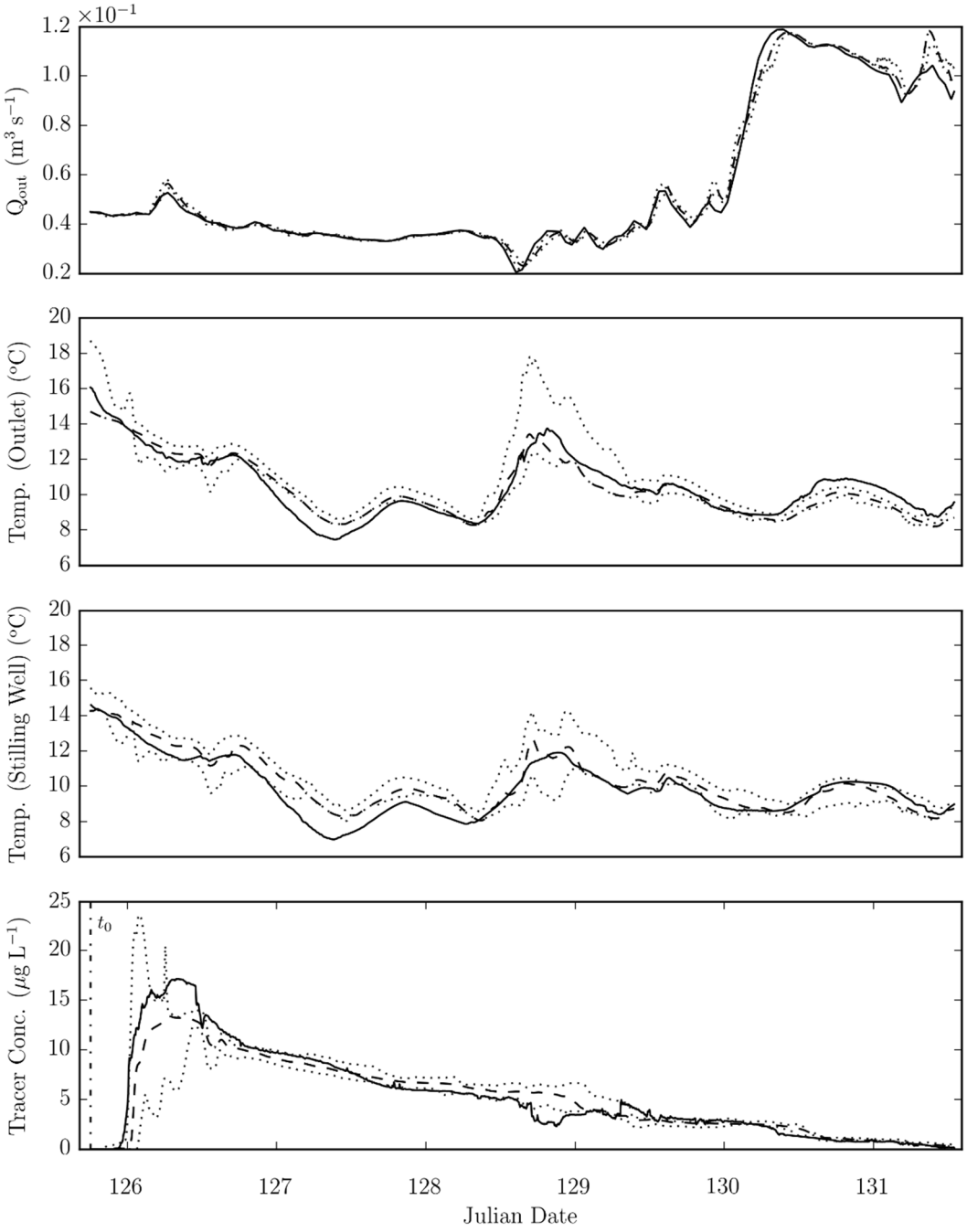

Figure 8. Time-series plots illustrating the correspondence between modeled and simulated variables for the study WL_2 conducted over the period 5/6/10 - 5/12/10. For each panel, the solid black line and thick dashed line represent the observed and modeled variables, respectively. The minimum-maximum prediction envelope for each variable is shown as the lighter dashed lines. The initial time of tracer injection is shown as a vertical dashed line in the bottom panel.

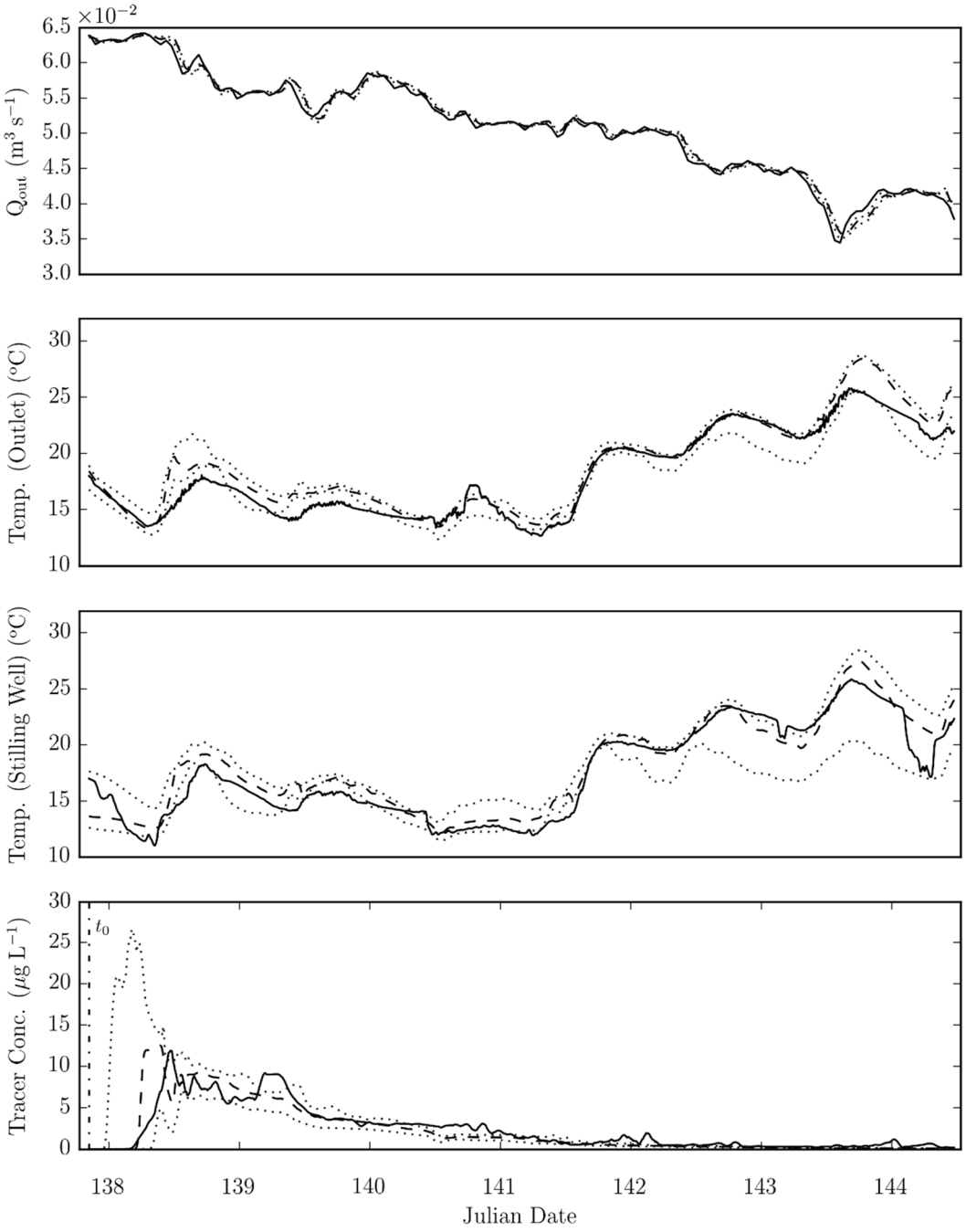

Figure 9. Time-series plots illustrating the correspondence between modeled and simulated variables for the study WL1_3 conducted over the period 5/18/10 - 5/25/10. For each panel, the solid black line and thick dashed line represent the observed and modeled variables, respectively. The minimum-maximum prediction envelope for each variable is shown as the lighter dashed lines. The initial time of tracer injection is shown as a vertical dashed line in the bottom panel.

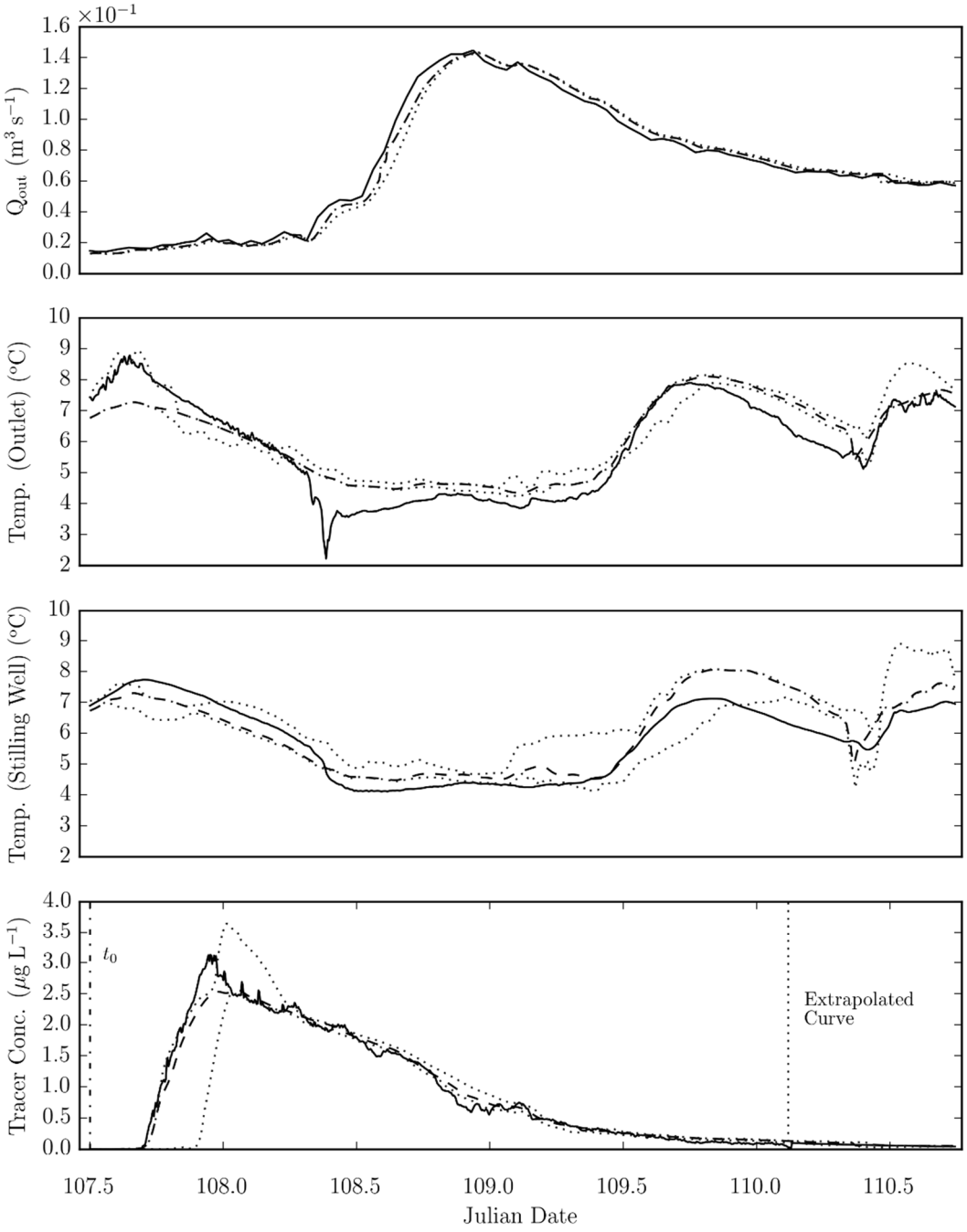

Figure 10. Time-series plots illustrating the correspondence between modeled and simulated variables for the study WL1_10 conducted over the period 4/18/11 - 4/21/11. For each panel, the solid black line and thick dashed line represent the observed and modeled variables, respectively. The minimum-maximum prediction envelope for each variable is shown as the lighter dashed lines. The initial time of tracer injection is shown as a vertical dashed line in the bottom panel.

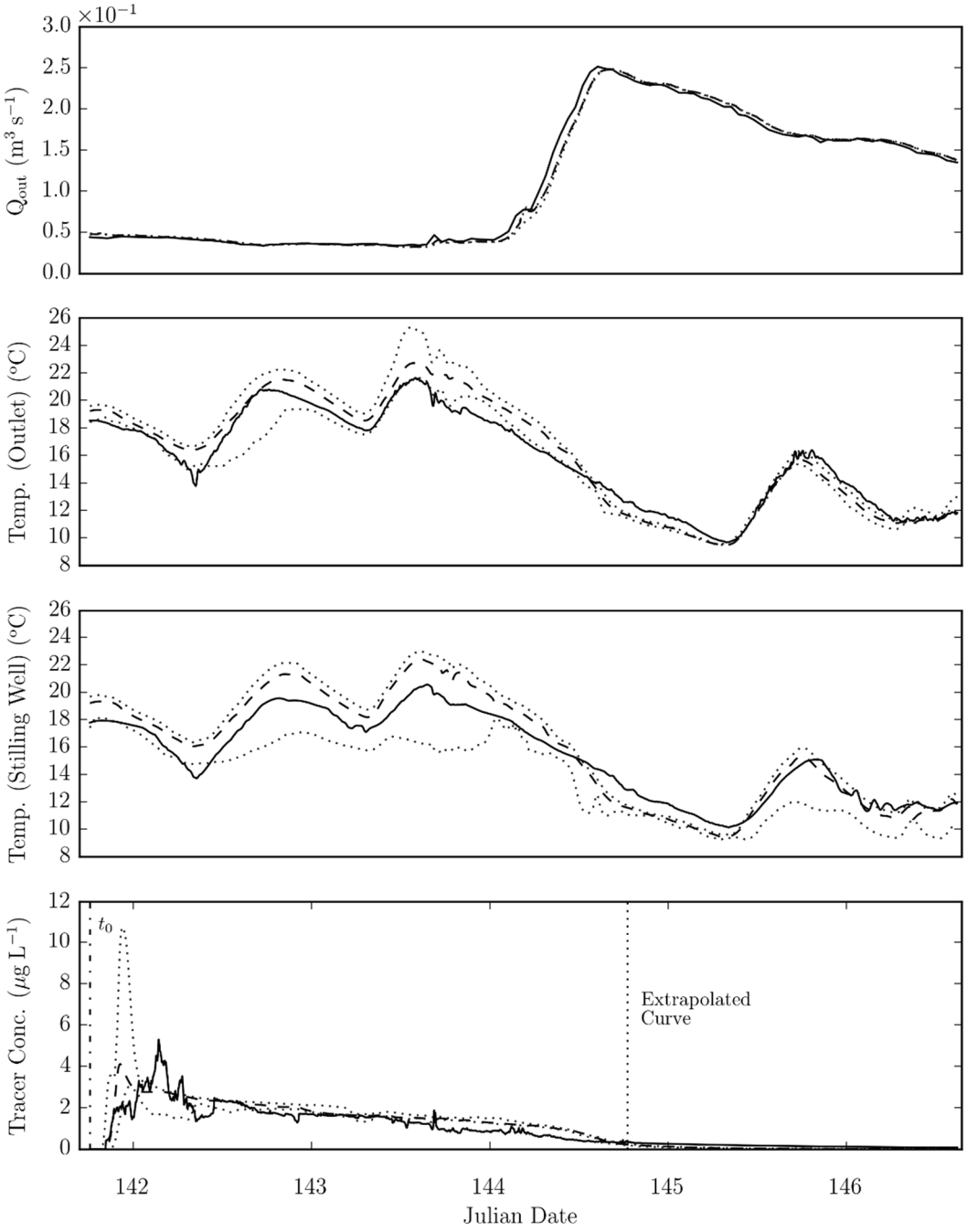

Figure 11. Time-series plots illustrating the correspondence between modeled and simulated variables for the study WL1_11 conducted over the period 5/22/11 - 5/27/11. For each panel, the solid black line and thick dashed line represent the observed and modeled variables, respectively. The minimum-maximum prediction envelope for each variable is shown as the lighter dashed lines. The initial time of tracer injection is shown as a vertical dashed line in the bottom panel. Tracer concentration monitoring was discontinued on 5/25/11 because of sensor malfunction.

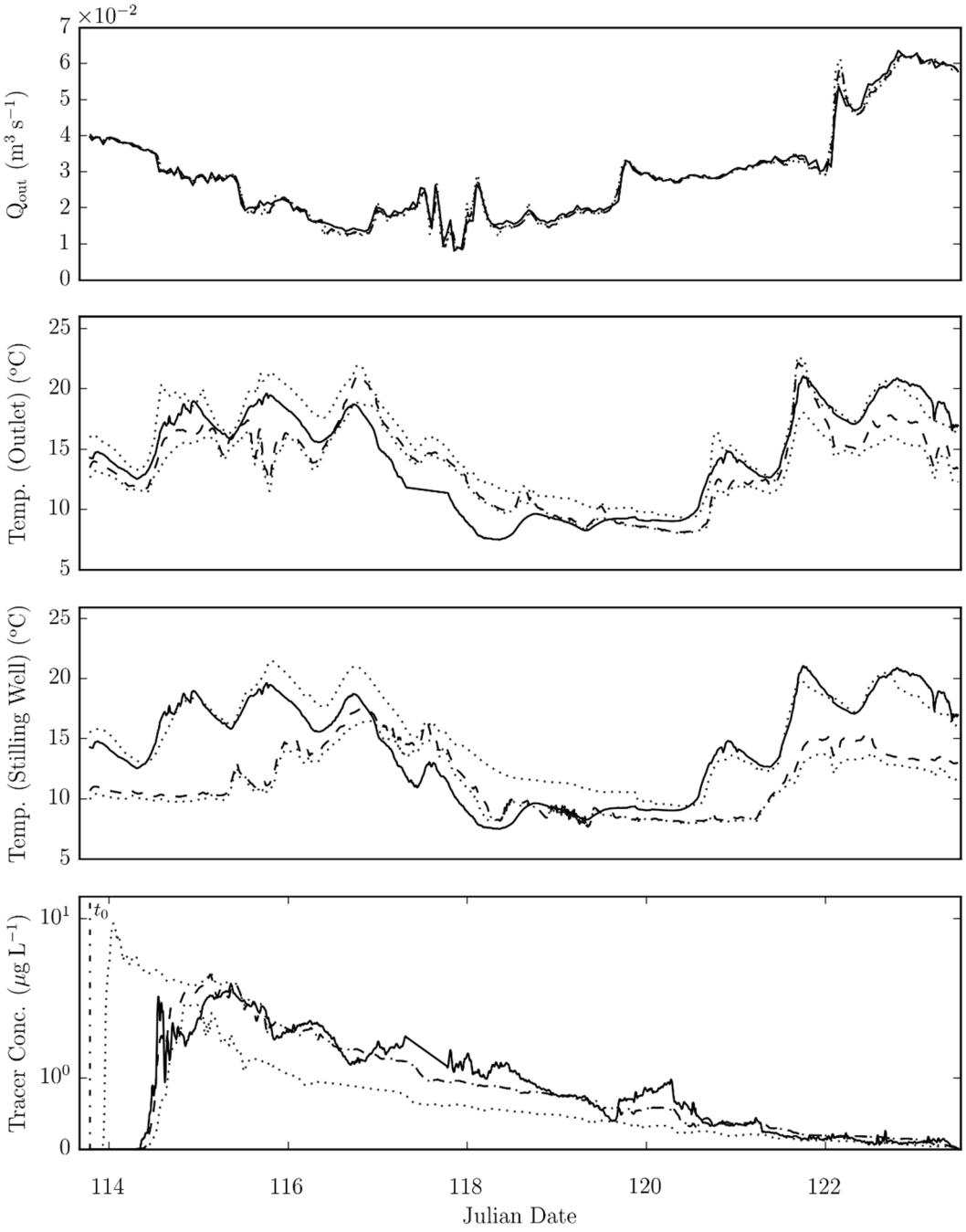

Figure 12. Time-series plots illustrating the correspondence between modeled and simulated variables for the study WL1_13 conducted over the period 4/23/12 - 5/3/12. For each panel, the solid black line and thick dashed line represent the observed and modeled variables, respectively. The minimum maximum prediction envelope for each variable is shown as the lighter dashed lines. The initial time of tracer injection is shown as a vertical dashed line in the bottom panel.

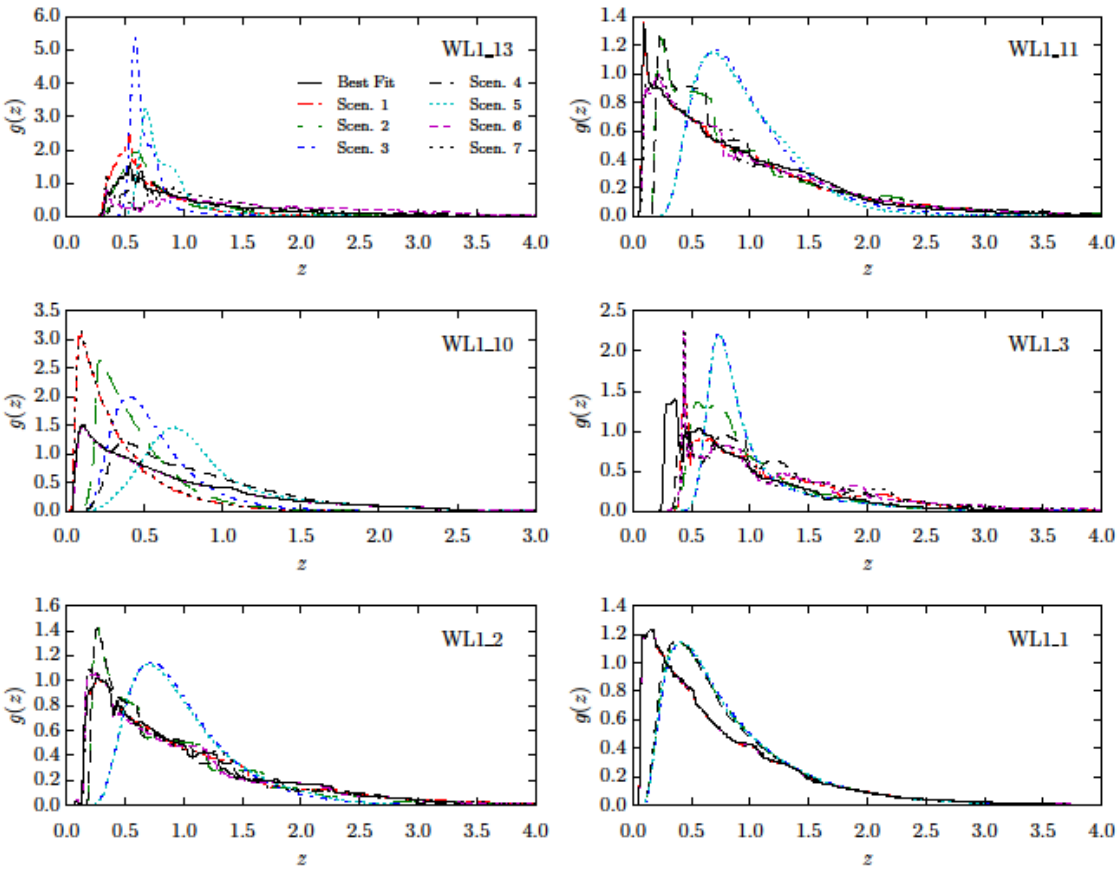

Figure 13. Simulated RTD curves for each tested scenario, as enumerated in Table 6. The base-line best-fit simulated RTD is given for reference.

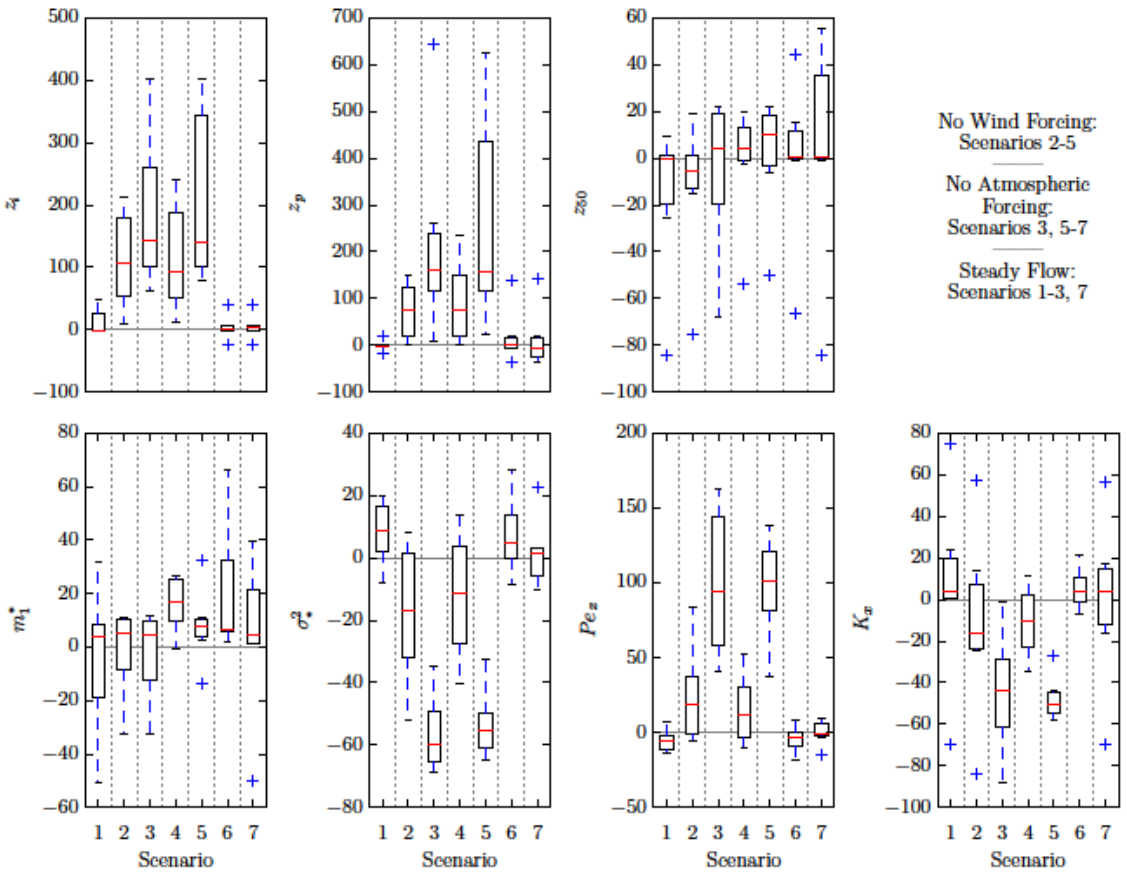

Figure 14. Box plots showing the percent deviation from the base-line best-fit simulation for each considered RTD characteristic and derived mixing metric for each tested scenario. The y axes represent percentage deviation from the best-fit cases.

Table 1. Selected tracer studies conducted on WL1 during the period 11/2009 - 4/2012.

Study	Date/Time Start	Date/Time End	Length (days)	Mass Inj.(kg)	Mass Rec. (kg)	Mass Rec. (%)	$\overline{Q_a}$ * (m^3 min^{-1})	$\overline{v_{w(10)}}$ (m s^{-1})
WL1_1	11/22/09	12/9/09 6:42	16.4	0.113	0.092	82	1.3	3.5
WL1_2	5/6/10 18:04	5/13/10 22:50	5.8	0.113	0.11	98	3.1	4.0
WL1_3	5/18/10 20:18	5/25/10 15:28	6.6	0.113	0.076	66	3.1	2.9
WL1_10	4/18/11 12:01	4/21/11 3:10	2.6	0.0226	0.013	55	4.2	4.0
WL1_11	5/22/11 18:09	5/25/11 21:04	4.9	0.0226	0.026	116	6.3	3.5
WL1_13	4/23/12 18:55	5/3/12 12:34	10.8	0.0226	0.017	74	1.8	3.4

*Equals the average of the instantaneous inflow and outflow rates.

Table 2. Estimated bulk morphometric characteristics resulting from each bathymetric survey.

Survey Date(s)	Survey Points	Volume-Depth Equation	Area-Depth Equation	$\overline{H_k}$ (m)	$H_{k(\max)}$ (m)	$\overline{z_0}$ (m)
4/11/2010; 4/12/2010	449	$V_s = 213.3H^6 + 733H^5 + 241.4H^4 + 120.8H^3 + 6449H^2 + 13411H+8008$	$A_s = 851.3H^6 + 4715.1H^5 + 7907.2H^4 - 2030.1H^3 - 512.4H^2 + 12624.7H + 13438$	0.59	1.96	0.011
4/2/2011	789	$V_s = -192.3H^4 + 1034.3H^3 + 7501.7H^2 + 13021H+7193$	$A_s = 1567.2H^6 + 6624.1H^5 + 6884.3H^4 - 3261.5H^3 - 2073.6H^2 + 14512H + 13347$	0.52	1.81	0.01

Table 3. Initial conditions for each simulation.

Study	z_0 (m)*	T_0 (°C)	T_{b0} (°C)
WL1_1	0.03	7	7
WL1_2	0.03	12	10
WL1_3	0.03	12	10
WL1_10	0.03	8	8
WL1_11	0.03	12	12
WL1_13	0.01	10	10

*Initial depth above the full pool elevation

Table 4. Parameter values for each 'best-fit' calibrated simulation.

Study	A_{vo} ($m^2\ s^{-1}$)	A_{ho} ($m^2\ s^{-1}$)	f_r (-)	λ ($m\ day^{-1}$)	% Rec	β (day^{-1})
WL1_1	1E-4	0.025	0.45	0.2	80	0.051
WL1_2	1E-4	0.01	0.9	0.45	98	0.008
WL1_3	2.5E-4	0.001	0.45	0.50	66	0.225
WL1_10	1E-6	0.01	0.9	0.45	55	0.425
WL1_11	1E-5	0.01	0.9	0.45	100	0
WL1_13	7.5E-4	0.0001	0.9	0.45	73	0.082

Table 5. Simulation performance indices and statistics.

Study	WL1_1	WL1_2	WL1_3	WL1_10	WL1_11	WL1_13	CV
Water Surface Elevation (WSE)*							
MIA	0.32	0.76	0.40	0.62	0.85	0.70	0.31
MAE (m)	2E-3	4E-3	5E-3	9E-3	5E-3	2.3E-3	0.51
MARE (%)	0.10	0.05	0.10	0.43	0.07	0.02	1.07
RRMSE (%)	18.50	13.20	32.40	25.60	12.50	11.35	0.41
ΔMax (m)	5E-3	0.012	0.015	0.017	0.012	0.015	0.30
Volume							
MIA	0.36	0.74	0.32	0.53	0.80	0.97	0.38
MAE (m^3)	41.70	2.64	79.30	152	50.56	26.50	0.81
MARE (%)	0.51	0.03	0.95	2.01	0.67	0.36	0.83
RRMSE (%)	36.60	12.6	45.01	31.80	12.72	12.61	0.52
ΔMax (m^3)	11.80	148.1	270.3	266.80	123.72	115.6	0.58
Outflow Discharge							
MIA	0.86	0.96	0.95	0.95	0.97	0.97	0.04
MAE ($m^3\ s^{-1}$)	1E-5	6E-4	1.8E-4	4E-4	2E-3	2.8E-4	1.14
MARE (%)	0.05	1.09	0.35	0.60	3.07	0.95	0.96
RRMSE (%)	4.76	3.12	2.62	3.37	3.23	2.13	0.25
ΔMax ($m^3\ s^{-1}$)	3E-3	0.01	1.8E-3	0.014	0.025	7.1E-3	0.77
Outlet Temperature							
MIA	0.84	0.83	0.87	0.80	0.79	0.82	0.03
MAE (°C)	0.65	0.07	0.76	0.25	0.76	0.42	0.54
MARE (%)	11.44	0.63	4.17	4.31	4.35	2.98	0.71
RRMSE (%)	9.50	6.76	9.25	9.41	10.96	15.07	0.25
ΔMax (°C)	1.82	1.36	1.27	1.53	1.31	7.06	0.88
Stilling Well Temperature							
MIA	0.78	0.79	0.86	0.77	0.71	0.67	0.08
MAE (°C)	0.75	0.38	0.58	0.27	0.95	2.32	0.78
MARE (%)	12.8	3.80	3.31	4.58	5.60	16.34	0.64
RRMSE (%)	17.8	9.15	8.61	16.27	16.18	28.54	0.41
ΔMax (°C)	3.03	0.64	3.38	0.75	1.94	8.74	0.89
Tracer Concentration							
MIA	0.79	0.87	0.83	0.95	0.75	0.88	0.08
MAE ($\mu g\ L^{-1}$)	0.39	0.22	0.10	0.002	0.21	0.02	0.85
MARE (%)	6.21	4.25	4.16	0.30	15.6	1.85	0.91
RRMSE (%)	11.74	8.85	13.10	3.98	9.50	8.10	0.31
ΔMax ($\mu g\ L^{-1}$)	5.16	9.10	6.24	0.67	2.52	1.19	0.72

*Water surface elevation measured at the stilling well.

Table 6. Comparison between observed and simulated RTD temporal characteristics and mixing indices. The subscripts m and o represent modeled and observed values, respectively.

Study	WL1_1	WL1_2	WL1_3	WL1_10	WL1_11	WL1_13	CV
$z_{i(o)}$	0.068	0.091	0.22	0.038	0.043	0.25	0.71
$z_{i(m)}$	0.045	0.091	0.24	0.034	0.05	0.28	0.80
$\|\%\Delta\|$	33.2	0	10.5	11.3	18.5	~12	0.74
$z_{p(o)}$	0.168	0.28	0.41	0.10	0.18	0.60	0.59
$z_{p(m)}$	0.163	0.26	0.36	0.11	0.09	0.54	0.62
$\|\%\Delta\|$	2.9	6.6	12.9	~11.1	~50	9.8	0.46
$z_{50(o)}$	0.65	0.65	0.89	0.51	0.92	0.82	0.20
$z_{50(m)}$	0.57	0.78	0.75	0.52	0.72	0.83	0.16
$\|\%\Delta\|$	5.8	20.4	16.1	0.74	~22	1.9	0.87
$m^*_{1(o)}$	0.79	0.89	1.09	0.67	1.42	1.07	0.25
$m^*_{1(m)}$	0.76	0.98	0.91	0.68	0.93	1.04	0.14
$\|\%\Delta\|$	3.2	10.1	16.5	~1.4	~35	~3.1	0.52
$m^*_{2c(o)}$	0.38	0.47	0.46	0.29	2.1	0.51	0.90
$m^*_{2c(m)}$	0.41	0.50	0.33	0.30	0.61	0.40	0.25
$\|\%\Delta\|$	~9.6	~6.4	28.2	5.4	70.9	~22.2	0.78
$o^{2*}_{(o)}$	0.61	0.59	0.38	0.64	0.94	0.42	0.31
$\sigma^{2*}_{(m)}$	0.71	0.52	0.39	0.66	0.71	0.37	0.25
$\|\%\Delta\|$	~16.9	9.4	~2.9	~2.6	~25	~12	0.00
$Pe_{x(\mathrm{o})}$	4.41	4.5	6.4	4.2	3.2	5.9	0.22
$Pe_{x(\mathrm{m})}$	3.9	4.97	6.3	4.1	3.9	6.6	0.22
$\|\%\Delta\|$	11.65	~8.2	2.4	~2	~24	~11	0.66
$K_{x(\mathrm{o})}$	3.62	7.0	6.9	9.3	18.4	4.1	0.60
$K_{x(\mathrm{m})}$	4.1	6.4	7.1	9.6	11	3.4	0.39
$\|\%\Delta\|$	13.1	~7.0	~4.2	3.6	~40	~18	0.57

*K_x is expressed in $m^2\ min^{-1}$. All other parameters are dimensionless.

Table 7. Tested sensitivity analysis scenarios

Scenario	Applied Environmental Effects
1	Applied wind series; Steady flow equal to the flow at dye injection; Applied atmospheric forcing
2	No applied wind series; Steady flow equal to the flow at dye injection; Applied atmospheric forcing
3	No applied wind series; Steady flow equal to the flow at dye injection; No applied atmospheric forcing
4	No applied wind series; Dynamic flow boundary conditions; Applied atmospheric forcing
5	No applied wind series; Dynamic flow boundary conditions; No applied atmospheric forcing
6	Applied wind series; Dynamic flow boundary conditions; No applied atmospheric forcing
7	Applied wind forcing; Steady flow equal to the flow at dye injection; No applied atmospheric forcing

Table 8. Estimated RTD temporal features and derived mixing metrics for each tested scenario. Values contained within the parentheses represent the percent deviation from the best-fit simulation for each tracer study.

Study	Scen.	$z_{i(m)}$	$z_{p(m)}$	$z_{50(m)}$	$m^{*}_{1(m)}$	$\sigma^{2*}_{(m)}$	$Pe_{x(m)}$	$K_{x(m)}$
	1	0.05(-1%)	0.17(0.8%)	0.58(1.4%)	0.78(2%)	0.73(3.4%)	3.8(-2.5%)	4.4(6.3%)
	2	0.10(124%)	0.38(130%)	0.68(19%)	0.85(11%)	0.48(-33%)	5.4(38%)	3.1(-25%)
	3	~0.10(117%)	0.41(150%)	0.69(21%)	0.85(12%)	0.46(-35%)	5.5(41%)	3.0(-26%)
WL1_1	4	0.09(100%)	0.37(127%)	0.66(16%)	0.83(9%)	0.50(-30%)	5.2(33%)	3.1(-25%)
	5	~0.1(112%)	0.41(150%)	0.68(19%)	0.85(11%)	0.48(-33%)	5.4(37%)	3.0(-27%)
	6	0.05(0.3%)	0.17(2%)	0.57(0.62%)	0.78(1.7%)	0.74(5%)	3.7(-3.4%)	4.2(3.6%)
	7	0.04(-1%)	0.17(3%)	0.84(47%)	0.78(2%)	0.73(3.4%)	3.8(-2.5%)	4.4(6.3%)
	1	0.12(36%)	0.26(-2%)	0.79(1%)	1.07(9%)	0.63(20%)	4.3(-14%)	7.9(24%)
	2	0.17(89%)	~0.26(0%)	0.75(-4%)	0.98(0.3%)	0.56(8%)	4.7(-6%)	7.3(14%)
	3	0.25(170%)	0.7(167%)	0.89(14%)	1(1.5%)	0.21(-60%)	10.8(117%)	3.2(-51%)
WL1_2	4	0.17(89%)	0.26(0%)	0.76(-2.7%)	~1(-0.8%)	0.55(3.9%)	4.8(-4.2%)	6.6(3.8%)
	5	0.25(170%)	0.7(167%)	0.89(14%)	1(2.8%)	0.21(-60%)	10.7(114%)	~3(-54%)
	6	0.07(-25%)	0.24(-6.7%)	0.79(1%)	~1(6%)	0.67(28%)	4.1(-18%)	7.8(21%)
	7	0.07(-25%)	0.19(-30%)	0.79(0.87)	~1(7%)	0.64(23%)	4.2(-15%)	7.5(17%)
	1	0.35(49%)	0.43(21%)	0.99(9.3%)	1.2(32%)	0.36(-7.8%)	6.7(7.1%)	7.2(~1%)
	2	0.34(43%)	0.55(52%)	0.83(-7.6)	1(10%)	0.28(-29%)	8.5(35%)	5.7(-20%)
	3	0.47(97%)	0.74(104%)	0.85(-6.6%)	1(10.6%)	0.21(-46%)	10.7(70%)	4.5(-37%)
WL1_3	4	0.33(37%)	0.43(18%)	0.95(5.3%)	1.1(23%)	0.31(-21%)	7.6(22%)	5.8(-19%)
	5	0.47(97%)	0.73(103%)	0.85(-6.4%)	1(9.5%)	0.19(-51%)	11.8(87.4%)	3.7(-48%)
	6	0.33(39%)	~0.43(20%)	1(15%)	1.3(41%)	0.39(-1.7%)	6.4(1.4%)	6.9(-3%)
	7	0.33(40%)	0.44(21%)	0.90(-1%)	1.3(40%)	0.36(-8%)	6.7(7.3%)	7.2(~1%)
	1	0.04(-2.5%)	0.09(-16%)	0.25(-84%)	0.3(-51%)	0.67(1.6%)	4.1(-1.3%)	2.6(-69%)
	2	0.10(196%)	0.22(99%)	0.39(-75%)	0.46(-32%)	0.32(-52%)	7.6(83.5%)	1.4(-84%)
	3	0.13(291%)	0.40(263%)	0.5(-68%)	0.56(-17%)	0.22(-67%)	10.4(153%)	1(-88.1%)
WL1_10	4	0.11(241%)	0.37(235%)	0.72(-54%)	0.86(26%)	0.39(-41%)	6.3(53%)	5.5(-35%)
	5	0.17(400%)	0.69(526%)	0.78(-50%)	0.90(33%)	0.25(-62%)	9.2(123%)	3.8(-55%)
	6	0.04(3%)	0.11(0.4%)	0.53(-66%)	0.72(6.3%)	0.77(17%)	3.7(-11%)	9.5(12.9%)
	7	0.03(0.34%)	0.09(-15%)	0.25(-84%)	0.34(-50%)	0.66(~0%)	4.1(~0%)	2.9(-70%)
	1	0.05(-1%)	0.09(-1.5%)	0.71(-1.3%)	0.98(5.2%)	0.8(14%)	3.5(-9.7%)	11.1(1%)
	2	0.15(211%)	0.24(151%)	0.74(2.2%)	~1(11%)	0.68(-4.5%)	~4(3.7%)	9.7(-12%)
	3	0.25(-13%)	0.7(644%)	0.88(22%)	0.99(7%)	0.22(-68%)	10(162%)	3.8(-65%)
WL1_11	4	0.16(218%)	0.24(156%)	0.75(3.7%)	~1(10.5%)	0.69(-2.3%)	~4(2%)	10.8(-2 %)
	5	0.25(402%)	0.68(625%)	0.88(22%)	0.99(7%)	0.25(-65%)	9.3(138%)	4.6(-58%)
	6	0.05(-1%)	0.22(139%)	0.72(-1%)	0.98(6.3%)	0.74(4.7%)	3.8(-3.6%)	11.4(3.7%)
	7	~0.05(4%)	0.23(144%)	0.73(0.5%)	0.94(~1%)	0.64(-10%)	4.3(9%)	9.2(-16%)
	1	0.28(-2.1%)	0.54(-0.4%)	0.62(-26%)	0.77(-25%)	0.43(17%)	5.8(-12.5%)	5.9(75%)
	2	0.31(10.5%)	0.59(8.8%)	0.7(-15.2%)	0.92(-12%)	0.38(3.7%)	6.4(-3.1%)	5.3(57.5%)
	3	0.46(62%)	0.59(8.3%)	0.63(-24%)	0.7(-32%)	0.15(-60%)	10.2(54.5%)	3.3(-1.2%)
WL1_13	4	0.32(38.6%)	0.66(13%)	0.99(19.5%)	1.3(26%)	0.42(13.8%)	5.9(19.5%)	3.8(11.5%)
	5	0.5(78%)	0.68(25%)	0.88(5.7%)	0.9(-14%)	0.19(-49%)	11.9(78.8%)	1.9(-44%)
	6	0.3(7.4%)	0.34(-36%)	0.88(44.3%)	1.7(66.1%)	0.34(-8.6%)	7.2(7.9%)	3.1(-7.3%)
	7	0.30(7%)	0.34(-36%)	1.3(56%)	1.3(26%)	0.38(3.2%)	6.4(-2.7%)	5.3(57%)

CHAPTER 4: THE EFFECTS OF TRACER RESPONSE CURVE SCALING ON ESTIMATION OF RESIDENT TIME DISTRIBUTION MOMENTS OF GENERIC FLOW DOMAINS

A paper to be submitted to the Journal of Hydrology

David I. Green, Greg Stenback, and William G. Crumpton

Abstract

Tracer mass loss during transport in a generic flow domain may result in the under-estimation of key hydraulic properties of the system being studied as based on analysis of the temporal moments of the tracer response curve observed at the domain outflow boundary. A common approach for accounting for mass loss is to scale the observed data by the mass recovered at the system outflow. This technique preserves the geometry of the mass loss-over time relationship, but does not adequately compensate for the effects of mass loss on the magnitude of estimated temporal moments. To address this problem in tracer hydrology, we derive formulas that can be used to algebraically estimate the moments of the conservative 'ideal' residence time distribution curve from an observed mass loss-affected tracer response curve for the individual cases of constant, zero, and first-order mass loss. In addition, the developed formulas allow for accurate estimation of the mass loss coefficient from the moments of the observed residence time distribution for the cases of zero and first-order loss. Numerical simulations (n = 90) of hypothetical residence time distribution curves derived from the mean hydraulic residence time normalized 2-parameter gamma distribution and subjected each to varying magnitudes of zero and first-order loss suggest that the equations

derived for the zero-order mass loss case correctly reproduce the moments of the conservative equivalent curves in addition to the zero-order mass loss coefficient. Error analysis for the first-order mass loss-affected simulated residence time distribution curves indicates that the formulas developed can estimate the conservative equivalent moments and the first-order mass loss coefficient with relative errors of order $O(10^{-2} – 10^{-6})$ and $O(10^{-3} – 10^{-5})$, respectively.

Introduction

Tracer mass loss occurring in a flowing system resulting in incomplete recovery at the domain outlet is known to affect the magnitude of the calculated moments of the developed residence time distribution (RTD) curve, and thus influence the magnitude of estimated system hydraulic and mixing properties (Cirpka and Kitanidis, 2000; Headly and Kadlec, 2007; Kadlec and Wallace, 2009). When a tracer undergoes decay or reaction during transit through a system the tracer response curve observed at the outlet reflects both transport through and mass transformation process occurring within the system. A critical issue that arises from reactive tracer transport is the inherent difficulty in separating, from interpretation of the statistical moments of the observed mass loss–affected response curve, the hydraulic properties of the system from the chemical transport properties of the system. This discrepancy results from a narrowing of the distribution of residence times because of tracer mass loss as determined from the observed mass loss-affected RTD.

The loss of mass during an impulse tracer study results in a deformation of the corresponding tracer response curve observed at the domain outlet. In general, and depending upon the type of mass consumption or transformation process occurring during transit, tracer

loss will cause a reduction of the peak tracer concentration, a narrowing of the total temporal dispersion, and a translation of the centroid of the curve toward the origin (Figure 1). These changes in the tracer response curve and the corresponding developed RTD result in underestimations of some of the critical RTD statistics that lend information about the hydraulics of the system being studied, notably the mean tracer detention time and the temporal variance of the RTD. Mean tracer detention times calculated from tracer response curves that have not been adjusted by the mass fraction recovered so that the zeroth moment evaluates to unity may be significantly underestimated depending upon the process occurring and the magnitude of the tracer mass loss (Kadlec and Wallace, 2008). The estimated value of the principal RTD parameters in each of these cases actually reflects the properties of the combined transport of the reactive tracer and the hydraulics of the flowing system (Maloszewski and Zuber, 1993).

The issue of reactive tracer transport has implications for both long and short-term tracer studies conducted on flowing systems, and in some cases the mass loss-affected tracer response curve is all that is available for interpretation of system hydraulic properties such as the mean residence time (e.g. as discussed in Keefe et al., 2004). If prior knowledge of the predominant type of mass loss or transformation process occurring in the system is known then theoretically there should be a direct way of transforming the observed reactive tracer response curve into a conservative tracer equivalent reflecting the "true" hydraulics of the system. In this work we address the issue of interpreting the actual hydraulic properties of a generic flow system using the moments of the mass loss-affected observed tracer response curve, and develop a set of equations that can be used to directly estimate the moments of the conservative RTD from the calculated moments of the observed non-conservative RTD as

well as respective loss rate coefficients for the cases of constant, zero-order, and first-order tracer mass loss.

Problem Statement

The reactive transport problem can be viewed from the perspective of RTD analysis as the transformation over time of the conservative curve (i.e. the tracer response curve that would be developed for a truly conservative tracer) into the non-conservative case. The rate of transformation is dictated by the predominant mass loss processes occurring in the system, and usually, in the aggregate can be described as constant (i.e. time-invariant), zero-order, or first-order (higher-order processes are not addressed in this work). A commonplace technique in RTD analysis to compensate for incomplete tracer mass recovery is to calculate at each time-step the scaled RTD function using the observed mass of tracer recovered in lieu of the mass of tracer injected (e.g. Holland et al., 2004; Wang and Jawitz, 2006, Headly and Kadlec, 2007; Bodin et al., 2012). This transformation is equivalent to scaling the observed concentration curve by the mass fraction of tracer recovered. Depending upon the underlying mass loss process (as will be shown in following sections), with the exception of the time-invariant case, scaling of the observed RTD function does not result in a geometrically equivalent RTD curve even though the mass recovery of the scaled curve, by definition, is complete (Figure 1). Implicit in this direct scaling is the assumption that the calculated statistical moments of the transformed observed tracer response curve are identical or similar to what would be estimated for an ideal tracer response curve featuring complete mass recovery.

While the assumption of moments equivalence between the ideal RTD curve that would be developed in a truly conservative system and the observed loss-affected curve seem reasonable for fractional mass recovery due to time-invariant tracer loss or gain, mathematical proof of this concept has not been presented in the literature. Further, mass loss occurring during a tracer study may result from a combination of processes which may not be reasonably considered to be constant in the aggregate. As such, there is a need to extend the analysis of the effects of tracer response curve scaling on moments estimations for RTD curves corrected for higher-order mass loss processes such as zeroth and first-order reactions.

In this work we address several issues related to the effects of tracer mass loss and RTD curve scaling on the analysis of the moments of observed tracer response curves: (1) How does mass loss resulting from constant, zero, or first-order processes affect the estimated moments of the transformed RTD curve?; (2) Is there a mathematical relationship between the scaled and conservative (ideal) RTD functions?; and (3) Does there exist for each mass loss process a set of equations that can be used to estimate the statistical temporal moments about the origin (the raw moments) of the conservative RTD from the moments of the non-conservative observed and scaled RTD curves?

Derivation of the Scaled RTD Function

The residence time distribution functions for the observed, scaled, and ideal RTD cases are defined here as, respectively:

$$g_m(t) = \frac{C_m(t)Q(t)}{m_i} \tag{4.1}$$

$$g_s(t) = \frac{C_m(t)Q(t)}{m_r} \tag{4.2}$$

$$g_i(t) = \frac{C_i(t)Q(t)}{m_i} \tag{4.3}$$

where $Q(t)$ is the steady-state volumetric flow rate; $C_m(t)$ and $C_i(t)$ are the measured observed and conservative time-dependent tracer concentrations; and m_i and m_r are the total mass injected (presumably known) and the total mass recovered, respectively. The total mass recovered is evaluated as:

$$m_r = \int_0^\infty C_m(t)Q(t)\,dt \tag{4.4}$$

In the case of an ideal tracer response curve observed at the system outlet, all of the mass injected into the flow domain would be recovered so that $m_r = m_i$. In application, the mass injected may not be fully recovered, so that often $m_r < m_i$.

The n^{th} temporal moment about the origin of the RTD curve can be calculated (Nuamann and Bufham, 1981; Kadlec and Wallace, 2008):

$$m_{n(m,s,i)} = \int_0^\infty t^n g_{(m,s,i)}(t)\,dt \tag{4.5}$$

where the m, s, and i subscripts represent the observed, scaled and conservative cases, respectively. With these definitions, for $n = 0$, the above integrates to $M_{0(m)} = m_r/m_i$, and both Eqns. 4.2 and 4.33 integrate to $M_{0(s)} = M_{0(i)} = 1$.

In terms of residence time distributions the zeroth and first moments about the origin represent the mass fraction recovered and the mean residence time of tracer, respectively. The loss of tracer mass in transit will be reflected in the zeroth moment of the observed RTD curve. An observed zeroth moment less than unity indicates mass loss, while a zeroth moment equal to unity indicates conservative transport.

Defining the function $S(t) = C_i(t)/C_m(t)$ the following relationships hold for equations 4.1, 4.22, and 4.3:

$$g_m(t) = \frac{m_r}{m_i} g_s(t) = M_{0(m)} g_s(t) \tag{4.6}$$

$$g_i(t) = S(t)\, g_m(t) = M_{0(m)} S(t)\, g_s(t) \tag{4.7}$$

Equation 4.7 shows direct proportionality between the scaled RTD function and the conservative RTD function. It should be noted that application of Eqn. 4.7 requires specification of the functional form of $S(t)$, but does not require an assumption of the functional forms of $g_s(t)$ or $g_i(t)$. The function $S(t)$, as defined, represents the ratio of the expected conservative tracer concentration to the observed tracer concentration at the system outlet, and can be considered to be a concentration-normalized mass loss equation. In this work we examine only three functional forms of $S(t)$: time-invariant mass loss, zero-order loss, and first-order loss (Figure 2). However, it should be noted that the derivations presented herein may be extended to include higher-order processes or combinations thereof.

Functional Forms of *S*(*t*) and Moments Analysis of the Scaled RTD Curve

Case 1: Time-invariant Mass Loss

The trivial case of a time-independent concentration ratio function S(t) may arise from consistent measurement error (systematic bias) occurring over the course of a study, due perhaps to incorrect instrument calibration, or from poor accounting of the mass of tracer injected into the system. The time-invariant loss case can be derived from the differential rate equation:

$$\frac{d\left(S(t)\right)}{dt} = 0 \tag{4.8}$$

which has the solution,

$$S(t) = S \tag{4.9}$$

where $0 \leq S < \infty$ represents the constant proportionality of the observed and conservative tracer concentrations, and is equal (as will be demonstrated) to the inverse of the fraction of mass of tracer recovered. The relationship between the zeroth moment about the origin for the ideal and scaled curves, using the identities established in equations 4.7 and 4.9, is:

$$M_{0(i)} = M_{0(m)} S \int_0^\infty g_s(t)\, dt \tag{4.10}$$

Using the definition of the zeroth moment of the residence time distribution, the form of the calculated zeroth moment of the conservative curve becomes:

$$M_{0(i)} = M_{0(m)} S M_{0(s)} \tag{4.11}$$

From the definitions given above in Eqns. 4.1 through 4.4, we find $S = m_i/m_r$. Having established that $S = C_i(t)/C_m(t) = m_i/m_r$, it follows that $g_s(t) = g_i(t)$ and hence the n^{th} moments about both the origin and the mean for the case of time-invariant $S(t)$ applied to the scaled RTD function can be shown to be equivalent to the n^{th} raw moment expected to be calculated from the conservative ideal RTD curve:

$$M_{n(i)} = M_{n(s)} \tag{4.12}$$

Case 2: Zero-order Mass Loss

The linear case of the functional form of $S(t)$ corresponds to a zero-order loss process defined by the rate equation:

$$\frac{d(S(t))}{dt} = \beta_{1(z)} \tag{4.13}$$

With the corresponding solution:

$$S(t) = \beta_0 + \beta_{1(z)} t \tag{4.14}$$

wherein β_0 and $\beta_{1(z)}$ (t^{-1}) are the initial concentration ratio at the time of tracer injection ($S(t)$ at $t = 0$) and the zero-order loss rate coefficient, respectively. In each separate case of the functional form of $S(t)$ discussed in this and proceeding sections, the rate coefficient $\beta_{1(z)}$ is positive for processes that result in mass loss.

Zeroth Moment and Mass Loss Rate Coefficient of the Scaled Zero-Order Case

Using the linear form of $S(t)$ (Eqn. 4.14) and Eqn. 4.11, the zeroth moment of the conservative RTD curve can be expressed as a function of the scaled RTD function:

$$M_{0(i)} = M_{0(m)} \int_0^\infty \left(\beta_0 + \beta_{1(z)} t\right) g_s(t)\, dt = \beta_0 \int_0^\infty g_s(t)\, dt + \beta_{1(z)} \int_0^\infty t g_s(t)\, dt \tag{4.15}$$

By the definition of the zeroth and first moments about the origin Eqn. 4.15 evaluates to:

$$M_{0(i)} = M_{0(m)} \left(\beta_0 M_{0(s)} + \beta_{1(z)} M_{1(s)}\right) \tag{4.16}$$

Because $S(t)$ represents the ratio of the ideal and mass loss-affected tracer concentrations in the system, we assume that at the time of tracer injection ($t = 0$) there is no net tracer loss, and thus $\beta_0 = 1$. Additionally, as discussed previously, the areas under both the conservative and scaled RTD curves, $M_{0(i)}$ and $M_{0(s)}$, are unity. Applying these substitutions and rearranging Eqn. 4.16 we obtain an expression for the zero-order mass loss rate coefficient as a function of the zeroth moment of the observed non-conservative RTD and the first moment about the origin of the scaled RTD:

$$\beta_{1(z)} = \frac{1 - M_{0(m)}}{M_{0(m)} M_{1(s)}} \tag{4.17}$$

First Moment about the Origin of the Scaled Zero-Order Mass Loss Case

As with the zeroth moment for the zero-order case, the first moment about the origin for the conservative RTD can be written in terms of the scaled RTD function:

$$M_{1(i)} = M_{0(m)} \int_0^\infty \left(\beta_0 + \beta_{1(z)} t\right) t g_s(t)\, dt = M_{0(m)} \left(\beta_0 \int_0^\infty t g_s(t) dt + \beta_{1(z)} \int_0^\infty t^2 g_s(t)\, dt \right) \quad (4.18)$$

Applying the definitions of the first and second moments about the origin and substituting Eqn. 4.17 into Eqn. 4.18 gives an expression for the first moment (the mean hydraulic residence time) of the conservative RTD curve as a function of the first and second moments about the origin of the scaled RTD and the mass fraction recovered:

$$M_{1(i)} = M_{0(m)} M_{1(s)} + \frac{M_{2(s)} \left(1 - M_{0(m)}\right)}{M_{1(s)}} \quad (4.19)$$

Second Moment about the Origin of the Scaled Zero-Order Decay Case

In a similar fashion to the above derivation the second moment about the origin of the conservative RTD can be expressed in terms of the scaled RTD function:

$$M_{2(i)} = M_{0(m)} \int_0^\infty \left(\beta_0 + \beta_{1(z)} t\right) t^2 g_s(t)\, dt = M_{0(m)} \left(\beta_0 \int_0^\infty t^2 g_s(t) dt + \beta_{1(z)} \int_0^\infty t^3 g_s(t)\, dt \right) \quad (4.20)$$

Applying the definitions of the second and third moments about the origin (equation 4) the second moment about the origin for the conservative case can be expressed as:

$$M_{2(i)} = M_{0(m)} M_{2(s)} + \frac{M_{3(s)} \left(1 - M_{0(m)}\right)}{M_{1(s)}} \quad (4.21)$$

Similarly, the n^{th} moment about the origin for the conservative curve for the zero-order loss case is given by (with $n > 0$):

$$M_{n(i)} = M_{0(m)} M_{n(s)} + \frac{M_{n+1(s)}\left(1 - M_{0(m)}\right)}{M_{1(s)}} \tag{4.22}$$

Case 3: First-order Decay

First order mass loss is a concentration-dependent process defined by the rate equation, (expressed in terms of $S(t)$):

$$\frac{d\left(S(t)\right)}{dt} = \beta_{1(z)} S(t) \tag{4.23}$$

With the general solution:

$$S(t) = \beta_o \, exp\left(\beta_{1(f)} t\right) \tag{4.24}$$

where β_0 and $\beta_{1(f)}$ (t^{-1}) are the initial concentration ratio (at $t = 0$) and first-order mass loss rate coefficient, respectively.

Zeroth Moment and Mass Loss Rate Coefficient of the Scaled First-order Case

The zeroth moment of the ideal RTD curve can be expressed in terms of the scaled RTD function and the exponential form of $S(t)$:

$$M_{0(i)} = M_{0(m)} \int_0^\infty \beta_0 \, exp\left(\beta_{1(f)} t\right) g_s(t)\, dt \tag{4.25}$$

The exponential function in the integral in Eqn. 4.25 can be approximated as a Taylor series expansion about $t = 0$, resulting in:

$$M_{0(i)} = M_{0(m)} \beta_0 \int_0^\infty \left[1 + \beta_{1(f)} t + \beta_{1(f)}^2 \frac{t^2}{2} + \cdots + \beta_{1(f)}^2 \frac{t^n}{n!} + \cdots\right] g_s(t)\, dt \tag{4.26}$$

Multiplying $g_s(t)$ through to each term in the brackets, and using the definition of the n^{th} moment about the origin (Eqn. 4.4) we obtain an expression for the zeroth moment about the origin for the conservative RTD:

$$M_{0(i)} = M_{0(m)}\beta_0\left[M_{0(s)} + \beta_{1(f)}M_{1(s)} + \frac{\beta_{1(f)}^2}{2}M_{2(s)} + \cdots + \frac{\beta_{1(f)}^n}{n!}M_{n(s)} + \cdots\right] \tag{4.27}$$

Utilizing the fact that the zeroth moments about the origin for the conservative and scaled RTD evaluate to unity, and that $\beta_0 = 1$ Eqn. 4.27 reduces to:

$$1 = M_{0(m)} + \beta_{1(f)}M_{0(m)}M_{1(s)} + \frac{\beta_{1(f)}^2}{2}M_{0(m)}M_{2(s)} + \cdots + \frac{\beta_{1(f)}^n}{n!}M_{0(m)}M_{n(s)} + \cdots \tag{4.28}$$

From Eqn. 4.28 (if truncated to a manageable number of higher order terms) the first-order rate coefficient can be estimated through trial and error or utilization of non-linear root finding algorithms such as Newton's method (e.g. Press et al.,1992). However, an initial estimate for $\beta_{1(f)}$ can be obtained by discarding all but the first two terms and rearranging:

$$\beta_{1(f)} \approx \frac{1 - M_{0(m)}}{M_{0(m)}M_{1(s)}} \tag{4.29}$$

which is the formula for the rate coefficient for the zero-order case defined previously (Eqn. 4.17). Similarly, the quadratic formula can be utilized to obtain a more accurate approximation of $\beta_{1(f)}$ from Eqn. 4.28 by discarding all but the first three terms:

$$\beta_{1(f)} \approx \frac{-M_{0(m)}M_{1(s)} \pm \sqrt{\left(M_{0(m)}M_{1(s)}\right)^2 - 2\left(M_{0(m)} - 1\right)\left(M_{0(m)}M_{2(s)}\right)}}{2\left(M_{0(m)} - 1\right)} \tag{4.30}$$

Of the two values of $\beta_{1(f)}$ obtained from Eqn. 4.30, the positive value will correspond to net tracer mass loss.

First and Second Moments of the Scaled First-order Case

Using similar reasoning to that which was employed for the zeroth moment for the first-order loss case, expressions for the 1st and 2nd moments about the origin for the conservative RTD are obtained, respectively:

$$M_{1(i)} = M_{0(m)}\left[M_{1(s)} + \beta_{1(f)}M_{2(s)} + \frac{\beta_{1(f)}^2}{2}M_{3(s)} + \cdots + \frac{\beta_{1(f)}^n}{n!}M_{(n+1)(s)} + \cdots\right] \tag{4.31}$$

$$M_{2(i)} = M_{0(m)}\left[M_{2(s)} + \beta_{1(f)}M_{3(s)} + \frac{\beta_{1(f)}^2}{2}M_{4(s)} + \cdots + \frac{\beta_{1(f)}^n}{n!}M_{(n+2)(s)} + \cdots\right] \tag{4.32}$$

In general, the n^{th} moment about the origin for the conservative RTD from the moments ($n > 0$) of the ideal RTD can be estimated by:

$$M_{n(i)} = M_{0(m)}\left[M_{n(s)} + \sum_{k=n+1}^{l}\frac{\beta_{1(f)}^{(k-n)}}{(k-n)!}M_{(k)(s)}\right] \tag{4.33}$$

Discussion of Moments Approximations and Equivalents

The preceding derivations assume that the mass loss process affecting the tracer response curve is representative of an aggregation of processes (i.e. photolysis, irreversible adsorption, chemical or biological transformation, radioactive decay) occurring throughout the flow system over the entire duration of the tracer study, and that the flow system possesses real boundaries. Additionally, implicit in these assumptions is that the mass loss rate coefficient is constant in space and time. These qualifications are common in reactive transport modeling (e.g. Zuber, 1986; Amin and Campana, 1996; Thomann and Mueller, 1987), and thus this work does not represent a significant departure from established practice. An additional critical supposition to this analysis is that the mass loss of tracer is attributable

only to irreversible reactions or adsorption, and not to premature termination of the tracer study resulting in truncation of the tracer response curve.

The two formulations for the rate coefficients (Eqns. 4.17 and 4.29) show strong dependence on the scaled mean residence time. This dependence on $m_{1(s)}$ suggests that the estimates for these coefficients reflect only the aggregate effect of tracer mass loss on the shape of the RTD curve, and which encompasses both the physical, chemical, or biological mechanisms responsible for the process in addition to the transport effect (i.e. dependency on the distribution of residence times which is in turn a reflection of the hydrodynamics of the flow system). Further, the result of Eqn. 4.29 suggests that the zero order loss is a special case of first-order mass loss.

Equation 4.22 suggests a direct geometric transformation between the zero-order mass loss-affected RTD and the conservative curve, with no apparent dependency between the rate coefficient and the raw moments of the conservative RTD for each moment greater than the zeroth. Thus, the effect of a zero-order loss process on the shape of the observed RTD curve is predictable regardless of the magnitude of the loss of tracer. In contrast, the approximation for the first-order mass loss-affected moments presented in Eqn. 4.33 implies that the n^{th} raw moment is strongly dependent on the choice of the maximum degree of the exponent on the mass loss coefficient and on the magnitude of the higher-order moments. This non-linearity suggests that although the derivations presented make no assumption about the mathematical form of the RTD curve, there nonetheless may be some significant residual effects of the form of the curve on the accuracy of the estimate for the first-order loss rate coefficient.

Alternative Formulations

The formulas presented can be recast from the scaled RTD to the observed (non-scaled) RTD by using the definition of the n^{th} raw moment and the relationship between the scaled and observed RTD functions (Eqns. 4.4 and 4.5, respectively) and substituting the appropriate observed moments:

$$M_{n(m)} = M_{0(m)} M_{n(s)} \tag{4.34}$$

Expressing the derived formulas in terms of the observed tracer response curve reduces the number of calculations required to obtain the conservative equivalents. The preceding formulas can be applied to the time-normalized RTD curve by defining the following transformations for time and the RTD functions $g_o(t)$, $g_s(t)$, and $g_i(t)$:

$$Z = \frac{t}{\overline{T}} \tag{4.35}$$

$$g_o(Z) = \frac{C_o(t)Q(t)}{m_i}\overline{T} \tag{4.36}$$

$$g_s(Z) = \frac{C_o(t)Q(t)}{m_r}\overline{T} \tag{4.37}$$

$$g_i(t) = \frac{C_i(t)Q(t)}{m_i}\overline{T} \tag{4.38}$$

where $\overline{T}$ is the mean hydraulic residence time. The dimensionless time, Z can be considered analogous to the fractional turn-over time (Malzewski and Zuber, 1993). Substituting $t = Z\overline{T}$ and defining $dt = \overline{T}dZ$ the time-normalized moments can be derived from:

$$\frac{M_{n(o,s,i)}}{\overline{T}^n} = M^*_{n(o,s,i)} = \int_0^\infty Z^n g_{(o,s,i)}(Z)\,dZ \tag{4.39}$$

Normalization of the mass loss rate coefficient results in the aggregate Damkohler number of the flow system representing the ratio of the relative time-scales of the mass loss process to the mean mass transport time:

$$D_{a(z,f)} = \overline{T}\beta_{1(z,f)} \tag{4.40}$$

where $D_{a(z,f)}$ is the Damkohler number (dimensionless), $\beta_{1(z,f)}$ is the mass loss rate coefficient, and the subscript z or f refers to the zero or first-order loss condition. The normalized mass loss functions for each process case can then be rewritten in terms of $D_{a(z,f)}$:

$$S(Z) = 1 + D_{a(z)}Z \tag{4.41}$$

$$S(Z) = exp\left(D_{a(f)}Z\right) \tag{4.42}$$

With the above definitions, and using the fact that the normalized first raw moment for the conservative case is unity for steady-flow conditions the above derivations to estimate the raw normalized moments $M^*_{n(o,s,i)}$ and Damkohler numbers ($D_{a(z,f)}$) can be used for each mass loss case without modification to the presented functional forms for the non-time normalized case.

Application and Testing

Steady flow Simulations

To test the developed formulas we conducted a series of numerical experiments on a set of artificially derived RTD curves developed from the dimensionless 2-parameter gamma probability distribution function (PDF) model subjected to zero and first-order losses. The 2-

parameter gamma PDF is commonly used to simulate or replicate hydraulic tracer studies developed on flow-through systems (Stokes and Naumann, 1970; Nardi et al., 1999; Maeda and Bergstrom, 2000). Simulations were conducted under steady-flow conditions and were designed to encompass the range of combinations of individual model parameter values that could reasonably be expected to be encountered in most practical applications. All simulations were conducted within the MATLAB computing environment (MathWorks; Natick, MA).

The 2-parameter gamma PDF arises from the tanks-in-series model as described in several existing texts (e.g. Kadlec and Wallace, 2008; Hayes, 2001) and is presented here in dimensionless form:

$$g\left(Z,N\right)_{2\gamma} = \frac{N^{N} Z^{(N-1)}}{\Gamma\left(N\right)} exp\left(-NZ\right) \tag{4.43}$$

where N represents the number of sequential tanks in series and determines the shape of the response curve, and $\Gamma(N)$ is the gamma function (Kadlec and Wallace, 2008) evaluated at N. The shape parameter can be estimated from the dimensionless variance $N = M^{*2}_{1(2\gamma)} \Big/ \left(M^{*}_{2(2\gamma)} - M^{*2}_{1(2\gamma)}\right)$ of the simulated RTD, and is closely related to the apparent system Péclet (Pe_a) number for a quasi-one-dimensional flow domain by $Pe_a \approx 2N$ (Cirpka and Kitanidis, 2000).

The residence time distribution curves developed from Eqn. 4.43 were subjected to zero and first order mass loss as defined in Eqns. 4.14 and 4.24, respectively:

$$g_{2\gamma(z)}\left(Z\right) = \frac{g\left(Z,N\right)_{2\gamma}}{1+D_{a(z)}Z} \tag{4.44}$$

$$g_{2\gamma(f)}(Z) = \frac{g(Z,N)_{2\gamma}}{exp\left(D_{a(f)}Z\right)} \tag{4.45}$$

Multiple simulations (n = 90) were conducted to test the solution convergence properties of the series expansion of Eqns. 4.28 and 4.33. Simulations were conducted for a period of up to 10 turn-over times (Z = 10) to ensure complete tracer recovery for the conservative case and minimize numerical error for the test cases. Each simulated curve was derived from a particular combination of N and $D_{a(f,z)}$ for the ranges in parameter values between 1 and 20 for the shape parameter N (i.e. 1,2,4,8,10,12,14,16,18,20); and between 0.01 and 10 for $D_{a(f,z)}$ (i.e. 0.01,0.1,0.5,1,2,3,4,5,6,8,10). For each simulated RTD curve for each and each parameter pair, up to the 50th raw moment was estimated by numerical integration of Eqn. 4.4 via the trapezoidal rule.

Error Analysis and Simulation Results

To assess the accuracy and convergence rate of the estimate for the mass loss coefficient for the first-order mass loss case Eqn. 4.28 was iteratively constructed up to the 50th raw moment with a new numerical estimate for $D_{a(f)}$ developed with each iteration using a non-linear equation solver (the *fsolve* function in MATLAB). This process led to successively more accurate estimates of the Damkohler number with each added term in the series expansion. The resultant tables were subsequently searched for the points at which the numerical estimate of $D_{a(f)}$ possessed a relative error $\leq 10^{-4}$ (Figures 3 and 4). These values provide an estimate of the convergence behavior of the series expansion, and can guide the practitioner in selecting an upper bound on the number of moments required to be evaluated

to implement Eqns. 4.28 and 4.33 with the desired level of precision and accuracy for the particular system behavior (i.e. unique combinations of D_a and Pe_a values).

With respect to estimates of the Damkohler number obtained using Eqn. 4.28, as evidenced in the preceding figures the potential error in the approximation is apparently dependent upon the degree of dispersion occurring within the system as indicated by the Péclet number; with more accurate estimates being obtained with decreased degrees of dispersion (i.e. higher Péclet number values). However, the accuracy of the estimate is also highly dependent upon the number of raw moments evaluated. As is evidenced by Figure 4 the relative error of the Damkohler number estimate for all degrees of mixing suggest error minima between 4 and 12 evaluated moments, with potential relative error of $O(10^{-3} - 10^{-5})$. These results indicate that for most applications an estimate of the system Damkohler number accurate to within four decimal places can be obtained by applying Eqn. 4.28 up to the twelfth raw temporal moment, with fewer higher moments requiring evaluation with increased Péclet number values. Further, as Figure 5 indicates, the potential error estimate is minimized for all degrees of mixing between Damkohler number values of between 0.1 and 1 suggesting that the most accurate estimates will be obtained for moderate values of this parameter.

Error in the Damkohler number estimate may become compounded with error developed in the application of Eqn. 4.28, potentially resulting in numerical divergence. To establish potential error bounds on estimates for the 1st through 5th raw moments of the simulated RTD we iteratively constructed Eqn. 4.28 up to the 50th raw moment of the first-order loss-affected curve for each simulated curve, using both the specified 'true' Damkohler number and the approximation given for the linear mass loss case (Eqn. 4.29) until the

absolute difference between successive estimations was less than 10^{-4}. The linear loss approximation for the Damkohler number was chosen to allow for evaluation of a 'worst-case' scenario on the potential minimum and maximum error in estimates of the 1st through 5th raw moments. More accurate estimates of the Damkohler number will result in more accurate estimates of the raw moments calculated from Eqn. 4.33. Increased relative error in the Damkohler number estimate will increase the error of the estimates of each of the 1st through 5th ideal raw moments, as indicated in Figure 6. However, as shown in Figure 5, the relative error range to be expected for a given Damkohler number is $O(10^{-2} - 10^{-5})$. This range corresponds to errors in each of the first four raw moments of $O(10^{-2} - 10^{-6})$ (Figure 5). Thus, estimates of each of the principal temporal moments commonly used in RTD analysis can be obtained to an accuracy of between 2 and 6 decimal places using the methods for first-order loss as outlined herein. With respect to the zero-order mass loss-affected RTD exact correspondence between the actual and approximated Damkohler numbers is achieved through employing Eqn. 4.20. By extension the actual and estimated temporal moments to the n^{th} moment are expected to exactly correspond as well. However, it should be cautioned that the approach presented herein may be hampered by the inherent accuracies in computing higher-order moments ($n > 5$), which are difficult to accurately estimate from experimental data (Nauman and Buffham, 1983).

Alternative Method for Estimating the Loss Rate Coefficient

The preceding Eqns. 4.29 and 4.30 are simple closed form formulas that can be readily placed into a spreadsheet or other computer application and may, in practice, provide an adequate approximation. However, the potential for error in estimating the moments for

the conservative RTD curve from the first-order mass loss case may, if the error is large enough, preclude use of these equation, and even a more complete expansion as given by Eqn. 4.28. Alternatively, the mass loss-affected RTD could be corrected by suitable choice of a loss rate coefficient that permits integration of the observed RTD to unity. To accomplish this, $\beta_{1(f)}$ is estimated directly by defining the function $g(t)^* = C_o(t)Q(t) \Big/ m_i \, exp\left(\beta_{1(f)} t\right)$ and applying an iterative root finding program to determine the value of $\beta_{1(f)}$ that causes this function to integrate to unity. This is relatively easy to accomplish numerically (in a spreadsheet for example) and will provide the loss rate constant without the approximations or complexity inherent in Eqns. 4.28 to 4.30. Efficient non-linear equation solvers such as the Solver utility in Microsoft Excel or the *fsolve* function in MATLAB can easily be adapted to this direct approach. With an estimate of $\beta_{1(f)}$, Eqns. 4.31, 4.32, and 4.33 can be used to estimate the moments of the conservative RTD curve.

Summary and Conclusions

By relating the scaled and ideal conservative RTD curves we have demonstrated that both the raw moments of the conservative RTD and the appropriate mass loss coefficient can be obtained or closely approximated algebraically for both zero and first-order mass loss processes from the analysis of the raw moments of the loss-affected (observed) RTD curve. Error analysis of simulated RTD subjected to zero and first-order mass loss suggests that estimates of the respective mass loss coefficients (i.e. Damkohler numbers) and conservative raw RTD moments can be obtained to accuracies of $O(10^{-2} - 10^{-4})$ using the techniques outlined herein. For most applications the first-order mass loss coefficient may reasonably be approximated using the formula for the zero-order loss rate coefficient (Eqn. 4.20). However,

error in the estimations of the moments tends to increase exponentially for highly reactive systems with very large residence times (i.e. large Damkohler numbers; Figure. 6) when using the zero-order mass loss approximation of Eqn. 4.17 in lieu of the more complicated expression for the first-order rate coefficient (Eqn. 4.28). For most practical applications, however, the error on the Damkohler number estimate will likely be $O(10^{-2} – 10^{-3})$, regardless of apparent dispersion. Thus the potential error in the estimates of the moments for the first-order case will likely be $O(10^{-2} - 10^{-3})$.

The techniques presented here may find practical application in re-estimation of RTD moments for currently published tracer studies for which tracer recovery is not unity, or alternatively, in estimating mass loss rate coefficients for tracer experiments conducted in flow-through systems within which tracer mass loss has occurred (e.g. Keefe et al., 2004). By extension these techniques may prove to be useful in reactive transport modeling of decayed tracer breakthrough curves on arbitrarily defined flow domains (e.g. Maeda and Bergstrom, 2000; Maloszewski and Zuber, 1993) as long as the tracer response curve is measured in flux at the domain outflow boundary. Further, the application of the techniques pertaining to zero and first-order losses are restricted to those situations for which the loss of tracer mass is strictly due to radioactive decay, or chemical or biological transformations, and not due to premature truncation of the tracer response curve or measurement error.

Acknowledgements

This work was supported by the Iowa Department of Agriculture and Land Stewardship, and the Department of Ecology, Evolution, and Organismal Biology at Iowa State University. The authors would like to thank Drs. Chris Rehmann, Jim Raich, Matt Helmers, and Roy Gu for their valuable contributions to this manuscript.

References

Bodin, H., A. Mietto, P.M. Ehde, J. Persson, S.E.B. Weisner. 2012. Tracer behaviour and analysis of hydraulics in experimental free water surface wetlands. Ecological Engineering 49, 201–211.

Chapra, S.C. 2008. *Surface Water-Quality Modeling*. Waveland Press, Long Grove IL. U.S.A..

Cirpka, O.A., P.K. Kitanidis. 2000. An advective-dispersive stream tube approach for the transfer of conservative-tracer data to reactive transport. Water Resources Research 36, 1209–1220.

Hayes, R.E. 2001. *Introduction to Chemical Reactor Analysis*. Taylor & Francis.

Headley, T.R., R.H. Kadlec. 2007. Conducting hydraulic tracer studies of constructed wetlands: a practical guide. Ecohydrology & Hydrobiology 7, 269–282.

Holland, J.F., J.F. Martin, T. Granata, V. Bouchard, M. Quigley, and L. Brown. 2004. Effects of wetland depth and flow rate on residence time distribution characteristics. Ecological Engineering 23, 189–203.

Kadlec, R.H., and S. Wallace. 2008. *Treatment Wetlands*, Second Edition. CRC Press.

Keefe, S.H., L.B. Barber, R.L. Runkel, J.N. Ryan, D.M. McKnight, and R.D. Wass. 2004. Conservative and reactive solute transport in constructed wetlands. Water Resources Research 40..

Maeda, M., L.F. Bergström. 2000. Leaching patterns of heavy metals and nitrogen evaluated with a modified tanks-in-series model. Journal of Contaminant Hydrology 43, 165–185.

Maloszewski, P., and A. Zuber. 1993. Principles and practice of calibration and validation of mathematical models for the interpretation of environmental tracer data in aquifers. Advances in Water Resources 16, 173–190.

Nauman, E.B., and B.A. Buffham. 1983. *Mixing in Continuous Flow Systems*. First Edition. John Wiley & Sons., Berlin, Germany

Press, W.H., 1992. *Numerical Recipes in C: The Art of Scientific Computing*. Cambridge University Press.

Stokes, R.L., and E.B. Nauman. 1970. Residence time distribution functions for stirred tanks in series. The Canadian Journal of Chemical Engineering 48, 723–725.

Thomann, R.V., J.A. Mueller. 1987. *Principles of surface water quality modeling and control*. Harper & Row.

Wang, H., and J.W. Jawitz. 2006. Hydraulic analysis of cell-network treatment wetlands. Journal of Hydrology 330, 721–734.

Table 1.Summary of derived formulas for estimating the conservative moments from decay affected RTD curves and respective zero and first-order decay coefficients. The formulas presented can be applied for dimensionless equivalents without modification.

Moment |Coefficient	Decay Formulation	Approximation | Equivalent
Time-invariant Case		
$M_{n(i)}$	$S(t) = S$	$M_{n(s)}$
Zero-order Case		
$\beta_{1(z)}$	$S(t) = \beta_0 + \beta_{1(z)}t$	$\beta_{1(z)} = \frac{1 - M_{0(m)}}{M_{0(m)}M_{1(s)}}$
$M_{n(i)}$		$M_{n(i)} = M_{0(m)}M_{n(s)} + \frac{M_{n+1(s)}\left(1 - M_{0(m)}\right)}{M_{1(s)}}, n > 0$
First-order Case		
$\beta_{1(f)}$	$S(t) = \beta_0 \exp\left(\beta_{1(f)}t\right)$	Estimated iteratively from: $1 = M_{0(m)} + \beta_{1(f)}M_{0(m)}M_{1(s)} + \frac{\beta_{1(f)}^2}{2}M_{0(m)}M_{2(s)} + \cdots + \frac{\beta_{1(f)}^n}{n!}M_{0(m)}M_{n(s)} + \cdots$
$M_{n(i)}$		$M_{n(i)} = M_{0(m)}\left[M_{n(s)} + \sum_{k=n+1}^{l} \frac{\beta_{1(f)}^{(k-n)}}{(k-n)!}M_{(k)(s)}\right], n > 0$

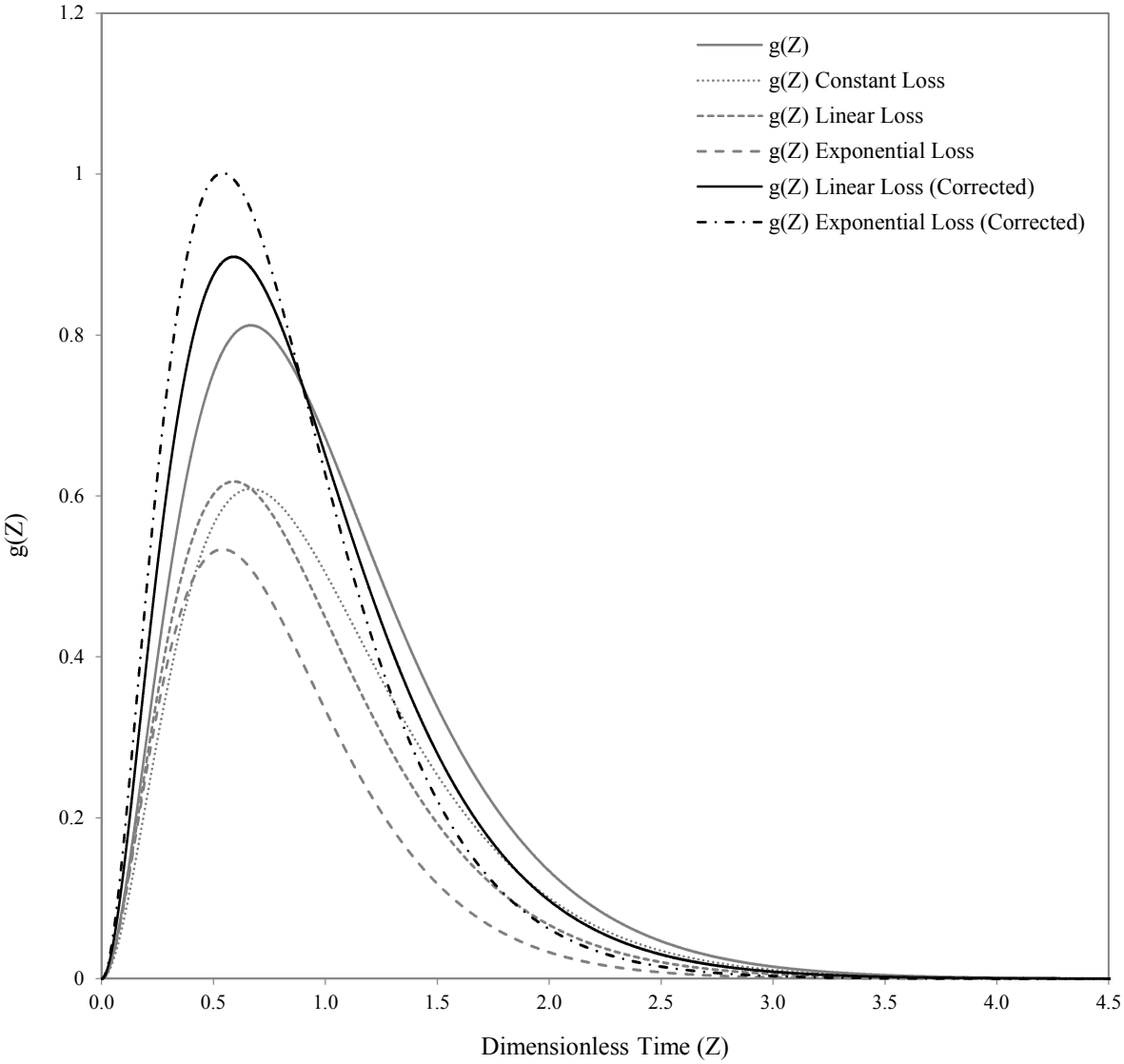

Figure 1. Examples of decay-affected RTD curves for the constant, zero, and first-order decay cases and their respective scaled counterparts. The zero and first-order curves result from application of equations 4.49 and 4.50, respectively, with a Damkohler number of 0.35. The constant case is subjected to a constant mass fraction of 0.75. Observe the shift of the center of mass toward the origin for each of the scaled cases.

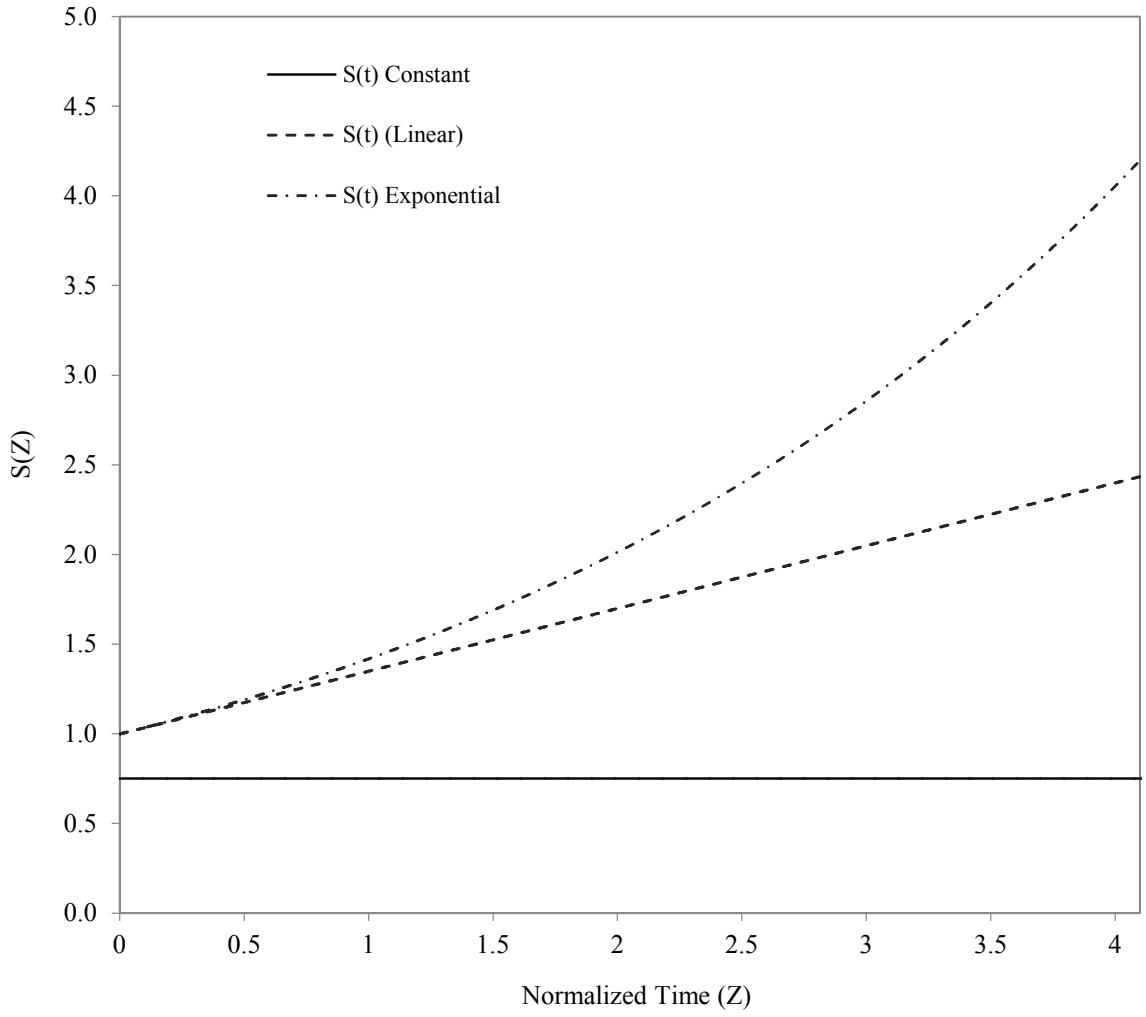

Figure 2. Examples of the decay function S(Z) for the constant, zero, and first-order decay case. The examples given here are for a Damkohler number of 0.35 for both the zero and first-order decay cases, and a mass fraction of 0.75 for the constant decay case.

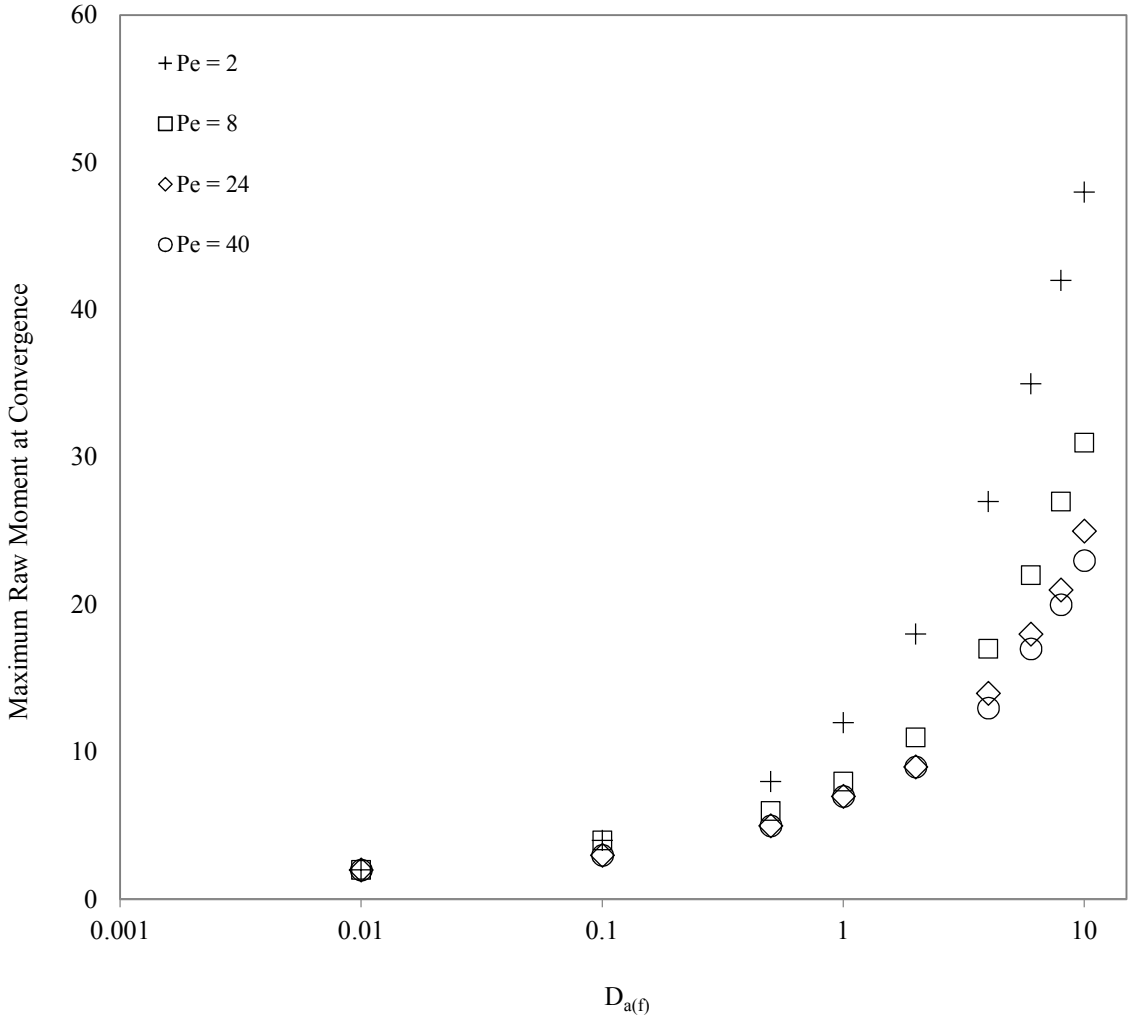

Figure 3. Maximum number of higher-order moments required to be evaluated to achieve convergence to a tolerance of 1E-4 for a given Damkohler number estimate.

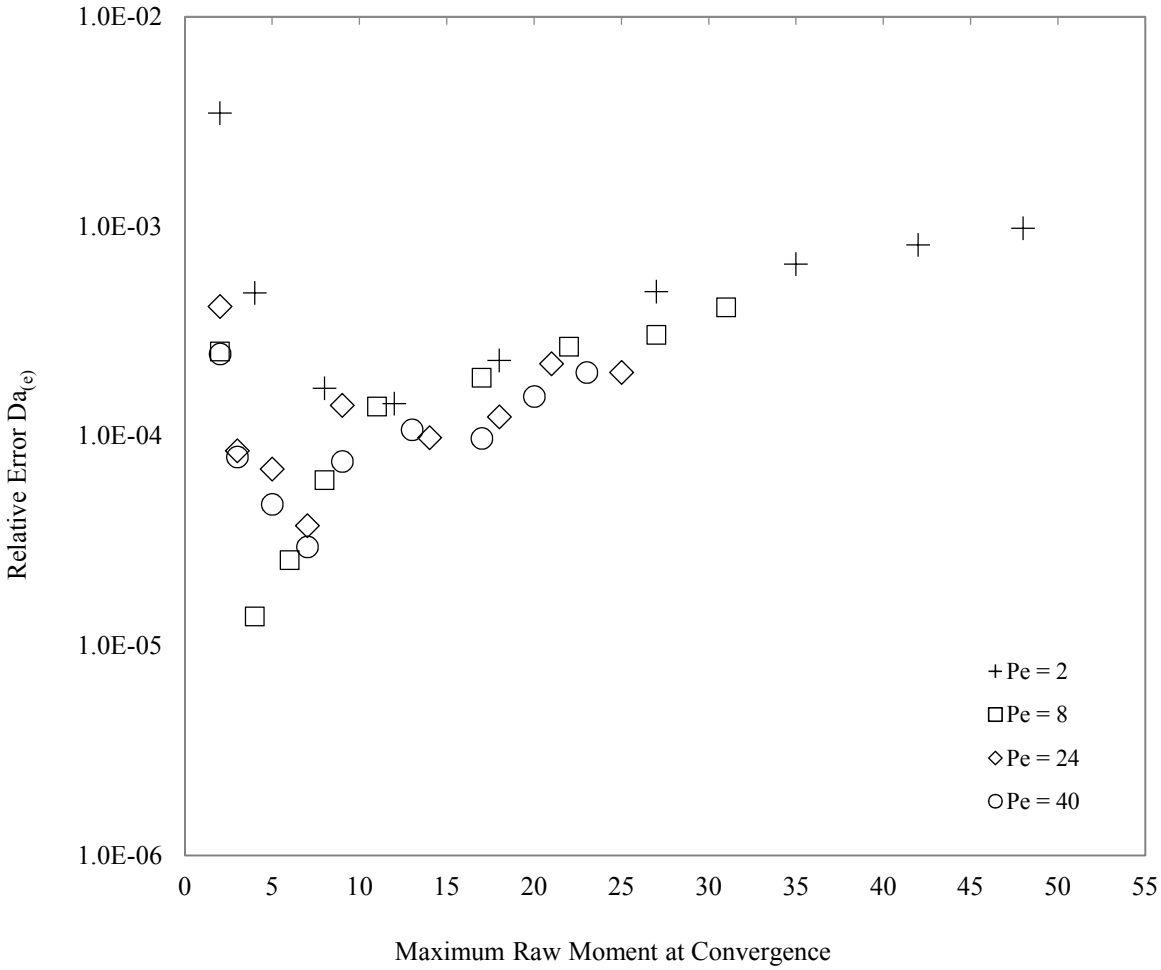

Figure 4. Relative error of the Damkohler number estimate at the maximum number of higher order raw RTD moments required to be evaluated for convergence of the solution presented in Eqn. 30.

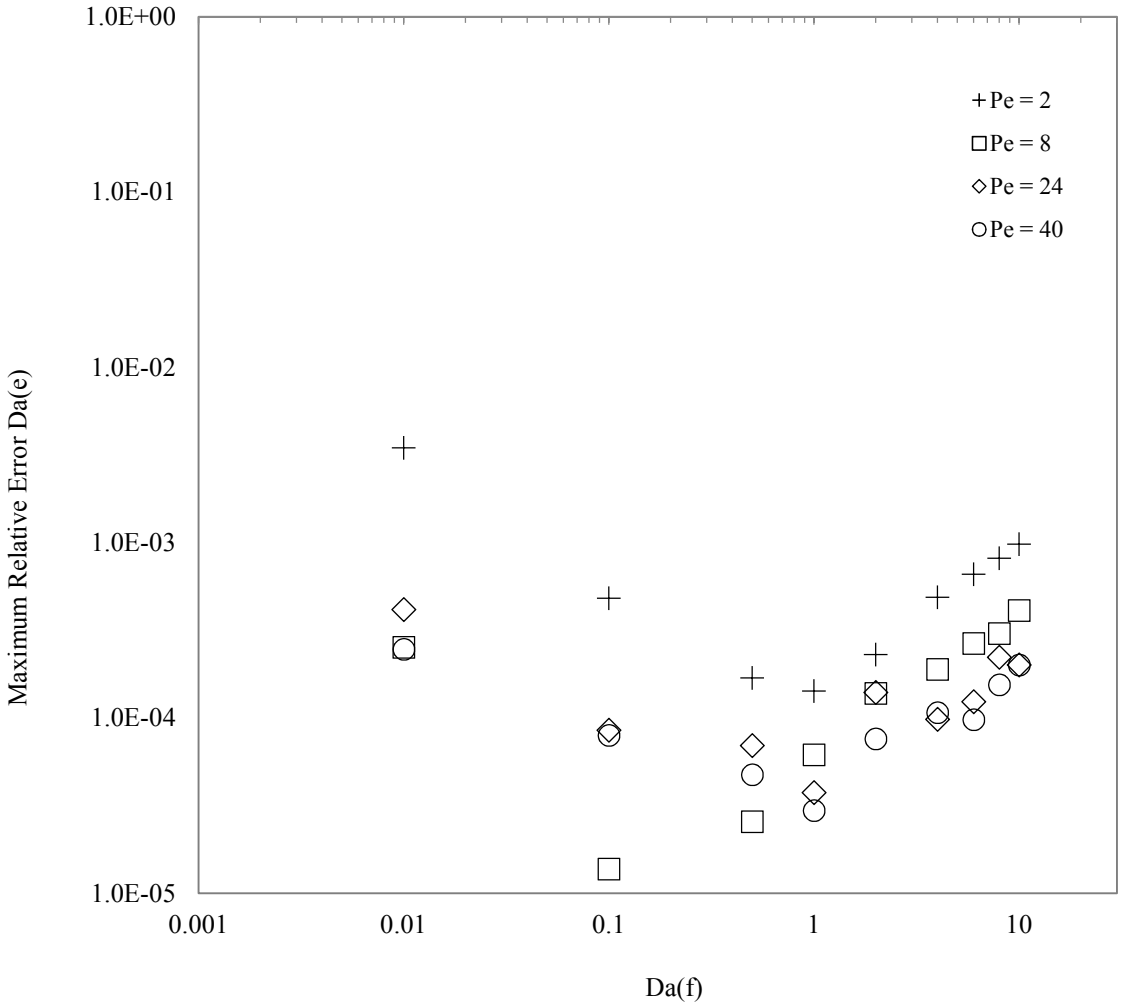

Figure 5. Relative error of the Damkohler number estimate at the point of solution convergence of Eqn. 30.

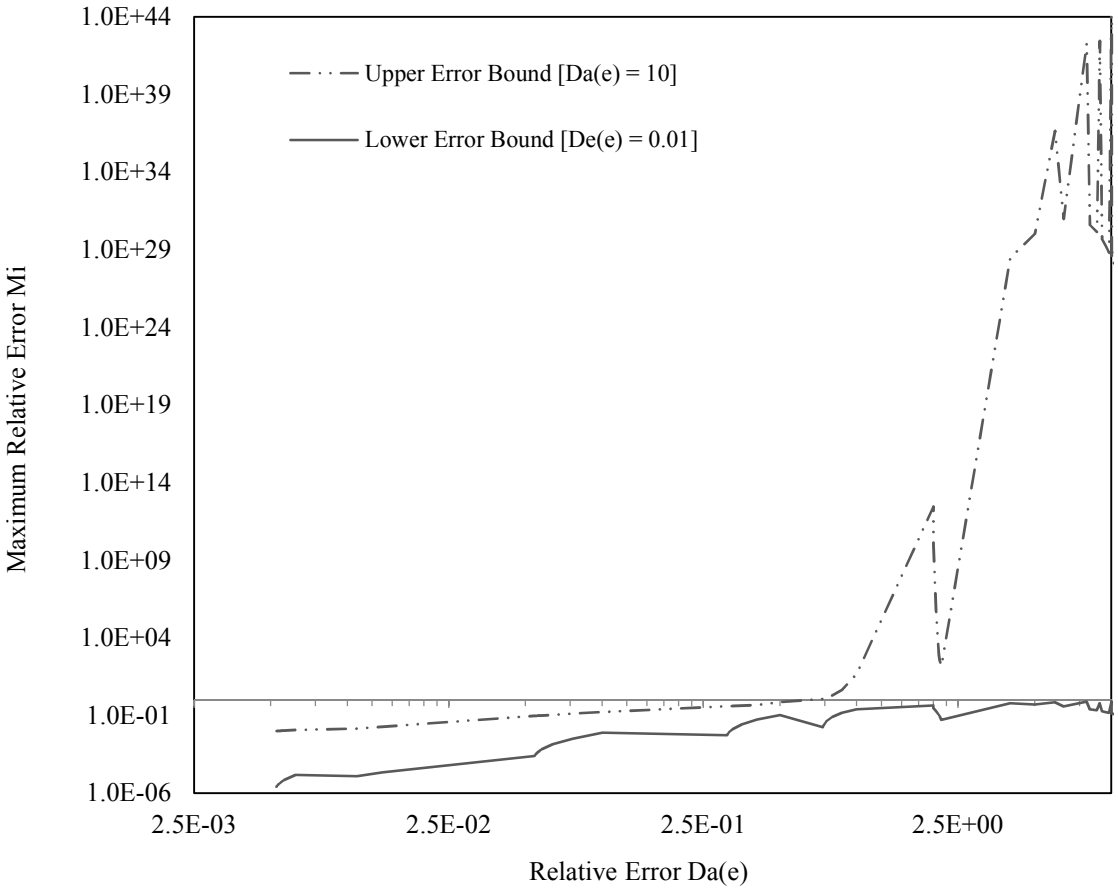

Figure 6. Maximum relative error in the first through fifth temporal moments estimated using Eqn. 33 with varying Damkohler number estimates with varying relative errors as given by the Damkohler number approximation of Eqn. 28. Most applications will feature Damkohler numbers with error estimates of $O(10^{-2} - 10^{-4})$, corresponding to potential error estimates for the n^{th} temporal moment of $O(10^{-2} - 10^{-6})$.

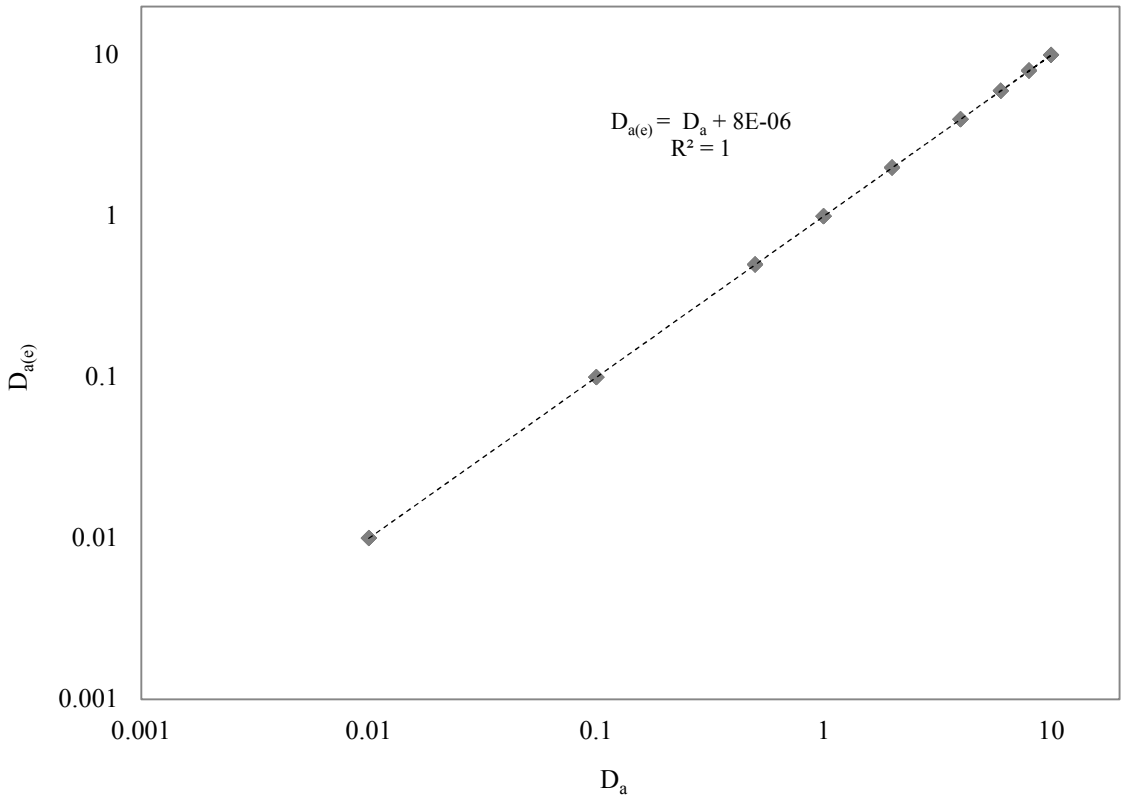

Figure 7. Actual versus approximated Damkohler numbers using Eqn. 17 for the zero-order decay case. This result is expected to extend to the n^{th} temporal moments approximated from Eqn. 22.

CHAPTER 5. GENERAL SUMMARY

Constructed wetlands are a promising technology for reducing nutrient loads from agricultural watersheds. However, the unique landscape positioning of these systems places distinct constraints on their design and implementation, and ensures that they are continually subjected to transient environmental conditions. As a result of this variability in environmental conditions, these systems, as demonstrated in Chapters 2 and 3 of this dissertation, experience highly dynamic and variable mixing properties, the characteristics of which, as realized from developed residence time distributions (RTD), are driven primarily by the complex interactions of transient ambient flow rates and wind speeds and directions, and are strongly influenced by the presence of aquatic vegetation.

The work presented in Chapter 2 has demonstrated, using multiple field-scale tracer studies on actual constructed agricultural wetlands, that the temporal features of developed RTD and derived mixing parameters are differentially influenced by measured environmental effects, and that these effects individually and together result in a significant amount of variability in measured RTD characteristics for these systems. Of the RTD characteristics evaluated, measures of mixing - such as the longitudinal dispersion coefficient, Péclet number, and normalized dimensionless variance - exhibited the highest degrees of variability, while measures of short-circuiting exhibited the lowest degrees of variability.

In general, our results show that ambient flow rates, as represented by mass-weighted mean shear velocity Reynold's numbers, strongly reduce short-circuiting as measured from dimensionless initial and peak arrival times, and significantly influence the dimensionless first moment of the RTD (and by extension, the amount of dead space in the systems studied)

and the degree and rate of mixing of these systems, as represented by the longitudinal dispersion coefficient, the Péclet number, and the normalized dimensionless variance; with each metric tending to increase with increasing flow rates. However, from a wetland performance perspective, the general reduction in short-circuiting and improvement in volumetric efficiency under higher flow rates is offset by a reduction in mean hydraulic residence times, thereby potentially resulting in a decrease in constituent removal performance.

Similarly, wind shear, expressed as a surface shear Reynold's number, was shown to be a primary driver of short-circuiting and dispersion for some of the wetlands evaluated, notably sites WL1, WL2, and WL3, particularly when vegetation was absent from these systems. Additionally, wind shear was observed to affect the dimensionless mean residence time for site WL1, causing a general reduction in volumetric efficiency (corresponding to an increase in dead space) with increasing wind speeds. However, the tendency for this system to experience a reduction in dead space with increasing wind shear contradicts the observed trend of an increase in bulk mixing with increasing wind speeds for this site. A more likely explanation is that wind shear increases the rate of surface advection, thus causing the centroid to arrive at the outlet earlier than would be dictated by ambient flow rates. This possibility is also reflected in the dimensionless initial arrival time for this system, but interestingly, is not reflected in the dimensionless peak arrival time. That applied wind shear to the surface of shallow flow-through basins can result in increases of surface advection, and thus short-circuiting, has been observed through numerical simulations (Bentzen et al., 2008) and direct observations of velocity fields of similar systems (e.g. Shaw et al., 1997; Andradóttir and Mortamet, 2016). The differential response to wind shear of the systems

featured in Chapter 2 is likely a result of differences in bathymetry and surrounding landscape topography.

In Chapter 2, wind directions increasing oriented against primary flow directions were observed to result in an increase in short-circuiting as measured by the dimensionless peak arrival time for all studies conducted under non-vegetated conditions for all systems, and a reduction in the dimensionless first moment of the RTD for WL3. Additionally, winds increasingly oriented against the primary flow direction were observed to result in a reduction in longitudinal dispersion for WL1 particularly for studies conducted in the absence of submergent vegetation, but contradictorily, results in an increase in the degree of total mixing as indicated by the normalized dimensionless variance of the RTD. This result suggests that the normalized dimensionless variance may be an indicator of the degree of transverse mixing, and is not necessarily a measure of total mixing within these systems, as has been suggested by several authors (e.g. Thackston et al., 1987; Kadlec and Wallace, 2008).

Interestingly, although differences in the aggregate medians of measured RTD characteristics between vegetated and non-vegetated conditions were not statistically significant, vegetation was shown to have a marked influence on some RTD features, notably dimensionless peak arrival times, dimensionless first moments, and estimates of longitudinal dispersion. In general, results indicate that short-circuiting, as measured by the dimensionless peak arrival time, is reduced with increasing percent vegetative cover; although this apparent effect is notably weak. Additionally, and in accordance with the findings of Nepf et al. (1997), increasing vegetative cover tends to result in an increase in dead space in these systems, as reflected in a tendency for the dimensionless mean residence time decrease with

increasing vegetative cover. Our results also suggest that longitudinal dispersion coefficients tend to decline with increasing vegetative cover up to a percent vegetative cover of approximately 30%, wherein dispersion tends to rebound. The reduction in longitudinal dispersion rates with increasing vegetative cover is in accordance with the findings of Nepf et al. (1997) and Shucksmith et al. (2010). The likely reasons for the observed decrease in longitudinal dispersion with increasing vegetative cover include increased rates of vertical and lateral mixing during early growth periods. However, our results diverge from the aforementioned studies with the observation of increasing longitudinal dispersion above a percent vegetative cover above approximately 30%. The mechanisms causing this apparent increase in longitudinal dispersion above a percent vegetative cover above 30% are uncertain, but may result from increased canopy patchiness (thus causing an increase in dead space). Additional tracer studies should be conducted on submergent vegetation dominated wetlands to determine whether this apparent relationship is persistent. Such studies should be performed in conjunction with multi-dimensional numerical hydrodynamic and mass transport models to help to further elucidate the mechanisms which cause cuase this apparent behavior.

In Chapter 3, the Environmental Fluid Dynamics Code (EFDC) numerical hydrodynamic and mass transport model was used to simulate a set of tracer studies conducted on WL1 under non-vegetated conditions. Models were developed to incorporate the external effects of transient ambient flow, wind, and thermal forcing. Simulations were performed to assess the efficacy of the EFDC model for simulating mixing in this system under natural conditions, and to serve as a test case for planned subsequent simulations of mixing in other constructed agricultural wetlands. The results of performed simulations show

that the EFDC model can accurately reproduce observed basin outflow rates, internal temperatures measured at two locations, as well as observed tracer response curves. Model calibration was most sensitive to values of the background vertical and horizontal turbulent viscosities, and least sensitive to values of the Smagorinsky horizontal eddy diffusivity coefficient (Smagorinsky, 1963), the sediment heat exchange coefficient, and the vertical light extinction coefficient. Variability in the vertical and horizontal background turbulent diffusion coefficients required for obtaining the best fits between observed and simulated tracer response curves implies that these variables are sensitive to ambient environmental conditions. This result suggests that 3-dimensional simulations of mixing in wetlands and other shallow flow-through basins using the EFDC platform for which tracer studies have not been conducted should be performed using a range of values for these parameters to characterize the potential range of responses of these systems to ambient environmental conditions.

Sensitivity analyses using the calibrated EFDC models, wherein the relative influences of transient flow, winds, and thermal forcing were alternately excluded from the calibrated simulations, indicated that transient inflow boundary conditions exerted strong influence on the dimensionless mean residence time for this system (and thus the degree of dead space), but had little influence on estimates of short-circuiting and dispersion for this system for the simulated conditions. In contrast, exclusion of wind forcing from the simulations tended to result in significantly lower measures of short-circuiting and dispersion for this system; however, these effects were moderated by exclusion of thermal forcing, suggesting that both wind and internal temperature dynamics, both individually and in

concert, strongly influence the shape of measured RTD (and thus derived mixing and hydraulic characteristics) for this system.

Thermal forcing is commonly neglected as a possible explanatory variable for variability in measured RTD developed on shallow flow-through basins (see Chapter 2), and is often excluded in multi-dimensional simulations of mixing in these systems (e.g. Shaw et al., 1995; Persson, 2000). The results given in Chapter 3 of this dissertation suggest that this potential source of mixing energy should not be neglected when simulating RTD on these types of systems, and particularly when using multi-dimensional hydrodynamic and mass transport models to assess the relative influences of external environmental effects on mixing in shallow flow-through basins. Furthermore, our research indicates that additional investigations into the roles that external thermal forcing and resultant vertical and horizontal temperature inhomogeneity on mixing in these systems should be undertaken.

The results presented from Chapters 2 and 3 demonstrate the inherently high degree of variability of the mixing characteristics of these systems and their sensitivity to environmental conditions. Further, these results suggest that multiple tracer studies should be conducted on a given system under a range of environmental conditions to more fully characterize its range of mixing behaviors. Results from Chapter 3 suggest that tracer studies conducted on these types of shallow flow-through basins should be interpreted with the aid of multi-dimensional numerical mixing models to assess the relative influences of environmental effects on observed RTD characteristics. Such information, when considered in the aggregate, can aid wetland designers by providing information about the influence of environmental effects on mixing in these types of systems, which may then serve as the basis

for basin design modifications which can mitigate for negative effects and encourage mixing behavior that is beneficial for wetland constituent removal performance.

Chapter 4 details the derivation of a set of algebraic equations relating the raw moments of the decay affected RTD to constant, zero, and first-order decay coefficients. This study was undertaken to address the potential common pitfalls of scaling RTD developed on general flow domains by the percent mass recovery. This is an issue that is persistent in tracer hydrology, and can affect estimates of raw and central moments of tracer response curves, and thus affect estimates of derived mixing parameters. The results presented in this chapter show that the derived equations can reasonably reproduce estimates of decay coefficients, with errors of these estimates ranging from order $O(10^{-2} – 10^{-4})$. The smallest error is observed for Damkohler numbers of approximately unity, and for higher values of the Péclet number. The formulas presented in this chapter may find use in re-evaluating decay affected RTD, and for estimating decay rate coefficients for reactive flow systems.

REFERENCES

Allen, A.W. 2005. The conservation reserve enhancement program. USGS Staff–Published Research. U.S. Department of the Interior

Andradóttir, H., and M-L. Mortamet. 2016. Impact of wind on storm-water pond hydraulics. Journal of Hydraulic Engineering 142(10) 4016034. doi:10.1061/(ASCE)HY.1943-7900.0001150.

Bentzen, T. R., T. Larsen, and M. R. Rasmussen. 2008. Wind effects on retention time in highway ponds. Water Science & Technology 57(11):1713. doi:10.2166/wst.2008.267.

Bodin, H., A M. Per Magnus, J.P. E., Jesper Persson, and S.E.B., and Weisner. 2012. Tracer behavior and analysis of hydraulics in experimental free water surface wetlands. Ecological Engineering 49(December):201–11. doi:10.1016/j.ecoleng.2012.07.009.

Crumpton, W. G., G.A Stenback, B.A. Miller, M.J. Helmers. 2006. Potential benefits of wetland filters for tile drainage systems: impact on nitrate loads to Mississippi River sub-basins. Final project report to US Department of Agriculture Project number: IOW06682.

Crumpton, W. G., A.G. van der Valk, W. Hoyer, and D. Osterberg. 2012. Wetland restoration in Iowa: challenges and opportunities. Iowa Policy Project Report. Iowa Policy Project, Iowa City, Iowa.

Fink, D.F., and W.J. Mitsch. 2004. Seasonal and storm event nutrient removal by a created wetland in an agricultural watershed. Ecological Engineering 23(4):313-325.

Holland, J. F., J.F. Martin, T. Granata, V. Bouchard, M. Quigley, L. Brown. 2004. Effects of wetland depth and flow rate on residence time distribution characteristics. Ecological Engineering 23(3):189–203. doi:10.1016/j.ecoleng.2004.09.003.

Iowa Department of Agriculture and Land Stewardship, Iowa Department of Natural Resources, Iowa State University College of Agriculture and Life Sciences. 2016. Iowa Nutrient Reduction Strategy: A science and technology-based framework to assess and reduce nutrients to Iowa waters and the Gulf of Mexico. *http://www.nutrientstrategy.iastate.edu/sites/default/files/documents/INRSfull-161001.pdf. Accessed online October, 2016*

Kadlec, R.H. 1994. Detention and mixing in free water wetlands. Ecological Engineering 3(4):345–80. doi:10.1016/0925-8574(94)00007-7.

Kadlec, R.H., and S. Wallace. 2008. *Treatment Wetlands, Second Edition*. CRC Press, Boca Raton, FL., U.S.A.

Keefe, S.H., J.S. Thullen-Daniels, R.L. Runkel, R.D. Wass, E.A. Stiles, and L.B. Barber. 2010. Influence of hummocks and emergent vegetation on hydraulic performance in a surface flow wastewater treatment wetland. Water Resources Research 46(11):W11518. doi:10.1029/2010WR009512.

Mitsch, W.J., and J.W. Day. 2006. Restoration of wetlands in the Mississippi–Ohio–Missouri (MOM) river basin: Experience and needed research. Ecological Engineering 26(1):55–69. doi:10.1016/j.ecoleng.2005.09.005.

Mossman, D.J., F.M. Holly, and J.L. Schnoor. 1991. Field observations of longitudinal dispersion in a run-of-the-river impoundment. Water Research 25(11):1405–15. doi:10.1016/0043-1354(91)90119-B.

Nepf, H. M., C. G. Mugnier, and R. A. Zavistoski. 1997. The effects of vegetation on longitudinal dispersion. Estuarine, Coastal and Shelf Science 44(6):675–84. doi:10.1006/ecss.1996.0169.

Persson, J. 2000. The hydraulic performance of ponds of various layouts. Urban Water 2(3):243–50. doi:10.1016/S1462-0758(00)00059-5.

Shucksmith, J. D., J. B. Boxall, and I. Guymer. 2010. Effects of emergent and submerged natural vegetation on longitudinal mixing in open channel flow. Water Resources Research 46(4):W04504. doi:10.1029/2008WR007657.

Stearman, G. K., D. B George, K. Carlson, S. Lansford. 2003. Pesticide removal from container nursery runoff in constructed wetland cells. Journal of Environmental Quality 32:1548-1556.

Thackston, E.L., D.Jr. Shields, and P.R. Schroeder. 1987. Residence time distributions of shallow basins. Journal of Environmental Engineering 113(6):1319–32. doi:10.1061/(ASCE)0733-9372(1987)113:6(1319).

Woltemade, C. J. 2000. Ability of restored wetlands to reduce nitrogen and phosphorus concentrations in agricultural drainage water. Journal of Soil and Water Conservation 55(3):303–9.

Wörman, A., and V. Kronnäs. 2005. Effect of pond shape and vegetation heterogeneity on flow and treatment performance of constructed wetlands. Journal of Hydrology 301(1–4):123–38. doi:10.1016/j.jhydrol.2004.06.038.

Yen, Ben Chie. 1992. *Channel Flow Resistance: Centennial of Manning's Formula*. Water Resources Publications.

Zedler, J.B. 2003. Wetlands at your service: Reducing impacts of agriculture at the watershed scale. Frontiers in Ecology and the Environment 1(2):65–72. doi:10.1890/1540-9295(2003)001[0065:WAYSRI]2.0.CO;2.